

Quantum transport in nanowire networks

de Moor, Michiel

DOI

[10.4233/uuid:59e7cafc-2345-44e0-8f26-4370288898a3](https://doi.org/10.4233/uuid:59e7cafc-2345-44e0-8f26-4370288898a3)

Publication date

2019

Document Version

Final published version

Citation (APA)

de Moor, M. (2019). *Quantum transport in nanowire networks*. [Dissertation (TU Delft), Delft University of Technology]. <https://doi.org/10.4233/uuid:59e7cafc-2345-44e0-8f26-4370288898a3>

Important note

To cite this publication, please use the final published version (if applicable).
Please check the document version above.

Copyright

Other than for strictly personal use, it is not permitted to download, forward or distribute the text or part of it, without the consent of the author(s) and/or copyright holder(s), unless the work is under an open content license such as Creative Commons.

Takedown policy

Please contact us and provide details if you believe this document breaches copyrights.
We will remove access to the work immediately and investigate your claim.

QUANTUM TRANSPORT IN NANOWIRE NETWORKS

QUANTUM TRANSPORT IN NANOWIRE NETWORKS

Proefschrift

ter verkrijging van de graad van doctor
aan de Technische Universiteit Delft,
op gezag van de Rector Magnificus prof. dr. ir. T.H.J.J. van der Hagen,
voorzitter van het College voor Promoties,
in het openbaar te verdedigen op dinsdag 16 april 2019 om 10:00 uur

door

Michiel Wouter Adrianus DE MOOR

Natuurkundig ingenieur, Technische Universiteit Eindhoven, Nederland
geboren te Tilburg, Nederland.

Dit proefschrift is goedgekeurd door de
promotor: prof. dr. ir. L. P. Kouwenhoven

Samenstelling promotiecommissie:

Rector Magnificus,	voorzitter
Prof. dr. ir. L. P. Kouwenhoven,	Technische Universiteit Delft, promotor
Dr. A. Geresdi,	Technische Universiteit Delft, copromotor

Onafhankelijke leden:

Prof. dr. T. Schäpers,	Forschungszentrum Jülich
Prof. dr. B. M. Terhal,	Technische Universiteit Delft
Dr. A. R. Akhmerov,	Technische Universiteit Delft
Prof. dr. A. F. Otte,	Technische Universiteit Delft



Keywords: Majorana zero modes, semiconductor nanowires, superconductors, nanoscale physics.

Printed by: Gildeprint

Cover: Drawing of a nanowire network device (front), sketches of several proposals for nanowire network based qubits (back).

Design by M. W. A. de Moor.

Copyright © 2019 by M. W. A. de Moor

Casimir PhD Series, Delft-Leiden 2019-11

ISBN 978-90-8593-393-9

An electronic version of this dissertation is available at
<http://repository.tudelft.nl/>.

*... Want tussen droom en daad
Staan wetten in de weg en praktische bezwaren*

Willem Elsschot, Het Huwelijk

CONTENTS

Summary	xi
Samenvatting	xiii
1 Introduction	1
1.1 From quantum physics to quantum technologies	2
1.2 Topological quantum states	3
1.3 Topological quantum computation in nanowire networks	5
1.4 Thesis outline	5
References	6
2 Theory	9
2.1 Superconductivity and the Bogoliubov-de Gennes equation	10
2.2 Transport through an NS-interface	11
2.3 Tunneling spectroscopy	12
2.4 The 1D Majorana nanowire model	13
2.5 Aharonov-Bohm effect in mesoscopic rings	17
References	20
3 Fabrication procedures and experimental methods	23
3.1 Fabrication of nanowire devices	24
3.2 Processing of InSb nanowires with epitaxial Al	26
3.3 Selective etching of epitaxial Al on InSb nanowires	28
3.4 Electrical measurement set-up	32
3.5 Low temperature set-ups	33
References	35
4 Epitaxy of advanced nanowire quantum devices	37
4.1 Introduction	38
4.2 Substrate fabrication and nanowire growth	38
4.3 Phase-coherent transport in nanohashtags	41
4.4 Superconducting gap in shadowed junctions	43
4.5 Conclusion	45
4.6 Methods and additional data	45
4.6.1 Substrate fabrication	45
4.6.2 Nanowire growth	48
4.6.3 Growth of superconducting aluminum islands	49
4.6.4 Aharonov-Bohm devices	49
4.6.5 Hard gap devices	53
References	55

5	Aharonov-Bohm effect in SAG nanowire networks	59
5.1	Growth and device fabrication	60
5.2	Magnetoconductance oscillations in SAG networks	61
5.3	Data processing to obtain AB amplitudes	62
5.4	Temperature dependence of AB oscillations	62
5.5	Aharonov-Bohm loop without dephasing stubs	66
5.6	Conclusion	68
	References	68
6	Electric field tunable superconductor-semiconductor coupling	71
6.1	Introduction	72
6.2	Experimental set-up	72
6.3	Theoretical model.	73
6.4	Gate voltage dependence of the induced superconducting gap	74
6.5	Effective g -factor	76
6.6	Level repulsion due to spin-orbit coupling	78
6.7	Zero Bias Peak in extended magnetic field range	80
6.8	Conclusion & Outlook.	81
6.9	Methods and additional data	82
6.9.1	Fabrication and device design	82
6.9.2	Simulation of electrostatics and nanowire spectrum	83
6.9.3	Electric field dependence of spin-orbit coupling.	85
6.9.4	Simulated band structure	87
6.9.5	Gap fitting & additional device data	87
6.9.6	g -factor fitting & additional device data	89
6.9.7	Anticrossing fitting.	91
6.9.8	Simulation of finite size nanowire system	92
6.9.9	Additional ZBP data	95
	References	97
7	Nanocrosses for Majorana correlation experiments	103
7.1	Introduction	104
7.2	Nanocross device layout and experimental setup	104
7.3	Ballistic NS junctions in nanocross devices	105
7.4	Zero bias conductance peaks in nanocross devices	108
7.5	Discussion and experimental outlook.	109
	References	111
8	Bound states in 1D Majorana nanowires	113
8.1	Introduction	114
8.2	Experimental context and theoretical model	114
8.3	Hard wall barrier	116
8.4	Smooth barrier confinement	118
8.5	Coupling to lead through the barrier	123
8.6	Armchair barrier	125
8.7	Conclusion	128
	References	129

9 Conclusion and outlook	133
9.1 Conclusions.	134
9.2 Materials and fabrication improvements	135
9.3 Majorana experiments in nanowire networks	136
9.4 Perspective on qubit proposals	139
References	142
Acknowledgements	145
Curriculum Vitæ	147
List of Publications	149

SUMMARY

Quantum technology is a promising area of research, with the quantum computer as the prime example. Quantum computers can perform calculations thought to be impossible by conventional means. The fundamental building block of a quantum computer is a qubit, which is a quantum system which can be used to process and store quantum information. Most qubits can hold on to this quantum information for only a short period of time due to environmental noise. The resulting errors can be mitigated by storing the information in multiple qubits. An alternative approach uses qubits which are insensitive to noise. This can be achieved by using topological quantum states.

An example of a topological quantum state is the Majorana zero mode. Majorana zero modes can be realized in a 1D system with strong spin-orbit coupling and superconductivity, in an external magnetic field. Such materials are not known in nature, but can be engineered by coupling a semiconductor nanowire to a superconducting material. To use these Majorana zero modes as qubits, multiple nanowires have to be connected to each other in a 2D network. The experiments described in this thesis aim to develop such networks based on InSb (indium antimonide) semiconductor nanowires.

A few necessary theoretical concepts are briefly introduced. Subsequently, the nanofabrication and electrical measurement techniques used to study the nanowires are described, with emphasis on the challenges related to working with hybrid semiconductor-superconductor (InSb-Al) materials. Two methods are then presented to realize nanowire networks. Transport experiments on these networks show strong phase coherence and a hard superconducting gap, demonstrating the high quality of the material.

In addition to the intrinsic quality of the material, the electrostatic environment plays an important role for the functionality of hybrid materials. The coupling between the superconductor (Al) and the semiconductor (InSb) is studied by applying an external electric field. This electric field influences material properties such as the spin-orbit coupling and the Landé g -factor. An essential property of the Majorana zero modes is the fact that their state cannot be described locally. Exploratory experiments with the aim of demonstrating this non-locality are described, followed by theoretical simulations demonstrating the limitations of common experimental practice based on local measurements. Finally, several suggestions for future experiments are made, aimed at demonstrating and manipulating Majorana zero modes.

SAMENVATTING

Kwantumtechnologie is een veelbelovend onderzoeksgebied, met als belangrijkste exponent de kwantumcomputer. Kwantumcomputers kunnen berekeningen uitvoeren die met conventionele computers onmogelijk worden geacht. De fundamentele bouwsteen van een kwantumcomputer is een qubit, een kwantumsysteem waar kwantum-informatie mee verwerkt en opgeslagen kan worden. De meeste qubits kunnen de kwantum-informatie echter slechts korte tijd vasthouden vanwege ruis. De resulterende fouten kunnen worden geminimaliseerd door de informatie in meer qubits op te slaan. Een alternatieve oplossing is de qubits ongevoelig te maken voor ruis. Dit kan worden bereikt met zogenaamde topologische kwantumtoestanden.

Een voorbeeld van een topologische kwantumtoestand is de Majorana toestand. Majorana toestanden kunnen worden gerealiseerd in een 1D systeem met sterke spin-baan koppeling en supergeleiding in een extern magnetisch veld. Een dergelijk materiaal komt niet voor in de natuur, maar kan worden gerealiseerd door een halfgeleider nanodraad te koppelen aan een supergeleidend materiaal. Om deze Majorana toestanden te kunnen gebruiken als qubit, moeten zulke nanodraden met elkaar worden verbonden in een 2D netwerk. De experimenten die zijn beschreven in dit proefschrift hebben als doel de ontwikkeling van dergelijke netwerken op basis van InSb (indiumantimonide) halfgeleider nanodraden.

Eerst worden enkele noodzakelijke theoretische concepten kort geïntroduceerd. Vervolgens worden de nanofabricagetechnieken en elektrische meettechnieken beschreven die zijn gebruikt om de nanodraden te bestuderen, met nadruk op de moeilijkheden die gepaard gaan met het werken met hybride halfgeleider-supergeleider (InSb-Al) materialen. Hierna worden twee verschillende methoden gepresenteerd om nanodraad-netwerken te realiseren. Transport experimenten in deze netwerken laten een sterke fasecoherentie en een zogenaamde harde supergeleidende kloof zien, wat de hoge kwaliteit van het materiaal aantoont.

Naast de kwaliteit van het materiaal zelf is de elektrostatische omgeving van groot belang voor het functioneren van hybride materialen. De koppeling tussen de supergeleider (Al) en de halfgeleider (InSb) wordt bestudeerd door de aanleg van een extern elektrisch veld. Dit elektrisch veld beïnvloedt de materiaaleigenschappen zoals de spin-baan koppeling en de Landé g -factor. Een essentiële eigenschap van de Majorana toestand is het feit dat deze niet lokaal beschreven kan worden. Inleidende experimenten met als doel het aantonen van deze niet-lokaliteit worden beschreven, gevolgd door theoretische berekeningen die de beperkingen laten zien van de gangbare experimentele praktijk gebaseerd op lokale metingen. Tot besluit worden enkele suggesties voor toekomstige experimenten gedaan, gericht op het aantonen en manipuleren van Majorana toestanden.

1

INTRODUCTION

There is nothing more difficult to take in hand, more perilous to conduct, or more uncertain in its success, than to take the lead in the introduction of a new order of things.

Niccolò Machiavelli, *Il Principe*

1.1. FROM QUANTUM PHYSICS TO QUANTUM TECHNOLOGIES

The defining technologies of the second half of the twentieth century, such as the laser and the semiconductor transistor, are rooted in our improved understanding of matter, enabled by quantum mechanics. In this sense, they can be considered the first generation of quantum technologies. In most cases, however, their operation can be understood in classical or semiclassical terms, without resorting to quantum principles such as superposition or entanglement. The second generation of quantum technologies promises to leverage these properties as resources for secure communication [1], high precision metrology [2] and sensors [3], and computation [4]. Quantum research has gone from the seminal experiments demonstrating entanglement [5, 6] and initial schemes for its use as a resource [7, 8] to large scale efforts to build a universal quantum computer, along with a plethora of other proposals [9], which appear to be on the cusp of entering the commercial domain.

The fundamental unit of a quantum computer is the quantum bit, or qubit [10]. A qubit consists of a two-level quantum system, or an isolated pair of states in a multi-level system, which can be decoupled from its environment and addressed using suitable control signals [11]. Interest in quantum computation has surged with the demonstration of qubits in solid state platforms, such as spin qubits [12] or superconducting transmon qubits [13]. Because they can be fabricated using natural extensions of current technological capabilities, paths towards scaling up these systems seem wide open [14]. However, several bottlenecks have been identified that have so far limited solid state platforms to a handful of qubits. An important limitation of these qubits is their susceptibility to noise from the surrounding material. One can think of electrical or charge noise [15], for example from dislocations in the crystal lattice or nearby surfaces, or magnetic noise due to localized magnetic moments in the nuclei of the constituent atoms [16] or at thin film interfaces [17]. These noise sources interact with the quantum bits in an uncontrolled manner, scrambling the information stored in them. This type of information loss can be mitigated by storing the information in a redundant fashion [18]. Following classical error correction codes used e.g. in hard drives, advances in the field of quantum error correction have brought optimism to the prospect of realizing a fault-tolerant universal quantum computer [19]. These error correction schemes work by discretizing and keeping track of errors as they occur, and then using feedback to keep the system in the desired state. As long as the additional errors applied due to imperfect feedback are small, and the errors that have to be corrected infrequent, architectures such as the surface code can be used to robustly store quantum information [20].

Although these schemes are expected to be successful in protecting quantum information, they require a large amount of overhead. One estimate puts the number of physical superconducting transmon qubits required for fault-tolerant operation of a single logical qubit at 49 [21], which represents a significant overhead for the execution of quantum algorithms. It is therefore of great interest to explore alternative ways of storing quantum information which are intrinsically protected from errors.

1.2. TOPOLOGICAL QUANTUM STATES

While in three dimensions the wave function representing a quantum state of many identical particles is either symmetric (bosons) or antisymmetric (fermions) with respect to the exchange of two particles, other possibilities arise if the system is two dimensional [22]. These new particles are referred to as anyons [23]. Anyonic excitations are found in topological phases of matter, which are characterized by a many-quasiparticle ground state that is degenerate as long as the quasiparticles are well-separated from each other [24]. Different types of anyons are distinguished by the effect of operations exchanging the positions of two particles (called braiding operations or braids), and the number of ways two anyons can be combined to form new quasiparticles (their fusion channels).

For Abelian anyons, consecutive braiding operations commute. Braiding two Abelian anyons results in the same state with an added global phase factor, and there is only one way to fuse two Abelian anyons. In contrast, for non-Abelian anyons braiding operations do not commute in general, and braiding two quasiparticles can result in a non-trivial rotation in the ground state subspace. Importantly, braiding is the only way to perform such a rotation. Additionally, there is more than one fusion channel for non-Abelian anyons, i.e. combining two of them can have multiple results. These properties allow us to use non-Abelian anyons to form topological quantum bits: we can initialize the qubit by creating anyonic particles in a well-defined state, perform qubit operations by braiding them, and read out the result by fusing the anyons at the end of the computation. As there are no local operations which can perturb the qubit, and the errors due to finite overlap between the quasiparticle wave functions decay exponentially with system size, a topological qubit is intrinsically fault-tolerant [25]. In a sense, it can be considered the physical manifestation of the surface code architecture mentioned in the previous section.

A seemingly unrelated topic is the study of band insulators and superconductors. In such systems, there is a finite energy cost for single particle excitations, called the energy gap. These systems can be classified according to the symmetries of their Hamiltonian and their dimensionality [26]. In this classification, two Hamiltonians are considered topologically distinct if they cannot be continuously changed into one another without closing the energy gap of the system. This means that when we create an interface between two gapped systems with a different topology, the gap must close at the interface. This can create zero energy surface states, which are protected against local perturbations as long as the bulk gap does not close. These surface or edge states (terminology depending on the dimensionality) are called symmetry protected topological states [27].

In one dimension, it has been demonstrated that the Hamiltonian in the class BDI describing a p -wave superconductor can harbor zero energy states which are localized at the ends of the one dimensional chain [28]. These zero energy states represent a non-local way to store a single fermionic degree of freedom, which can be described by two Majorana bound states. These Majoranas are non-Abelian anyons, following the braiding statistics and fusion rules of so-called Ising anyons. The wave function overlap of

the Majoranas can be used to fuse them and read out the occupation of the fermionic state. The states of the qubit are given by the parity of the Majorana state: $|0\rangle = \text{even}$, $|1\rangle = \text{odd}$. As changing the parity requires an additional fermion to enter the superconductor, two Majorana bound states are insufficient to form a qubit in a closed system. However, one can use four Majorana bound states, which combined with parity conservation create a two level system that can be manipulated using braiding operations. In principle, every pair of Majorana zero modes which is added to the system will increase the ground state degeneracy by a factor of 2, adding a qubit to the computational space. However, because the effect of specific braiding operations changes depending on the number of anyons present, this is impractical because the gate operations have to be redefined every time a qubit is added or removed [24]. Therefore, qubits are generally defined in closed systems with a fixed number of Majorana zero modes, which can then be connected to other qubits via a suitable interface. Although braiding and fusing Ising anyons is not sufficient for topologically protected universal quantum computation, one can achieve universal operation by using an ancillary qubit and a distillation procedure [29], or a magic gate protocol [30].

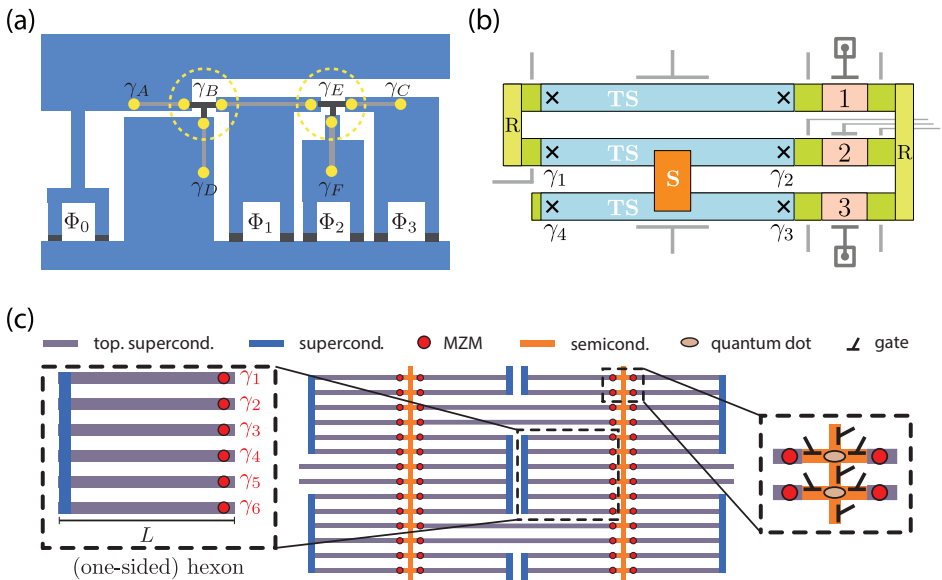


Figure 1.1: **Proposals for topological qubits based on nanowire networks.** (a) Flux controlled Majorana interaction using nanowire T-junctions and SQUID loops. Adapted from ref. [31]. (b) Majorana box qubit based on a superconducting island coupled to multiple quantum dots via a nanowire grid. Adapted from ref. [32]. (c) Topological qubit based on a comb-like nanowire structure connected to quantum dots to form a nanowire network. Adapted from ref. [33].

1.3. TOPOLOGICAL QUANTUM COMPUTATION IN NANOWIRE NETWORKS

During the discussion of Majorana zero modes in the previous section, we neglected to mention that there are no known 1D p -wave superconductors in nature. They can, however, be engineered by combining an s -wave superconductor with a semiconductor nanowire with strong spin-orbit coupling [34, 35]. The system is predicted to go through a topological phase transition upon application of a suitable magnetic field, creating Majorana zero modes at the wire ends. In such a 1D system, there is no well defined way to exchange two particles, which is problematic because we want to use braiding for our qubit operations. To overcome this particular hurdle, it has been suggested to connect multiple 1D Majorana wires in a 2D network to create the required connectivity [36]. While this type of architecture can be utilized to physically move the domain walls where the MZMs are localized, this is impractical. Several other proposals have emerged which use the controlled interaction between Majorana bound states to effectively braid and fuse them. In Fig. 1.1, we show several such proposals. Instead of physically moving the positions of the Majoranas, these schemes control the Majorana interactions via Coulomb energy [31, 37], or by coupling the MZMs to an external quantum dot which can be used to make projective measurements [32, 33]. While these schemes differ in their details, they all require semiconductor nanowires hybridized with superconductors and connected in some kind of two dimensional network.

1.4. THESIS OUTLINE

The work presented in this thesis aims to develop semiconductor nanowire networks as a platform for topological information processing. This is achieved by using nanofabrication techniques to make nanowire based devices and exploring their properties using electrical measurements.

Chapter 2 introduces theoretical concepts that are useful to understand the components of nanowire network based topological qubits, such as the 1D nanowire model developed by Lutchyn et al. [34] and Oreg et al. [35], which is the workhorse of nanowire based Majorana physics. We also give brief introductions to superconductivity, transport through an interface between a semiconductor and a superconductor, and the Aharonov-Bohm effect in mesoscopic rings. The methods used to fabricate samples and measure devices are introduced in **chapter 3**. Specifically, results relating to the selective etching of Al on InSb nanowires are presented. **Chapter 4** describes the growth of nanowire networks using the vapor-liquid-solid (VLS) growth technique. The transport properties of these networks are characterized by measuring the Aharonov-Bohm effect in the magnetoconductance, as well as by tunneling spectroscopy measurements of the superconducting gap. An alternative method of growing nanowire networks, the selective area growth method (SAG), is described in **chapter 5**. We use the Aharonov-Bohm effect to investigate dephasing mechanisms in these nanostructures. **Chapter 6** describes experiments performed on hybrid superconductor-semiconductor nanowires to explore the effects of the electrostatic environment on the hybridization between the two materi-

als. We find that the device behavior is strongly affected by the electric fields generated by the gates surrounding the nanowire device. In **chapter 7** we describe experiments performed in InSb nanocrosses with the aim of investigating the non-local structure of Majorana zero modes. **Chapter 8** provides an overview of recent literature on the topic of local zero modes, which can mimic Majorana properties under certain experimental conditions. This discussion is supplemented by numerical simulations. Finally, in **chapter 9** we provide an outlook on future experiments in nanowire networks, with an eye towards Majorana physics.

REFERENCES

- [1] S. Wehner, D. Elkouss, and R. Hanson, *Quantum internet: A vision for the road ahead*, *Science* **362**, eaam9288 (2018).
- [2] V. Giovannetti, S. Lloyd, and L. Maccone, *Advances in quantum metrology*, *Nature Photonics* **5**, 222 (2011).
- [3] C. L. Degen, F. Reinhard, and P. Cappellaro, *Quantum sensing*, *Rev. Mod. Phys.* **89**, 035002 (2017).
- [4] T. D. Ladd, F. Jelezko, R. Laflamme, Y. Nakamura, C. Monroe, and J. L. O'Brien, *Quantum computers*, *Nature* **464**, 45 (2010).
- [5] S. J. Freedman and J. F. Clauser, *Experimental Test of Local Hidden-Variable Theories*, *Phys. Rev. Lett.* **28**, 938 (1972).
- [6] A. Aspect, P. Grangier, and G. Roger, *Experimental Realization of Einstein-Podolsky-Rosen-Bohm Gedankenexperiment: A New Violation of Bell's Inequalities*, *Phys. Rev. Lett.* **49**, 91 (1982).
- [7] P. W. Shor, *Polynomial-Time Algorithms for Prime Factorization and Discrete Logarithms on a Quantum Computer*, *SIAM Journal on Computing* **26**, 1484 (1997).
- [8] L. K. Grover, *Quantum Mechanics Helps in Searching for a Needle in a Haystack*, *Phys. Rev. Lett.* **79**, 325 (1997).
- [9] High-Level Steering Committee, *Quantum Technologies Flagship Final Report*, Tech. Rep. (European Commission, 2017).
- [10] M. A. Nielsen and I. L. Chuang, *Quantum Computation and Quantum Information*, 10th ed. (Cambridge University Press, 2010).
- [11] D. P. DiVincenzo, *The Physical Implementation of Quantum Computation*, *Fortschritte der Physik* **48**, 771 (2000).
- [12] R. Hanson, L. P. Kouwenhoven, J. R. Petta, S. Tarucha, and L. M. K. Vandersypen, *Spins in few-electron quantum dots*, *Rev. Mod. Phys.* **79**, 1217 (2007).
- [13] J. Koch, T. M. Yu, J. Gambetta, A. A. Houck, D. I. Schuster, J. Majer, A. Blais, M. H. Devoret, S. M. Girvin, and R. J. Schoelkopf, *Charge-insensitive qubit design derived from the Cooper pair box*, *Phys. Rev. A* **76**, 042319 (2007).

- [14] A. S. Dzurak, *Spin-based quantum computing in silicon CMOS-compatible platforms*, in *2016 IEEE International Electron Devices Meeting (IEDM)* (2016) pp. 13.2.1–13.2.2.
- [15] F. Luthi, T. Stavenga, O. W. Enzing, A. Bruno, C. Dickel, N. K. Langford, M. A. Rol, T. S. Jespersen, J. Nygård, P. Krogstrup, and L. DiCarlo, *Evolution of Nanowire Transmon Qubits and Their Coherence in a Magnetic Field*, *Phys. Rev. Lett.* **120**, 100502 (2018).
- [16] H. Bluhm, S. Foletti, I. Neder, M. Rudner, D. Mahalu, V. Umansky, and A. Yacoby, *Dephasing time of GaAs electron-spin qubits coupled to a nuclear bath exceeding 200 μ s*, *Nature Physics* **7**, 109 (2011).
- [17] M. D. Hutchings, J. B. Hertzberg, Y. Liu, N. T. Bronn, G. A. Keefe, M. Brink, J. M. Chow, and B. L. T. Plourde, *Tunable Superconducting Qubits with Flux-Independent Coherence*, *Phys. Rev. Applied* **8**, 044003 (2017).
- [18] D. Gottesman, *An Introduction to Quantum Error Correction and Fault-Tolerant Quantum Computation*, *Proceedings of Symposia in Applied Mathematics* **68**, 2762145 (2010).
- [19] J. Preskill, *Quantum Computing in the NISQ era and beyond*, *Quantum* **2**, 79 (2018).
- [20] B. M. Terhal, *Quantum error correction for quantum memories*, *Rev. Mod. Phys.* **87**, 307 (2015).
- [21] T. E. O’Brien, B. Tarasinski, and L. DiCarlo, *Density-matrix simulation of small surface codes under current and projected experimental noise*, *npj Quantum Information* **3**, 39 (2017).
- [22] J. M. Leinaas and J. Myrheim, *On the theory of identical particles*, *Il Nuovo Cimento B* **37**, 1 (1977).
- [23] F. Wilczek, *Magnetic Flux, Angular Momentum, and Statistics*, *Phys. Rev. Lett.* **48**, 1144 (1982).
- [24] C. Nayak, S. H. Simon, A. Stern, M. Freedman, and S. Das Sarma, *Non-Abelian anyons and topological quantum computation*, *Rev. Mod. Phys.* **80**, 1083 (2008).
- [25] A. Y. Kitaev, *Fault-tolerant quantum computation by anyons*, *Annals of Physics* **303**, 2 (2003).
- [26] S. Ryu, A. P. Schnyder, A. Furusaki, and A. W. W. Ludwig, *Topological insulators and superconductors: tenfold way and dimensional hierarchy*, *New Journal of Physics* **12**, 065010 (2010).
- [27] T. Senthil, *Symmetry-Protected Topological Phases of Quantum Matter*, *Annual Review of Condensed Matter Physics* **6**, 299 (2015).
- [28] A. Y. Kitaev, *Unpaired majorana fermions in quantum wires*, *Physics-Uspekhi* **44**, 131 (2001).

- [29] S. Bravyi and A. Kitaev, *Universal quantum computation with ideal Clifford gates and noisy ancillas*, Phys. Rev. A **71**, 022316 (2005).
- [30] T. Karzig, Y. Oreg, G. Refael, and M. H. Freedman, *Universal Geometric Path to a Robust Majorana Magic Gate*, Phys. Rev. X **6**, 031019 (2016).
- [31] T. Hyart, B. van Heck, I. C. Fulga, M. Burrello, A. R. Akhmerov, and C. W. J. Beenakker, *Flux-controlled quantum computation with Majorana fermions*, Phys. Rev. B **88**, 035121 (2013).
- [32] S. Plugge, A. Rasmussen, R. Egger, and K. Flensberg, *Majorana box qubits*, New Journal of Physics **19**, 012001 (2017).
- [33] T. Karzig, C. Knapp, R. M. Lutchyn, P. Bonderson, M. B. Hastings, C. Nayak, J. Alicea, K. Flensberg, S. Plugge, Y. Oreg, C. M. Marcus, and M. H. Freedman, *Scalable designs for quasiparticle-poisoning-protected topological quantum computation with Majorana zero modes*, Phys. Rev. B **95**, 235305 (2017).
- [34] R. M. Lutchyn, J. D. Sau, and S. Das Sarma, *Majorana Fermions and a Topological Phase Transition in Semiconductor-Superconductor Heterostructures*, Phys. Rev. Lett. **105**, 077001 (2010).
- [35] Y. Oreg, G. Refael, and F. von Oppen, *Helical Liquids and Majorana Bound States in Quantum Wires*, Phys. Rev. Lett. **105**, 177002 (2010).
- [36] J. Alicea, Y. Oreg, F. von Oppen, and M. P. A. Fisher, *Non-Abelian statistics and topological quantum information processing in 1D wire networks*, Nature Physics **7**, 412 (2011).
- [37] D. Aasen, M. Hell, R. V. Mishmash, A. Higginbotham, J. Danon, M. Leijnse, T. S. Jespersen, J. A. Folk, C. M. Marcus, K. Flensberg, and J. Alicea, *Milestones Toward Majorana-Based Quantum Computing*, Phys. Rev. X **6**, 031016 (2016).

2

THEORY

I have a theoretical degree in physics.

Fantastic, Fallout New Vegas

This chapter describes theoretical concepts which are useful for understanding the work performed in this thesis. We start with an overview of BCS superconductivity. Then we describe the transport through an interface between a normal conductor and a superconductor. The principles behind tunneling spectroscopy are briefly introduced. We also give an overview of the 1D Majorana nanowire model, which will be expanded upon in the rest of the thesis. Finally, we review the Aharonov-Bohm effect in mesoscopic devices.

2.1. SUPERCONDUCTIVITY AND THE BOGOLIUBOV-DE GENNES EQUATION

Superconductivity describes the scenario where the electrical resistivity of certain materials goes to zero when they are cooled to low enough temperatures, allowing charge to flow without dissipation [1]. These freely flowing currents can screen any magnetic fields from the interior of the superconductor, resulting in perfect diamagnetism, also known as the Meissner effect [2]. The superconducting state is a consequence of a low temperature phase transition, which can be understood macroscopically using Ginzburg-Landau theory [3].

At the microscopic level, superconductivity is generally described using the theory by Bardeen, Cooper, and Schrieffer (BCS theory) [4]. We follow the treatment of ref. [5], and write the following pairing Hamiltonian:

$$H_k = \sum_{k,\sigma} \xi_k c_{k\sigma}^\dagger c_{k\sigma} + \sum_{k,k'} V_{kk'} c_{k'\uparrow}^\dagger c_{-k'\downarrow}^\dagger c_{-k\downarrow} c_{k\uparrow}. \quad (2.1)$$

In this Hamiltonian, ξ_k is the single particle energy relative to the Fermi energy E_F , the operators $c_{k\sigma}^\dagger$ ($c_{k\sigma}$) are the creation (annihilation) operators for an electron with momentum k and spin σ , respectively, and $V_{kk'}$ is the matrix element of the pairwise interaction between two electrons. In the BCS description of superconductivity, this interaction is mediated by phonons. Furthermore, it is assumed that this interaction is attractive and is non-zero only in a small range of energies around E_F , with the cut-off set by the Debye energy. Under these conditions, pairs of electrons will form bound states called Cooper pairs. All that is required for the formation of Cooper pairs is a Fermi sea with an interaction which is attractive for energies close to the Fermi energy, and negligible beyond a certain cut-off energy determined by the nature of the interaction [6]. The Cooper pairs condense into a new ground state, called the BCS condensate.

If the density of states at E_F is large, we can assume that the expectation value of the number of particles taking part in the superconducting state is also large, and that fluctuations around the expectation value are small. In this case, we can use a mean field approximation to convert equation 2.1 to

$$H_{MF} = \sum_{k,\sigma} \xi_k c_{k\sigma}^\dagger c_{k\sigma} - \sum_k \left(\Delta_k c_{k\uparrow}^\dagger c_{-k\downarrow}^\dagger + \Delta_k^* c_{-k\downarrow} c_{k\uparrow} \right), \quad (2.2)$$

with $\Delta_k = -\sum_{k'} V_{kk'} \langle c_{-k'\downarrow} c_{k'\uparrow} \rangle$. Note that this description no longer conserves the number of particles, but rather the parity. Because we are interested in single particle excitations from the ground state, terms that add only to the ground state energy have been omitted. We can diagonalize this Hamiltonian via a transformation introduced by Bogoliubov [7]:

$$\begin{aligned} c_{k\uparrow} &= u_k^* \gamma_{k,1} + v_k \gamma_{k,2}^\dagger, \\ c_{-k\downarrow}^\dagger &= -v_k^* \gamma_{k,1} + u_k \gamma_{k,2}^\dagger. \end{aligned} \quad (2.3)$$

The eigenstates of the Hamiltonian are Bogoliubov quasiparticles, or Bogoliubons, $\gamma_{k,(1,2)}$, with energies $E_k = \sqrt{\xi_k^2 + \Delta_k^2}$. They consist of electron-like (u) and hole-like (v) compo-

nents. We see that the minimum energy cost for a quasiparticle excitation is Δ , the superconducting gap. Taking $\Delta_k = \Delta$, we can calculate u and v by solving the Bogoliubov-de Gennes (BdG) equation:

$$H_{\text{BdG}} \begin{pmatrix} u_k \\ v_k \end{pmatrix} = E_k \begin{pmatrix} u_k \\ v_k \end{pmatrix}, \quad H_{\text{BdG}} = \begin{pmatrix} \xi_k & \Delta \\ \Delta^* & -\xi_k^* \end{pmatrix}, \quad (2.4)$$

with the solution

$$|u_k|^2 = 1 - |v_k|^2 = \frac{1}{2} \left(1 + \frac{\xi_k}{E_k} \right). \quad (2.5)$$

Note that while it appears we have obtained two solutions to the BdG equation, these solutions are in fact not independent. For each solution with an energy E , there is a corresponding solution with energy $-E$. This particle-hole symmetry is the result of the mean field approximation. Together the two solutions describe the same single particle excitation.

2.2. TRANSPORT THROUGH AN NS-INTERFACE

The Bogoliubov-de Gennes equation can also be used in case the superconductor is not uniform in space. To illustrate this, we examine the interface between a normal conductor (N) and a superconductor (S). In Fig. 2.1 we show the linearized dispersion of the normal conductor, $E(k) = \hbar v_F k - E_F$, on the left, and the dispersion calculated using the solution to the BdG equation with $\xi(k) = \hbar v_F k - E_F$ on the right. At the interface, we include a potential barrier $V(x) = V_0 \delta(x)$.

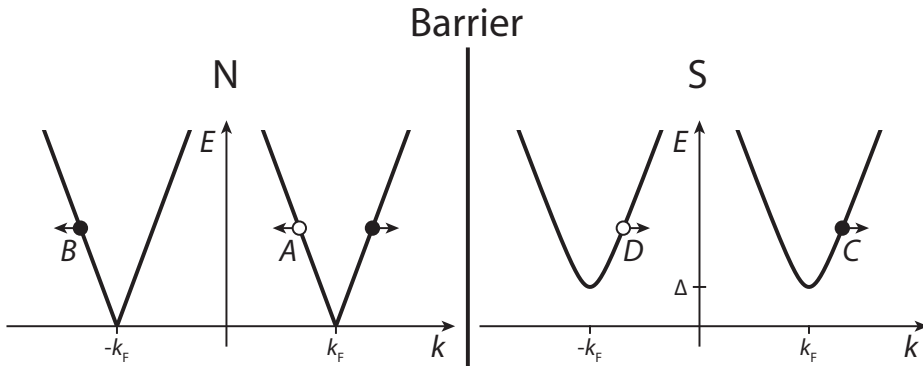


Figure 2.1: **Transport processes at an NS-interface.** Interface between a normal conductor (N) and a superconductor (S). Depending on the energy of the electron incident from the N side, it can be reflected or transmitted as a hole or an electron.

An electron incident on the interface from the N side can undergo four processes. It can be reflected back into the normal conductor as an electron (normal reflection, amplitude B), or as a hole, transferring a Cooper pair into the superconductor in the process (Andreev reflection, amplitude A). Additionally, if the energy of the electron is larger

than Δ , it can be transmitted as an electron- (amplitude C) or hole-like (amplitude D) quasiparticle. Describing the electron as a plane wave, we can write the wave functions in the N and S regions as

$$\begin{aligned}\psi_N &= \begin{pmatrix} 1 \\ 0 \end{pmatrix} e^{ik_e^N x} + A \begin{pmatrix} 0 \\ 1 \end{pmatrix} e^{ik_h^N x} + B \begin{pmatrix} 1 \\ 0 \end{pmatrix} e^{-ik_e^N x} \\ \psi_S &= C \begin{pmatrix} u \\ v \end{pmatrix} e^{ik_e^S x} + D \begin{pmatrix} u \\ v \end{pmatrix} e^{-ik_h^S x}.\end{aligned}\quad (2.6)$$

The coefficients A , B , C , and D are found by matching the wave functions at the interface. Their derivatives should also be matched, taking into account the barrier, which we parameterize as $Z = V_0 / (\hbar v_F)$. The conductance through the interface can then be written as [8] $G_{NS}(E) = \frac{2e^2}{h} (1 + A(E) - B(E))$, with

$$A(E) = \begin{cases} \frac{\Delta^2}{E^2 + (\Delta^2 - E^2)(1 + 2Z^2)^2} & E < \Delta \\ \frac{u^2 v^2}{\gamma^2} & E > \Delta \end{cases}, \quad (2.7)$$

$$B(E) = \begin{cases} 1 - A & E < \Delta \\ \frac{(u^2 - v^2)^2 Z^2 (1 + Z^2)}{\gamma^2} & E > \Delta \end{cases}, \quad (2.8)$$

$$\gamma = (u^2 + Z^2 (u^2 - v^2))^2. \quad (2.9)$$

At $E = 0$, this result can be simplified to [9]

$$G_{NS}(0) = \frac{2e^2}{h} \frac{2T^2}{(2 - T)^2}, \quad T = \frac{1}{1 + Z^2}. \quad (2.10)$$

If the normal conductor and superconductor are not made of the same material, their Fermi velocities will generally be different, which will cause additional reflections at the interface. This can be accounted for by changing the effective barrier strength to [10]

$$Z_{\text{eff}} = \left(Z^2 + \left(1 - \frac{v_{F,N}}{v_{F,S}} \right)^2 \frac{v_{F,S}}{4v_{F,N}} \right)^{1/2}. \quad (2.11)$$

In the above discussion we have used a linearized dispersion for both the normal conductor and the superconductor, which is a good approximation if $E_F \gg \Delta$. This is generally true for metals, but the approximation fails in the case of low density materials such as semiconductors. In this case, more sophisticated treatments are required, as discussed in Ref. [11].

2.3. TUNNELING SPECTROSCOPY

We can generalize the situation described in the previous section to transport between two general conductors separated by a barrier using the Landauer-Büttiker formalism [12,

13]. The density of states on the left (right) side of the barrier is $D_{L(R)}(E)$, with the occupation of the states determined by the Fermi-Dirac distribution $f_{L,R}(E)$ with a chemical potential $\mu_{L(R)}$. If we assume the transition probability \mathcal{T} from a state on the left to a state on the right only depends on energy, we can write the current at a voltage difference $eV = \mu_L - \mu_R$ as [14]

$$I(V) = -\frac{(2\pi)^2 |e|}{h} \int dE \mathcal{T}(E) D_L(E) D_R(E) (f_L(E) - f_R(E)). \quad (2.12)$$

For small bias voltages $eV \ll k_B T$, the differential conductance $G = \frac{dI}{dV}$ is then given by

$$\frac{dI}{dV} = \frac{(2\pi)^2 e^2}{h} \int dE \mathcal{T}(E) D_L(E) D_R(E) \frac{-\partial f(E + eV)}{\partial eV}. \quad (2.13)$$

In the tunneling limit, $\mathcal{T} \ll 1$, the transmission can be considered independent of energy. If in addition the density of states of the left reservoir is approximately independent of energy in the range of interest, the differential conductance is directly proportional to the density of states of the right reservoir, with a spectroscopic resolution which is set by the derivative of the Fermi-Dirac distribution.

2.4. THE 1D MAJORANA NANOWIRE MODEL

While there are several candidate systems for the realization of Majorana zero modes [15–17], the most commonly studied system consists of a one dimensional semiconductor nanowire coupled to a superconductor. At the interface between the nanowire and the superconductor, Andreev reflection processes introduce superconducting correlations in the semiconductor. This is called the proximity effect [18]. While in general the proximity effect depends on details of the materials involved as well as the interface between them, here we assume that it simply introduces a superconducting pairing with strength Δ into the semiconductor. The proximity effect will be explored in more detail in chapter 6. Combined with spin-orbit coupling and a suitable magnetic field, this system can go through a topological phase transition which results in Majorana bound states at the nanowire's ends. We will give a short overview of the general concepts, with a more detailed discussion in chapter 8. For further information we direct the reader to refs. [19–21].

The 1D Majorana nanowire system is described by the Hamiltonian [22, 23]

$$H = \left(\frac{p_x^2}{2m^*} - \mu \right) \tau_z - \frac{\alpha}{\hbar} p_x \sigma_y \tau_z + E_Z + \Delta \tau_x. \quad (2.14)$$

Here we have used to Nambu basis, $\Psi = (\psi_\uparrow, \psi_\downarrow, \psi_\uparrow^\dagger, -\psi_\downarrow^\dagger)^\top$, with ψ_σ and ψ_σ^\dagger describing electron and hole states, respectively. The first term in the Hamiltonian describes a one dimensional conductor oriented in the x -direction, with an effective mass m^* and chemical potential μ . The second term describes the Rashba spin-orbit interaction, which introduces an effective magnetic field $\frac{\alpha}{\hbar} p_x E_Z \hat{y} = B_{SO} \hat{y}$. Here we have assumed

there is an effective electric field along the z -direction. In general, this can be the result of any perturbation which breaks the symmetry along the z -direction, such as the presence of the superconducting material. The next term describes the Zeeman energy $E_Z = \frac{1}{2}g\mu_B\mathbf{B}\cdot\boldsymbol{\sigma}$, with g the Landé g -factor of the material, μ_B the Bohr magneton, and \mathbf{B} the magnetic field. Finally, the superconducting pairing potential is given by Δ . The matrices σ and τ are the Pauli matrices acting in spin and particle-hole space, respectively.

For an infinitely long wire, we can substitute $p_x = \hbar k_x$, and calculate the dispersion. First we examine the superconducting nanowire without spin-orbit coupling, $\alpha = 0$. In the absence of a magnetic field ($E_Z = 0$, Fig. 2.2(a)), the dispersion consists of electron- (blue) and hole-like (red) spin degenerate parabolas, which are coupled by the superconducting pairing, creating a gap at $k = k_F^1$. The spin degeneracy is lifted by applying a finite magnetic field (Fig. 2.2(d)). Once the Zeeman energy exceeds the superconducting gap (Fig. 2.2(g,j)), the system becomes gapped.

When we include a finite spin-orbit coupling strength, the picture changes. Because the spin-orbit field is momentum dependent, spin is no longer a good quantum number, and the previously spin degenerate parabolas are shifted in momentum by $\pm k_{SO}$ (Fig. 2.2(b)). At $E_Z = 0$, the electrons and holes are spin polarized parallel or antiparallel to the spin-orbit field. If we then apply a magnetic field perpendicular to the spin-orbit field, the electrons at finite momentum are only weakly influenced by the field because their spin projection on the magnetic field axis is minimal. This does not happen at $k = 0$, however, because there the spin-orbit field is zero. At $E_Z = \sqrt{\mu^2 + \Delta^2} = E_{Z,\text{crit}}$, the gap at $k = 0$ closes (Fig. 2.2(h)), and subsequently reopens if E_Z is increased further (Fig. 2.2(k)). We see that now, even though the Zeeman energy exceeds Δ , the system remains gapped because the states at larger momenta are insensitive to the magnetic field. Additionally, the character of the states near $k = 0$ has changed, with electron-like (blue) states now above the Fermi energy and hole-like (red) states below. This inversion of the energy gap is a topological phase transition. The inverted gap regime is generally referred to as the topological regime, with the gap ordering at E_Z called the trivial regime. These two regimes correspond to the two possible values of the topological invariant in one dimensional class D Hamiltonians such as the one of equation 2.14, which have particle-hole symmetry and broken spinful time-reversal symmetry [24].

If the magnetic field is aligned with the spin-orbit field, the system again becomes gapless for $E_Z > \Delta$ (Fig. 2.2, right column). This is due to the fact that now the spin states can simultaneously be eigenstates of the spin-orbit and magnetic field, which is in effect the same as the situation described in the left column of Fig. 2.2.

The transition to the topological regime is accompanied by the appearance of Majorana bound states (MBSs) localized at the wire ends, with a wave function amplitude which decays exponentially into the bulk with a characteristic length scale ξ . If the length of

¹The Fermi wave vector k_F is defined as $k_F = \sqrt{\left(\frac{m^*\alpha}{\hbar^2}\right)^2 + \frac{2\mu m^*}{\hbar^2}}$. For finite α , the shifted parabolas cross the Fermi energy at $k = \pm k_F \pm k_{SO}$, with $k_{SO} = \frac{m^*\alpha}{\hbar^2}$.

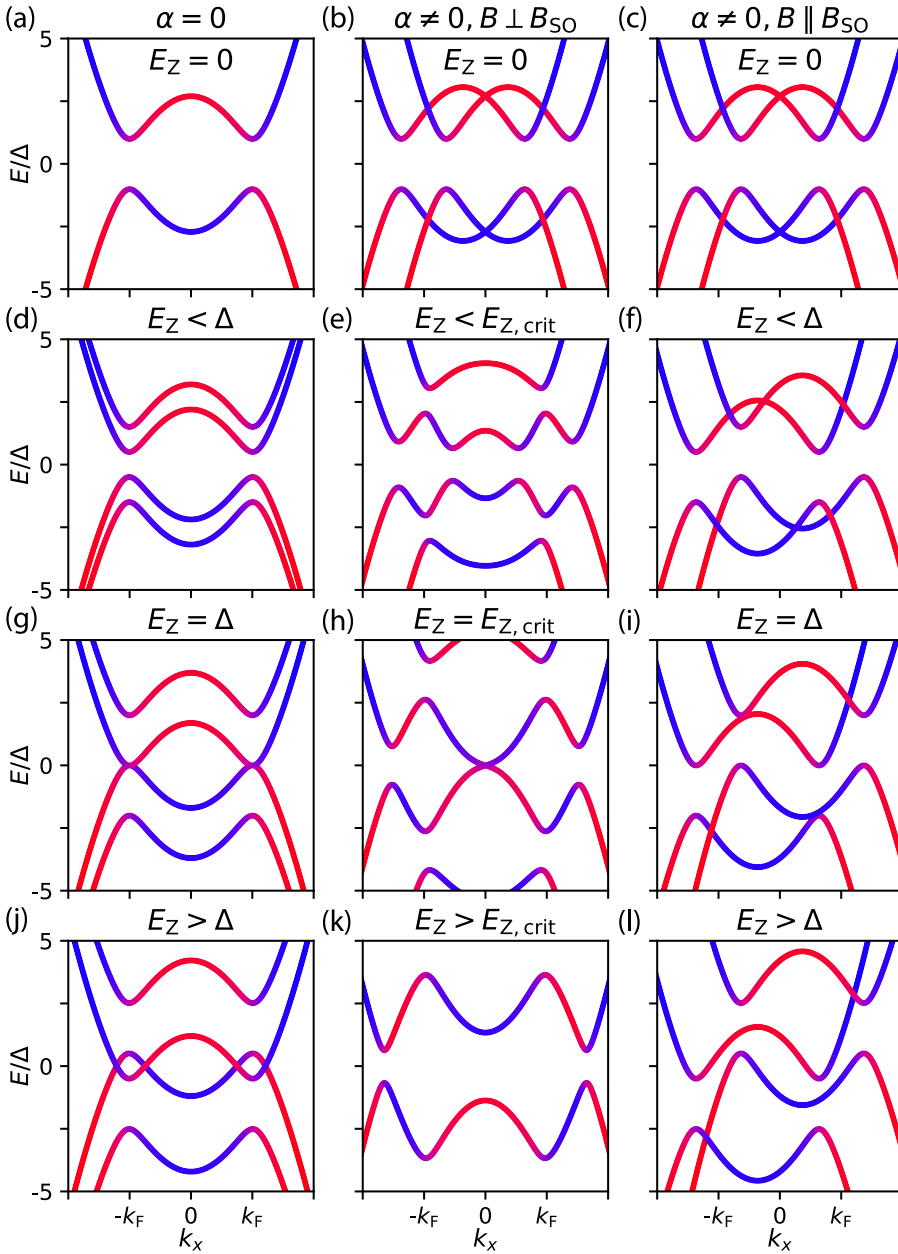


Figure 2.2: **Dispersion of the 1D Majorana nanowire for different values of the Zeeman energy.** For a wire without spin-orbit coupling (left column), the gap closes when $E_Z = \Delta$. Finite spin-orbit coupling protects the gap at finite k from closing as long as the magnetic field is aligned perpendicular to the spin-orbit field (middle column). If the magnetic field and spin-orbit field are aligned, the gap is again closed for $E_Z \geq \Delta$ (right column). Parameters used in the calculation: $m^* = 0.013m_e$, $\mu = 0.5$ meV, and $\Delta = 0.2$ meV. When $\alpha \neq 0$, it is set to 0.3 eVÅ.

the nanowire L is finite, the wave functions of the Majorana zero modes at opposite ends will overlap, causing them to couple and split to finite energy. For a long wire, $L \gg \xi$, the energy of the Majorana state can be approximated by [25]

$$\Delta E \approx \hbar^2 k_{F,\text{eff}} \frac{e^{-2L/\xi}}{m^* \xi} \cos(k_{F,\text{eff}} L). \quad (2.15)$$

Here the parameter $k_{F,\text{eff}}$ is the wave vector describing the oscillatory part of the Majorana wave function. For weak spin-orbit interaction ($E_Z \gg m^* \alpha^2 / \hbar^2$), $k_{F,\text{eff}} \approx k_F$, while for strong spin-orbit interaction ($E_Z \ll m^* \alpha^2 / \hbar^2$) $k_{F,\text{eff}} \approx k_{\text{SO}}$ [26]. While in general the splitting depends on α , μ , and E_Z in a non-trivial way, we can identify three regimes.

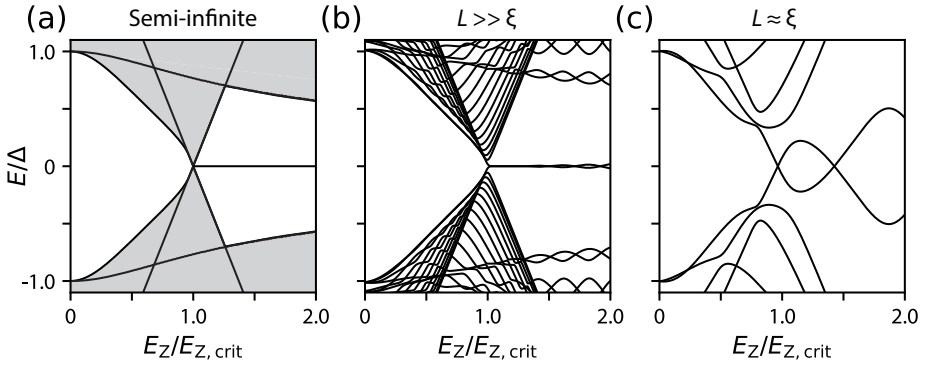


Figure 2.3: **Effect of finite wire length.** Spectrum of the Majorana nanowire as a function of Zeeman energy for different lengths. (a) In a semi-infinite wire, the energy of the Majorana bound states is exactly 0. Above the gap, there is a continuum of states (shaded area). (b) In a relatively long wire ($L \gg \xi$), the energy of the Majorana state oscillates with increasing Zeeman energy due to the finite overlap between the two ends. The continuum of states is replaced by discrete energy levels due to finite size quantization. (c) In a short wire ($L \approx \xi$), the finite size effects are so strong that the energy of the Majorana state is considerable on the scale of the gap. Parameters used in the simulation: $m^* = 0.013 m_e$, $\mu = 0.5 \text{ meV}$, $\alpha = 0.3 \text{ eV \AA}$, and $\Delta = 0.2 \text{ meV}$. For the finite length wires, $L = 4 \mu\text{m}$ in panel (b), and $L = 1 \mu\text{m}$ in panel (c).

In Fig. 2.3 we plot the Majorana nanowire spectrum as a function of Zeeman energy for different lengths of the nanowire. For a semi-infinite wire (Fig. 2.3(a)), the nanowire spectrum is a continuum of states above the gap. After the closing and reopening of the gap at $k = 0$ for $E_Z = E_{Z,\text{crit}}$, a zero energy Majorana state emerges. Because the two Majorana bound states are infinitely far apart, there is no energy splitting. This changes when the wire is long, but finite, as shown in Fig. 2.3(b). Instead of the continuum of states above the gap we now have energy levels due to finite size quantization. For $E_Z > E_{Z,\text{crit}}$, the energy of the Majorana states oscillates with increasing Zeeman energy due to the fact that it changes $k_{F,\text{eff}}$. The amplitude of the oscillation remains small compared to the gap. This is no longer the case when the wire length becomes comparable to ξ , Fig. 2.3(c). The Majorana bound states overlap so strongly that their energy becomes comparable to Δ . In this situation, equation 2.15 no longer applies, and one generally needs to resort to numerical methods to calculate the overlap energy [27].

The 1D Majorana nanowire model considers only a single subband in the semiconductor wire. This can be generalized to a quasi-1D system with multiple transverse subbands. Because Majorana zero modes originating from different subbands can couple to each other at end of the wire, splitting them to finite energy, the total number of zero modes in a system with N occupied subbands will be $N \bmod 2$ [28]. Thus, the nanowire will have a pair of Majorana zero modes at its ends when the number of spin resolved bands crossing the Fermi level is odd [29].

2.5. AHARONOV-BOHM EFFECT IN MESOSCOPIC RINGS

The Aharonov-Bohm effect describes the effect of the electromagnetic vector potential on a charged particle [30]. Remarkably, this effect persists even if the electromagnetic fields vanish at every point along the particle's trajectory. This is due to the fact that the vector potential couples directly to the phase of the particle's wave function. As such, the Aharonov-Bohm effect has no classical analogue, making it a quintessentially quantum mechanical phenomenon.

The effect of the magnetic flux on the electronic wave function can be observed in interference experiments, for example in the magnetic field dependent conductance through a mesoscopic ring. We schematically depict such a set-up in Fig. 2.4. The ring consists of an upper and a lower channel, labeled 1 and 2 respectively, connected to the lead modes $3_{L(R)}$ via the scattering matrices $s_{L(R)}$. Electron waves propagating in the upper arm acquire a dynamic phase χ_1 , while those traveling in the lower arm acquire a phase χ_2 . Additionally, the electrons acquire a magnetic phase $\phi_{1(2)}$ while traveling along the upper (lower) arm of the ring, with the sign depending on the direction of propagation (clockwise: +, counterclockwise: -). The sum of the phases $\phi_{1,2}$ is determined by the magnetic field penetrating the ring:

$$\phi_1 + \phi_2 = \frac{e}{\hbar} \oint_L \mathbf{A} \cdot d\mathbf{l} = \frac{e}{\hbar} \iint_S \mathbf{B} \cdot d\mathbf{S} = \frac{2\pi\Phi}{\Phi_0}, \quad (2.16)$$

where L is the closed trajectory along the ring's perimeter, S is the area of the ring, \mathbf{A} is the electromagnetic vector potential, \mathbf{B} is the magnetic field, and $\Phi_0 = \frac{h}{e}$ is the magnetic flux quantum².

We assume that an electron incident upon the ring from the leads has a probability $|r|^2$ to be reflected back into the lead. Additionally, we assume that the ring is symmetric with respect to the upper and lower arms. For a time-reversal symmetric system³, the scattering matrices $s_{L,R}$ are then given by

$$s_{L,R} = \begin{bmatrix} -\frac{1-r}{2} & \frac{1+r}{2} & \sqrt{\frac{1-|r|^2}{2}} \\ \frac{1+r}{2} & -\frac{1-r}{2} & \sqrt{\frac{1-|r|^2}{2}} \\ \sqrt{\frac{1-|r|^2}{2}} & \sqrt{\frac{1-|r|^2}{2}} & -r \end{bmatrix}. \quad (2.17)$$

²Note that the magnetic flux quantum is often defined as $\Phi_0 = \frac{h}{2e}$, the superconducting flux quantum.

³Although we apply a magnetic field, we assume the field is weak enough to approximately preserve time-reversal symmetry.

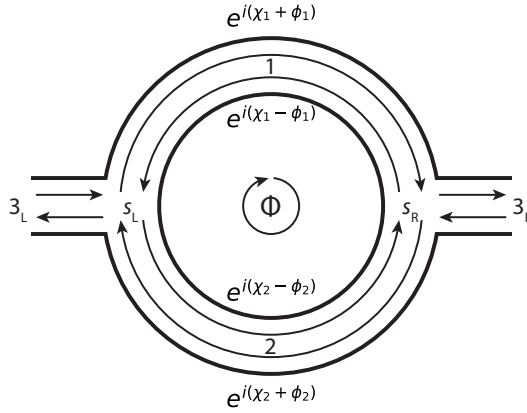


Figure 2.4: **Schematic representation of a mesoscopic Aharonov-Bohm ring.** A single mode ring, consisting of transport channels 1 and 2 connected in parallel, is connected to leads through the scattering matrices $s_{L,R}$. While propagating through the ring, electrons pick up a phase which has a dynamic ($\chi_{1,2}$) and magnetic ($\phi_{1,2}$) component.

To calculate the conductance through the ring, we follow the procedure of ref. [31]. The conductance can be calculated by using the Landauer formula $G = \frac{2e^2}{h} |t|^2$ [32], where t is the coherent sum of all the transport processes connecting the left and the right leads. The simplest of such processes is an electron wave being scattered from the left lead into the upper branch of the ring, picking up a phase while propagating inside the ring, and then being scattered from the ring into the right lead. The amplitude of this process is given by $\sqrt{\frac{1-|r|^2}{2}} e^{i(\chi_1 + \phi_1)} \sqrt{\frac{1-|r|^2}{2}}$. There is an equivalent process which has the electron wave being scattered into the lower branch before being transmitted to the right lead, with amplitude $\sqrt{\frac{1-|r|^2}{2}} e^{i(\chi_2 - \phi_2)} \sqrt{\frac{1-|r|^2}{2}}$.

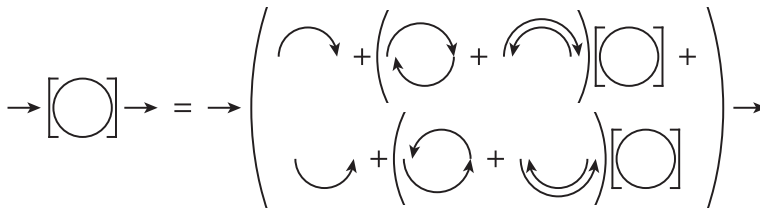


Figure 2.5: **Diagram of the scattering processes contributing to the conductance through an Aharonov-Bohm ring.**

There is a finite probability the electron wave is reflected back into either the upper or lower branch of the ring instead of continuing to the right lead, before arriving back at the left scattering region. For the process to contribute to the conductance from left to right, the electron wave should be again reflected back into the ring, into either the up-

per or lower branch, which was the previous starting point for the propagation through the ring. We can thus recursively list all the processes contributing to the conductance through this general scheme, illustrated in Fig. 2.5.

Each process must start with the electron being transmitted from the left lead into the ring, and end with the electron being transmitted from the ring to the right lead (straight arrows pointing to the right). All processes that connect these two events are represented by the circle between square brackets. As described above, the simplest such processes are propagation through the upper (clockwise half circle, arrow pointing to the right) or lower (counterclockwise half circle, arrow pointing to the right) branch of the ring. There are four distinct ways to be scattered back to this starting point without leaving the ring (listed between small parentheses), each of which is again followed by all possible processes which connect left and right (square brackets).

While it is straightforward to sum up all of these processes, the resulting expression is rather cumbersome [33]. For the special case of $r = 0$ and $\chi_1 = \chi_2 = \frac{1}{2}\chi$, a more elegant expression can be obtained [31, 34]:

$$G(\Phi) = \frac{2e^2}{h} \frac{(1 - \cos\chi) \left(1 + \cos^2\left(\frac{2\pi\Phi}{\Phi_0}\right)\right)}{\sin^2\chi + \left(\cos\chi - \left(\frac{1}{2} + \frac{1}{2}\cos\left(\frac{2\pi\Phi}{\Phi_0}\right)\right)\right)^2}. \quad (2.18)$$

The conductance is h/e periodic in the magnetic flux, with an amplitude of $\frac{2e^2}{h}$. A more intuitive way of looking at this expression is to write it as a Fourier series:

$$G(\Phi) = \frac{2e^2}{h} \sum_n |t_n|^2 \cos\left(\frac{2n\pi\Phi}{\Phi_0}\right). \quad (2.19)$$

We see that the conductance can be written as a sum of harmonics, with the n th harmonic being h/ne periodic with amplitude $|t_n|^2$. The lowest order process contributing to the n th harmonic involve electrons travelling a distance of $n\pi R$, where R is the radius of the ring.

So far we have assumed that all possible paths through the loop sum up coherently. In reality, electron waves suffer from decoherence due to fluctuations in the environment, leading to an uncertainty in the phase when the partial waves interfere with each other [14]. If we describe this fluctuating environment by a potential $V(t)$, we can approximate the phase uncertainty as

$$\langle \delta\phi^2 \rangle \approx \frac{1}{\hbar^2} \int_0^{t_0} dt \int_0^{t_0} dt' \langle V(t)V(t') \rangle. \quad (2.20)$$

Here t_0 is the time the electron wave spends in the loop. The interference amplitude is decreased by a factor $e^{-1/2\langle \delta\phi^2 \rangle}$ [35]. The fluctuation-dissipation theorem tells us that the amplitude of the environmental fluctuations increases with temperature. Assuming

the phase uncertainty grows linearly in time⁴, we can write

$$\langle \delta\phi^2 \rangle = \frac{t_0}{\tau_\phi(T)} = \frac{L}{L_\phi^{\text{AB}}(T)}, \quad (2.21)$$

where $\tau_\phi(T)$ is the dephasing time, L is the distance travelled along the loop, and $L_\phi^{\text{AB}}(T)$ is the phase coherence length. We infer that the amplitude of the n th harmonic is decreased by a factor $e^{-\frac{n\pi R}{L_\phi^{\text{AB}}}}$, with R the radius of the ring, and L_ϕ^{AB} the phase coherence length. For ballistic systems, $L_\phi^{\text{AB}} \propto T^{-1}$, while for diffusive systems $L_\phi^{\text{AB}} \propto T^{-1/2}$ [36]. It is important to note that while the concept of a phase coherence length also plays a role in weak localization, in general L_ϕ^{AB} can be device geometry dependent, while L_ϕ^{WL} is considered to be universal [37].

REFERENCES

- [1] H. Kamerlingh Onnes, *Further experiments with liquid helium. c. on the change of electric resistance of pure metals at very low temperatures etc. iv. the resistance of pure mercury at helium temperatures*, Leiden Communications **120b** (1911).
- [2] W. Meissner and R. Ochsenfeld, *Ein neuer Effekt bei Eintritt der Supraleitfähigkeit*, Naturwissenschaften **21**, 787 (1933).
- [3] L. D. Landau and V. L. Ginzburg, *On the theory of superconductivity*, Zhurnal Eksp. Teor. Fiz. **20**, 1064 (1950).
- [4] J. Bardeen, L. N. Cooper, and J. R. Schrieffer, *Theory of Superconductivity*, Phys. Rev. **108**, 1175 (1957).
- [5] M. Tinkham, *Introduction to Superconductivity*, Dover Books on Physics Series (Dover Publications, 1996).
- [6] L. N. Cooper, *Bound Electron Pairs in a Degenerate Fermi Gas*, Phys. Rev. **104**, 1189 (1956).
- [7] N. N. Bogoliubov, *On a new method in the theory of superconductivity*, Nuovo Cimento **7**, 794 (1958).
- [8] G. E. Blonder, M. Tinkham, and T. M. Klapwijk, *Transition from metallic to tunneling regimes in superconducting microconstrictions: Excess current, charge imbalance, and supercurrent conversion*, Phys. Rev. B **25**, 4515 (1982).
- [9] C. W. J. Beenakker, *Quantum transport in semiconductor-superconductor microjunctions*, Phys. Rev. B **46**, 12841 (1992).
- [10] G. E. Blonder and M. Tinkham, *Metallic to tunneling transition in Cu-Nb point contacts*, Phys. Rev. B **27**, 112 (1983).

⁴Strictly speaking, this is not true in a one dimensional system, but holds in two or three dimensional systems, see ref. [35].

- [11] C.-X. Liu, F. Setiawan, J. D. Sau, and S. Das Sarma, *Phenomenology of the soft gap, zero-bias peak, and zero-mode splitting in ideal Majorana nanowires*, Phys. Rev. B **96**, 054520 (2017).
- [12] M. Büttiker, *Four-Terminal Phase-Coherent Conductance*, Phys. Rev. Lett. **57**, 1761 (1986).
- [13] C. W. J. Beenakker and H. van Houten, *Quantum Transport in Semiconductor Nanostructures*, in *Semiconductor Heterostructures and Nanostructures*, Solid State Physics, Vol. 44, edited by H. Ehrenreich and D. Turnbull (Academic Press, 1991) pp. 1–228.
- [14] T. Ihn, *Semiconductor Nanostructures: Quantum States and Electronic Transport* (Oxford University Press, 2011).
- [15] A. Y. Kitaev, *Unpaired majorana fermions in quantum wires*, Physics-Uspekhi **44**, 131 (2001).
- [16] D. A. Ivanov, *Non-Abelian Statistics of Half-Quantum Vortices in p-Wave Superconductors*, Phys. Rev. Lett. **86**, 268 (2001).
- [17] L. Fu and C. L. Kane, *Superconducting Proximity Effect and Majorana Fermions at the Surface of a Topological Insulator*, Phys. Rev. Lett. **100**, 096407 (2008).
- [18] P. G. de Gennes, *Boundary Effects in Superconductors*, Rev. Mod. Phys. **36**, 225 (1964).
- [19] M. Leijnse and K. Flensberg, *Introduction to topological superconductivity and Majorana fermions*, Semiconductor Science and Technology **27**, 124003 (2012).
- [20] R. Aguado, *Majorana quasiparticles in condensed matter*, La Rivista del Nuovo Cimento **40**, 523 (2017).
- [21] R. M. Lutchyn, E. P. A. M. Bakkers, L. P. Kouwenhoven, P. Krogstrup, C. M. Marcus, and Y. Oreg, *Majorana zero modes in superconductor–semiconductor heterostructures*, Nature Reviews Materials **3**, 52 (2018).
- [22] R. M. Lutchyn, J. D. Sau, and S. Das Sarma, *Majorana Fermions and a Topological Phase Transition in Semiconductor-Superconductor Heterostructures*, Phys. Rev. Lett. **105**, 077001 (2010).
- [23] Y. Oreg, G. Refael, and F. von Oppen, *Helical Liquids and Majorana Bound States in Quantum Wires*, Phys. Rev. Lett. **105**, 177002 (2010).
- [24] S. Ryu, A. P. Schnyder, A. Furusaki, and A. W. W. Ludwig, *Topological insulators and superconductors: tenfold way and dimensional hierarchy*, New Journal of Physics **12**, 065010 (2010).
- [25] S. Das Sarma, J. D. Sau, and T. D. Stanescu, *Splitting of the zero-bias conductance peak as smoking gun evidence for the existence of the Majorana mode in a superconductor-semiconductor nanowire*, Phys. Rev. B **86**, 220506 (2012).

- [26] J. Klinovaja and D. Loss, *Composite Majorana fermion wave functions in nanowires*, Phys. Rev. B **86**, 085408 (2012).
- [27] T. D. Stanescu, R. M. Lutchyn, and S. Das Sarma, *Dimensional crossover in spin-orbit-coupled semiconductor nanowires with induced superconducting pairing*, Phys. Rev. B **87**, 094518 (2013).
- [28] S. Tewari, T. D. Stanescu, J. D. Sau, and S. Das Sarma, *Topological minigap in quasi-one-dimensional spin-orbit-coupled semiconductor Majorana wires*, Phys. Rev. B **86**, 024504 (2012).
- [29] R. M. Lutchyn, T. D. Stanescu, and S. Das Sarma, *Search for Majorana Fermions in Multiband Semiconducting Nanowires*, Phys. Rev. Lett. **106**, 127001 (2011).
- [30] Y. Aharonov and D. Bohm, *Significance of Electromagnetic Potentials in the Quantum Theory*, Phys. Rev. **115**, 485 (1959).
- [31] Y. V. Nazarov and Y. M. Blanter, *Quantum Transport* (Cambridge University Press, 2009).
- [32] E. N. Economou and C. M. Soukoulis, *Static Conductance and Scaling Theory of Localization in One Dimension*, Phys. Rev. Lett. **46**, 618 (1981).
- [33] S. Datta and S. Bandyopadhyay, *Aharonov-Bohm effect in semiconductor microstructures*, Phys. Rev. Lett. **58**, 717 (1987).
- [34] Y. Gefen, Y. Imry, and M. Y. Azbel, *Quantum Oscillations and the Aharonov-Bohm Effect for Parallel Resistors*, Phys. Rev. Lett. **52**, 129 (1984).
- [35] A. Stern, Y. Aharonov, and Y. Imry, *Phase uncertainty and loss of interference: A general picture*, Phys. Rev. A **41**, 3436 (1990).
- [36] T. Ludwig and A. D. Mirlin, *Interaction-induced dephasing of Aharonov-Bohm oscillations*, Phys. Rev. B **69**, 193306 (2004).
- [37] P. A. Lee and A. D. Stone, *Universal Conductance Fluctuations in Metals*, Phys. Rev. Lett. **55**, 1622 (1985).

3

FABRICATION PROCEDURES AND EXPERIMENTAL METHODS

A test device is never a good test for a real device.

Önder Gül

This chapter describes the device fabrication and measurement methods used to obtain the results presented in this thesis. For our experiments we use InSb nanowires grown by MOVPE in the group of Erik Bakkers at TU/e. Epitaxial Al is deposited by MBE in the group of Chris Palmstrøm at UCSB. Additional details of the InSb nanowire growth and Al deposition are given in chapter 4. Over the course of this chapter we will describe how to transfer nanowires or nanowire networks from a growth chip to a sample substrate, how contacts are made, and how the devices are measured. Particular attention is given to the handling of InSb nanowires with an epitaxial Al shell, which require a careful approach during fabrication. The focus is on the general workflow, with more detailed recipes for the devices used to generate experimental results provided in their respective chapters.

3.1. FABRICATION OF NANOWIRE DEVICES

The nanowires are transferred from the growth substrate to the device chip with a micromanipulator. The micromanipulator consists of a needle with a very sharp tip, made of tungsten or indium. Tungsten tips are commercially available, whereas the indium tips are freshly made from an indium melt [1] prior to each deposition session. Figure 3.1 shows an optical microscope image of a nanowire growth chip at 1000x magnification. The nanowires are perpendicular to the substrate, and can be seen as small black dots. The manipulator tip can be seen on the right, indicated by the black arrow. The manipulator tip can be seen on the right, indicated by the black arrow.

3

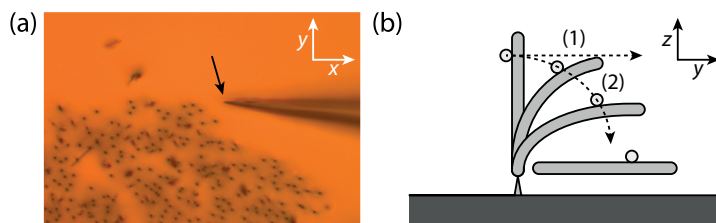


Figure 3.1: **Nanowire deposition.** (a) Optical microscope image of a nanowire growth chip. The nanowires are visible as black dots. The tungsten tip of the micromanipulator is indicated by the black arrow. (b) Schematic illustration of wire pick-up methods. Trajectories (1) and (2) illustrate different approaches to picking up nanowires. Figure adapted from ref. [2].

In order to pick up a nanowire (NW) from the growth chip and deposit it on the device substrate, the tip has to make contact with the wire and break the connection to the growth chip. To facilitate the transfer to the device chip, it is most convenient if the nanowire lies in the xy -plane. This can most easily be achieved by pushing the tip sideways against the wire, and subsequently pushing it down as the wire is bending under the force exerted by the tip (as indicated by trajectory (2) in Fig. 3.1(b)). Once the tip has collected the wire in this fashion, it can be brought into contact with the device substrate. As the surface area of the wire making contact with the substrate is larger than the area making contact with the tip, the wire can be transferred to the device chip at a desired position through van der Waals forces. If trajectory (1) is followed, wires tend to bend but not break off from the growth substrate. Even when they do, their angle and position on the tip are usually unfavorable for controlled deposition on the device substrate [2]. Therefore, it is recommended to use trajectory (2) when possible.

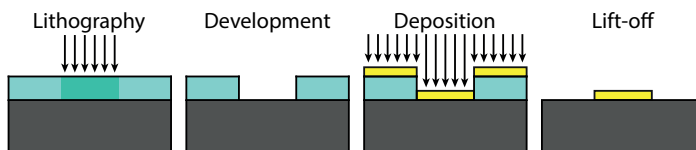


Figure 3.2: **Schematic representation of the fabrication process.** A general nanofabrication process consists of these four steps: lithography, development, deposition/etching, and lift-off.

Once the nanowires have been deposited onto the device substrate at the desired location, we use CAD software to design a mask for electron-beam lithography. This mask is then used to selective deposit or remove materials from specific regions on the chip. The general process is schematically depicted in Fig. 3.2. The chip is covered by an electron-beam sensitive polymer resist (cyan), such as PMMA, and is exposed to a beam of energetic electrons in a selected region (dark cyan). This lithography process is performed using a Raith EBPG 5000 or 5200, with electron beams of 100 kV. In the case of positive resist shown here, the parts of the resist exposed to the electron beam will be removed in the development step. The electron beam breaks the bonds in the resist layer, making the exposed polymer more soluble in a suitable developing chemical. This allows the selective removal of resist to form the desired pattern. For PMMA, we use MIBK:IPA in a ratio of 1:3 for 60 s to dissolve the exposed polymers, followed by 60 s in IPA as an etch stop. Once the mask has been realized, we can perform the desired process, such as metal deposition. Finally, the remaining resist layer is removed in a lift-off process, leaving the deposited metal behind only in the patterned regions. For PMMA lift-off, we use acetone, even though it is known to leave behind polymer residue. More aggressive resist strippers such as PRS-3000 have been found to adversely affect the InSb nanowires.

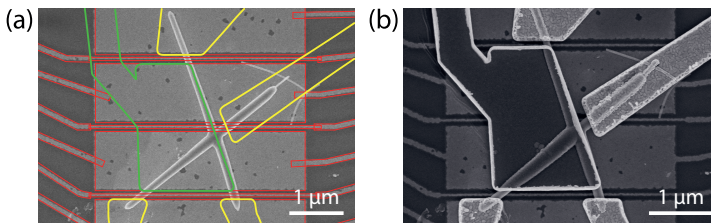


Figure 3.3: **Example nanowire device.** (a) Scanning electron micrograph of an InSb nanowire cross on a pre-fabricated bottom gate pattern, overlaid with the lithographic mask design. Different colors correspond to separate processing steps. (b) Finished device using the mask designs in (a).

Figure 3.3 shows an example of a nanowire cross device. Panel (a) is a scanning electron micrograph overlaid with the designed mask. Different colors indicate shapes that will be written in separate lithography steps. The yellow pattern will be used to create a Cr/Au contact to the cross, while superconducting NbTiN will be deposited in the areas enclosed by the green pattern. The finished device is shown in Fig. 3.3(b). Comparing Fig. 3.3(a) and (b) shows devices can be made with high (<20 nm) precision.

To create transparent contacts to the nanowires, we need to remove the native oxide before depositing the metal or superconductor. This can be done by e.g. ion milling. The advantage of this method is that it can be done in situ, preventing contamination of the nanowire surface before contact deposition. However, as this is a physical etching process, it is not selective to just the oxide, and causes substantial damage to the semiconductor crystal. An alternative method uses an ammonium polysulfide solution to selectively remove the native oxide, and passivate the surface to prevent reoxidation [3]. This sulfur passivation process gives highly transparent ohmic contacts, and has been shown

to produce devices with ballistic transport characteristics with high yield [4]. The solution is prepared by mixing 3 ml ammonium sulfide, $(\text{NH}_4)_2\text{S}$ (20% in H_2O), with 290 mg of sulfur powder, creating ammonium polysulfide, $(\text{NH}_4)_2\text{S}_x$. We take 2 ml of this mixture and dilute it in DI water at a ratio of 1:200. The sample chip with contacting area exposed through the mask is then submerged in the solution for 30 minutes at 60°C . Afterwards, the sample is rinsed in DI water and loaded into the deposition machine of choice. For normal contacts, Cr/Au is evaporated (about 10 nm of Cr is used as a sticking layer to promote adhesion of the gold to the substrate). The best results are obtained if the sulfur passivated surface is exposed to a brief, mild ion mill prior to metal deposition.

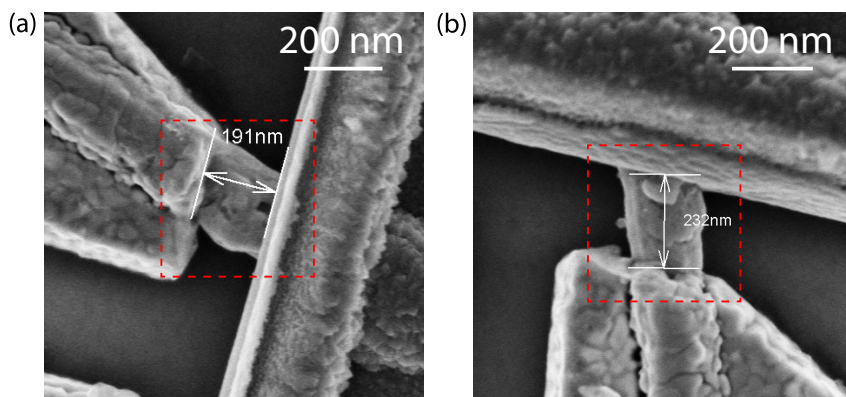


Figure 3.4: **Gold diffusion along the InSb nanowire surface.** (a) Scanning electron micrograph of an InSb nanowire cross contacted by Cr/Au (left contact) and NbTiN (right contact). Gold has diffused over the surface of the nanowire (visible in the red rectangle), shorting the junction. (b) A similar device from the same chip as shown in (a), with visible gold grains on the InSb nanowire junction.

If a device needs to be processed further after gold contacts have been made, excessive heating should be avoided. The reason for this is showcased in Fig. 3.4: the gold diffuses into the InSb nanowire, causing a metallic short in the device. In this instance, the chip was baked for a total of 20 minutes at 175°C after Cr/Au contacts had already been evaporated onto the nanowires. Choice of sticking layer (Cr or Ti) doesn't appear to make a large difference. Performing a second sulfur passivation step (at 60°C) after gold deposition doesn't lead to shorts, suggesting the activation temperature for the diffusion process is higher than this.

3.2. PROCESSING OF INSB NANOWIRES WITH EPITAXIAL AL

When fabricating devices out of InSb nanowires with an epitaxially grown Al shell, several additional considerations come into play. The Al can diffuse into the InSb semiconductor through an exchange reaction, substituting the Al for In, forming AlSb and $\text{Al}_x\text{In}_{1-x}\text{Sb}$ compounds. Notably, this reaction occurs at room temperature [5, 6], and results in the interface between the two materials degrading over time. It is therefore

imperative that elevated temperatures are avoided during the fabrication process. Instead of relying on baking to remove the resist solvent during mask preparation, we put the chip in a high vacuum system (vacuum of approximately $1 \cdot 10^{-4}$ mTorr) for several hours. This method has been tested for masks up to 700 nm thick, with no difference in performance when compared to masks baked on a hot plate.

The ammoniumpolysulfide solution reacts with the Al shell, removing it from the wire. Therefore, it can't be used to create clean contacts to the InSb nanowire while keeping the Al shell intact. Instead, we use a plasma based Ar bombardment to clean the surface before depositing metallic contacts. To avoid excessive heating during the bombardment, we turn on the plasma in cycles of 20 s, with a 40 s cooldown period in between. The etching time is usually 4-6 minutes, requiring 12-18 cycles.

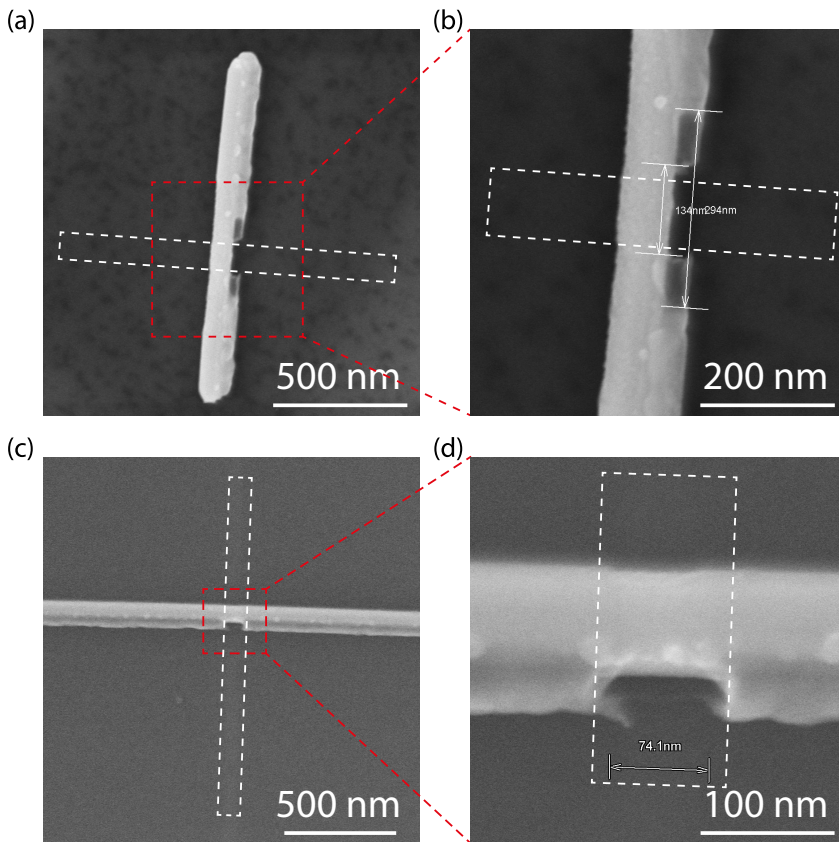


Figure 3.5: **Selective etching of Al on InSb NWs.** (a) InSb nanowire etched for 90 s in Transene D:H₂O 1:2 at 40 °C. (b) Close-up of the image in (a), showing extensive damage in the etched region. (c) InSb nanowire etched for 210 s in MF-321 at RT. (d) Close-up of the image in (c). The white dashed rectangle indicates the lithographically defined etch window for all panels.

3.3. SELECTIVE ETCHING OF EPITAXIAL AL ON INSB NANOWIRES

The InSb nanowires with epitaxial Al used in this thesis are typically covered by Al along their entire length. In order to make devices out of these wires, we would like to selectively remove the Al from certain parts, while preserving it in the areas of the device where we want to induce superconductivity. One approach to this uses wet chemical etchants in combination with electron-beam lithography. Another approach is to use masking techniques during the deposition of the Al on the wires. In this section we will describe our efforts on the former approach, while the latter is described in detail in chapter 4.

Several factors determine whether an etchant can be used for our purpose. It should selectively remove the Al while minimally damaging the nanowire, as defects act as scattering centers and deteriorate the transport properties. It should also conform to the lithographically defined mask, such that devices can be made with high precision. It should be homogeneous across a chip, such that the spread in results between the wires etched in the same run is small, as well as repeatable, such that the variation between runs is small. Finally, the etchant should not leave any residues as these can act as scattering centers and charge traps. Four different wet chemical etches have been investigated.

TRANSENE D ALUMINUM ETCHANT

Transene D is an aluminum etchant developed for use with III-V materials [7]. It consists of 55-65 wt.% phosphoric acid, 5-10 wt.% sodium-M-nitrobenzene sulfonate, 1-5 wt.% acetic acid, and DI water. The sodium-M-nitrobenzene sulfonate oxidizes the Al, with the phosphoric acid subsequently removing the AlO_x [8]. This reaction is exothermic and produces H_2 gas, which can cause problems with etching homogeneity across a chip due to bubble formation. Therefore, long etching times (>30 s for the pure solution) without intermittent rinsing are not recommended. The solution is buffered by acetic acid. Transene D has proven successful in selectively removing epitaxial Al films from InAs nanowires [9]. Because the pure solution aggressively reacts with InSb, it is diluted in DI water for most etching tests. The tests are conducted on a wire batch with an Al shell of ≈ 40 nm thick, grown at 250°C and oxidized at room temperature (RT)¹. Various recipes have been attempted, with variations in dilution (1:2 and 1:4 in DI water), etching time (25 to 120 s), and temperature (40°C and 50°C). Figure 3.5(a) shows the result for a 90 s etch at 40°C in a Transene D:H₂O 1:2 solution, followed by a 45 s rinse in H₂O (50°C), a 45 s rinse in H₂O (room temperature (RT)), and a 180 s bath in H₂O (RT). The extensive rinsing procedure is necessary to achieve a homogeneous result across the chip. Zooming in on the etched region (Fig. 3.5(b)), it becomes clear that Transene D successfully removes the Al from the etch window defined by the mask. A small undercut is seen, which is common for isotropic etching processes. The darkened layer hanging over the etched region is likely residual native AlO_x , which is etched at a different rate than the Al underneath it. The InSb nanowire is substantially damaged by

¹Note that this is a different procedure from the one described in chapter 4, which could impact the characteristics of the Al shell.

the etching process, as is evident from the rough surface in the etched region (especially when compared to the smooth faceting in the non-etched parts visible in Fig. 3.5(a)). Several combinations of dilution, temperature, and etching time have been attempted, with none yielding an acceptable degree of selectivity.

MF-321

Microposit MF-321 is a developer for photo resists which is made by the Shipley Company [10]. It contains 2.14 wt.% TMAH, which is known to etch both Al [11] and Al_2O_3 [12]. Etching is performed for 150 to 300 s with the solution at room temperature, followed by a 20 s rinse in DI water. Figure 3.5(c) shows an InSb nanowire with Al shell etched for 210 s in MF-321 (RT). In Fig. 3.5(d) we see that the etch conforms nicely to the window defined by the mask, making it possible to create small features. However, damage to the InSb nanowire is visible, although it is not as severe as in the case of Transene D. Transport through these kinds of channels invariably shows Coulomb blockade, which is indicative of significant disorder.

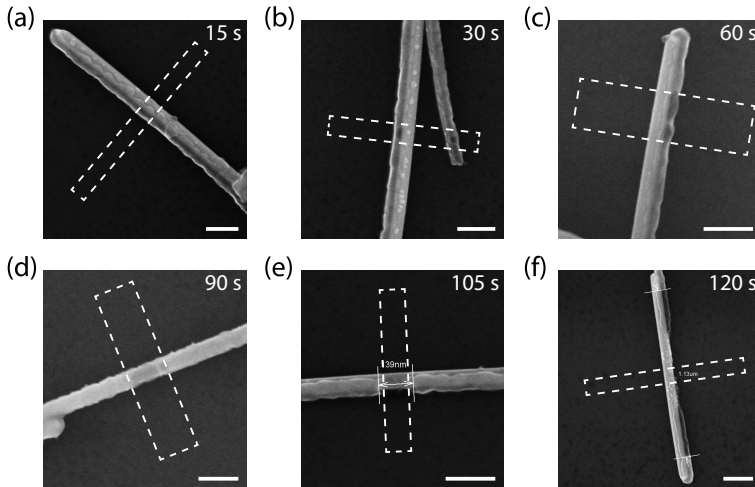


Figure 3.6: **Sulfur-based etching of Al on InSb NWs.** (a-f) InSb nanowires with Al shell etched in ammonium polysulfide solution (diluted 1:200 in DI water) at 60 °C for different durations. The dashed white rectangles indicate the exposed etching windows. Scale bars correspond to 200 nm.

AMMONIUM POLYSULFIDE

The ammonium polysulfide solution used to remove the native oxide from InSb nanowires also removes the Al shell. Because it leaves a clean, nicely terminated surface on the InSb nanowires [13], it seems an ideal choice as an etchant. In Fig. 3.6, we show the results of etching InSb-Al nanowires with ammonium polysulfide solution (diluted in H_2O with a 1:200 ratio) at 60 °C, the same solution that is used to clean the nanowire surface before making contact (see section 3.1). Initially, a dark spot appears in the etch window, which grows as the etching time is increased. As mentioned before, this darkened material is

likely AlO_x . After about 90 s, this darkened material starts to disappear, with a completely etching channel opening at around 105 s. However, the etching progresses very rapidly from this point, underetching the mask and removing the Al shell over about $1 \mu\text{m}$ length in the span of 15 s. This process is not homogeneous across the chip, with the onset time varying at least 20 s between different wires (i.e. the result shown in Fig. 3.6(f) can also be observed on the chip which was etched for 105 s). The etching process leaves significant residue on the wire channel, which could be reaction products or the collapsed native oxide shell. In either case, this is likely detrimental to device performance. The rapid etch rate combined with varying delay time makes it difficult to control the process. Etching with room temperature ammonium polysulfide solution has shown no discernible effect on the nanowires and the shell.

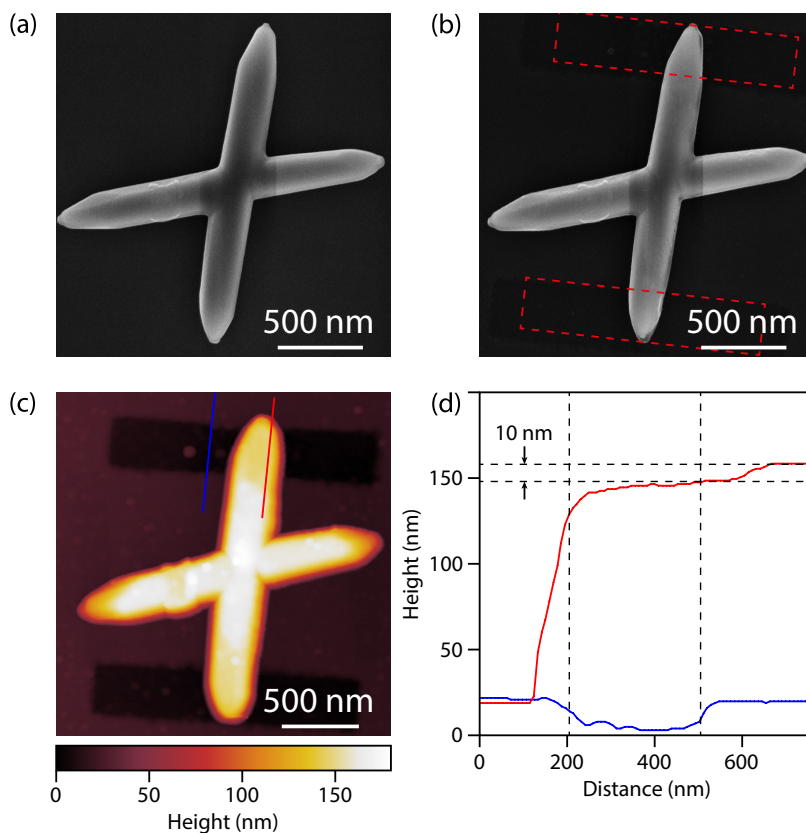


Figure 3.7: **BOE etch of Al on InSb NWs.** (a) Scanning electron micrograph of an InSb nanowire cross with epitaxial Al shell, before BOE treatment. (b) The same nanowire cross after 10 s of etching in BOE 7:1. The areas exposed to the etch (etch windows indicated by red dashed rectangles) show significant darkening of the contrast. (c) AFM image of the same nanowire cross. The etched regions are clearly visible in the underlying substrate. (d) Height along the red and blue lines indicated in (c), showing a step of ~ 10 nm between etched and unetched regions.

BUFFERED OXIDE ETCH

The Al shell on InSb nanowire crosses is grown at lower temperature than the shell on the wires described in the previous sections², which changes its etching properties. For this batch of nanowires, we use a buffered oxide etch (BOE) consisting of $\text{NH}_4\text{F}:\text{HF}$ in a ratio of 7:1, for a duration of 10 to 20 s. A SEM image of an InSb nanowire cross before BOE treatment is shown in Fig. 3.7(a). The chip is dipped in BOE 7:1 for 10 s, followed by a 60 s rinse in DI water. The exposed areas of the Al shell (etch masks indicated by the red dashed rectangles) show a significant darkening, which indicates removal of the Al and possibly residual AlO_x . AFM imaging (Fig. 3.7(c)) shows the etch mask as dark regions where the SiO_2 of the substrate has been partially etched away. In Fig. 3.7(d) we show the height measured along the blue (substrate) and red (nanowire cross) lines indicated in Fig. 3.7(c). A 10 nm step is observed on the nanowire cross near the edge of the etch mask, which is the expected thickness of the Al shell. This suggests that the Al has been removed in this area. The etched region extends roughly 100 nm beyond the edge of the mask in this case, which is sufficient for most fabrication purposes. However, the amount of underetching varies wildly even on the same chip, which combined with the short etching time makes it difficult to reliably control the process.

We summarize the results of our various wet etching experiences in Table 3.1. The recipe deemed most successful for each etchant is listed as an indication, but should not be taken as definitive. Judging each etchant at a qualitative level on the criteria we set out at the beginning of this section, it seems that none meet all of our demands. Priority should be given to selectivity, as this seems to be the best predictor of device performance. A score of “Very poor” in any category practically renders the etchant unusable, which disqualifies Transene D.

Etchant	Best recipe	Selectivity	Mask conformity	Control	Residue
Transene D	1:2 in H_2O , 90 s (40 °C)	Very poor	Excellent	Excellent	Good
MF-321	210 s (RT)	Mediocre	Good	Excellent	Good
Ammo- nium polysulfide	1:200 in H_2O , 105 s (60 °C)	Excellent	Mediocre	Poor	Poor
BOE 7:1	10 s (RT)	Good	Poor	Mediocre	Mediocre

Table 3.1: Comparison of different wet chemical etchants for selective removal of Al from InSb NWs.

The other etchants could possibly be considered, given further optimization. In partic-

²The nanowire crosses described in this section are grown by the method described in chapter 4.

ular, BOE 7:1 and ammonium polysulfide show good selectivity, which we identified as the most important criterium. Literature suggests more concentrated HF should have a lower Al etch rate than the BOE used here [14], which could be an attractive option to make the etch more controllable if the underetching is not too severe.

3.4. ELECTRICAL MEASUREMENT SET-UP

Electrical measurements are performed using the IVVI rack, a low noise electronics system developed in house by Raymond Schouten and DEMO [15]. It allows us to reliably apply and measure voltages and currents in the nV and fA regime. To isolate the measurement modules from external electrical noise sources, the rack is powered by batteries and communicates with the data acquisition system via an optical link. A schematic overview of a typical experiment is shown in Fig. 3.8. We measure the conductance of our device (shown as a variable resistance R_{Device} ³) in a two-terminal voltage bias configuration. The voltage is supplied by a S3b module, which can be used to simultaneously apply a dc (V_{Bias}) and low frequency ac (V_{Exc}) voltage to the sample. It has an output impedance R_{Out} which depends on the gain setting (typically in the range of 10-100 Ω).

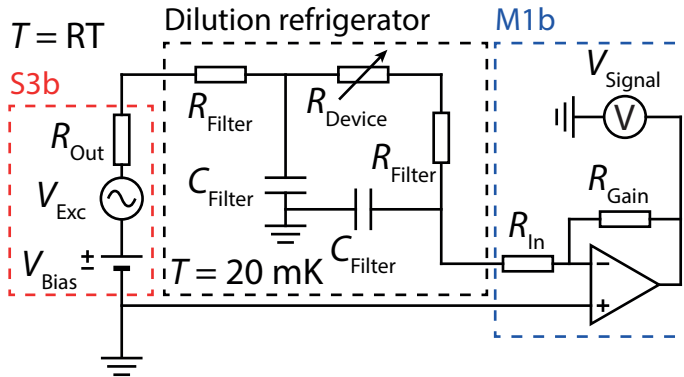


Figure 3.8: **Schematic overview of the electrical measurement set-up.** Measurement set-up used to measure the conductance through a nanowire device, shown as a variable resistance R_{Device} . Additional contributions from the filters are represented by R_{Filter} and C_{Filter} , respectively. The room temperature voltage bias (S3b) and IV-converter (M1b) modules are used to bias the sample and measure the resulting current.

We connect the bias voltage to the electrical lines going into the dilution refrigerator, which are connected to our sample which is mounted to the cold finger. The electrical lines are filtered at the mixing chamber plate, with the filtering consisting of low-pass RC-filters (<40 kHz), low-pass π -filters (<100 MHz to <1 GHz) and low-pass Cu-powder (<1 GHz) filters. The current through the sample is measured with a M1b module, which converts the current to a voltage with the gain determined by R_{Gain} . The resulting volt-

³The capacitance of the device to ground is typically in the fF range, which is too small to be significant at the typical frequencies used in our experiments.

age V_{Signal} is then measured with a Keithley 2000 multimeter. The input impedance R_{In} is determined by the gain. For typical gain settings of 1-10 MV/A, R_{In} is 2-12 k Ω .

To measure the differential conductance $\left. \frac{dI}{dV} \right|_{V=V_{\text{Bias}}}$ we use a SR830 digital lock-in amplifier to apply a sinusoidal excitation $V_{\text{Exc}} \sin(\omega_{\text{Exc}} t)$ to the sample, which will result in a voltage signal V_{Response} , which is then used as an input for the lock-in. The total signal can be written as a Fourier series:

$$V_{\text{signal}}(t) = V_{\text{Response}} \sin(\omega_{\text{Exc}} t + \phi_{\text{Response}}) + \sum_k V_k \sin(\omega_k t + \phi_k). \quad (3.1)$$

Here we have singled out the contribution at the excitation frequency ω_{Exc} , V_{Response} . Components V_k at other frequencies ω_k can be caused by e.g. non-linearities in the circuit or noise. The lock-in amplifier multiplies $V_{\text{signal}}(t)$ by an internal reference $V_{\text{Ref}} \sin(\omega_{\text{Ref}} t)$. It then uses a low-pass filter to filter out any ac components of the signal. This leaves a dc component proportional to V_{Response} if $\omega_{\text{Ref}} = \omega_{\text{Exc}}$, allowing a very low noise detection of the circuit response to the applied excitation [16].

For small deviations δV , and low frequencies such that the response of the circuit can be considered purely resistive, we can write the dc current due to an applied bias voltage as

$$I(V_{\text{Bias}} + \delta V) \approx I(V_{\text{Bias}}) + \left. \frac{dI}{dV} \right|_{V=V_{\text{Bias}}} \delta V, \quad (3.2)$$

Setting $\delta V = V_{\text{Exc}} \sin(\omega_{\text{Exc}} t)$, we see that the signal recorded by the lock-in amplifier is a direct measure for the differential conductance at the dc bias voltage V_{Bias} , as long as V_{Exc} is small.

The bandwidth of the lock-in amplifier detection is set by the integration time constant. For typical experiments, this time constant is 0.1-0.3 s, resulting in a bandwidth of \approx 3-10 Hz. The frequency ω is typically in the range of 20-100 Hz. Because of excessive noise coming from the main power grid, frequencies around multiples of 50 Hz should be avoided. For tunneling spectroscopy, the spectroscopic resolution is set by the excitation amplitude V_{exc} . We use typical amplitudes of 5-10 μ V at the sample, which is below the smearing expected from the finite sample temperature.

3.5. LOW TEMPERATURE SET-UPS

The experiments in this thesis have been performed in bottom loading Oxford Triton 200 (K4) and Oxford Triton 400 (K3, K5) dilution refrigerators, with a base temperature of about 20 mK on the mixing chamber plate. The Aharanov-Bohm measurements presented in chapter 4 have been performed in a closed cycle He-3 cryostat from Janis (known as Vector Janis), with a base temperature of about 300 mK. Because a high sample temperature limits the resolution that can be achieved in tunneling spectroscopy experiments, very low temperatures are required. In order to achieve the lowest temperature, the sample must be sufficiently isolated from the warmer parts of the set-up.

The relevant temperature for our experiments is the temperature of the electrons as they enter our devices from the attached leads. This temperature can be significantly higher than the temperature of the mixing chamber if thermalization at the coldest stage of the fridge is weak, for example due to thermal decoupling of the electrons from the substrate lattice [17].

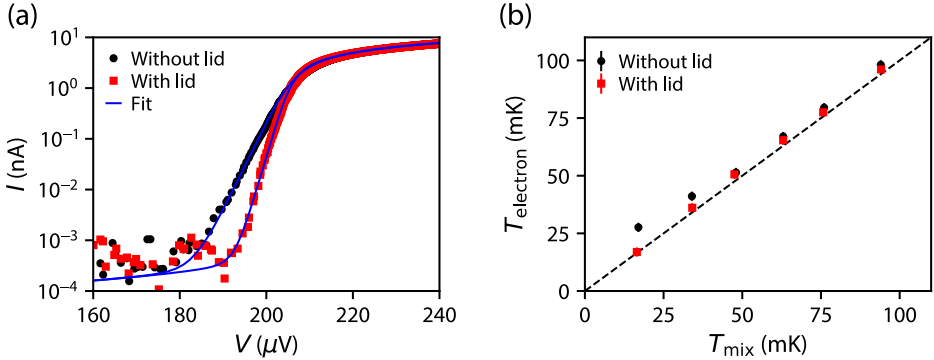


Figure 3.9: **Effect of sample lid on electron temperature in K4.** (a) $I - V$ characteristics of a NIS junction without (black circles) and with (red squares) a copper sample lid. Fits to the model of ref. [18] indicated by the blue lines. (b) Extracted electron temperature as a function of the mixing chamber temperature. The addition of the sample lid significantly lowers the temperature of the electrons going through the device.

We characterize the electron temperature of the K4 dilution refrigerator with a Cu-AlO_x-Al NIS junction device, developed by the group of J. Pekola at Aalto University [18]. When the device is voltage biased below the gap of the superconductor, the sub-gap current depends on the smearing of the Fermi-Dirac distribution in the normal metal. We measure the $I - V$ characteristic and then fit the sub-gap current using the model of ref. [18] to extract the electron temperature (Fig. 3.9(a)).

In 3.9(b), we plot the extracted electron temperature as a function of the mixing chamber temperature, T_{mix} . If the electrons are well thermalized, we expect the data points to fall onto the dashed line. However, T_{electron} becomes significantly higher than T_{mix} as the fridge is cooled to base temperature (black circles). One possible reason is insufficient shielding from radiation close to the sample stage, which heats up the electrons. We cover the sample with a light-tight copper lid, which is coated with an absorptive black paint on the inside, in order to minimize heating due to residual radiation, which significantly reduces the electron temperature (red squares), and keeps the electrons well thermalized all the way to base temperature. The difference can also clearly be seen in Fig. 3.9(a), where the rise of the current with bias voltage is much sharper with (red squares) than without the lid (black circles).

A few additional remarks are in order. The fitting procedure requires estimates for the superconducting gap, the normal state resistance of the junction, and the Dynes parameter, which are then assumed to be temperature independent in the range of interest.

For these fits, we fixed the parameters to the following values: $R_N = 16 \text{ k}\Omega$, $\gamma = 1 \cdot 10^{-5}$, and $\Delta = 205 \text{ }\mu\text{eV}$.

For the experiment without the sample lid, the sample was loaded using the bottom loading system. During this procedure, the fridge is at low temperature ($\sim 20 \text{ K}$) when the sample is inserted. For the experiment with the lid, the sample was loaded while the fridge was at room temperature. The thermalization of the sample depends on the anchoring to the mixing chamber plate, which is different between a cold and warm load. This means not all of the difference is necessarily related to the sample lid. Because warming up the entire dilution refrigerator to room temperature for every sample load is a significant time investment, all of the nanowire experiments in this thesis have been performed with cold loaded samples.

Previously it was found that extracting the electron temperature by fitting the Coulomb peaks in a nanowire quantum dot gives slightly different results than the NIS junctions [19]. As the NIS junction consists of micron size metallic leads, it is plausible that it will thermalize better to the substrate than our nanowire devices, which are significantly smaller (similar to the nanowire quantum dot case). Therefore, the relevant temperature in our experiments is most likely slightly higher than the temperature measured using the NIS junction. When we apply the same model to the hard gap tunneling data from e.g. chapter 4, the extracted electron temperature is typically 15-25 mK higher than what we would expect based on the NIS measurements, giving us a typical T_{electron} of 50 mK for practical purposes.

REFERENCES

- [1] K. Flöhr, M. Liebmann, K. Sladek, H. Y. Günel, R. Frielinghaus, F. Haas, C. Meyer, H. Hardtdegen, T. Schäpers, D. Grützmacher, and M. Morgenstern, *Manipulating InAs nanowires with submicrometer precision*, Review of Scientific Instruments **82**, 113705 (2011).
- [2] D. J. van Woerkom, *Majorana fermions in well aligned InSb-nanowires with superconducting and normal contacts*, Master's thesis, Technische Universiteit Delft (2012).
- [3] D. B. Suyatin, C. Thelander, M. T. Björk, I. Maximov, and L. Samuelson, *Sulfur passivation for ohmic contact formation to InAs nanowires*, Nanotechnology **18**, 105307 (2007).
- [4] J. Kammhuber, M. C. Cassidy, H. Zhang, O. Gül, F. Pei, M. W. A. de Moor, B. Nijholt, K. Watanabe, T. Taniguchi, D. Car, S. R. Plissard, E. P. A. M. Bakkers, and L. P. Kouwenhoven, *Conductance Quantization at Zero Magnetic Field in InSb Nanowires*, Nano Letters **16**, 3482 (2016).
- [5] F. Boscherini, Y. Shapira, C. Capasso, C. Aldao, M. del Giudice, and J. H. Weaver, *Exchange reaction, clustering, and surface segregation at the Al/InSb(110) interface*, Phys. Rev. B **35**, 9580 (1987).

- [6] R. Sporcken, P. Xhonneux, R. Caudano, and J. P. Delrue, *The formation of the Al-InSb(110) interface*, *Surface Science* **193**, 47 (1988).
- [7] Transene Company, Inc., *Aluminum Etchants*, <https://transene.com/aluminum/> (Online, accessed October 1st 2018).
- [8] K. R. Williams and R. S. Muller, *Etch rates for micromachining processing*, *Journal of Microelectromechanical Systems* **5**, 256 (1996).
- [9] W. Chang, *Superconducting Proximity Effect in InAs Nanowires*, Ph.D. thesis, Harvard University (2014).
- [10] Shipley Company, *Material safety data sheet Microposit MF-321 developer*.
- [11] *Etch characteristics of KOH, TMAH and dual doped TMAH for bulk micromachining of silicon*, *Microelectronics Journal* **37**, 519 (2006).
- [12] J. Oh, J. Myoung, J. S. Bae, and S. Lim, *Etch Behavior of ALD Al₂O₃ on HfSiO and HfSiON Stacks in Acidic and Basic Etchants*, *Journal of The Electrochemical Society* **158**, D217 (2011).
- [13] H. Zhang, O. Gül, S. Conesa-Boj, M. P. Nowak, M. Wimmer, K. Zuo, V. Mourik, F. K. de Vries, J. van Veen, M. W. A. de Moor, J. D. S. Bommer, D. J. van Woerkom, D. Car, S. R. Plissard, E. P. A. M. Bakkers, M. Quintero-Pérez, M. Cassidy, S. Koelling, S. Goswami, K. Watanabe, T. Taniguchi, and L. P. Kouwenhoven, *Ballistic superconductivity in semiconductor nanowires*, *Nature Communications* **8**, 16025 (2017).
- [14] P. T. J. Gennissen and P. J. French, *Sacrificial oxide etching compatible with aluminum metallization*, in *Proceedings of International Solid State Sensors and Actuators Conference (Transducers '97)*, Vol. 1 (1997) pp. 225–228.
- [15] R. Schouten, *QT designed instrumentation*, <http://qtwork.tudelft.nl/~schouten/> (Online, accessed October 1st 2018).
- [16] S. R. Systems, *Model SR830 DSP Lock-In Amplifier*.
- [17] F. Pobell, *Matter and Methods at Low Temperatures*, Third ed. (Springer Berlin Heidelberg New York, 2007).
- [18] A. V. Feshchenko, L. Casparis, I. M. Khaymovich, D. Maradan, O.-P. Saira, M. Palma, M. Meschke, J. P. Pekola, and D. M. Zumbühl, *Tunnel-Junction Thermometry Down to Millikelvin Temperatures*, *Phys. Rev. Applied* **4**, 034001 (2015).
- [19] D. J. van Woerkom, *Semiconductor nanowire Josephson junctions*, Ph.D. thesis, Technische Universiteit Delft (2017).

4

EPITAXY OF ADVANCED NANOWIRE QUANTUM DEVICES

S. Gazibegovic*, D. Car*, H. Zhang*, S. C. Balk, J. A. Logan, **M. W. A. de Moor**, M. C. Cassidy, R. Schmits, D. Xu, G. Wang, P. Krogstrup, R. L. M. Ophel Veld, K. Zuo, Y. Vos, J. Shen, D. Bouman, B. Shojaei, D. Pennachio, J. S. Lee, P. J. van Veldhoven, S. Koelling, M. A. Verheijen, L. P. Kouwenhoven, C. J. Palmstrøm, and E. P. A. M. Bakkers

Semiconductor nanowires are ideal for realizing various low-dimensional quantum devices. In particular, topological phases of matter hosting non-Abelian quasiparticles (such as anyons) can emerge when a semiconductor nanowire with strong spin-orbit coupling is brought into contact with a superconductor [1, 2]. To exploit the potential of non-Abelian anyons—which are key elements of topological quantum computing—fully, they need to be exchanged in a well-controlled braiding operation [3–8]. Essential hardware for braiding is a network of crystalline nanowires coupled to superconducting islands. Here we demonstrate a technique for generic bottom-up synthesis of complex quantum devices with a special focus on nanowire networks with a predefined number of superconducting islands. Structural analysis confirms the high crystalline quality of the nanowire junctions, as well as an epitaxial superconductor-semiconductor interface. Quantum transport measurements of nanowire ‘hashtags’ reveal Aharonov-Bohm and weak antilocalization effects, indicating a phase-coherent system with strong spin-orbit coupling. In addition, a proximity-induced hard superconducting gap (with vanishing sub-gap conductance) is demonstrated in these hybrid superconductor-semiconductor nanowires, highlighting the successful materials development necessary for a first braiding experiment. Our approach opens up new avenues for the realization of epitaxial three-dimensional quantum architectures which have the potential to become key components of various quantum devices.

This chapter has been published in *Nature* **548**, 434–438 (2017).

*These authors contributed equally to this work.

4.1. INTRODUCTION

Majorana zero modes are predicted to emerge once a superconductor is coupled to a semiconductor nanowire with a strong spin-orbit interaction in an external magnetic field [1, 2]. InSb nanowires are a prime choice for this application owing to the large Landé g -factor (about 50) and strong Rashba spin-orbit interaction [9], crucial for the realization of Majorana zero modes. In addition, InSb nanowires generally show high mobility and ballistic transport [10–12]. Indeed, signatures of Majorana zero modes have been detected in hybrid superconductor-semiconductor InSb and InAs nanowire systems [11, 13–15]. Multiple schemes for topological quantum computing based on braiding of Majorana zero modes have been reported, all employing hybrid nanowire networks [3–8].

4

Top-down fabrication of InSb nanowire networks is an attractive route towards scalability [16]; however, the large lattice mismatch between InSb and insulating growth substrates limits the quality of the crystal. An alternative approach is bottom-up synthesis of out-of-plane nanowire networks which, owing to their large surface-to-volume ratio, effectively relieve strain on their sidewalls, enabling the growth of monocrystalline nanowires on highly lattice-mismatched substrates [17–19]. Recently, different schemes have been reported for merging nanowires into networks [20–22]. Unfortunately, these structures are either not monocrystalline, owing to a mismatch of the crystal structure of the wires with that of the substrate (that is, hexagonal nanowires on a cubic substrate) [22], or the yield is low owing to limited control over the multiple accessible growth directions (the yield decreases with the number of junctions in the network) [23].

Here, we develop a technique for bottom-up synthesis of monocrystalline InSb nanowire networks with an unprecedented yield of crossed junctions. Accurate control over the nanowire position and growth direction enables us to grow complicated networks of up to four crossed junctions, such as closed loops of four interconnected nanowires (referred to as ‘hashtags’). Furthermore, this platform allows *in situ* growth of a predefined number of separated superconducting islands on the nanowires. This eliminates the need for metal etching during device fabrication. Therefore, the integration of semiconductors with metals (for example, niobium) is possible without an additional etching process. This guarantees that the pristine atomically flat InSb(110) facets are left intact, a key element for high device performance. At the same time a clean epitaxial superconductor-nanowire interface is established, which has recently been proven to be crucial for the quality of the induced superconducting gap [24, 25].

4.2. SUBSTRATE FABRICATION AND NANOWIRE GROWTH

For the growth of the nanowire networks a substrate with trenches is first fabricated (see Fig. 4.1a). These structures are defined by electron-beam lithography, a reactive ion etch and a subsequent wet etch to expose (111)B facets on an InP(100) crystal surface (Fig. 4.1a). See section 4.6 and Fig. 4.5 for the fabrication of InP substrate with trenches. A second lithography step is then used to position gold particles, which catalyze nanowire growth via the vapor-liquid-solid mechanism, on the inclined facets (Figs. 4.6 and 4.7).

Owing to the geometry of the (111)B facets, the nanowires are forced to grow towards each other and can fuse into a network.

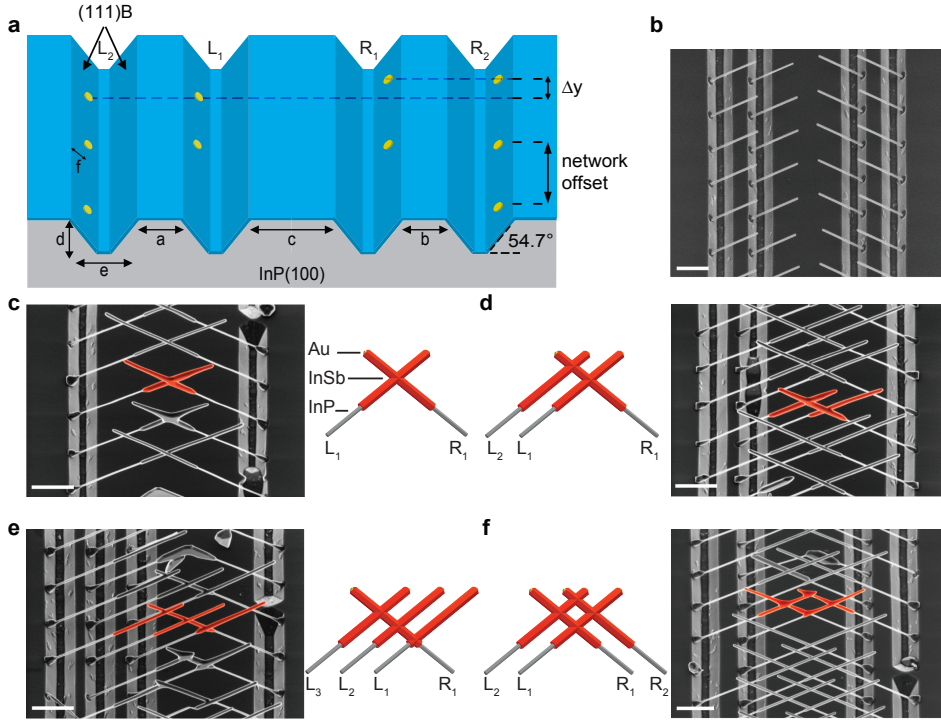


Figure 4.1: **Deterministic growth of InSb nanowire networks.** **a**, Schematic illustration of the substrate with etched trenches. Gold catalysts are lithographically defined on the inclined facets. The offset between the catalyst particles (Δy) is critical for the realization of nanowire networks and shadowed superconducting islands. The size and the symmetry of the networks are controlled by the dimensions of the trenches indicated in the schematic: the spacing between the left-left (L_1 , L_2), a , right-right (R_1 , R_2), b , and left-right (L_1 , R_1), trenches, c , as well as the trench depth, d , width, e , and position of the gold particles on the inclined facets, f . **b**, A scanning electron microscopy (SEM) image of InP nanowires which serve as stems for InSb nanowire growth. **c-f**, SEM images and schematic illustrations of accomplished nanowire structures having one junction (**c**), two junctions (**d**), three junctions (**e**) or four junctions (**f**; hashtag). All SEM images are taken at 30° tilt. All scale bars are $1 \mu\text{m}$.

The final size and symmetry of the networks are controlled by the dimensions of the trenches and the spacing between them, that is, the parameters $a-f$, as indicated in Fig. 4.1a and Fig. 4.8. The left (right) trenches and wires grown from them are labelled L_1 , L_2 (R_1 , R_2). The offset (Δy) between the gold particles is an important parameter to control for two reasons. First, if $\Delta y < D$, where D is the nanowire diameter, nanowires will merge during growth (specifically, for $\Delta y \approx 0$ ($\Delta y \leq D$), resulting in the formation of a T-junction (X-junction) [23]); second, $\Delta y > D$ enables shadow growth of the superconducting islands, as discussed later in the text. In Fig. 4.1b we show a uniform array of InP nanowires that are used as stems to facilitate uniform nucleation of InSb

nanowires. When InSb nanowires (highlighted in red in Fig. 4.1c-f) are grown on top of these InP stems, nanowire networks with 1-4 wire-wire junctions are formed, depending on the trench design (Fig. 4.1c-f). Importantly, this approach is generic and can be used to synthesize interconnected nanowires of various semiconductor materials which grow along a $\langle 111 \rangle$ B direction. The number of wire-wire junctions can be increased by allowing for longer nanowire growth times and/or fabricating a larger number of left and right trenches. The high crystal quality of the InSb nanowire junctions is confirmed by high-resolution transmission electron microscopy (HRTEM) imaging of a hashtag structure (see Fig. 4.9).

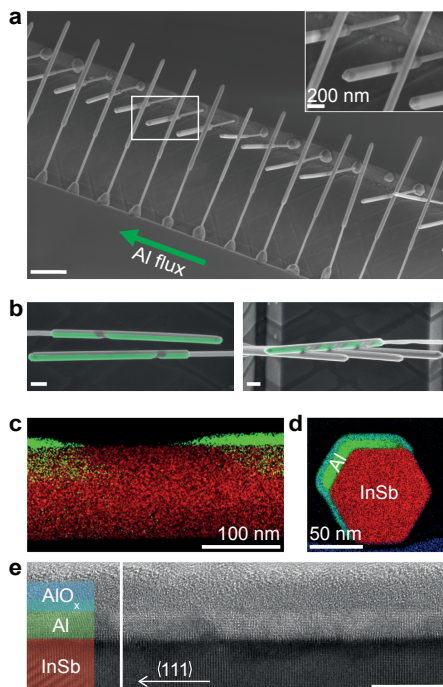


Figure 4.2: Epitaxial growth of Al islands on InSb nanowires. **a**, A 45° -tilted SEM image of an array of Al-InSb nanowires. The green arrow indicates the direction of Al beam flux during deposition. Scale bar is $1 \mu\text{m}$. Inset, magnified area indicated by a white rectangle in the main panel. Each InSb nanowire is covered by two Al islands separated by a shadowed region. The number of shadows, n , and hence the number of superconducting islands, $n + 1$, is determined by the number of wires directly in front of the shadowed wire. **b**, SEM images of InSb nanowires with two (left) and four (right) Al islands (pseudo-colored green). Both scale bars are 200 nm . **c**, STEM-EDX chemical composition map of an InSb nanowire (red) with Al islands (green) separated by an Al-free shadowed region. **d**, EDX chemical composition map of the nanowire cross-section. Al (green) is covering two out of the six $\{110\}$ InSb side-facets. The Al-InSb interface is oxygen-free. **e**, High-resolution transmission electron microscopy image of an InSb nanowire (red) covered with a thin (about 10 nm), crystalline film of Al (green) and a layer of AlO_x (blue). InSb growth direction $\langle 111 \rangle$ is indicated by a white arrow. The image is taken along the $\langle 110 \rangle$ zone axis. The scale bar is 10 nm .

Next, we combine the nanowire-network geometry with the directionality of molecular beam epitaxy (MBE) to shadow-grow aluminum superconducting islands on the InSb wires. The aluminum flux is aligned parallel to the trenches (Fig. 4.2a), such that a frontal wire casts a shadow on a wire in the background (inset of Fig. 4.2a). This causes interruptions in a uniform layer of aluminum as shown in Fig. 4.2b (left). For effective shadowing, it is important that the frontal wire does not merge with the shadowed wire, that is, $\Delta y > D$. The number of shadows, n , (and, accordingly, the number of superconducting islands, $n + 1$) on any InSb nanowire is determined by the number of wires directly in front of that nanowire. For example, Fig. 4.2b (right) and Fig. 4.10 depict an InSb nanowire with three shadows cast by three frontal nanowires. The position and the width of the shadows are uniform for all wires examined and are set by the relative position of the wires and the solid angle of the aluminum effusion cell. The abrupt transition between the shadowed region of the nanowire and the segment covered with aluminum is evident from the chemical composition map (Fig. 4.2c) acquired by energy-dispersive X-ray spectroscopy (EDX) combined with scanning transmission electron microscopy (STEM). The line-of-sight directionality of MBE growth results in aluminum being deposited on two out of six facets of an InSb nanowire, as can be seen from a STEM-EDX map of a nanowire cross-section (Fig. 4.2d). The partial coverage of a nanowire with aluminum is essential as it allows tuning of the electron density of the proximitized nanowire by an external gate electrode, which is necessary for accessing the topological phase. The epitaxial interface between the InSb nanowire and a uniform, thin layer of aluminum is revealed by HRTEM imaging (Fig. 4.2e). In the next section, we assess the electronic quality of our structures.

4.3. PHASE-COHERENT TRANSPORT IN NANOHASHTAGS

Phase-coherent transport is a basic requirement for certain measurement-based braiding schemes which make use of an interferometric readout [7, 8]. This interferometer requires tuning towards a maximum amplitude of the Aharonov-Bohm oscillations. To investigate the Aharonov-Bohm effect in our nanowire networks, nanowire hashtags were transferred onto a $\text{SiO}_2/\text{p-Si}$ substrate and contacted by metal electrodes (Au/Cr, 4.3a left inset). Figure 4.3a shows the magnetoconductance of a representative device (device A).

Periodic Aharonov-Bohm oscillations can clearly be seen (Fig. 4.3a right inset), as well as a pronounced weak antilocalization conductance peak at $B = 0$ T. The weak antilocalization conductance peak is present in most of the measured hashtag devices, for both in- and out-of-plane magnetic field orientations (Fig. 4.11), indicating a strong spin-orbit coupling in this system. The observed weak antilocalization effect also suggests diffusive transport in our hashtag devices, since the hashtag length is several times longer than the estimated mean free path, approximately 250 nm for InSb nanowires [10, 26]. The period of the Aharonov-Bohm oscillations is extracted from a discrete Fourier transform of the magnetoconductance. Figure 4.3b shows the averaged fast Fourier transform (FFT) spectrum of which the peak frequency (60 T^{-1} with a standard deviation of 2 T^{-1}) corresponds to a period ΔB of 16.7 mT with a standard deviation of 0.6 mT.

The effective area (A) calculated from this Aharonov-Bohm period ($A = \Phi/\Delta B = 0.25 \mu\text{m}^2$ with a standard deviation of $0.01 \mu\text{m}^2$, where $\Phi = h/e$ is the flux quantum) is in agreement with the measured area of a hashtag loop ($A \approx 0.25 \mu\text{m}^2$ with a standard deviation of $0.02 \mu\text{m}^2$).

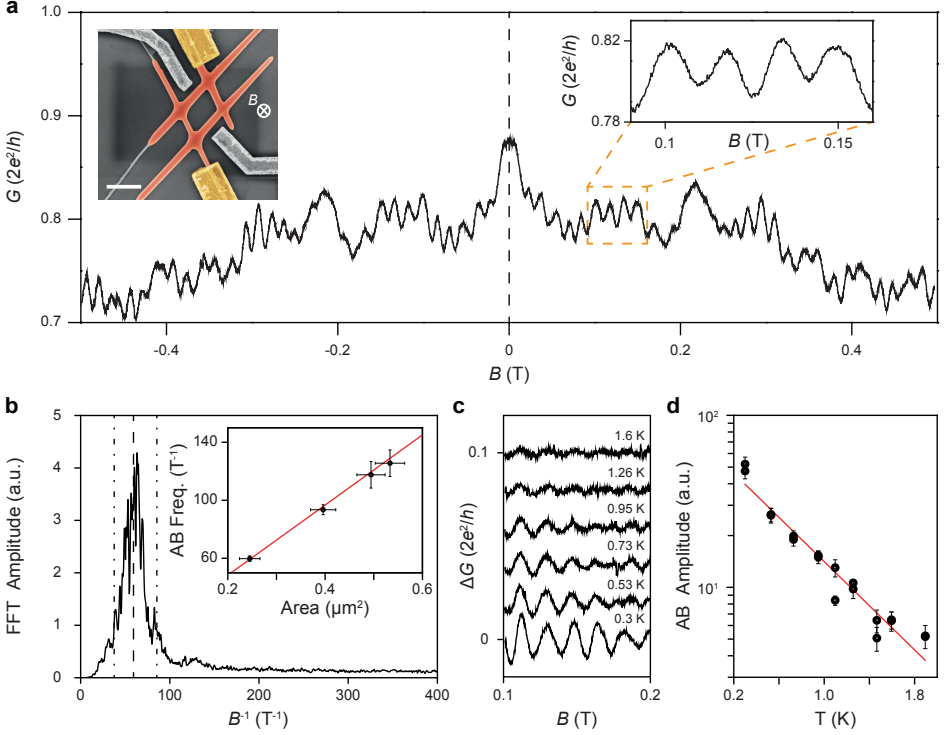


Figure 4.3: Aharonov-Bohm and weak antilocalization effects in nanowire hashtags. **a**, Magnetoconductance of a hashtag shows periodic Aharonov-Bohm oscillations and a weak antilocalization peak at $B = 0$ T. Inset (left), a pseudo-colored SEM image of the device. An InSb hashtag (red) is in contact with normal metal electrodes (yellow) and measured in an out-of-plane magnetic field at 300 mK. Scale bar is 500 nm. Inset (right), magnification of the region indicated by an orange rectangle in the main panel, containing four Aharonov-Bohm periods. **b**, FFT spectrum of the magnetoconductance of this device (ensemble averaged), indicating the Aharonov-Bohm (AB) oscillation frequency. The dashed line indicates the expected frequency based on the area calculated from the SEM image, dash-dotted lines indicate the expected minimum and maximum frequencies due to the finite thickness of the interferometer arms. Inset, plot of the peak frequency, assigned from the averaged FFT spectra, as a function of the loop area for four different hashtag devices. The red line corresponds to the expected frequency of an h/e periodic oscillation for a given loop area. a.u., arbitrary units. **c**, Temperature dependence of Aharonov-Bohm oscillations (background subtracted). The Aharonov-Bohm effect persists up to 1.6 K. Curves are offset vertically for clarity. **d**, Aharonov-Bohm (AB) amplitude as a function of temperature. The red line is a fit to the data, showing an exponential decay of the oscillation amplitude.

We determine the peak frequency for four different devices with different loop areas, showing good agreement with the expected values (Fig. 4.3b inset). This agreement between theory and experiment confirms that the observed Aharonov-Bohm oscillations

are indeed a result of the quantum interference of electron waves emanating from the two transport channels that constitute the hashtag.

Magnetoconductance traces taken at increasing temperature values are shown in Fig. 4.3c. Aharonov-Bohm oscillations persist up to about 1.6 K. The amplitude of the Aharonov-Bohm oscillations decays exponentially with temperature (Fig. 4.3d). This exponential behaviour, observed in early Aharonov-Bohm experiments with similar loop size [27], suggests that the phase coherence length is proportional to T^{-1} . Following the method described in ref. [27], we can estimate a phase coherence length on the basis of the suppression slope in Fig. 4.3d, to be $0.7 \mu\text{m}$ with a standard deviation of $0.1 \mu\text{m}$ at 1 K, which translates to $2.3 \mu\text{m}$ with a standard deviation of $0.3 \mu\text{m}$ at 300 mK.

4.4. SUPERCONDUCTING GAP IN SHADOWED JUNCTIONS

The last essential requirement for a topological phase is induced superconductivity in the InSb nanowires. For this study, InSb wires with two superconducting islands were used to fabricate N-nanowire-S devices by replacing one superconducting island with a normal metal electrode (see section 4.6 for the device fabrication recipe). The shadowed region of the nanowire is situated in between the normal contact and the other superconducting island, and can be depleted by a bottom gate (inset Fig. 4.4c), to form a tunnel barrier.

In the tunneling regime, the differential conductance reflects the quasiparticle density-of-states in the proximitized nanowire segment. Figure 4.4a shows a plot of differential conductance (dI/dV) versus bias voltage (V) and back gate voltage (V_{gate}) at 20 mK. Hence, the two high-conductance horizontal lines (at $V = \pm 0.24$ mV) in Fig. 4.4a correspond to the superconducting coherence peaks. The shape of the superconducting gap can be clearly resolved in Fig. 4.4b, which shows a vertical line-cut plotted on both linear (left) and logarithmic (right) scales, indicating the ratio of the above-gap to sub-gap conductance $G_N/G_S \approx 100$.

Figure 4.4c maps out the obtained values of G_S versus G_N (black dots) together with the Beenakker expression (red line) for an N-quantum point contact (QPC)-S system. This expression assumes that G_S is due to a single-channel Andreev reflection in the shadowed region (see Fig. 4.12) [28]. Theory and experiment are in agreement over two orders of magnitude in conductance. This shows that the G_S in this system is dominated by the Andreev process in the absence of quasiparticle transport.

Figure 4.4d shows the differential conductance (dI/dV) of the same device as a function of bias voltage (V) and magnetic field (B) pointing along the nanowire, taken at $V_{\text{gate}} = -5.7$ V. From the horizontal line-cut at $V = 0$ V (lower panel), it can be seen that G_S is pinned to extremely low values of conductance for magnetic field values up to 0.9 T. The evolution of the induced superconducting gap in the magnetic field is illustrated in Fig. 4.4e. The black, green and orange line cuts are taken at $B = 0$ T, 0.5 T and 1 T, respectively. Importantly, the induced hard superconducting gap in Al-InSb nanowires endures

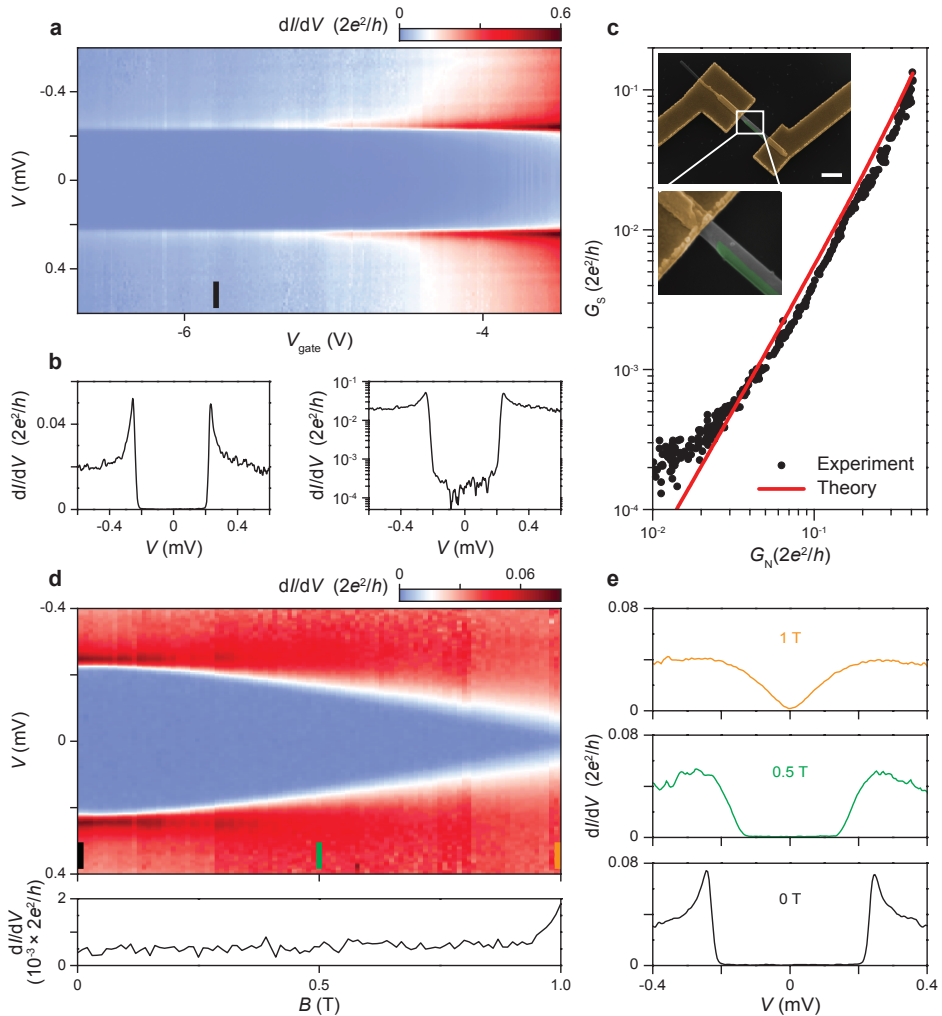


Figure 4.4: Induced hard superconducting gap in a shadowed Al-InSb nanowire device. **a**, Differential conductance (dI/dV) as a function of bias voltage (V) and back gate voltage (V_{gate}) in the tunneling regime, resolving a hard superconducting gap (at about 20 mK). **b**, A line cut taken at the position indicated by the black bar in **a** (at $V_{\text{gate}} = -5.8$ V), plotted on linear (left) and logarithmic scale (right). The ratio of above-gap and sub-gap conductance (G_N/G_S) reaches about 100. The induced superconducting gap size is $\Delta \approx 0.24$ meV. **c**, Sub-gap conductance as a function of above-gap conductance. The red line is the theoretical curve calculated assuming only Andreev processes [28]. Inset, a pseudo-colored SEM image of the similar device. The device is an N (yellow)-nanowire (gray)-S (green) system. The scale bar is 500 nm. **d**, Magnetic field dependence of the superconducting gap ($V_{\text{gate}} \approx -5.7$ V) in the device. The magnetic field direction is aligned with the nanowire axis. The lower panel shows a horizontal line-cut taken at $V = 0$ V (in the middle of the superconducting gap). **e**, Vertical line cuts taken at positions indicated by a black ($B = 0$ T), green ($B = 0.5$ T) and orange bar ($B = 1$ T) in the upper panel in **d**, illustrating the evolution of the induced superconducting gap in the increasing magnetic field.

up to $B \approx 0.9$ T, which surpasses the value of the magnetic field required for achieving a topological phase transition in InSb ($B \approx 0.2$ T) [1, 2, 11]. Figure 4.12 shows data of additional devices and the corresponding analysis.

4.5. CONCLUSION

The combination of phase-coherent transport in a network of nanowires and a hard superconducting gap in InSb nanowires, induced by local superconductor islands, is a substantial materials advancement that paves the road for the first Majorana braiding experiments. We emphasize that the platform developed in this work is generic and can be used for many different superconductor-semiconductor combinations, presenting opportunities in new quantum devices. For instance, devices working on the principle of beam splitting and interference of electrons (that is, Aharonov-Bohm interferometers, Cooper pair splitters), as well as other, less-investigated quasiparticles, that is, phonons.

AUTHOR CONTRIBUTIONS

S.G., D.C., J.A.L., C.J.P. and E.P.A.M.B. carried out the material synthesis. H.Z. and **M.W.A.d.M.** fabricated the devices and performed the transport measurements and data analysis. S.C.B., M.C.C. and R.S. carried out the substrate preparation. D.X. and G.W. fabricated the hard gap devices and contributed to the measurement. S.G. and R.L.M.O.h.V. did the nanowire manipulation for the TEM analysis and transport measurements. M.A.V. performed TEM analysis. B.S., D.P. and J.S.L. contributed to the experiments at University of California, Santa Barbara. S.K. prepared the lamellae for TEM analysis. J.S. and D.B. contributed to the hard gap device fabrication. K.Z. and Y.V. contributed to the Aharonov-Bohm device fabrication and data analysis. P.J.v.V. supported work with the MOVPE reactor. E.P.A.M.B., C.J.P. and P.K. provided key suggestions on the experiments. E.P.A.M.B., C.J.P. and L.P.K. supervised the projects. All authors contributed to the writing of the manuscript.

4.6. METHODS AND ADDITIONAL DATA

4.6.1. SUBSTRATE FABRICATION

Fabrication of substrates with trenches is a three-step lithography process: First, electron-beam lithography (EBL) and metal lift-off are used to deposit alignment markers on a (100) InP substrate.

Substrate cleaning. InP(100) wafer is cleaned with buffered oxide etch ($\text{NH}_4\text{F}:\text{HF} = 7:1$) (5 min), rinsed with H_2O , IPA (10 min).

Fabrication of markers. Spin resist AR-P 6200.13 at 6000 r.p.m., bake at 150°C for 3 min; write marker patterns using e-beam lithography (dose $300 \mu\text{C cm}^{-2}$); developing in AR 600-546 for 1:30 min in ultrasonic agitation; ultrasonic rinse in IPA for 30 s, blow dry; evaporation of 80 nm Au; lift-off in PRS-3000 at 88°C for 2 h; rinse in warm ($>50^\circ\text{C}$) H_2O ; rinse in IPA for 1 min, blow dry.

Second, the InP(100) wafer is cleaned in buffered oxide etch ($\text{NH}_4\text{F}:\text{HF} = 7:1$) for 5 min and exposed to O_2 microwave plasma to create a thin (about 2 nm) sacrificial layer of native oxide on the surface before deposition of 50 nm of SiO_x by plasma-enhanced chemical vapor deposition (PECVD). EBL and reactive ion etching (RIE) in CHF_3/Ar plasma are used to define rectangular openings in SiO_x , whose long edge is aligned with the $[0\bar{1}\bar{1}]$ direction of the substrate. The alignment of the openings is crucial to achieve trenches with inclined $(111)\text{B}$ facets after the subsequent anisotropic wet etch step ($\text{HCl}:\text{H}_3\text{PO}_4 = 5:1$, for 15 s at 1°C) [29].

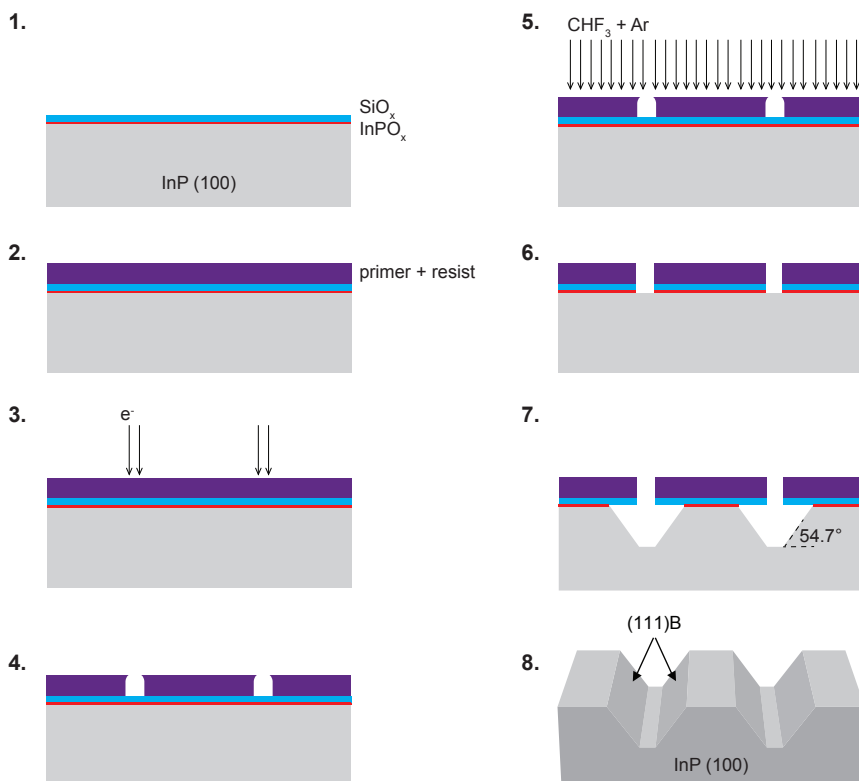


Figure 4.5: **Fabrication of InP substrate with trenches.** 1-8: Schematic illustration of the processing steps.

1, An out of the box wafer is etched in 7:1 buffered HF; an oxygen plasma step is performed to create a 'sacrificial' native oxide layer of 1.9 ± 0.1 nm [30]; a 20 nm SiO_x hard mask is deposited followed by another oxygen plasma treatment. **2, 3, 4**, The electron-beam primer and resist layer is spun; rectangular windows of ~ 200 nm are written using EBL and subsequently developed. **5, 6**, The hard mask is etched using reactive ion etching (RIE) with CHF_3 and Ar. **7, 8**, The wet etch in HCl (37%): H_3PO_4 (85%) with 5:1 ratio is performed to expose $(111)\text{B}$ facets in InP (100) and the hard mask is removed using 7:1 buffered HF.

Substrate cleaning. InP(100) wafer with markers is cleaned with buffered oxide etch ($\text{NH}_4\text{F}:\text{HF} = 7:1$) (5 min), rinsed with H_2O , IPA (10 min).

Hard mask (1 in Fig. 4.5). Sacrificial layer deposition microwave oxygen plasma (10 min, 200 ml min^{-1} , power 100 W, PVA Tepla 300); PECVD 20 nm SiO_x deposition (300°C , Oxford Instruments PlasmaLab 80 Plus); oxygen plasma (60 s, power 40 W).

Fabrication of trenches (2-8 in Fig. 4.5). Spin primer (sticking layer) AR 300-80 at 2000 r.p.m., bake at 180°C for 2 min; spin resist AR-P 6200.13 at 6000 r.p.m., bake at 150°C for 3 min; write trench patterns using EBL (dose $350 \mu\text{C cm}^{-2}$); developing in AR 600-546 for 1:30 min in ultrasonic agitation; ultrasonic rinse in IPA for 30 s, blow dry; RIE (reactive ion etch) mask (23 W, 50 standard cubic centimetres (sccm) CHF_3 , 2 sccm Ar, Leybold Hereaus, 12 min); wet etch in HCl (37%): H_3PO_4 (85%) ratio 5:1 (15 s, 1°C); strip the resist in PRS-3000 at 88°C for 20 min; removing hard mask in buffered oxide etch ($\text{NH}_4\text{F}:\text{HF} = 7:1$) (5 min).

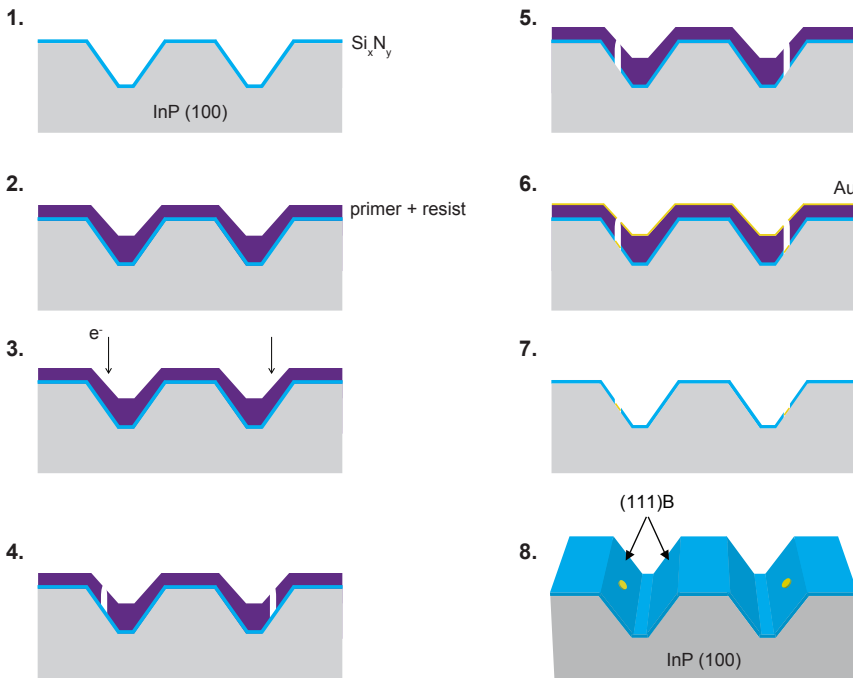


Figure 4.6: **Catalyst deposition.** 1-8: Schematic illustration of the processing steps. 1, 20 nm SiN_x mask is deposited followed by an oxygen plasma treatment. 2-4, E-beam primer and resist layer is spun (nominal resist thickness needs to be half of the depth of the trenches); arrays of dots (10-50 nm) are written on inclined (111)B facets using e-beam lithography and the resist is then developed. 5, Openings in SiN_x mask are defined using short 20:1 buffered HF etch. 6-8, 10 nm of gold is evaporated through the opening in SiN_x mask followed by a lift-off.

Third, SiO_x is stripped in BHF (5 min) and 20 nm of PECVD SiN_x is deposited on the substrate to prevent the parasitic InSb thin film growth which competes with nanowire growth [31]. EBL step followed by a short (40 s) buffered oxide etch ($\text{NH}_4\text{F}:\text{HF} = 20:1$ + surfactant (Triton)) is used to define openings in the SiN_x mask. Metal evaporation (8 nm of Au) and lift-off are used to position Au catalysts (10-50 nm in size) in the openings in

the SiN_x (Fig. 4.6).

Deposition of the mask (1 in Fig. 4.6). PECVD 20 nm SiN_x deposition (300 °C, Oxford Instrumentals PlasmaLab 80 Plus); oxygen plasma (60 s, power 40 W).

Dots formation (2-8 in Fig. 4.6). Spin primer (sticking layer) AR 300-80 at 2000 r.p.m., bake at 180 °C for 2 min; spin resist AR-P 6200.04 at 4000 r.p.m., bake at 150 °C for 3 min; write dot patterns using e-beam lithography (dose 700-800 $\mu\text{C cm}^{-2}$); developing in AR 600-546 for 1:30 min in ultrasonic agitation; ultrasonic rinse in IPA for 30 s, blow dry; opening the holes in SiN_x mask with buffered oxide etch ($\text{NH}_4\text{F}:\text{HF} = 20:1$) + 5 drops of surfactant Triton X-100 (40-60 s); rinse with H_2O , IPA (10 min); evaporation of 10 nm Au; lift-off in PRS-3000 at 88 °C for 2 h; rinse in warm (>50 °C) H_2O ; rinse in IPA for 1 min, blow dry.

4

4.6.2. NANOWIRE GROWTH

To remove organic residues from the wafer caused by the photoresist layer, O_2 plasma (10 min, 55 sccm O_2 , 300 W plasma power) was used before loading into an horizontal Aixtron 200 metal-organic vapor phase epitaxy (MOVPE) reactor with infrared lamp heating. InP nanowires, which act as the mediator for InSb nanowire growth, were grown at 450 °C for 19 min using tri-methyl-indium (TMI), phosphine (PH_3) and HCl (1%) with precursor molar fractions X_i (TMI) = 7.6×10^{-6} and X_i (PH_3) = 9×10^{-3} and X_i (HCl) = 8.3×10^{-6} . HCl was used to suppress unwanted sidewall growth. InSb nanowires were grown at 495 °C using tri-methyl-indium (TMI) and tri-methyl-antimony (TMSb) with precursor molar fractions X_i (TMI) = 2.8×10^{-7} and X_i (TMSb) = 5.1×10^{-5} , for 35 min. For both processes, the reactor pressure was 50 mbar, with a total flow of 6000 sccm and H_2 was used as a carrier gas.

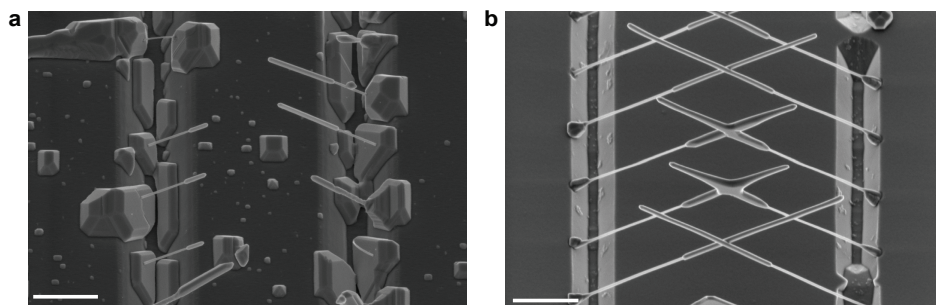


Figure 4.7: **Role of the SiN_x mask in InSb nanowire growth.** **a, b**, A 30°-tilted SEM image of InP-InSb nanowires grown on a substrate without **(a)** and with **(b)** SiN_x mask. A substantial amount of parasitic thin film growth is observed in **a**. Concave edges of the trenches act as a preferential nucleation site for InSb growth. Thin-film InSb growth is in direct competition with InSb nanowire growth, resulting in short nanowires and a very low yield of crossed junctions. By covering the substrate with a SiN_x mask, the growth is restricted to areas where the InP substrate is exposed [31]. This, in combination with approximately 100 times lower molar fractions of TMI and TMSb used for the growth of wires shown in **b**, eliminates the unwanted InSb layer growth and allows for growth of high-aspect-ratio InSb nanowires which merge into networks. Both scale bars are 1 μm .

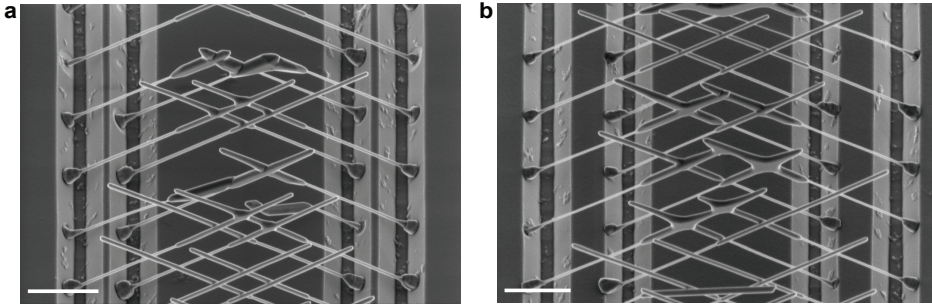


Figure 4.8: **Lithographic control over the trench design layout enables growth of hashtags spanning different loop areas.** **a, b,** InSb nanowire networks grown on trenches with different spacing between the left-left (L_1 , L_2) and right-right (R_1 , R_2) trenches, labelled *a* and *b* in Fig. 4.1a, respectively. Control over the dimensions of the trenches allows us to tune the length of the hashtag parallelogram. The scale bars are $1\ \mu\text{m}$.

4.6.3. GROWTH OF SUPERCONDUCTING ALUMINUM ISLANDS

Nanowire networks are transferred *ex situ* to a molecular beam epitaxy (MBE) chamber where an atomic hydrogen clean (20 min under continuous rotation, $380\ ^\circ\text{C}$, 5×10^{-6} torr H_2 pressure) is first performed to remove the native oxide from the InSb nanowire surface [32]. Subsequently, samples were cooled down to about 120 K by active liquid nitrogen cooling. Careful alignment of nanowires relative to the Al source is important for well-controlled shadowing of the nanowires. Samples are aligned such that the Al flux is parallel to the long edge of the trenches, as illustrated in Fig. 4.2a. Al cell temperature was $1085\ ^\circ\text{C}$, resulting in a growth rate of around $2\ \text{\AA}\ \text{min}^{-1}$. Immediately after growth, samples were transferred *in situ* to an MBE chamber equipped with an ultra-high purity O_2 source where they were dosed with approximately 10^{-5} torr of O_2 for 15 min. This step is important because a so-formed self-terminating oxide layer will ‘freeze-in’ the Al film, preventing it from diffusing and forming Stranski-Krastanov Al islands, while the sample is being heated up to room temperature in an ultra-high vacuum, before unloading from the MBE chamber.

4.6.4. AHARONOV-BOHM DEVICES

Device fabrication recipe.

1. Transfer hashtag nanowires onto a p-doped Si substrate covered by 285 nm SiO_2 layer, serving as a back gate dielectric.
2. Spinning bilayer PMMA: first PMMA 495K A6 at 3000 r.p.m. spinning rate, bake at $175\ ^\circ\text{C}$ for 10 min. Then PMMA 950K A2 at 2000 r.p.m., bake at $175\ ^\circ\text{C}$ for 10 min.
3. Write designed contacts and side gates patterns with e-beam.
4. Develop in developer (MIBK:IPA = 1:3) for 1 min, clean in IPA for 1 min, air-gun blow dry.

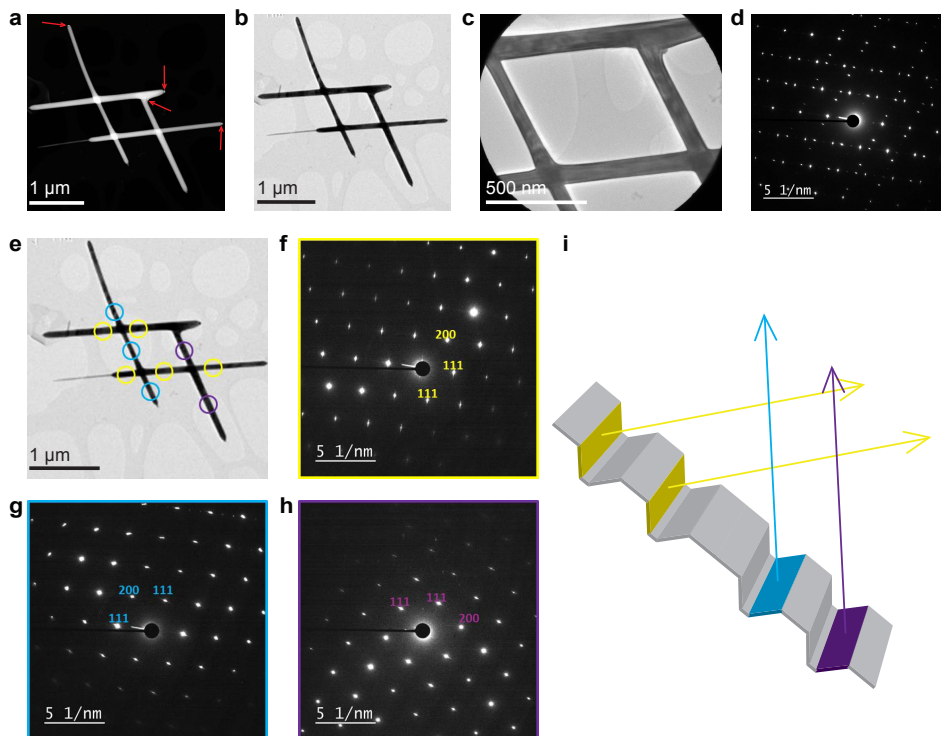


Figure 4.9: **Structural analysis of a hashtag taken from the substrate and deposited on a holey carbon film using a micromanipulator in the SEM.** **a**, High-angle annular dark field (HAADF) scanning TEM image of the hashtag. The red arrows indicate the positions of the gold catalyst particles. For one wire, the InP stem is present and recognizable. **b**, Corresponding bright field (BF) TEM image. **c**, BFTEM image displaying the central part of the hashtag as well as the $1.3\ \mu\text{m}$ aperture inserted for the selected area electron diffraction (SAED) pattern displayed in **d**. The pattern represents a superposition of three twin-related $\langle 110 \rangle$ zone axis patterns. **e**, To reveal the orientation of the individual wires of the hashtag, SAED patterns for all the wires were acquired, using a smaller SAED aperture diameter of $0.25\ \mu\text{m}$. Three different $\langle 110 \rangle$ zone axis patterns were recorded. The color coding of the apertures in **e** corresponds to the SAED patterns in **f-h**. **i**, Schematic representation of the formation of the hashtag presented in the TEM images. The blue and purple nanowires have two different orientations, related by a 180° rotation around their long axis. Thus, one of the wires has the same orientation as the substrate wafer, while the other one is twin related. The two yellow wires have identical orientations that differ from the orientations of the two other wires. Thus, these yellow wires are also twin-related to the substrate, though their rotation axis is different from that of the blue and purple wires.

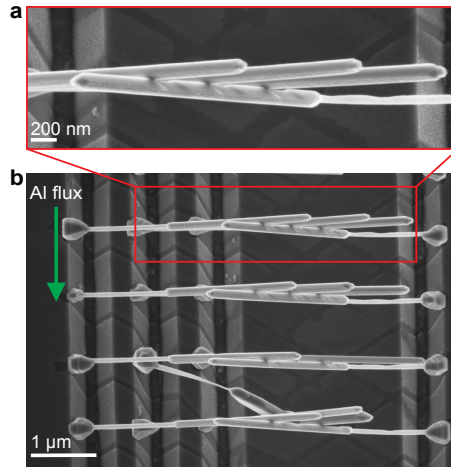


Figure 4.10: **The number of superconducting islands, $n + 1$, is determined by the number of wires, n , directly in front of the shadowed nanowire.** **a**, A high-magnification top-down SEM image of the region indicated by a red rectangle in **b**. The three nanowires facing the Al flux cast shadows on the wire directly behind them, resulting in InSb nanowires with four superconducting islands. The shadowing offset is about 200 nm. The nanowires bend towards each other owing to the e-beam exposure during imaging.

5. Remove scum, oxygen plasma 1 min with power 100 W, pressure 1.95 mbar (with Faraday cage in to screen the plasma).
6. Sulfur passivation: dip the chip in ammonium sulfide solution (3 ml $(\text{NH}_4)_2\text{S}$ mixed with 290 mg sulfur powder, then diluted with de-ionized water at a volume ratio of 1:200) at 60°C for 30 min. Then, rinse the chip in de-ionized water and transfer to an evaporator.
7. Helium milling for 30 s with a Kauffman ion source. Then continue to evaporate 10 nm Cr, followed by 200 nm of Au.
8. Lift-off in acetone.

Measurement and analysis. All the four Aharonov-Bohm devices were measured in a He-3 fridge with base temperature of about 300 mK. During the measurement, the side gates (gray in Fig. 4.3a left inset) were kept grounded, and the global back gate is used to turn on the conducting channels in the hashtag arms. The back gate voltage is 13.35 V for the measurement in Fig. 4.3a.

Ensemble average of FFT. The FFT spectrum shown in Fig. 4.3b is an ensemble average of the absolute values of 25 individual FFT spectra [33]. The individual FFTs were calculated from the corresponding magnetoconductance traces (including the one in Fig. 4.3a), which were measured successively with gate voltage values between 13.3 V and 13.7 V (resulting in conductance values between $0.7 \times 2e^2/h$ and $0.9 \times 2e^2/h$). A smooth background is subtracted from the original magnetoconductance curves before the FFT is calculated.

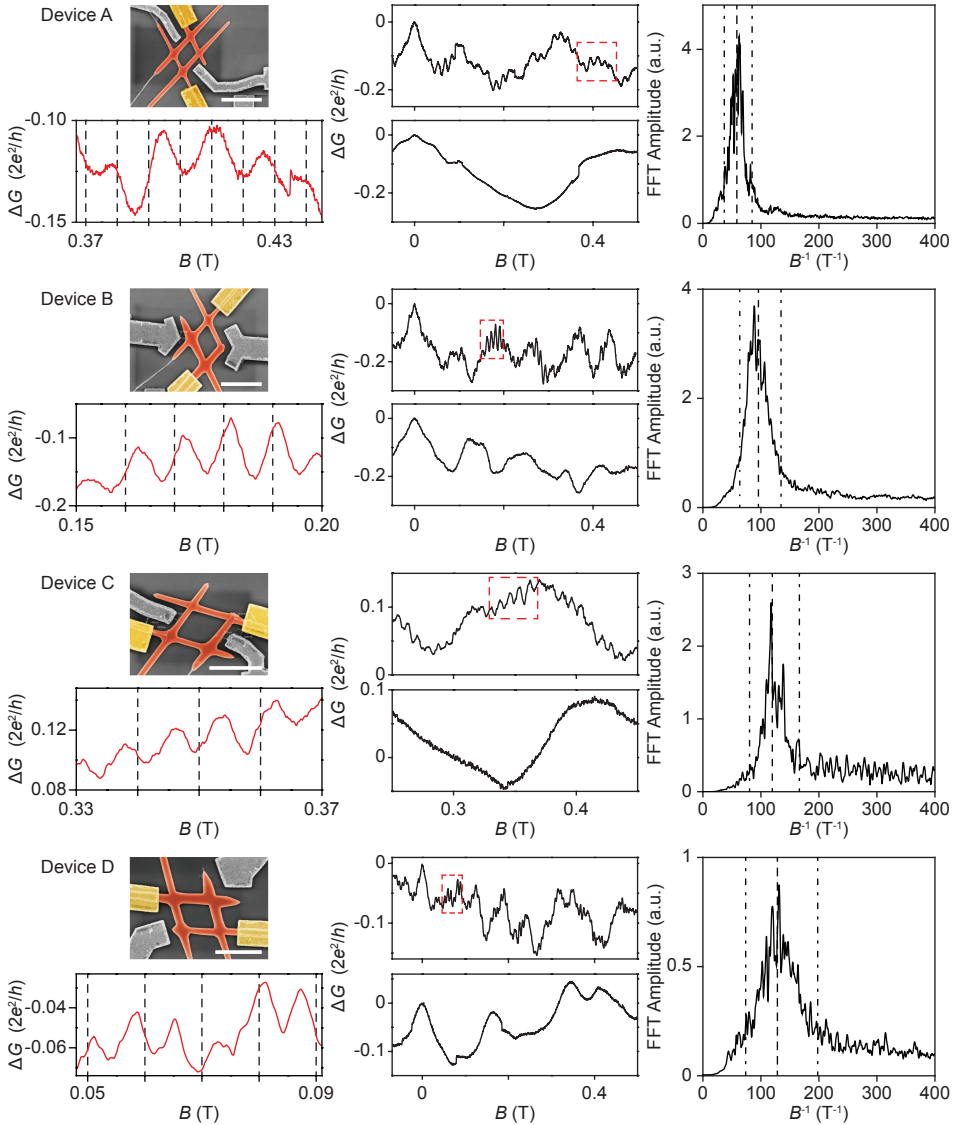


Figure 4.11: **Aharonov-Bohm oscillations in four devices with different hashtag surface areas.** Device A has been studied in detail in Fig. 4.3. For all devices, left upper panel shows the pseudo-colored SEM image of the device, middle panels show the conductance measured in the out-of-plane (top) and in-plane (bottom) magnetic field and right panel shows the ensemble averaged FFT spectrum. Only the out-of-plane magnetic field, whose flux penetrates through the hashtag loop, gives Aharonov-Bohm oscillations which indicates that the Aharonov-Bohm oscillations indeed originate from the coherent interference of electron waves of the two separated conducting nanowire arms. A magnified view of the Aharonov-Bohm oscillations (a zoom-in on the region indicated by a red rectangle in the upper middle panel) is shown in the lower left panel, while the right panel shows the averaged FFT spectrum. Plot of the peak frequency, assigned from the averaged FFT spectra, as a function of the measured loop area of the four devices is shown in the inset of Fig. 4.3b. Weak antilocalization peak at $B = 0$ T is present for both field directions, and in three (A, B, D) out of four devices, suggesting the strong spin-orbit nature of the InSb nanowire network. The corresponding back gate voltages of the four devices are: 15 V, 9 V, 12 V and 9 V, respectively. Temperature is 300 mK. The scale bar is 1 μm .

Estimation of hashtag loop area. The estimation is based on the SEM images of the device. We took the middle of the wire as the loop boundary to estimate the area, while the error bar of the area is estimated based on the accuracy of the nanowire length we measured from SEM images.

Estimation of phase coherence length. The amplitude of the Aharonov-Bohm oscillations is calculated by integrating the obtained Fourier spectrum over the frequency range corresponding to the expected h/e peak. This amplitude decays as $\Delta G \propto \exp(-L/L_\Phi(T))$, where L is the relevant device length (we took as half of the loop circumference, that is, $L = 1 \mu\text{m}$). L_Φ is the phase coherence length which is a function of temperature. The exponential suppression of ΔG over temperature suggests that L_Φ is proportional to T^{-1} : $L_\Phi = a/T$ (ref. [27]). The coefficient a can be extracted from the slope of exponential suppression in Fig. 4.3d, to be about $0.7 \mu\text{m K}$. This allows us to estimate phase coherence length at different temperatures.

4.6.5. HARD GAP DEVICES

InSb nanowire with two shadowed aluminum islands is contacted by Au/Cr. Argon plasma etching was used to remove the aluminum film before evaporation of normal contacts. One normal contact is deposited right next to the shadowed region to replace one aluminum island. The second normal contact is on the other end of the nanowire, sufficiently apart from the shadowed region not to affect the superconducting properties in its vicinity, serving as a current drain for the superconducting contact.

Device fabrication recipe.

1. Transfer InSb-Al nanowires onto a p-doped Si substrate covered by 285 nm SiO_2 layer, serving as a back gate dielectric.
2. Spinning PMMA 950KA6 at 4000 r.p.m., leave the chip in a vacuum chamber pumped with a turbo for overnight.
3. Write designed electrode contact patterns with e-beam, beam dosage: $2300 \mu\text{C cm}^{-2}$, $1900 \mu\text{C cm}^{-2}$ and $1800 \mu\text{C cm}^{-2}$ for fine, coarse and bonding pads pattern, respectively.
4. Development: (MIBK:IPA = 1:3) for 1 min, IPA for 1 min, blow dry.
5. Ar plasma etch for 4 min (with Ar pressure 3 mTorr, 100 W) to etch away Al, AlO_x , InSb surface oxide and part of the InSb nanowires. To prevent the PMMA from burning due to a long plasma etch, one can perform short plasma etch (for example, 20 s) for 12 times with 40 s break between each etch to let the chip cool down.
6. Evaporate 10 nm Cr, followed by 100 nm of Au.
7. Lift-off in acetone.

Measurement and analysis. Devices X (Fig. 4.4), Z (Fig. 4.12d,e), and M (Fig. 4.12f-h) were measured in a dilution refrigerator with a base temperature of about 20 mK, while device Y (Fig. 4.12a-c) was measured in a He-3 fridge with a base temperature of about 300 mK.

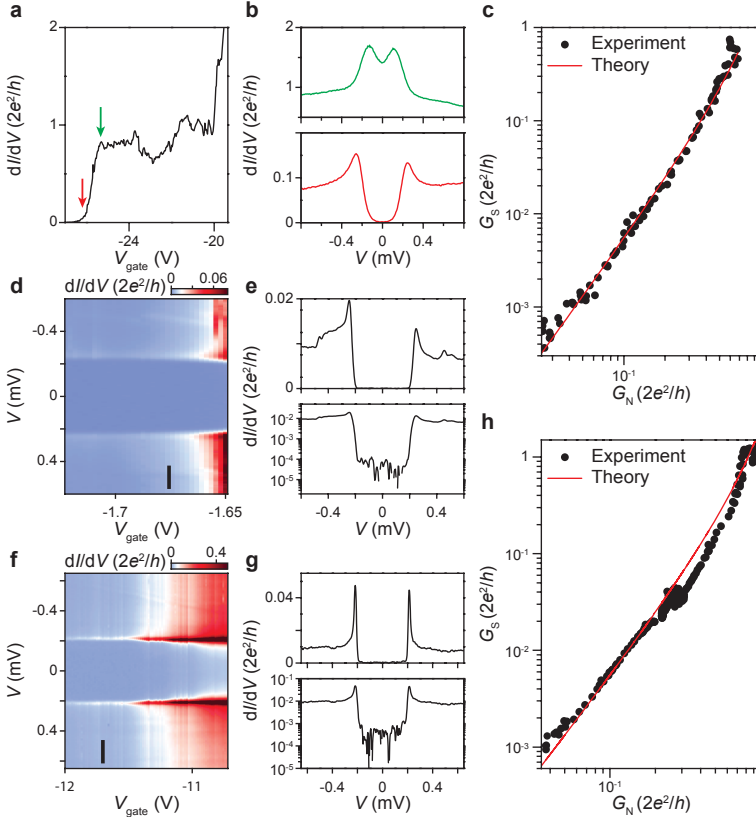


Figure 4.12: **Ballistic transport, Andreev enhancement and hard gap in additional Al-InSb devices.** **a**, Above-gap (normal carriers) conductance of device Y as a function of V_{gate} . A conductance plateau near the quantized value ($2e^2/h$) can clearly be seen, indicating ballistic transport. **b**, dI/dV versus bias voltage in the open and tunnelling regime, resolving strong Andreev enhancement (green) and a hard gap (red), respectively, with V_{gate} indicated by arrows in panel **a**. The coherence peaks are smeared out owing to thermal broadening (temperature of about 300 mK for this device). The Andreev enhancement is due to Andreev reflection: an incoming electron reflects as a hole at the N-S interface generating a Cooper pair. This process effectively doubles the transported charge from e to $2e$, enhancing the sub-gap conductance. Our enhancement factor reaches $1.7 \times 2e^2/h$, indicating the high Al-InSb interface transparency, with transmission larger than 0.96. The small dip in Andreev enhancement near zero bias is due to mode mixing induced by minimal residual disorder [11]. **c**, Sub-gap versus above-gap conductance of device Y (black dots), and a theoretical fit (red) based on the Beenakker formula, showing perfect agreement over three orders of magnitude conductance change. **d**, dI/dV of device Z as a function of V_{gate} . **e**, A line cut from panel **d** (black bar), plotted in linear (top) and logarithmic scale (bottom). The above-gap/sub-gap ratio is larger than 300. **f**, dI/dV of device M as a function of V_{gate} . **g**, A line cut from panel **f** (black bar), plotted on linear (left) and logarithmic scale (right). **h**, Sub-gap versus above-gap conductance of device M (black dots), and the Beenakker theoretical fit (red).

Sub-gap versus above-gap conductance fitting in Al-InSb devices. We assume there is a single transmitting channel in the shadow region with transmission T . The above-gap conductance is conductance of normal carriers: $G_N = (2e^2/h) \times T$, while sub-gap conductance, based on Beenakker's formula [28], is: $G_S = (2e^2/h) \times 2T^2/(2-T)^2$. Thus G_S can be plotted as a function of G_N as shown in Fig. 4.4c (red line). For the experimental data, at each gate voltage, we get the above-gap conductance by averaging the conductance at bias (V) much larger than the gap (Δ), while the sub-gap conductance is obtained by averaging a small bias window at zero bias.

Contact transparency estimation based on Andreev enhancement. In Fig. 4.12b, we obtain Andreev enhancement for sub-gap conductance reaching $1.7 \times 2e^2/h$. Based on Beenakker's formula, setting this value equal to G_S , we can extract a transparency $T \approx 0.96$.

REFERENCES

- [1] R. M. Lutchyn, J. D. Sau, and S. Das Sarma, *Majorana Fermions and a Topological Phase Transition in Semiconductor-Superconductor Heterostructures*, Phys. Rev. Lett. **105**, 077001 (2010).
- [2] Y. Oreg, G. Refael, and F. von Oppen, *Helical Liquids and Majorana Bound States in Quantum Wires*, Phys. Rev. Lett. **105**, 177002 (2010).
- [3] J. Alicea, Y. Oreg, G. Refael, F. von Oppen, and M. P. A. Fisher, *Non-Abelian statistics and topological quantum information processing in 1D wire networks*, Nature Physics **7**, 412 (2011).
- [4] T. Hyart, B. van Heck, I. C. Fulga, M. Burrello, A. R. Akhmerov, and C. W. J. Beenakker, *Flux-controlled quantum computation with Majorana fermions*, Phys. Rev. B **88**, 035121 (2013).
- [5] D. Aasen, M. Hell, R. V. Mishmash, A. Higginbotham, J. Danon, M. Leijnse, T. S. Jespersen, J. A. Folk, C. M. Marcus, K. Flensberg, and J. Alicea, *Milestones Toward Majorana-Based Quantum Computing*, Phys. Rev. X **6**, 031016 (2016).
- [6] S. Plugge, A. Rasmussen, R. Egger, and K. Flensberg, *Majorana box qubits*, New Journal of Physics **19**, 012001 (2017).
- [7] S. Vijay and L. Fu, *Teleportation-based quantum information processing with Majorana zero modes*, Phys. Rev. B **94**, 235446 (2016).
- [8] T. Karzig, C. Knapp, R. M. Lutchyn, P. Bonderson, M. B. Hastings, C. Nayak, J. Alicea, K. Flensberg, S. Plugge, Y. Oreg, C. M. Marcus, and M. H. Freedman, *Scalable designs for quasiparticle-poisoning-protected topological quantum computation with Majorana zero modes*, Phys. Rev. B **95**, 235305 (2017).
- [9] I. van Weperen, B. Tarasinski, D. Eeltink, V. S. Pribiag, S. R. Plissard, E. P. A. M. Bakkers, L. P. Kouwenhoven, and M. Wimmer, *Spin-orbit interaction in InSb nanowires*, Phys. Rev. B **91**, 201413 (2015).

- [10] J. Kammhuber, M. C. Cassidy, H. Zhang, Ö. Gül, F. Pei, M. W. A. de Moor, B. Nijholt, K. Watanabe, T. Taniguchi, D. Car, S. R. Plissard, E. P. A. M. Bakkers, and L. P. Kouwenhoven, *Conductance Quantization at Zero Magnetic Field in InSb Nanowires*, Nano Letters **16**, 3482 (2016).
- [11] Ö. Gül, H. Zhang, J. D. S. Bommer, M. W. A. de Moor, D. Car, S. R. Plissard, E. P. A. M. Bakkers, A. Geresdi, K. Watanabe, T. Taniguchi, and L. P. Kouwenhoven, *Ballistic Majorana nanowire devices*, Nature Nanotechnology **13**, 192 (2018).
- [12] E. M. T. Fadaly, H. Zhang, S. Conesa-Boj, D. Car, Ö. Gül, S. R. Plissard, R. L. M. Op het Veld, S. Kölling, L. P. Kouwenhoven, and E. P. A. M. Bakkers, *Observation of Conductance Quantization in InSb Nanowire Networks*, Nano Letters **17**, 6511 (2017).
- [13] V. Mourik, K. Zuo, S. M. Frolov, S. R. Plissard, E. P. A. M. Bakkers, and L. P. Kouwenhoven, *Signatures of Majorana Fermions in Hybrid Superconductor-Semiconductor Nanowire Devices*, Science **336**, 1003 (2012).
- [14] M. T. Deng, S. Vaitiekėnas, E. B. Hansen, J. Danon, M. Leijnse, K. Flensberg, J. Nygård, P. Krogstrup, and C. M. Marcus, *Majorana bound state in a coupled quantum-dot hybrid-nanowire system*, Science **354**, 1557 (2016).
- [15] S. M. Albrecht, A. P. Higginbotham, M. Madsen, F. Kuemmeth, T. S. Jespersen, J. Nygård, P. Krogstrup, and C. M. Marcus, *Exponential protection of zero modes in Majorana islands*, Nature **531**, 206 (2016).
- [16] J. Shabani, M. Kjaergaard, H. J. Suominen, Y. Kim, F. Nichele, K. Pakrouski, T. Stankevic, R. M. Lutchyn, P. Krogstrup, R. Feidenhans'l, S. Kraemer, C. Nayak, M. Troyer, C. M. Marcus, and C. J. Palmstrøm, *Two-dimensional epitaxial superconductor-semiconductor heterostructures: A platform for topological superconducting networks*, Phys. Rev. B **93**, 155402 (2016).
- [17] S. Conesa-Boj, D. Kriegner, X.-L. Han, S. Plissard, X. Wallart, J. Stangl, A. Fontcuberta i Morral, and P. Caroff, *Gold-Free Ternary III-V Antimonide Nanowire Arrays on Silicon: Twin-Free down to the First Bilayer*, Nano Letters **14**, 326 (2014).
- [18] S. R. Plissard, D. R. Slapak, M. A. Verheijen, M. Hocevar, G. W. G. Immink, I. van Weperen, S. Nadj-Perge, S. M. Frolov, L. P. Kouwenhoven, and E. P. A. M. Bakkers, *From InSb Nanowires to Nanocubes: Looking for the Sweet Spot*, Nano Letters **12**, 1794 (2012).
- [19] P. Caroff, M. E. Messing, B. M. Borg, K. A. Dick, K. Deppert, and L.-E. Wernersson, *InSb heterostructure nanowires: MOVPE growth under extreme lattice mismatch*, Nanotechnology **20**, 495606 (2009).
- [20] D. Dalacu, A. Kam, D. G. Austing, and P. J. Poole, *Droplet Dynamics in Controlled InAs Nanowire Interconnections*, Nano Letters **13**, 2676 (2013).
- [21] J.-H. Kang, Y. Cohen, Y. Ronen, M. Heiblum, R. Buczko, P. Kacman, R. Popovitz-Biro, and H. Shtrikman, *Crystal Structure and Transport in Merged InAs Nanowires MBE Grown on (001) InAs*, Nano Letters **13**, 5190 (2013).

- [22] T. Rieger, D. Rosenbach, D. Vakulov, S. Heedt, T. Schäpers, D. Grützmacher, and M. I. Lepsa, *Crystal Phase Transformation in Self-Assembled InAs Nanowire Junctions on Patterned Si Substrates*, *Nano Letters* **16**, 1933 (2016).
- [23] D. Car, J. Wang, M. A. Verheijen, E. P. A. M. Bakkers, and S. R. Plissard, *Rationally Designed Single-Crystalline Nanowire Networks*, *Advanced Materials* **26**, 4875 (2014).
- [24] P. Krogstrup, N. L. B. Ziino, W. Chang, S. M. Albrecht, M. H. Madsen, E. Johnson, J. Nygård, C. M. Marcus, and T. S. Jespersen, *Epitaxy of semiconductor-superconductor nanowires*, *Nature Materials* **14**, 400 (2015).
- [25] Ö. Gül, H. Zhang, F. K. de Vries, J. van Veen, K. Zuo, V. Mourik, S. Conesa-Boj, M. P. Nowak, D. J. van Woerkom, M. Quintero-Pérez, M. C. Cassidy, A. Geresdi, S. Koelling, D. Car, S. R. Plissard, E. P. A. M. Bakkers, and L. P. Kouwenhoven, *Hard Superconducting Gap in InSb Nanowires*, *Nano Letters* **17**, 2690 (2017).
- [26] Ö. Gül, D. J. van Woerkom, I. van Weperen, D. Car, S. Plissard, E. P. A. M. Bakkers, and L. P. Kouwenhoven, *Towards high mobility InSb nanowire devices*, *Nanotechnology* **26**, 215202 (2015).
- [27] A. E. Hansen, A. Kristensen, S. Pedersen, C. B. Sørensen, and P. E. Lindelof, *Mesoscopic decoherence in Aharonov-Bohm rings*, *Phys. Rev. B* **64**, 045327 (2001).
- [28] C. W. J. Beenakker, *Quantum transport in semiconductor-superconductor microjunctions*, *Phys. Rev. B* **46**, 12841 (1992).
- [29] S. Adachi and H. Kawaguchi, *Chemical Etching Characteristics of (001)InP*, *J. Electrochem. Soc.* **128**, 1342 (1981).
- [30] L. K. White, *Bilayer taper etching of field oxides and passivation layers*, *J. Electrochem. Soc.* **127**, 2687 (1980).
- [31] D. Dalacu, A. Kam, D. G. Austing, X. Wu, J. Lapointe, G. C. Aers, and P. J. Poole, *Selective-area vapour-liquid-solid growth of InP nanowires*, *Nanotechnology* **20**, 395602 (2009).
- [32] J. L. Webb, J. Knutsson, M. Hjort, S. Gorji Ghalestani, K. A. Dick, R. Timm, and A. Mikkelsen, *Electrical and Surface Properties of InAs/InSb Nanowires Cleaned by Atomic Hydrogen*, *Nano Letters* **15**, 4865 (2015).
- [33] F. E. Meijer, A. F. Morpurgo, T. M. Klapwijk, T. Koga, and J. Nitta, *Statistical significance of the fine structure in the frequency spectrum of Aharonov-Bohm conductance oscillations*, *Phys. Rev. B* **69**, 035308 (2004).

5

AHARONOV-BOHM EFFECT IN SAG NANOWIRE NETWORKS

In the previous chapter, we have shown that nanohashtags grown by the VLS method on patterned substrates show phase-coherent transport, one of the requirements for various braiding schemes. While this realization is innovative in its approach, it is not straightforward to scale to more complex networks. Therefore, an alternative approach based on selective area growth (SAG) [1] is developed. In this chapter, we will describe experiments performed on these networks to demonstrate their phase coherence properties.

5.1. GROWTH AND DEVICE FABRICATION

The SAG InSb nanowire networks are grown using MOVPE on an InP (111)B substrate. To create the mask for selective growth, the substrate is first covered by 20 nm of PECVD SiN_x . By locally removing the SiN_x , subsequent growth of InSb can be confined to these regions under the right growth conditions. This makes the platform very flexible, allowing the creation of any shapes that can be patterned in the SiN_x mask through electron-beam lithography followed by reactive ion etching [2]. Because the nanowires are epitaxially connected to the substrate, it is important that the lattice mismatch is not too large to avoid dislocations, as these will be detrimental to the transport properties [3]. In addition, the bandgaps of the substrate material and the nanowire material should align such that the nanowire can be galvanically isolated from the substrate at low temperatures. Finally, the nanowires and other structures should be patterned along high symmetry directions of the underlying substrate to get the best growth results. For (111)B substrates, this can be achieved by patterning the wires along $\langle 110 \rangle$ or $\langle 112 \rangle$ directions.

5

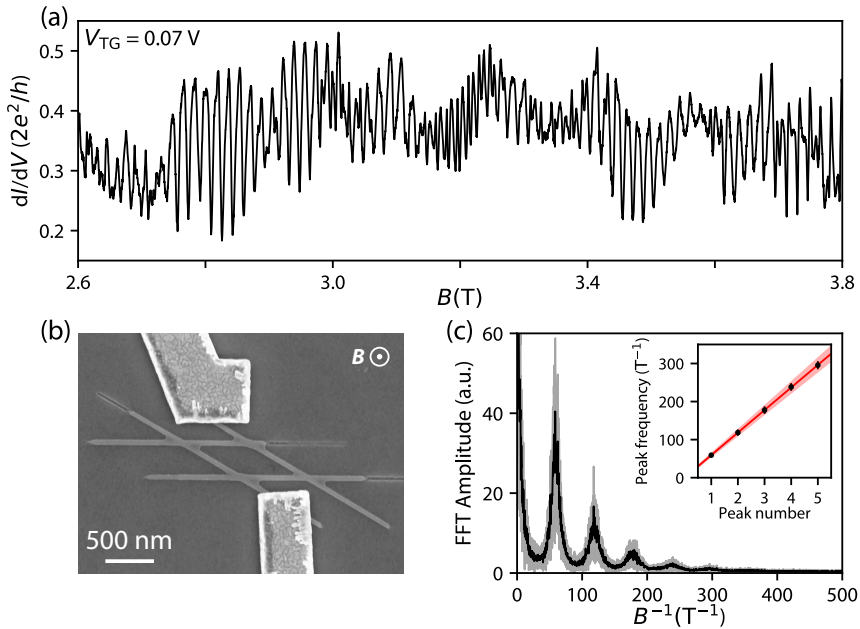


Figure 5.1: **Aharonov-Bohm effect in a SAG InSb nanowire network.** (a) Magnetoconductance in SAG device A, showing Aharonov-Bohm oscillations. (b) Scanning electron micrograph of SAG device A. The device is covered by sputtered SiN_x dielectric and a Cr/Au top gate (not shown). The magnetic field is applied perpendicular to the substrate. (c) Fourier transform of the magnetoconductance, averaged over 16 gate voltages. The black line shows the average value, while the gray shading indicates the spread as measured by the standard deviation. Up to 5 peaks are visible, indicating the Aharonov-Bohm frequency and its higher harmonics. Inset: peak frequency as a function of peak number (black circles), matching the values expected based on the loop size as measured by SEM (red line), with the red shaded region indicating the estimated uncertainty.

Using this method, nanowire hashtags similar to the ones used in chapter 4 have been

grown [4]. Devices are fabricated by first creating ohmic contacts by Ar plasma etching, followed by evaporation of 10/140 nm Cr/Au. Afterwards, the devices are covered by sputtered SiN_x dielectric, to galvanically isolate them from the Ti/Au top gate. Because the InP substrate is brittle, NbTiN/Ti/Au bond pads are fabricated to facilitate the wire-bonding process. The devices are then cooled down in a dilution refrigerator with a base temperature of 20 mK.

5.2. MAGNETOCONDUCTANCE OSCILLATIONS IN SAG NETWORKS

The phase coherence properties can be revealed by measuring the conductance through the hashtag as a function of an out-of-plane applied magnetic field. We measure the magnetoconductance in SAG device A between 1 and 5 T for 16 top gate voltages in the range of 0 to 0.15 V, with part of one such trace shown in Fig. 5.1(a). Clear oscillations are visible, with amplitudes reaching up to $0.2 \cdot 2e^2/h$. To find the periodicity of these oscillations, we apply a discrete Fourier transform using a Hann window, and average the resulting spectrum over the 16 gate voltages (Fig. 5.1(c), black line). Aside from a peak at low frequencies related to universal conductance fluctuations (UCF) [5, 6], we find 5 regularly spaced peaks in the spectrum. Based on the size of the hashtag as measured by SEM (see Fig. 5.1(b)), we estimate the magnetic field period for the h/e periodic Aharonov-Bohm oscillations [7, 8] to be $\Delta B = 17$ mT. Plotting the peak frequencies as a function of peak number (inset of Fig. 5.1(c)), we find that they nicely match the expected frequencies for Aharonov-Bohm oscillations and the related higher harmonics. The device A hashtag consists of two pairs of parallel wires intersecting at a 30° angle, which means one pair was grown along the $\langle 110 \rangle$ direction while the other was grown along the $\langle 112 \rangle$ direction.

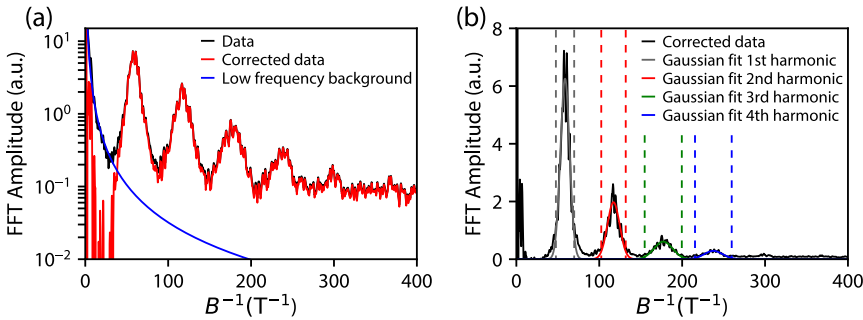


Figure 5.2: **Data processing to extract AB amplitudes.** (a) Fourier spectrum of the magnetoconductance in SAG device A (black line) at 20 mK. The low frequency background due to UCF is fitted with a power law (blue line), and subtracted from the data (corrected data shown by the red line). (b) Gaussian fits to the first four peaks (solid gray, red, green, and blue lines, respectively). The integration windows, determined by the width of the Gaussians, are indicated by the dashed lines.

5.3. DATA PROCESSING TO OBTAIN AB AMPLITUDES

We can fit the decay of the Aharonov-Bohm peak amplitude with increasing temperature to extract the phase coherence length in these SAG networks, similar to the method described in chapter 4. For each temperature, we measure the magnetoconductance between -1.4 and -0.4 T, at 6 top gate voltages between 0.130 and 0.135 V. The Fourier spectra are averaged, resulting in a spectrum such as the one shown by the black line in Fig. 5.2(a). To remove the influence of the UCF background, we fit the low frequency ($B^{-1} < 40$) part of the spectrum with a power law (blue line), and subtract it from the data (corrected spectrum shown in red). This procedure is found to give more robust results for the peak amplitudes than the smooth background subtraction calculated by moving average used in chapter 4, especially when there is substantial overlap between the frequency ranges of the UCF and Aharonov-Bohm peaks.

We extract the amplitudes of the different harmonics by numerically integrating the data over the frequency range associated with each peak. By integrating the data instead of taking the value at a specific frequency, we avoid fluctuations in the extracted amplitudes by small shifts in frequency between different measurements [8]. The integration range is found by taking the data measured at 20 mK and fitting a Gaussian profile to each peak. The integration ranges are set to $[f_n - 2\sigma_n, f_n + 2\sigma_n]$, with f_n the mean of the Gaussian fit to the n th harmonic, and σ_n its standard deviation. In Fig. 5.2(b), we plot the Gaussian fits (colored solid lines) as well as the integration windows (colored dashed lines). These windows correspond roughly to the ones expected based on the finite thickness of the wires making up the hashtag, making it plausible to assign all frequencies within the n th integration range to the n th harmonic of the Aharonov-Bohm effect.

Once the background has been removed and integration windows have been defined, we extract the amplitudes of the different harmonics for each gate voltage and temperature by numerical integration. The amplitude associated with the n th harmonic at temperature T , $G_{AB,n}(T)$, is calculated from the gate voltage averaged spectrum, while the error is calculated by taking standard deviation of the amplitudes extracted from the individual traces. To check that our procedure is internally consistent, we also calculate the average of the individually extracted amplitudes, finding almost no difference with the amplitude extracted from the averaged spectrum.

5.4. TEMPERATURE DEPENDENCE OF AB OSCILLATIONS

The values of $G_{AB,n}(T)$ obtained using the procedure described in the previous section are plotted in Fig. 5.3. The amplitude of the oscillations decreases with increasing temperature, as expected. Additionally, the decay is more rapid for higher n . Defining the phase coherence length as $L_\phi = \frac{L}{a} T^{-k}$ (see also section 2.5), we can describe the temperature dependence by

$$G_{AB,n}(T) = Ct^2(1-t)^{n-1}\exp((-na+b)T^k). \quad (5.1)$$

The amplitude is exponentially suppressed with increasing temperature. The exponent

k is determined by the transport regime in the ring: in the ballistic case, $k = 1$ [9], while $k = 1/2$ if the ring is diffusive [10]. The factor a (b) describes dephasing mechanisms which are dependent on (independent of) the amount of times an electron goes around the loop. The coefficient a allows us to estimate the phase coherence length [11]. The value of the coefficient b gives us information about the importance of additional dephasing mechanisms, such as localization traps [12], energy averaging effects [11], and other sources of dephasing coming from the set-up [9]. Note that these contributions to dephasing might have a very different functional dependence on the temperature than the one assumed here. Therefore, we mainly use a large value of b as a sign that we are missing something in our description of the temperature dependence of Aharonov-Bohm conductance oscillations in our device.

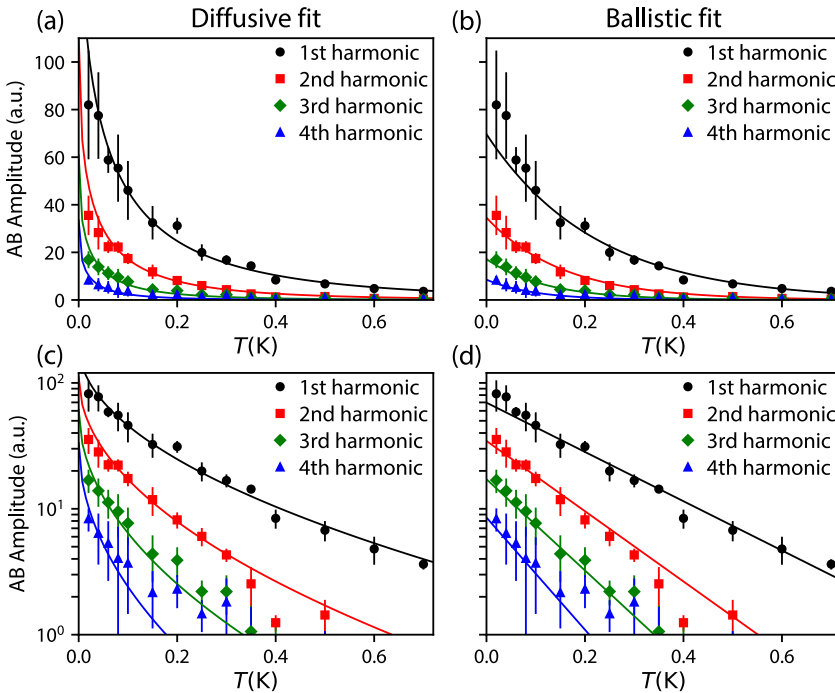


Figure 5.3: **Temperature dependence of the AB amplitude in device A.** Extracted amplitudes for the first four harmonics (black circles, red squares, green diamonds, and blue triangles, respectively) as a function of temperature. Solid lines indicate fits to equation 5.1. (a) Linear scale, $k = 1/2$ (diffusive). (b) Linear scale, $k = 1$ (ballistic). To more clearly demonstrate the exponential decay of the oscillations with temperature, the same data is plotted in logarithmic scale in (c) (diffusive), and (d) (ballistic).

The relative amplitudes of the different harmonics also depend on the transmission from the loop to the leads, t . Here, we assume this transmission is the same for both leads, giving a factor t^2 (to pass from the first lead to the loop and then from the loop to the second lead), as well as a factor $(1 - t)^{n-1}$ to account for the reflections necessary to obtain higher order oscillations.

The prefactor C depends on details of the data acquisition and numerical procedures (the number of collected data points, the magnetic field range, and the integration window). This prefactor can be calculated by assuming a perfect oscillation amplitude of $2e^2/h$ at $T = 0$, and performing the same data processing as is done to the real data. The prefactor obtained this way is then fixed during the fitting process for the diffusive fit (Fig. 5.3(a,c)). In the ballistic case (Fig. 5.3(b,d)), it was not possible to obtain a good fit with a fixed prefactor, so it was left as a free fitting parameter instead. To fit the data, we use a least squares optimization with the data points weighted by their relative error.

Fit to equation 5.1		Ballistic fit ($k = 1$)		Diffusive fit ($k = 1/2$)	
Parameter	Unit	Value	Standard deviation	Value	Standard deviation
t	-	0.50	0.04	0.45	0.03
C	a.u.	275	36	993.28	-
a	K^{-1}	1.92	0.33	1.21	0.13
b	K^{-1}	-2.59	0.48	-3.48	0.31
R_1^2	-	0.91	-	0.94	-
R_2^2	-	0.98	-	0.88	-
R_3^2	-	0.97	-	0.91	-
R_4^2	-	0.89	-	0.82	-
L_ϕ (1 K)	μm	0.73	0.12	1.16	0.12
L_ϕ (20 mK)	μm	36	6	8.2	0.9

Table 5.1: **Parameters corresponding to the fits shown in Fig. 5.3.** The parameter R_n^2 refers to the coefficient of determination of the fit of the n th harmonic. Phase coherence lengths calculated based on $L_\phi = \frac{L}{a} T^{-k}$, with $L = 1.4 \mu\text{m}$.

The parameters obtained from the fits shown in Fig. 5.3 are summarized in Table 5.1. Both models predict an average transmission from the leads to the loop of around 0.5, which is consistent with the average conductance of about $0.3 - 0.4 \cdot 2e^2/h$ shown in

Fig. 5.1(a). The ballistic fit describes the higher order data better, while the diffusive fit is better for the first harmonic. This is due to the fact that the diffusive model better captures the behavior at higher temperatures, where only the first harmonic gives a measurable signal. The ballistic model gives a better fit to the low temperature data. One caveat is the fact that below 100 mK, it is unknown how close the electron temperature on the chip is to the temperature measured on the mixing chamber plate in the particular set-up used during these experiments. As was shown in section 3.5, the electron temperature could deviate from the mixing chamber temperature in this regime. The diffusive model fits well with the assumption of a $2e^2/h$ oscillation amplitude at $T = 0$ K, without the need for an extra fitting parameter. We expect diffusive behavior due to dislocations at the nanowire-substrate interface. For these reasons, we consider the diffusive scenario the most likely. Both models give a large value for the parameter b , suggesting a strong contribution from dephasing mechanisms that do not dependent on the path travelled along the loop. We speculate that the main contribution to this type of dephasing comes from the additional sections of InSb nanowire extending from the corners of the loop. These “dephasing stubs” have been extensively studied in the context quantum dots, and have been shown to significantly affect the phase coherence properties of mesoscopic systems [13, 14].

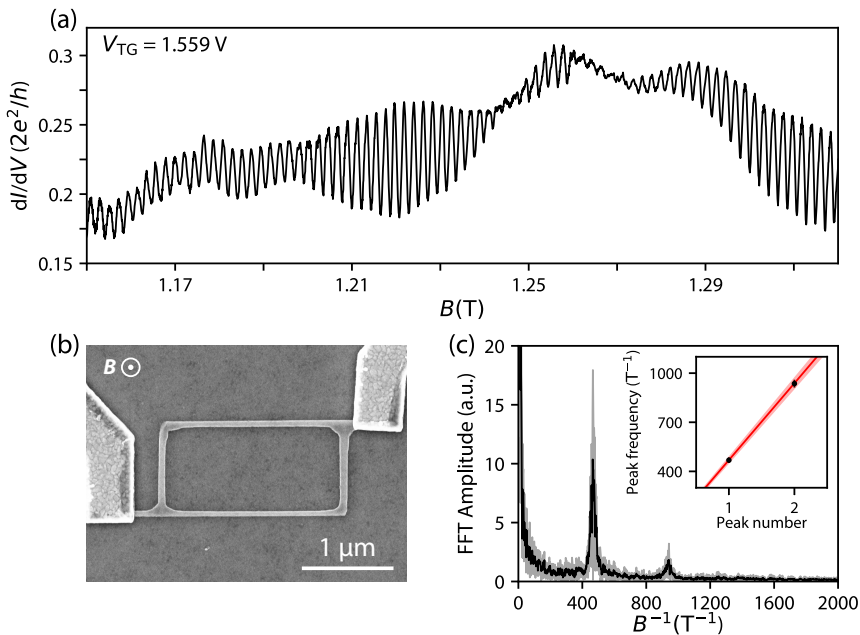


Figure 5.4: **Aharonov-Bohm network without dephasing stubs.** (a) Magnetoconductance in SAG device B, showing Aharonov-Bohm oscillations. (b) Scanning electron micrograph of SAG device B. There are no additional stubs protruding from the corners of the hashtag, unlike in device A. (c) Fourier transform of the magnetoconductance, averaged over 6 gate voltages. The black line shows the average value, while the gray region indicates the spread as measured by the standard deviation. The frequencies of the two visible peaks are close to the expected values based on the loop size as measured in SEM (inset).

5.5. AHARONOV-BOHM LOOP WITHOUT DEPHASING STUBS

To test our hypothesis that the additional dephasing is due to the dephasing stubs protruding from the corners of the Aharonov-Bohm loop, we change the pattern used to define the SAG nanowire networks to make loops without dephasing stubs. A SEM image of device B is shown in Fig. 5.4(b)). Because the angle between the two parallel wire pairs constituting the loop is 90° , we can infer that this hashtag consists of both $\langle 110 \rangle$ and $\langle 112 \rangle$ growth direction, just like device A. We measure the magnetoconductance between 1.0 and 1.5 T, which is partially plotted in Fig. 5.4(a). In Fig. 5.4(c) we plot the Fourier transform of the magnetoconductance averaged over 6 gate voltages. The first peak in the spectrum corresponds to an oscillation period of 2.1 mT, which is close to the period expected for h/e periodic oscillations in a loop this size. Only two harmonics are observed in this device, which is likely related to the fact that the loop circumference is significantly larger than in device A.

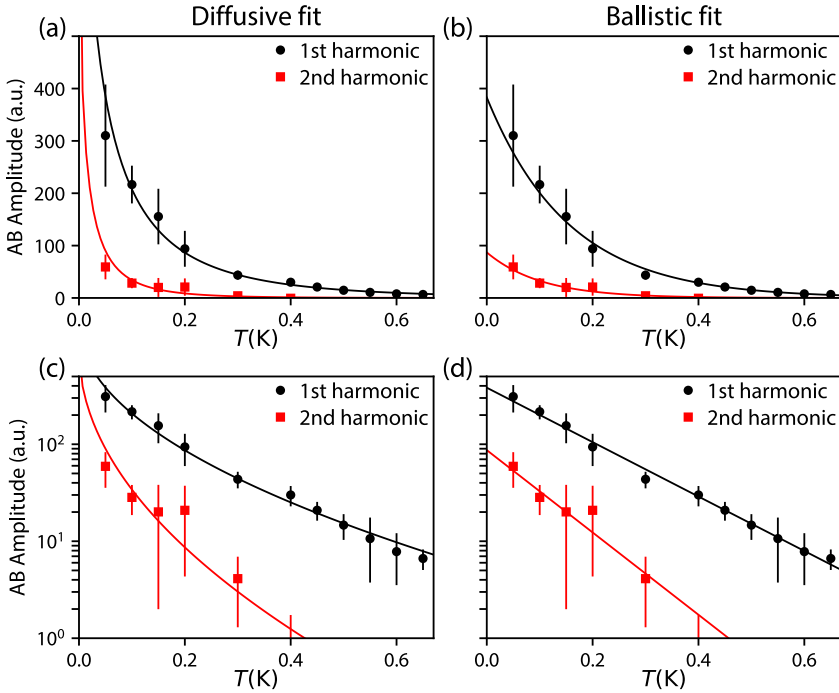


Figure 5.5: **Temperature dependence of the AB amplitude in device B.** Extracted amplitudes for the first two harmonics (black circles and red squares, respectively) as a function of temperature. Solid lines indicate fits to equation 5.1. (a) Linear scale, $k = 1/2$ (diffusive). (b) Linear scale, $k = 1$ (ballistic). To more clearly demonstrate the exponential decay of the oscillations with temperature, the same data is plotted in logarithmic scale in (c) (diffusive), and (d) (ballistic).

In principle two harmonics are sufficient to perform the same analysis as was done on device A. However, as two is the bare minimum required to separate the dephasing contributions captured by coefficients a and b (as it essentially constitutes a linear fit of two

points), we should be careful when drawing conclusions. The results of the data analysis are shown in Fig. 5.5. Both ballistic and diffusive models seem to fit the first harmonic reasonably well. The amplitude of the second harmonic drops below noise level for temperatures above 250 mK, making it harder to draw conclusions based on those fits.

We summarize the fitting results in Table 5.2. The values obtained for the coefficient b are similar in magnitude to those obtained in device A, suggesting no improvement by removing the dephasing stubs. As noted before, however, distinguishing mechanisms captured by a and b using only two harmonics is challenging, as is also apparent from the significant standard deviations of these parameters, especially in the ballistic case. We obtain similar values for the phase coherence length as those reported in device A, although the diffusive estimate is a bit lower. It's worth noting that the phase coherence length determining the oscillation amplitude of the Aharonov-Bohm effect is not universal, and depends on the size of the loop [10]. A better comparison would therefore be made by taking loops of the same size, with and without dephasing stubs protruding from the corners.

Fit to equation 5.1		Ballistic fit ($k = 1$)		Diffusive fit ($k = 1/2$)	
Parameter	Unit	Value	Standard deviation	Value	Standard deviation
t	-	0.77	0.05	0.45	0.03
C	a.u.	641	81	8349.6	-
a	K^{-1}	3.3	1.5	3.80	0.42
b	K^{-1}	-3.1	1.6	-2.87	0.52
R_1^2	-	0.98	-	0.94	-
R_2^2	-	0.94	-	0.49	-
L_ϕ (1 K)	μm	0.89	0.41	0.78	0.09
L_ϕ (20 mK)	μm	45	20	5.5	0.6

Table 5.2: **Parameters corresponding to the fits shown in Fig. 5.5.** The parameter R_n^2 refers to the coefficient of determination of the fit of the n th harmonic. Phase coherence lengths calculated based on $L_\phi = \frac{L}{a} T^{-k}$, with $L = 2.96 \mu\text{m}$.

5.6. CONCLUSION

We have investigated the phase coherence in selective area grown InSb nanowire networks by studying the temperature dependence of Aharonov-Bohm oscillations. We find up to 5 harmonics of the Aharonov-Bohm effect in these networks, demonstrating good phase coherence properties. The temperature dependence of the Aharonov-Bohm oscillations allows us to extract a phase coherence length of L_ϕ (20 mK) = $8.2 \pm 0.9 \mu\text{m}$, assuming diffusive transport. We also find an additional contribution to dephasing which does not depend on the length of the path travelled around the loop, which we speculate is due to additional dephasing stubs protruding from the corners of the loop. However, additional experiments on loops without these dephasing stubs show a similar contribution to dephasing, suggesting it is caused by other effects. To draw definitive conclusions, loops of the same size without and without dephasing stubs should be studied. Because the transmission from the leads to the loop plays an important role in determining the visibility of higher harmonics, additional electrostatic gates should be patterned such that this transmission can be tuned independently from the transport in the loop. Furthermore, loops consisting of wires grown along only the $\langle 110 \rangle$ or $\langle 112 \rangle$ directions should be compared to the heterogeneous loops studied here, to see if reflections at the wire junctions could be responsible for additional localization and dephasing.

Because the odd harmonics are much more susceptible to energy averaging effects due to a small asymmetry between the two paths, many experiments have used multiple loops in series to promote the visibility of Aharonov-Casher [15, 16] oscillations over the regular Aharonov-Bohm oscillations. While it is highly impractical to grow such structures using the method described in chapter 4, the SAG method can easily be implemented due to the fact that the growth mask can be lithographically defined. This opens new avenues to studying the effects of spin-orbit coupling and quasi-1D confinement on the magnetoconductance of semiconductor nanowire networks.

CONTRIBUTIONS TO THE PROJECT

The selective area grown InSb networks used in this chapter were grown by R. L. M. Ophet Veld under the supervision of E. P. A. M. Bakkers at the Eindhoven University of Technology. The devices were fabricated and measured at Delft University of Technology. D. Xu, V. Schaller, K. Vermeulen, Q. Wang, and B. Hesselmann fabricated the devices. The measurements were performed **M. W. A. de Moor**, D. Xu, K. Vermeulen, and B. Hesselmann. The analysis presented in this chapter was performed by **M. W. A. de Moor**. The project was supervised by H. Zhang and L. P. Kouwenhoven.

REFERENCES

- [1] Y. Ujiie and T. Nishinaga, *Epitaxial Lateral Overgrowth of GaAs on a Si Substrate*, Japanese Journal of Applied Physics **28**, L337 (1989).
- [2] P. Aseev, A. Fursina, F. Boekhout, F. Krizek, J. E. Sestoft, F. Borsoi, S. Heedt, G. Wang, L. Binci, S. Martí-Sánchez, T. Swoboda, R. Koops, E. Uccelli, J. Arbiol, P. Krogstrup,

- L. P. Kouwenhoven, and P. Caroff, *Selectivity Map for Molecular Beam Epitaxy of Advanced III-V Quantum Nanowire Networks*, Nano Letters **19**, 218 (2018).
- [3] F. Krizek, J. E. Sestoft, P. Aseev, S. Marti-Sanchez, S. Vaitiekėnas, L. Casparis, S. A. Khan, Y. Liu, T. Stankevič, A. M. Whitar, A. Fursina, F. Boekhout, R. Koops, E. Uccelli, L. P. Kouwenhoven, C. M. Marcus, J. Arbiol, and P. Krogstrup, *Field effect enhancement in buffered quantum nanowire networks*, Phys. Rev. Materials **2**, 093401 (2018).
- [4] R. L. M. Op het Veld et al., To be published.
- [5] P. A. Lee and A. D. Stone, *Universal Conductance Fluctuations in Metals*, Phys. Rev. Lett. **55**, 1622 (1985).
- [6] C. W. J. Beenakker, *Random-matrix theory of quantum transport*, Rev. Mod. Phys. **69**, 731 (1997).
- [7] Y. Aharonov and D. Bohm, *Significance of Electromagnetic Potentials in the Quantum Theory*, Phys. Rev. **115**, 485 (1959).
- [8] R. A. Webb, S. Washburn, C. P. Umbach, and R. B. Laibowitz, *Observation of $\frac{h}{e}$ Aharonov-Bohm Oscillations in Normal-Metal Rings*, Phys. Rev. Lett. **54**, 2696 (1985).
- [9] G. Seelig and M. Büttiker, *Charge-fluctuation-induced dephasing in a gated mesoscopic interferometer*, Phys. Rev. B **64**, 245313 (2001).
- [10] T. Ludwig and A. D. Mirlin, *Interaction-induced dephasing of Aharonov-Bohm oscillations*, Phys. Rev. B **69**, 193306 (2004).
- [11] A. E. Hansen, A. Kristensen, S. Pedersen, C. B. Sørensen, and P. E. Lindelof, *Mesoscopic decoherence in Aharonov-Bohm rings*, Phys. Rev. B **64**, 045327 (2001).
- [12] M. Cassé, Z. D. Kvon, G. M. Gusev, E. B. Olshanetskii, L. V. Litvin, A. V. Plotnikov, D. K. Maude, and J. C. Portal, *Temperature dependence of the Aharonov-Bohm oscillations and the energy spectrum in a single-mode ballistic ring*, Phys. Rev. B **62**, 2624 (2000).
- [13] M. L. Polianski and P. W. Brouwer, *Scattering matrix ensemble for time-dependent transport through a chaotic quantum dot*, Journal of Physics A: Mathematical and General **36**, 3215 (2003).
- [14] C. W. J. Beenakker and B. Michaelis, *Stub model for dephasing in a quantum dot*, Journal of Physics A: Mathematical and General **38**, 10639 (2005).
- [15] Y. Aharonov and A. Casher, *Topological Quantum Effects for Neutral Particles*, Phys. Rev. Lett. **53**, 319 (1984).
- [16] F. Qu, F. Yang, J. Chen, J. Shen, Y. Ding, J. Lu, Y. Song, H. Yang, G. Liu, J. Fan, Y. Li, Z. Ji, C. Yang, and L. Lu, *Aharonov-Casher effect in bi_2se_3 Square-Ring Interferometers*, Phys. Rev. Lett. **107**, 016802 (2011).

6

ELECTRIC FIELD TUNABLE SUPERCONDUCTOR- SEMICONDUCTOR COUPLING IN MAJORANA NANOWIRES

M. W. A. de Moor^{*}, J. D. S. Bommer^{*}, D. Xu^{*}, G. W. Winkler, A. E. Antipov, A. Bargerbos, G. Wang, N. van Loo, R. L. M. Op het Veld, S. Gazibegovic, D. Car, J. A. Logan, M. Pendharkar, J. S. Lee, E. P. A. M. Bakkers, C. J. Palmstrøm, R. M. Lutchyn, L. P. Kouwenhoven, and H. Zhang.

We study the effect of external electric fields on superconductor-semiconductor coupling by measuring the electron transport in InSb semiconductor nanowires coupled to an epitaxially grown Al superconductor. We find that the gate voltage induced electric fields can greatly modify the coupling strength, which has consequences for the proximity induced superconducting gap, effective g -factor, and spin-orbit coupling, which all play a key role in understanding Majorana physics. We further show that level repulsion due to spin-orbit coupling in a finite size system can lead to seemingly stable zero bias conductance peaks, which mimic the behavior of Majorana zero modes. Our results improve the understanding of realistic Majorana nanowire systems.

This chapter has been published in *New Journal of Physics* **20**, 103049 (2018).

^{*}These authors contributed equally to this work.

6.1. INTRODUCTION

The hybrid superconductor-semiconductor nanowire system is the prime candidate to realize, control, and manipulate Majorana zero modes (MZMs) for topological quantum information processing [1–3]. Majorana zero modes can be engineered in these hybrid nanowire systems by combining the one dimensional nature of the nanowire, strong spin-orbit coupling, superconductivity, and appropriate external electric (to control the chemical potential) and magnetic fields (to control the Zeeman energy) to drive the system into a topologically non-trivial phase [4, 5]. To induce superconductivity in the semiconductor nanowire, it needs to be coupled to a superconductor. The electronic coupling between the two systems turns the nanowire superconducting [6], known as the proximity effect. Following this scheme, the first signatures of MZMs were observed in these hybrid systems, characterized by a zero bias peak (ZBP) in the tunneling conductance spectrum [7–10]. Since then, significant progress has been made in Majorana experiments [11–14], enabled by more uniform coupling between the superconductor and semiconductor nanowire. This has been achieved by improved interface engineering: through careful ex situ processing [15–17], by depositing the superconductor on the nanowires in situ [18, 19], and a combination of in situ and ex situ techniques [20], finally leading to the quantization of the Majorana conductance [13].

6

However, the treatment of the superconductor-semiconductor coupling in the interpretation of experiments is often oversimplified. This coupling has recently been predicted to depend substantially on the confinement induced by external electric fields [21]. In this work, we experimentally show that the superconductor-semiconductor coupling, as parameterized by the induced superconducting gap, is affected by gate induced electric fields. Due to the change in coupling, the renormalization of material parameters is altered, as evidenced by a change in the effective g -factor of the hybrid system. Furthermore, the electric field is shown to affect the spin-orbit interaction, revealed by a change in the level repulsion between Andreev states. Our experimental findings are corroborated by numerical simulations.

6.2. EXPERIMENTAL SET-UP

We have performed tunneling spectroscopy experiments on four InSb-Al hybrid nanowire devices, labeled A-D, all showing consistent behaviour. The nanowire growth procedure is described in reference [20]. A scanning electron micrograph (SEM) of device A is shown in Fig. 6.1(a). Figure 6.1(b) shows a schematic of this device and the measurement set-up. For clarity, the wrap-around tunnel gate, tunnel gate dielectric and contacts have been removed on one side. A normal-superconductor (NS) junction is formed between the part of the nanowire covered by a thin shell of aluminum (10 nm thick, indicated in green, S), and the Cr/Au contact (yellow, N). The transmission of the junction is controlled by applying a voltage V_{Tunnel} to the tunnel gate (red), galvanically isolated from the nanowire by 35 nm of sputtered SiN_x dielectric. The electric field is induced by a global back gate voltage V_{BG} , except in the case of device B, where this role is played by the side gate voltage V_{SG} . Further details on device fabrication and design are included

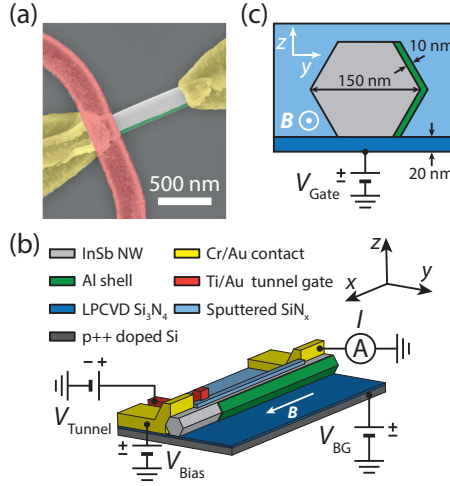


Figure 6.1: **Device schematics.** (a) SEM of device A, with InSb nanowire in gray, superconducting aluminum shell in green, Cr/Au contacts in yellow, and local tunnel gate in red. Scale bar is 500 nm. (b) Schematic of experimental set-up. The substrate acts as a global back gate. The magnetic field is applied along the nanowire direction (x -axis). (c) Geometry used in the numerical simulations. A uniform potential V_{Gate} is applied as a boundary condition at the interface between substrate and dielectric. The superconductor (green) is kept at a fixed potential, which is set by the work function difference at the superconductor-semiconductor interface.

in section 6.9.1. To obtain information about the density of states in the proximitized nanowire, we measure the differential conductance dI/dV_{Bias} as a function of applied bias voltage V_{Bias} . In the following, we will label this quantity as dI/dV for brevity. A magnetic field is applied along the nanowire direction (x -axis in Figs. 6.1(b), 6.1(c)). All measurements are performed in a dilution refrigerator with a base temperature of 20 mK.

6.3. THEORETICAL MODEL

The device geometry used in the simulation is shown in Fig. 6.1(c). We consider a nanowire oriented along the x -direction, with a hexagonal cross-section in the yz -plane. The hybrid superconductor-nanowire system is described by the Bogoliubov-de Gennes Hamiltonian

$$\begin{aligned}
 H = & \left[\frac{\hbar^2 \mathbf{k}^2}{2m^*} - \mu - e\phi \right] \tau_z + \alpha_y (k_z \sigma_x - k_x \sigma_z) \tau_z \\
 & + \alpha_z (k_x \sigma_y - k_y \sigma_x) \tau_z + \frac{1}{2} g \mu_B B \sigma_x + \Delta \tau_x.
 \end{aligned} \tag{6.1}$$

The first term contains contributions from the kinetic energy and the chemical potential, as well as the electrostatic potential ϕ . The second and third terms describe the Rashba spin-orbit coupling, with the coupling strength α_y (α_z) depending on the y -component (z -component) of the electric field. The Zeeman energy contribution, proportional to g , the Landé g -factor, is given by the fourth term. Finally, the superconducting pairing Δ is included as the fifth term. All material parameters are position dependent, taking different values in the InSb nanowire and the Al superconductor. For additional details

about the simulation, see sections 6.9.2 and 6.9.3.

If the coupling between the superconductor and semiconductor is small (compared to the bulk gap of the superconductor Δ , known as weak coupling), superconductivity can be treated as a constant pairing potential term in the nanowire Hamiltonian, with the induced superconducting gap being proportional to the coupling strength [22]. However, if the coupling becomes strong, the wave functions of the two materials hybridize, and the superconductor and semiconductor have to be considered on equal footing [23]. We achieve this by solving the Schrödinger equation in both materials simultaneously. When desired, the orbital effect of the magnetic field is added via Peierls substitution [24]. The simulations are performed using the kwant package [25].

The electrostatic potential in the nanowire cross-section is calculated from the Poisson equation, assuming an infinitely long wire. We use a fixed potential V_{Gate} as a boundary condition at the dielectric-substrate interface. The superconductor enters as the second boundary condition, with a fixed potential to account for the work function difference between superconductor and semiconductor [26]. We approximate the mobile charges in the nanowire by a 3D electron gas (Thomas-Fermi approximation). It has been demonstrated that the potentials calculated using this approximation give good agreement with results obtained by self-consistent Schrödinger-Poisson simulations [27]. The calculated potential for a given V_{Gate} is then inserted into the Hamiltonian (6.1).

By solving the Schrödinger equation for a given electrostatic environment, we can see how the gate potential alters the electronic states in the nanowire, how they are coupled to the superconductor, and how this coupling affects parameters such as the induced gap, effective g -factor, and spin-orbit energy.

6.4. GATE VOLTAGE DEPENDENCE OF THE INDUCED SUPERCONDUCTING GAP

When the transmission of the NS-junction is sufficiently low (i.e., in the tunneling regime), the differential conductance dI/dV is a direct measure of the density of states (DOS) in the proximitized nanowire [28]. In Fig. 6.2(a), we plot dI/dV measured in device A as a function of applied bias voltage V_{Bias} and tunnel gate voltage V_{Tunnel} , for $V_{\text{BG}} = -0.6$ V. In the low transmission regime, we resolve the superconducting gap Δ around 250 μeV , indicated by the position of the coherence peaks. The ratio of sub-gap to above-gap conductance (proportional to the normal state transmission of the junction, T) follows the behavior expected from BTK theory [29, 30], indicating the sub-gap conductance is dominated by Andreev reflection processes (proportional to T^2). This is generally referred to as a hard gap. However, for more positive back gate voltages, the sub-gap conductance is larger and shows more resonances, as is illustrated in Fig. 6.2(b) for $V_{\text{BG}} = -0.3$ V. Figure 6.2(c) shows line traces taken at a similar transmission (above-gap conductance) for both cases. The sub-gap conductance for $V_{\text{BG}} = -0.3$ V (black line) exceeds that of the hard gap case (red line) by an order of magnitude. This is indicative of a surplus of quasi-particle states inside the gap, referred to as a soft gap.

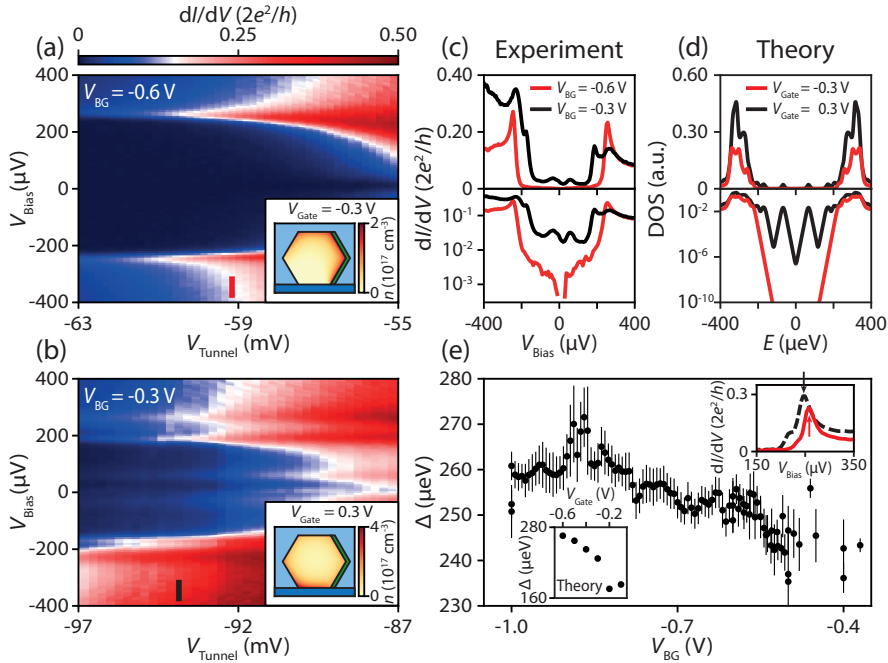


Figure 6.2: **Gate dependence of the induced superconducting gap.** (a, b) Differential conductance dI/dV measured in device A as a function of V_{Bias} and V_{Tunnel} for $V_{\text{BG}} = -0.6$ V (a) and $V_{\text{BG}} = -0.3$ V (b). Insets show the calculated electron density in the wire for $V_{\text{Gate}} = -0.3$ V and $V_{\text{Gate}} = 0.3$ V, respectively. (c) Line-cuts from (a) and (b), indicated by the colored bars, in linear (top) and logarithmic (bottom) scale. (d) Calculated DOS for the density profiles shown in the insets of (a) and (b), shown in red and black, respectively. (e) Induced gap magnitude Δ as a function of V_{BG} , showing a decrease for more positive gate voltages. Top right inset: line traces showing the coherence peak position (indicated by the arrow) for $V_{\text{BG}} = -0.6$ V (solid red line) and $V_{\text{BG}} = -0.4$ V (dashed black line). Bottom left inset: induced gap from the calculated DOS as a function of V_{Gate} , consistent with the experimental observation.

The gate voltage induced transition from soft to hard gap is generically observed in multiple devices. To understand this phenomenology, we calculate the electron density in the nanowire cross-section for different values of V_{Gate} . Because the charge neutrality point in our devices is unknown, there is a difference between the gate voltages used in the experiment and the values of V_{Gate} used in the simulation. By comparing the transition point between hard and soft gaps in the experiment and the simulation, we estimate that the experimental gate voltage range -0.6 V $< V_{\text{BG}} < -0.4$ V roughly corresponds to the simulated gate voltage range -0.4 V $< V_{\text{Gate}} < -0.2$ V.

For more negative V_{Gate} , the electric field from the gate pushes the electrons towards interface with the superconductor (inset of Fig. 6.2(a)). We solve the Schrödinger equation for the calculated electrostatic potential and find that this stronger confinement near the interface leads to a stronger coupling. This results in a hard gap, as illustrated by

the calculated energy spectrum (Fig. 6.2(d), red line). However, for more positive voltages, the electrons are attracted to the back gate, creating a high density pocket far away from the superconductor (inset of Fig. 6.2(b)). These states are weakly coupled to the superconductor, as demonstrated by a soft gap structure (Fig. 6.2(d), black line, see also section 6.9.4). We can therefore conclude that the electron tunneling between the semiconductor and the superconductor is strongly affected by the gate potential.

The change in superconductor-semiconductor coupling does not just affect the hardness, but also the size of the gap. For each back gate voltage, we fit the BCS-Dynes expression [31] for the DOS in order to extract the position of the coherence peaks, giving the gap size Δ . The results are shown in Fig. 6.2(e). Further details on the fitting procedure are given in section 6.9.5. As V_{BG} becomes more positive, the superconductor-semiconductor coupling becomes weaker, reducing the size of the gap. From $V_{BG} > -0.4$ V onward it becomes difficult to accurately determine the gap, as it tends to become too soft and the coherence peaks are not always clearly distinguishable. The top right inset shows the shift of the coherence peak (indicated by the arrows) to lower bias voltage as V_{BG} is increased. The lower left inset shows the extracted coherence peak position from the numerical simulations, showing the same trend with gate voltage. However, the theoretically calculated induced gap is generally smaller than the experimentally observed gap. It has been demonstrated that disorder at the outer surface of the superconductor (e.g., due to oxidation) leads to an increase in the induced gap due to breaking of momentum conservation, which increases the superconductor-semiconductor hybridization [21]. Additionally, the gap decreases more slowly when the gate voltage is more positive. As this kind of disorder is present in our devices, but was not included in the simulation, this is a likely cause for the discrepancy between theory and experiment.

6

6.5. EFFECTIVE g -FACTOR

As the electric field induced by the back gate clearly has an important effect on the hybridization between the nanowire and the superconductor, we now look at the effect this has on the Zeeman term in the Hamiltonian. This term affects the energy dispersion of spinful states in a magnetic field. We study the dispersion of the states in the nanowire by measuring dI/dV in device A as a function of applied bias voltage and magnetic field, as shown in Fig. 6.3(a) and Fig. 6.3(b). We define the effective g -factor as $g_{\text{eff}} = \frac{2}{\mu_B} \left| \frac{\Delta E}{\Delta B} \right|$, with $\left| \frac{\Delta E}{\Delta B} \right|$ the absolute value of the average slope of the observed peak in the differential conductance as it disperses in magnetic field. This effective g -factor is different from the pure spin g -factor g_{spin} , as the dispersion used to estimate g_{eff} is generally not purely linear in magnetic field, and has additional contributions from the spin-orbit coupling, magnetic field induced changes in chemical potential, and orbital effects [21, 26, 32]. The effective g -factor is the parameter which determines the critical magnetic field required to drive the system through the topological phase transition [33]. We obtain the slope $\frac{\Delta E}{\Delta B}$ from a linear fit (shown as black dashed lines in Figs. 6.3(a),(b), see section 6.9.6 for details) of the observed peak position. Figure 6.3(c) shows the extracted g_{eff} for device A, with more positive back gate voltages leading to larger g_{eff} (visible as a steeper

slope). A similar result has recently been reported in hybrid InAs-Al nanowires [34].

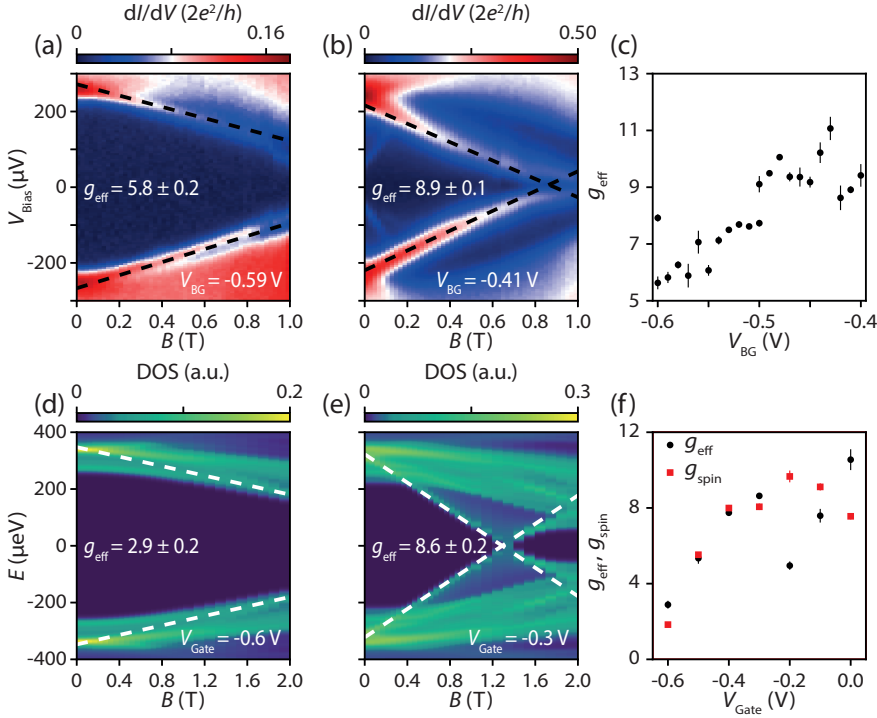


Figure 6.3: **Effective g -factor.** (a,b) dI/dV measured in device A as a function of applied bias voltage V_{Bias} and magnetic field B for $V_{\text{BG}} = -0.59$ V and $V_{\text{BG}} = -0.41$ V, respectively. The effective g -factor is extracted from a linear fit of the lowest energy state dispersion (dashed lines). (c) g_{eff} as a function of V_{BG} , showing an increase as the gate voltage becomes more positive. Data from device A. (d,e) Simulated DOS in the nanowire as a function of magnetic field for $V_{\text{Gate}} = -0.6$ V and $V_{\text{Gate}} = -0.3$ V, respectively. (f) Extracted g_{eff} (based on lowest energy state in the spectrum, black circles) and g_{spin} (based on the spectrum at $k = 0$, red squares) from the simulation.

We use our numerical model to calculate the DOS in the nanowire as a function of applied magnetic field, shown in Fig. 6.3(d) and Fig. 6.3(e). From the calculated spectrum, we apply the same procedure used to fit the experimental data to extract g_{eff} (white dashed lines). The results for different values of V_{Gate} are given in Fig. 6.3(f) as black circles. The applied back gate voltage changes the hybridization of the states in the InSb ($|g_{\text{spin}}| = 40$ [35]) and the Al ($|g_{\text{spin}}| = 2$). As a more positive gate voltage increases the weight of the wave function in the InSb, we expect the renormalized g -factor to increase as the gate voltage is increased, consistent with the results of Fig. 6.3(c) and Fig. 6.3(f).

To see how well g_{eff} describes the Zeeman term in the Hamiltonian, we turn our attention to the energy spectrum at $k = 0$. At this point, the effect of spin-orbit coupling vanishes. If orbital effects are excluded, we can then define the absolute value of the pure spin g -

factor as $g_{\text{spin}} = \frac{2}{\mu_B} \left| \frac{\Delta E(k=0)}{\Delta B} \right|$. The resulting values for g_{spin} are shown as red squares in Fig. 6.3(f). By comparing the results for g_{eff} and g_{spin} , we can conclude that when the lowest energy state has a momentum near $k = 0$ (as is the case for $V_{\text{Gate}} < -0.2\text{V}$), the effect of spin-orbit coupling is negligible, and g_{eff} is a good proxy for the pure spin g -factor. However, when this is no longer the case, deviations can be observed, as is the case for $V_{\text{Gate}} \geq -0.2\text{V}$. As we expect the experimental gate voltage range of Fig. 6.3(c) to be comparable to values of $V_{\text{Gate}} < -0.2\text{V}$, we conclude that the experimentally obtained g_{eff} is a reasonable approximation of g_{spin} in this parameter regime. However, we stress once more that in general, one needs to be careful when interpreting the g_{eff} extracted from experimental data as the g -factor entering the Hamiltonian in the Zeeman term.

The increasing trend of g_{eff} does not change when the orbital effect of magnetic field is considered (see section 6.9.6, Fig. 6.16). However, there is a significant increase in the predicted values, in agreement with previous findings for InAs nanowires [32]. The values in Fig. 6.16 are larger than the ones generally observed in our experiment (see Fig. 6.3(c)), suggesting that the orbital effect is not a dominant mechanism in determining the effective g -factor in these devices. We note that the data from device A used to make these plots was taken solely in the hard gap regime, where one expects a strong confinement near the superconductor. This suppresses the orbital contribution of the magnetic field. Another possible explanation for the discrepancy between the results of the simulation and the experimental data is an overestimation of the density in the nanowire, as higher sub-bands have a stronger contribution from the orbital effect. Minimizing the orbital effect is desirable for Majorana physics, as the orbital contributions of the magnetic field are detrimental to the topological gap [24].

6.6. LEVEL REPULSION DUE TO SPIN-ORBIT COUPLING

The term in the Hamiltonian that remains to be explored describes the Rashba spin-orbit coupling. The strength of the spin-orbit coupling is determined by the parameter α , which depends on the material (and thus, on the superconductor-semiconductor coupling), and the electric field [36–38]. Therefore, we expect that this term will be affected by the gate potential as well. In finite systems, the spin-orbit interaction can couple states with different orbitals and spins [39]. These states are thus no longer orthogonal to each other, and the spin-orbit mediated overlap between them causes energy splitting, leading to level repulsion [40–42]. This level repulsion, which is generic in class D systems in the presence of superconductivity, magnetic field and spin-orbit coupling [43, 44], can be extracted from the low energy nanowire spectrum as measured by tunneling spectroscopy [45].

In Figs. 6.4(a)–(c), we show the evolution of the level repulsion between the two lowest energy sub-gap states (labeled L_1 and L_2 , as indicated by the white dashed lines in panel c) in device B. For these measurements, the global back gate is grounded, with the electric field being induced by applying a voltage to the side gate (side gate shown in Fig. 6.6).

We parameterize the level repulsion by two quantities: the coupling strength δ_{SO} , and

the splitting A , defined as the maximum deviation of L_1 from zero energy after the first zero crossing. This splitting has previously been linked to the overlap between two MZM in a finite system [46]. In Fig. 6.4(e), we zoom in on the anticrossing feature in panel Fig. 6.4(b), showing the minimum energy difference between L_1 and L_2 (given by $2\delta_{\text{SO}}$) and the splitting A . We extract these parameters by a fit of the anticrossing (solid green lines), with the uncoupled states shown by the dashed black lines, details of the fitting procedure are in section 6.9.7).

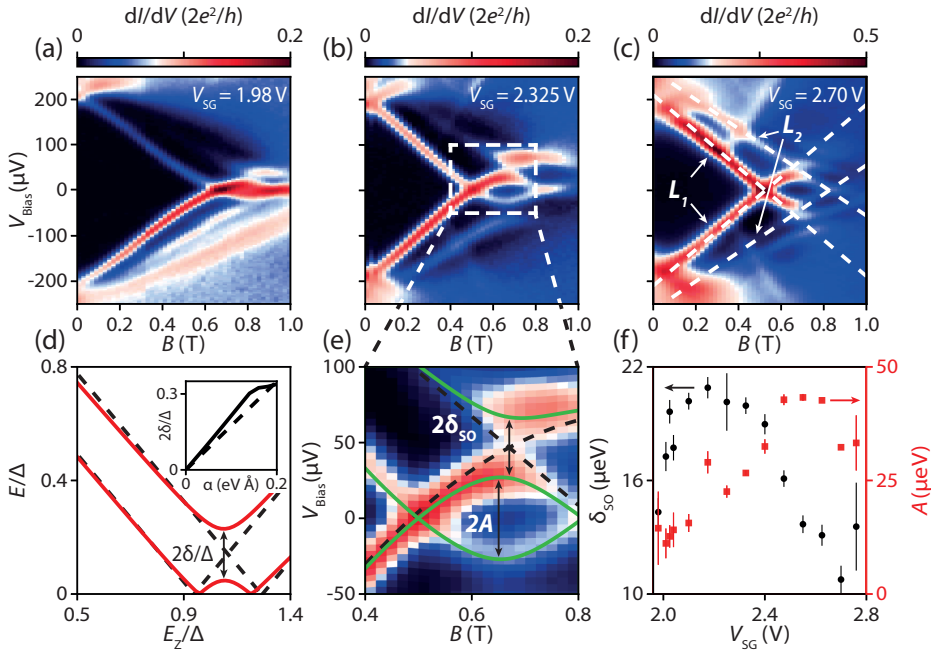


Figure 6.4: **Spin-orbit coupling induced level repulsion.** (a-c) dI/dV as a function of V_{Bias} for device B, showing the dispersion of subgap states in magnetic field, for $V_{\text{SG}} = 1.98$ V, 2.325 V, and 2.70 V, respectively. The two lowest energy states L_1 , L_2 , and their particle-hole symmetric partners are indicated by the white dashed lines. (d) Calculated low energy spectrum of the finite nanowire system as a function of the Zeeman energy E_Z for $\alpha = 0$ eV Å (dashed black lines) and $\alpha = 0.1$ eV Å (solid red lines), showing the opening of an energy gap 2δ due to spin-orbit coupling. Inset: the energy gap 2δ as a function of the Rashba α parameter (solid line), and the estimate $2\delta = \alpha\pi/l$ (dashed line), with l the nanowire length. All energy scales are in units of the superconducting gap Δ . (e) Zoom-in of the anticrossing in (b), showing the splitting A and the coupling strength δ_{SO} . Green solid lines indicate a fit of the anticrossing, with the dashed black lines showing the uncoupled energy levels. (f) Coupling δ_{SO} (black circles) and splitting A (red squares) as a function of V_{SG} , showing opposite trends for these parameters.

Because we expect finite size effects to be relevant, we cannot use our previous theoretical model, as it is based on an infinitely long nanowire. Therefore, we modify the model to take into account the finite size of the nanowire system, and calculate the low energy spectrum for different values of the Rashba spin-orbit strength (see section 6.9.8). In Fig. 6.4(d), we plot the two lowest energy states in the nanowire as a function of the Zeeman energy ($E_Z = \frac{1}{2}g\mu_B B$), in units of the superconducting gap Δ . If $\alpha = 0$ (no spin-orbit

coupling, dashed black lines), there is no coupling between the states, and no level repulsion occurs. However, if spin-orbit coupling is included (e.g., $\alpha = 0.1 \text{ eV}\text{\AA}$, solid red lines), the levels repel each other, with the magnitude of the anticrossing given by 2δ . The level repulsion strength scales with α (inset of Fig. 6.4(d)), providing a way to estimate α based on the low energy spectrum using $2\delta \sim \alpha\pi/l$, where l is the length of the nanowire.

In Fig. 6.4(f), we plot δ_{SO} (black circles) and A (red squares) as a function of the applied side gate voltage. The two parameters follow opposite trends, with A being maximal when δ_{SO} is minimal. When δ_{SO} is larger, the levels repel each other more, leading to L_1 being pushed closer to zero energy, reducing the splitting A . When $V_{\text{SG}} < 2.0 \text{ V}$, both parameters become smaller with decreasing V_{SG} . At this point, other states at higher energies become relevant for the lowest energy dispersion (a situation demonstrated in Fig. 6.4(a)), and our method to extract these parameters breaks down. We expect this method to be reliable when the energetically lowest two states can be clearly separated from the rest.

Because δ_{SO} depends not only on α , but also on the details of the confinement potential, as well as the coupling to the superconductor, a precise estimate goes beyond the current approximations in our model. That being said, based on the observed magnitude of δ_{SO} and our simulations of the finite nanowire system, we can estimate the Rashba parameter α to be around $0.1 \text{ eV}\text{\AA}$ in this gate voltage range. This value is comparable to the values reported in InSb nanowire based quantum dots [47], and smaller than the values measured in weak anti-localization experiments [37]. A large value of α is beneficial for Majorana physics, as it determines the maximum size of the topological gap [48].

6.7. ZERO BIAS PEAK IN EXTENDED MAGNETIC FIELD RANGE

In the previous sections, we have described the effect of the gate induced electric field on the various terms in the Hamiltonian (6.1). As this Hamiltonian is known to describe Majorana physics, we now turn our attention to possible signatures of MZMs in this system. In particular, when $2\delta_{\text{SO}}$ becomes comparable to the energy of L_2 , we find that L_1 can become pinned close to zero bias over an extended range in magnetic field, as demonstrated in Fig. 6.5(b) (data from device A). Figure 6.5(d) shows that the state stays pinned to zero energy over a range of over 0.2 T , corresponding to a Zeeman energy of over $300 \mu\text{eV}$, which is larger than the induced gap. The stability of the ZBP in terms of the ratio of Zeeman energy to induced gap is comparable to the most stable ZBPs reported in literature [11, 12]. When we fix the magnetic field to $B = 0.26 \text{ T}$ and change the back gate voltage (Fig. 6.5(e)), it appears that there is a stable ZBP over a few mV as well.

We might be tempted to conclude that this stability implies this is a Majorana zero mode. However, if we change either the gate voltage (Fig. 6.5(a), Fig. 6.5(c)) or the magnetic field (Fig. 6.5(f)) a little bit, we observe that this stability applies only to very particular combinations of gate voltage and magnetic field. One should keep in mind that in a finite system, MZMs are not expected to be stable with respect to local perturbations if the system size is comparable to the Majorana coherence length, which is likely the case

in our devices. This further complicates the determination of the origin of the observed peaks. As we find no extended region of stability, we conclude that it is unlikely that this state pinned to zero energy is caused by a topological phase transition. Rather, this seems to be due to a fine-tuned coincidence in which the repulsion between two states combined with particle-hole symmetry leads to one of the states being pinned to $E = 0$. We reiterate that simply having a stable zero energy state over an extended range in magnetic field is not sufficient to make claims about robust Majorana modes [49–51]. Further experimental checks, such as stability of the ZBP in an extended region of the parameter space spanned by the relevant gate voltages [11], as well as magnetic field, are required in order to assign a possible Majorana origin.

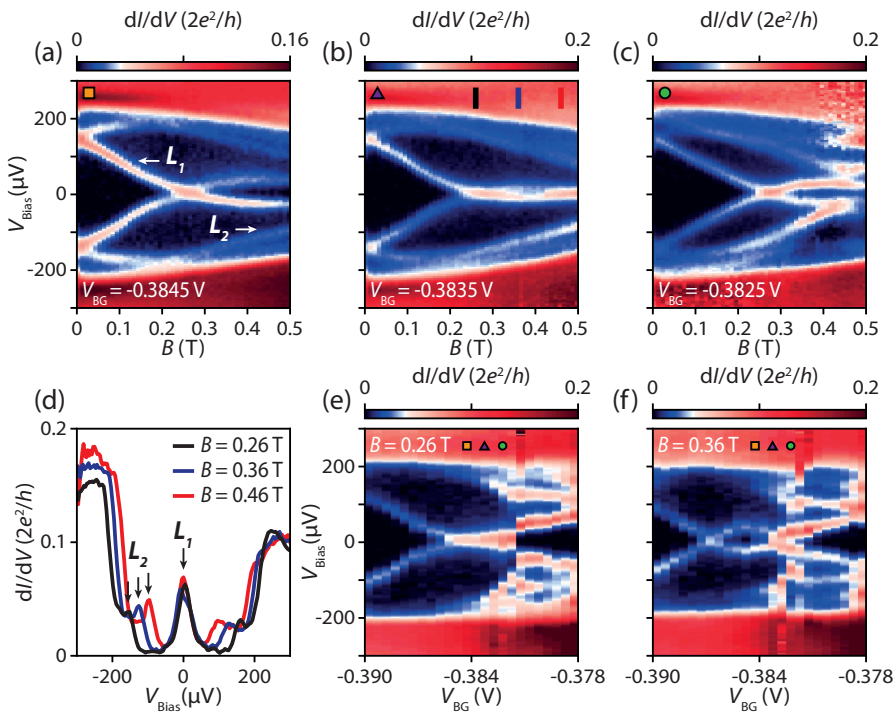


Figure 6.5: **Zero bias pinning due to strong level repulsion.** (a–c) dI/dV as a function of V_{Bias} for device A, showing the dispersion of L_1 and L_2 as a function of magnetic field for $V_{\text{BG}} = -0.3845$ V, -0.3835 V, and -0.3825 V, respectively. (d) Line traces at magnetic fields indicated by the colored bars in (b), showing the stable pinning of L_1 to zero bias voltage. (e, f) dI/dV measured as a function of V_{BG} at fixed magnetic field $B = 0.26$ T and 0.36 T, respectively. Gate voltages from (a), (b), and (c) are indicated by orange square, purple triangle, and green circle, respectively.

6.8. CONCLUSION & OUTLOOK

We have used InSb nanowires with epitaxial Al superconductor to investigate the effect of the gate voltage induced electric field on the superconductor-semiconductor coupling.

This coupling is determined by the distribution of the wave function over the superconductor and semiconductor, and controls essential parameters of the Majorana Hamiltonian: the proximity induced superconducting gap, the effective g -factor, and spin-orbit coupling. Our observations show that the induced superconductivity, as parameterized by the hardness and size of the induced gap, is stronger when the electrons are confined to a region close to the superconductor. The stronger coupling leads to a lower effective g -factor. We also determine that the gate voltage dependence of the effective g -factor is dominated by the change in coupling to the superconductor, rather than by orbital effects of the magnetic field. Finally, we study the effect of level repulsion due to spin-orbit coupling. Appropriate tuning of the repulsion leads to level pinning to zero energy over extended parameter ranges, mimicking the behavior expected from MZMs. Our result deepens the understanding of a more realistic Majorana nanowire system. More importantly, it is relevant for the design and optimization of future advanced nanowire systems for topological quantum information applications.

AUTHOR CONTRIBUTIONS

M.W.A.d.M., J.D.S.B., D.X., and H.Z. fabricated the devices, performed the measurements, and analyzed the data. G.W.W., A.B., A.E.A., and R.M.L. performed the numerical simulations. N.v.L. and G.W. contributed to the device fabrication. R.L.M.O.h.V., S.G., and D.C. grew the InSb nanowires under the supervision of E.P.A.M.B.. J.A.L., M.P., and J.S.L. deposited the aluminum shell on the nanowires under the supervision of C.J.P. L.P.K. and H.Z. supervised the project. **M.W.A.d.M.** and H.Z. wrote the manuscript with comments from all authors. **M.W.A.d.M.**, J.D.S.B., and D.X. contributed equally to this work.

6.9. METHODS AND ADDITIONAL DATA

6.9.1. FABRICATION AND DEVICE DESIGN

1. **Nanowire deposition:** a SEM-based nanomanipulator is used to deterministically place the InSb-Al nanowires onto a degenerately p-doped Si substrate covered by 20 nm of LPCVD Si_3N_4 (devices A, C, and D) or 285 nm of thermal SiO_2 (device B).
2. **Mask preparation & lithography:** for every fabrication step, we use standard electron-beam lithography techniques to create the mask. The mask consists of a layer of PMMA 950KA6 spun at 4000 rpm. After writing, the mask is developed in a solution of MIBK:IPA (1:3 ratio) for 60 s, followed by a IPA rinse for 60 s. After each deposition step, lift-off is done using acetone.
3. **Contact preparation & deposition:** before depositing the contact material, the Al and AlO_x are locally removed by Ar plasma etch. The contacts are deposited by electron-beam evaporation of Cr/Au (10/100-200 nm). For device B, the side gates are also evaporated in this step.
4. **Dielectric deposition:** as a top gate dielectric we sputter 35 nm of SiN_x (devices A, C, and D).
5. **Top gate deposition:** the top gates are deposited by electron-beam evaporation of Ti/Au (10/200 nm) (devices A, C, and D).

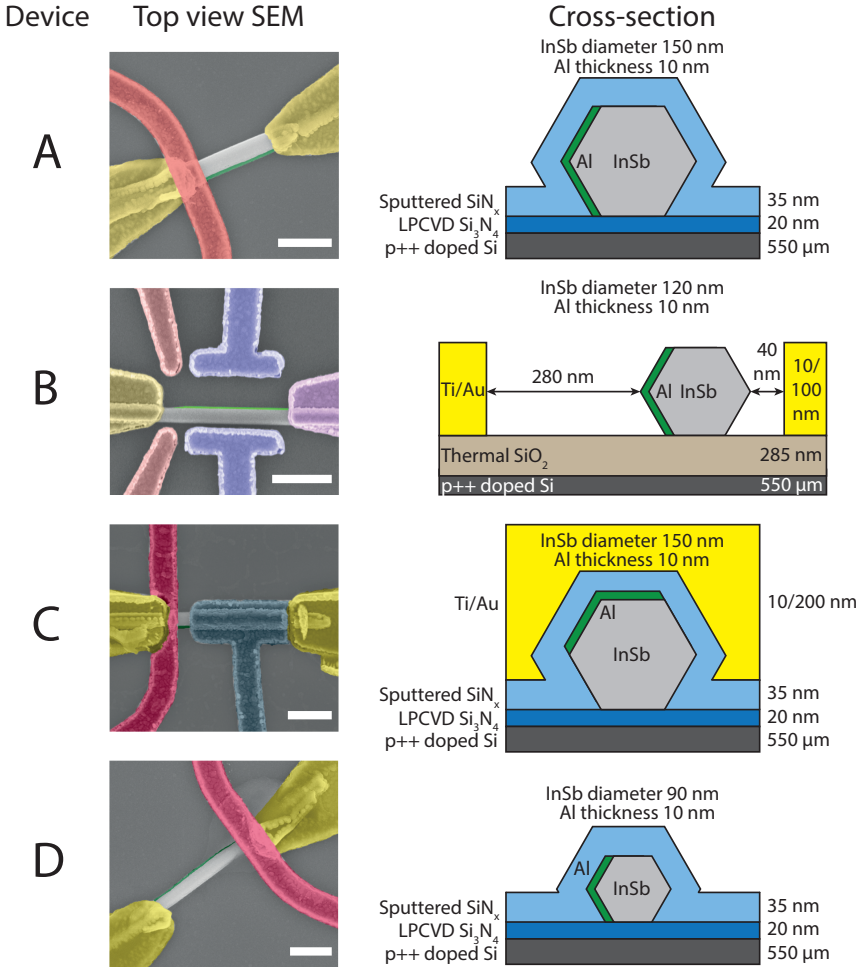


Figure 6.6: **SEM images and schematic cross-sectional views of the devices used as part of this research.** Data from devices A and B is presented in the main text. Additional data from devices C and D is presented for completeness. Note that the data for device B is obtained by changing the voltage on the side gate (V_{SG}), shown in blue in the SEM image. Scale bar is 500 nm.

6.9.2. SIMULATION OF ELECTROSTATICS AND NANOWIRE SPECTRUM

For the electrostatics simulations we use the geometry of device A (as shown in Fig. 6.1(c)). We describe the device as an infinite wire oriented along the x -direction, with a hexagonal cross-section in the yz -plane. The electrostatics are described by the Poisson equation

$$\nabla \cdot (\epsilon_r(\mathbf{r}) \nabla \phi(\mathbf{r})) = \frac{\rho_{\text{tot}}[\phi(\mathbf{r})]}{\epsilon_0}, \quad (6.2)$$

Parameter	InSb	Al
m^*	0.0139 [52]	1
g	-40 [35]	2
Δ	0 meV	0.34 meV [54]
E_F	0 eV	10 eV [55]

Table 6.1: Material parameters for InSb and Al.

where $\rho_{\text{tot}}[\phi(\mathbf{r})]$ is a functional of the potential $\phi(\mathbf{r})$. We include four contributions to ρ_{tot} ,

$$\rho_{\text{tot}} = \rho_e + \rho_{\text{hh}} + \rho_{\text{lh}} + \rho_{\text{fixed}}, \quad (6.3)$$

where ρ_e , ρ_{hh} and ρ_{lh} are the mobile charges of the conduction band, heavy hole band and light hole band of the InSb nanowire and ρ_{fixed} are the fixed charges in the system. For the mobile electron charges we assume a 3D electron gas density (Thomas-Fermi approximation)

$$\rho_e(\phi) = -\frac{e}{3\pi^2} \left(\frac{2m_e|\phi|\theta(-\phi)}{\hbar^2} \right)^{3/2}, \quad (6.4)$$

with θ the Heaviside step function, and for the holes

$$\rho_i(\phi) = \frac{e}{3\pi^2} \left(\frac{2m_i|\phi - E_G|\theta(\phi - E_G)}{\hbar^2} \right)^{3/2}, \quad (6.5)$$

with E_G the band gap and i corresponding to the heavy hole (hh) and light hole (lh) band respectively. For the effective masses, we take the bulk InSb values [52]. We include hole bands to describe the additional screening when the electrochemical potential is in the valence band, which can become relevant for very negative gate voltages due to the narrow band gap of InSb. To model the influence of the sputtered dielectric on the nanowire surface, the wire is wrapped in a 1 nm surface layer of $2.5 \times 10^{18} \text{ cm}^{-3}$ positive charge density. In the absence of other charges and gates this charge pins the conduction band of InSb at about -0.069 eV below the Fermi level at the surface. For the InSb-Al interface we assume the conduction band of InSb is pinned -0.08 eV below the Fermi level due to the work function difference between the two materials. A negative band offset of the semiconductor to the superconductor is required for a hard induced gap in the InAs-Al system [21], and we assume a similar situation in InSb-Al hybrid devices. While the precise numbers for the surface accumulation and band-offset at the InSb-Al interface are unknown, it is known that InSb wires have about a 10 times smaller density than InAs wires [19, 53], and the parameters were adjusted from the InAs ones accordingly. The Al layer is assumed to be grounded, and enters as a Dirichlet boundary condition which is set to +0.08 V. The boundary condition at the substrate-dielectric interface is set to the applied gate voltage, V_{Gate} . On the remaining three boundaries of the system we use Neumann conditions. For the dielectric constant of InSb, the sputtered SiN_x , and the LPCVD Si_3N_4 we take 15.15, 7.5, and 8 respectively.

After the electrostatic potential has been calculated for a given V_{Gate} , we plug it into the Schrödinger equation and solve it for the cross-section of the device. We use a Rashba Hamiltonian with a Bogoliubov-de Gennes (BdG) superconducting term [56]

$$H = \frac{\hbar^2}{2m^*(y,z)}(k_x^2 + k_y^2 + k_z^2)\tau_z - (E_F(y,z) + e\phi(y,z))\tau_z + \alpha_y(y,z)(k_z\sigma_x - k_x\sigma_z)\tau_z + \alpha_z(y,z)(k_x\sigma_y - k_y\sigma_x)\tau_z + \frac{1}{2}g(y,z)\mu_B B\sigma_x + \Delta(y,z)\tau_x, \quad (6.6)$$

where the effective mass m^* , the Fermi level E_F , the electrostatic potential ϕ , the Rashba parameters α_i , the g -factor and the superconducting pairing Δ are functions of the (y, z) -coordinates and depend on the material. Since ϕ is not solved in Al it is correspondingly set to zero there. The material parameters for InSb and Al are summarized in Tab. 6.1. If desired, the orbital effect is added to Eq. (6.6) by the Peierls substitution $k_z \rightarrow k_z - \frac{\pi}{\phi_0}B(y - y_0)$, with ϕ_0 the magnetic flux quantum. y_0 is chosen such that the average vector potential in Al is zero, resulting in a vanishing supercurrent [24]. The Hamiltonian is discretized on a quadratic mesh and constructed using the kwant package [25]. To accommodate the small Fermi wavelength of Al a discretization length of 0.1 nm is used.

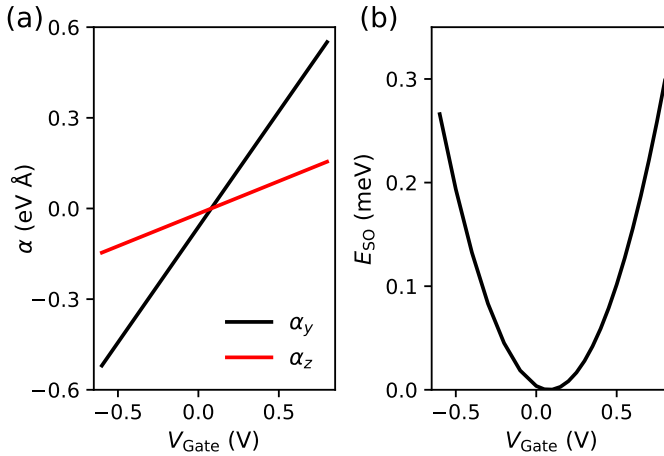


Figure 6.7: **Gate dependence of Rashba coefficients.** (a) Rashba coefficients α_y and α_z as a function of V_{Gate} . At $V_{\text{Gate}} = 0.08$ V, the average electric field in the wire goes to zero due to symmetry, leading to vanishing spin-orbit coupling. (b) Calculated E_{SO} as a function of V_{Gate} .

6.9.3. ELECTRIC FIELD DEPENDENCE OF SPIN-ORBIT COUPLING

The Rashba couplings α_y and α_z , which are nonzero only in the semiconductor region, result from the symmetry breaking by the electrostatic potential and are obtained from [52]

$$\alpha_i = \frac{eP^2}{3} \left[\frac{1}{E_0} - \frac{1}{(E_0 + \Delta_0)^2} \right] \bar{\mathcal{E}}_i, \quad (6.7)$$

where the average electric field in direction i is obtained by averaging \mathcal{E}_i over the whole semiconductor region. Parameters for bulk InSb are used [52]: the Kane matrix element $P = 0.9641$ eV nm, the bandgap $E_0 = 0.237$ eV, and the spin-orbit gap $\Delta_0 = 0.810$ eV. The resulting Rashba parameters α_i are plotted in Fig. 6.7(a).

We define the spin-orbit energy $E_{\text{SO}} = \frac{m^*(\alpha_y^2 + \alpha_z^2)}{2\hbar^2}$. The spin-orbit energy is plotted as a function of V_{Gate} in Fig. 6.7(b). The average electric field in the nanowire increases as the applied gate voltage becomes more negative, leading to an enhancement of the spin-orbit coupling. At $V_{\text{Gate}} = 0.08$ V, the average electric field in the nanowire becomes equal to 0 due to symmetry, eliminating the influence of spin-orbit coupling on the nanowire spectrum.

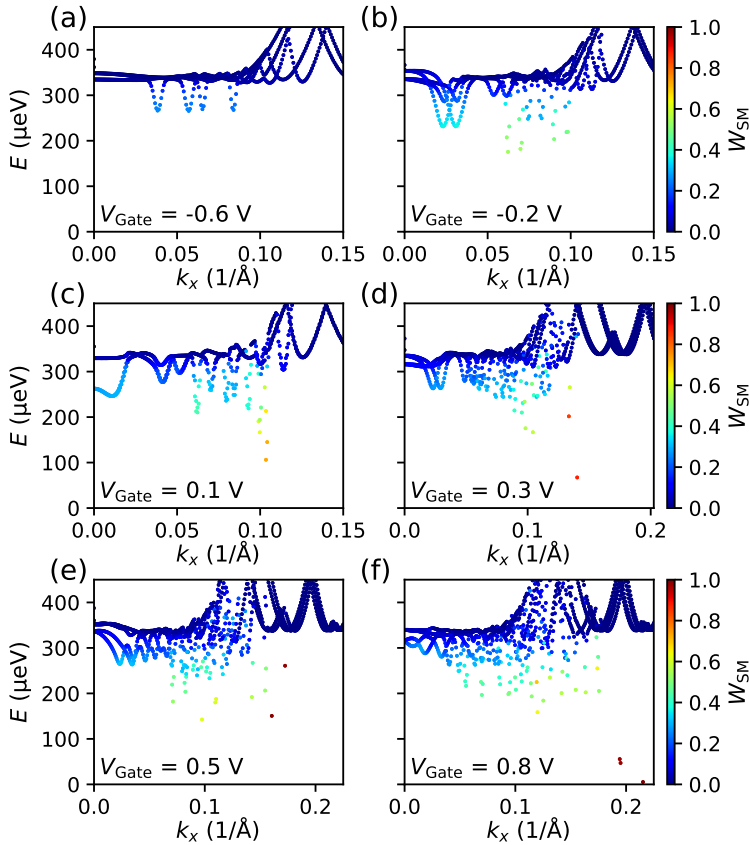


Figure 6.8: **Band structure of the hybrid system calculated at $B = 0$ T for different values of V_{Gate} .** The color indicates the weight of a given state in the semiconducting region. As the gate voltage is increased, the population of states with higher W_{SM} leads to a soft gap.

6.9.4. SIMULATED BAND STRUCTURE

The band structure of the superconductor-semiconductor nanowire system for different values of V_{Gate} is shown in Fig. 6.8. To quantify the coupling of a given state to the superconductor, we calculate the weight of the state in the semiconducting region SM (see Fig. 6.1(c)) as $W_{\text{SM}} = \iint_{\text{SM}} |\Psi(k_{\text{F}})|^2 dy dz$.

6.9.5. GAP FITTING & ADDITIONAL DEVICE DATA

To extract the gap, we measure the differential conductance dI/dV as a function of V_{Bias} and tunnel gate voltage V_{Tunnel} for different back gate voltages V_{BG} . In the tunneling limit, dI/dV is approximately proportional to the density of states. To ensure we are in this limit, we take only the traces where the conductance at high bias ($\sim 500 \mu\text{V}$) is between 0.03 and $0.08 \cdot 2e^2/h$. We use the BCS-Dynes expression for a dissipation broadened superconducting density of states [31] to arrive at the following expression for the conductance:

$$\frac{dI}{dV} = G_{\text{N}} \text{Re} \left\{ \frac{V_{\text{Bias}} - i\Gamma}{\sqrt{(V_{\text{Bias}} - i\Gamma)^2 - \Delta^2}} \right\}. \quad (6.8)$$

This equation is fitted to the data (separately for positive and negative bias), as shown in Fig. 6.9 for $V_{\text{BG}} = -0.6 \text{ V}$. We take the average of the extracted gap values for different values of V_{Tunnel} , with the errorbar given by the standard deviation (results plotted in Fig. 6.2(e)).

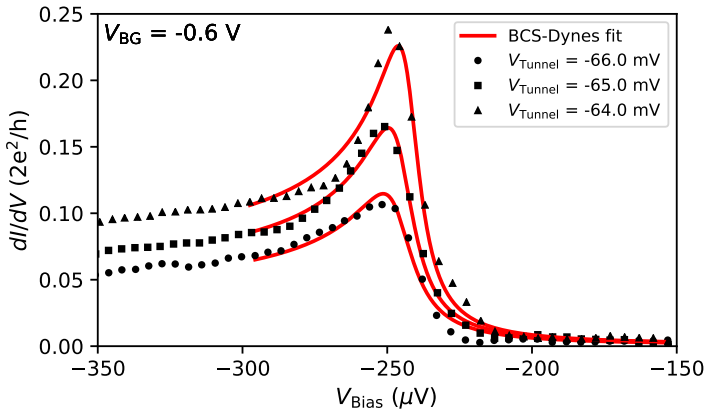


Figure 6.9: **BCS-Dynes fit.** Fit (red line) of equation (6.8) to conductance data from device A (black circles, squares and triangles) for different values of the tunnel gate voltage.

Device B shows similar behavior to device A: as the side gate voltage is increased, the observed gap becomes smaller (as illustrated in Fig. 6.10).

In Fig. 6.11, we show differential conductance traces as a function of V_{Bias} in device D for different values of the back gate voltage. The voltage on the tunnel gate is chosen such that the transmission through the junction (parameterized by G_{N}) is constant.

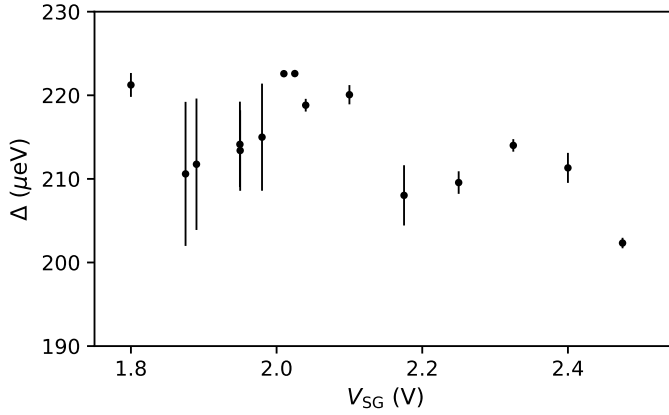


Figure 6.10: Extracted gap Δ as a function of V_{SG} for device B.

Although the sub-gap conductance is similar for all three gate voltages, there is a strong broadening of the coherence peak as the gate voltage becomes more positive. This broadening is associated with dissipation due to an increase in the number of quasiparticles, caused by pair breaking in the superconductor. We plot the extracted gap Δ and dissipation broadening Γ in Fig. 6.12.

6

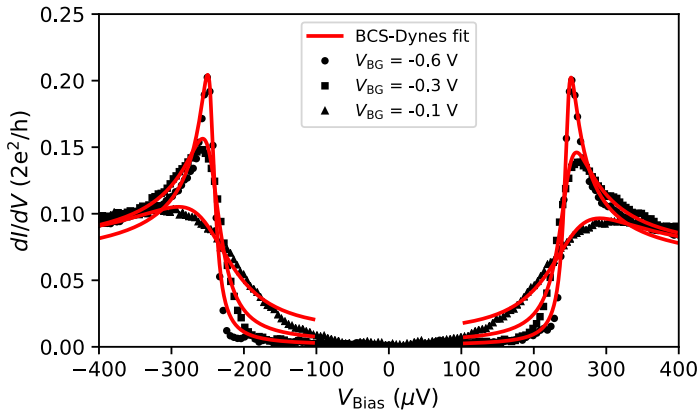


Figure 6.11: **Device D gap fitting.** Fit (red line) of equation 6.8 to conductance data from device D (black circles, squares and triangles) for different V_{BG} at similar junction transparencies. The dissipation broadening sharply decreases for more negative gate voltages.

As in the other devices, the gap decreases for more positive gate voltages, although in this case the effect is minor. The size of the gap is quite stable over an extended range in gate voltage. We speculate that this is related to the diameter of the wire, which is smaller than in the other devices. The reduced thickness means the superconductor can screen the gate voltage more effectively throughout the wire diameter, reducing the effect of the

gate on the superconductor-semiconductor coupling.

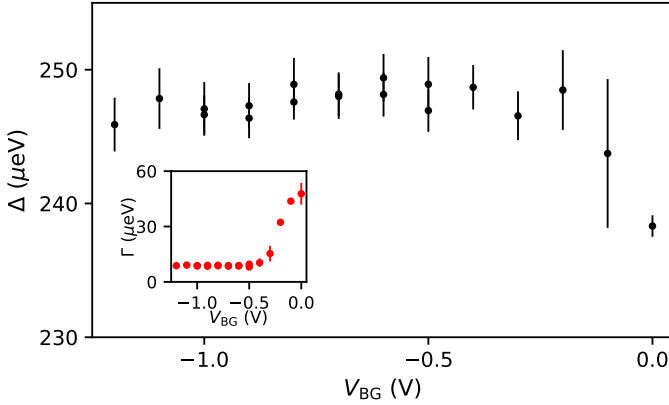


Figure 6.12: **Extracted gap Δ as a function of V_{BG} for device D.** Inset: dissipation broadening Γ as a function of V_{BG} . A decrease in the gap is accompanied by an increase in broadening, signalling the emergence of a soft gap.

6.9.6. g -FACTOR FITTING & ADDITIONAL DEVICE DATA

For each back gate voltage, we measure the dI/dV as a function of V_{Bias} and the magnetic field B . We then identify the lowest energy peak in the spectrum. The position of this peak at a given field is obtained by a peak finding algorithm, the results of which are shown as the green circles in Fig. 6.13. The slope $|\frac{\Delta E}{\Delta B}|$ is determined by a linear fit (dashed black line in Fig. 6.13). From the slope, we get g_{eff} by using the relation $|\Delta E| = \frac{1}{2} g_{eff} \mu_B |\Delta B|$ for a spin- $\frac{1}{2}$ particle, with μ_B the Bohr magneton. This procedure is performed separately for positive and negative bias. The reported g_{eff} is then calculated as a weighted average of the absolute value of the positive and negative bias results (weights determined by the variance of the fit parameters).

The effective g -factor for device A is reported in Fig. 6.3(c). In Fig. 6.14, we plot the extracted g -factors of both L_1 and L_2 in device B. For completeness, data from device C is shown in Fig. 6.15.

The effective g -factor of L_1 (black circles) changes appreciably when the side gate voltage is changed, with the effect comparable to the one observed in device A. In contrast, g_{eff} of L_2 (red squares) is almost unaffected by the gate and has a lower value. This may be due to L_2 being closely confined near the superconductor, leading to a decreased g -factor due to stronger hybridization, and a weaker gate response due to enhanced screening.

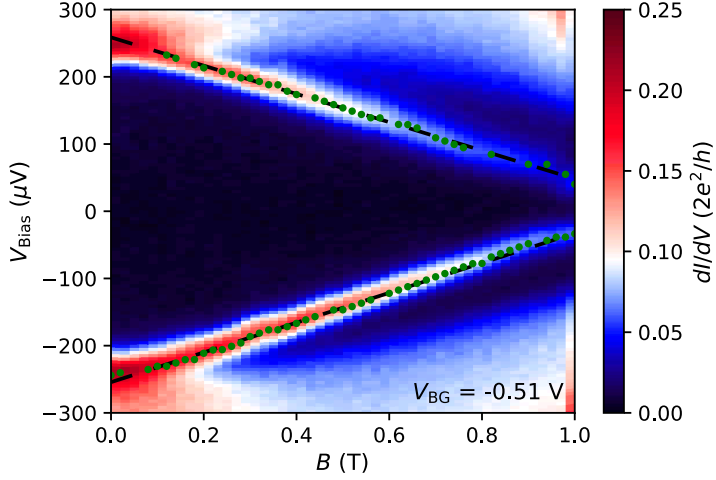


Figure 6.13: ***g*-factor fitting procedure.** Differential conductance as a function of V_{Bias} and magnetic field. We apply a linear fit (dashed black lines) to the extracted peak positions (green circles) to obtain the average slope $\frac{\Delta E}{\Delta B}$.

6

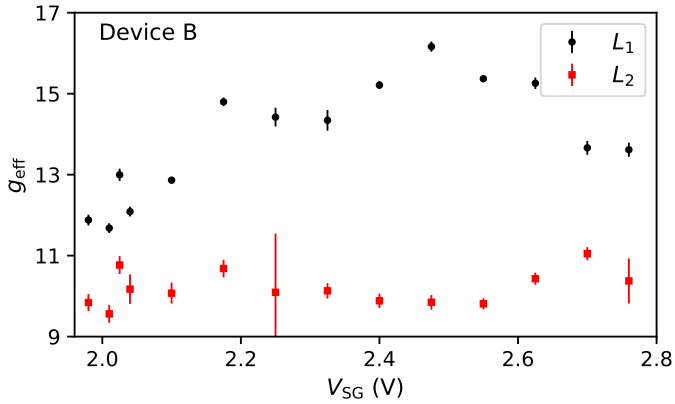
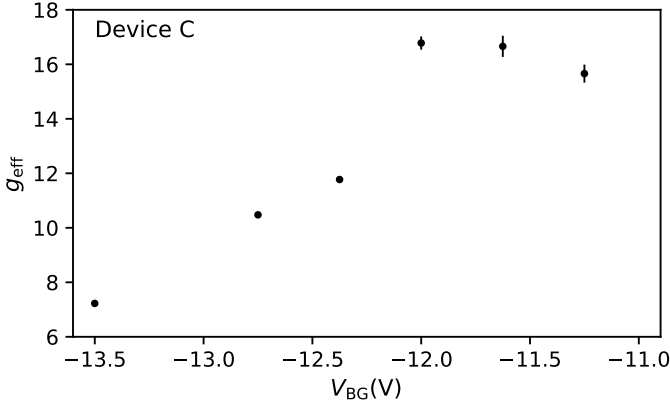
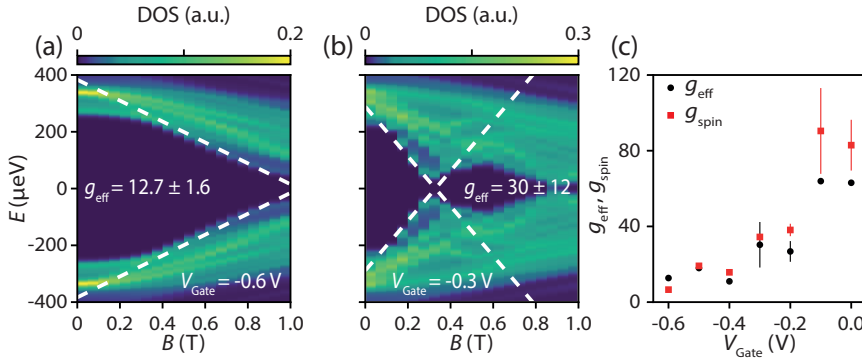


Figure 6.14: **Effective *g*-factor in device B.** Extracted values of g_{eff} as a function of V_{SG} for L_1 (black circles) and L_2 (red squares) in device B.

To determine the importance of orbital effects, we calculate the nanowire spectrum as a function of magnetic field including this effect (Figs. 6.16(a),(b)). The orbital effect leads to an increase of the extracted values of g_{eff} and g_{spin} (Fig. 6.16(c)). Note that the definition of g_{spin} used in section 6.5 is no longer valid when the orbital effect is included. Nevertheless, for consistency we apply the same procedure. As we do not observe these high g -factors in any of our devices, we conclude that the orbital effect does not give a significant contribution to the observed changes of g_{eff} with the gate voltage.

Figure 6.15: Extracted values of g_{eff} for device C.Figure 6.16: **Simulation of nanowire DOS including orbital effect.** (a,b) Simulated nanowire spectrum as a function of magnetic field including orbital effects. (c) Extracted g_{eff} (black circles) and g_{spin} (red squares) as a function of V_{Gate} .

6.9.7. ANTICROSSING FITTING

Near the anticrossing, we approximate the energy of the lowest subgap state L_1 as $E_1 + \frac{1}{2}g_1\mu_B B + aB^2$. The linear term represents the Zeeman contribution to the energy, while the quadratic term is a correction to account for the curvature at high fields. This is possibly due to the presence of additional levels interacting with L_1 in this field range. As the dispersion of L_2 is mostly linear in the field range of interest, we approximate it as $E_2 - \frac{1}{2}g_2\mu_B B$. Adding the coupling parameter δ_{SO} , we find the energy levels of the coupled system from the eigenvalues of the matrix

$$\begin{bmatrix} E_1 + \frac{1}{2}g_1\mu_B B + aB^2 & \delta_{\text{SO}} \\ \delta_{\text{SO}} & E_2 - \frac{1}{2}g_2\mu_B B \end{bmatrix}. \quad (6.9)$$

By fitting the expression for the eigenvalues to the data (see Fig. 6.17), we extract the parameters $E_{1,2}$, $g_{1,2}$, a , and δ_{SO} . To prevent overfitting, we use estimates for the un-

coupled asymptotes to constrain the fit parameters. From the obtained parameters we also calculate the splitting A , defined as the maximum deviation from zero energy of the lowest energy state L_1 , after the first zero energy crossing has occurred.

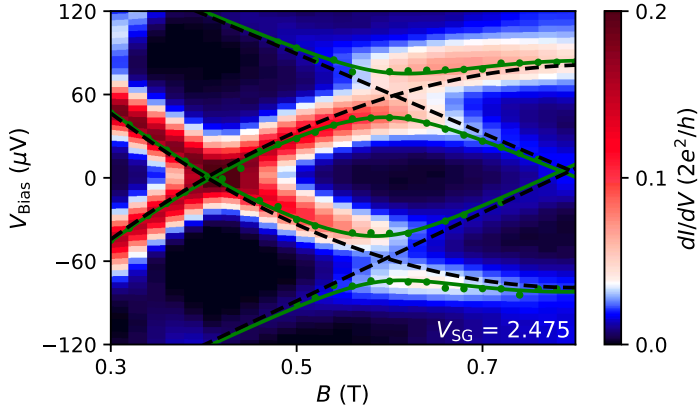


Figure 6.17: **Level repulsion fitting procedure.** Data from device B, showing the differential conductance dI/dV as a function of V_{Bias} and B for $V_{\text{BG}} = 2.475$ V. Green dots indicate the peak positions found using a peak finding algorithm. The fit to the data is shown in green, with the uncoupled asymptotes as the black dashed lines.

6

6.9.8. SIMULATION OF FINITE SIZE NANOWIRE SYSTEM

To simulate the finite nanowire system, we solve the Hamiltonian (6.1) in a simplified setup. We consider a rectangular cross-section in the yz -plane similar to the one used in reference [21], where the top facet of the rectangle is covered by the superconductor, and a uniform gate voltage V_{Gate} is applied to the bottom facet, as illustrated in Fig. 6.18. First, we assume an infinitely long nanowire oriented in the x -direction, and calculate the electrostatic potential in the Thomas-Fermi approximation, similar to the procedure described in section 6.9.2. The fermi level in the nanowire is tuned such that it supports the same number of transverse modes at $V_{\text{Gate}} = 0$ as the hexagonal nanowire studied previously. We use the same material parameters as in the previous simulation, which can be found in table 6.1.

We then plug the resulting electrostatic potential into 6.1 and solve the Schrödinger equation to find the low energy spectrum of the finite nanowire. We take a length of 750 nm, similar to the studied devices. We calculate only the modes in the semiconductor, assuming a superconducting gap of $\Delta = 250 \mu\text{eV}$. We find that the origin of the level repulsion between states is indeed spin-orbit coupling, which couples different longitudinal (along the x -direction) states within the same transverse (y - and z -directions) subband.

The result is illustrated in Fig. 6.19, where we plot the low energy spectrum as a function

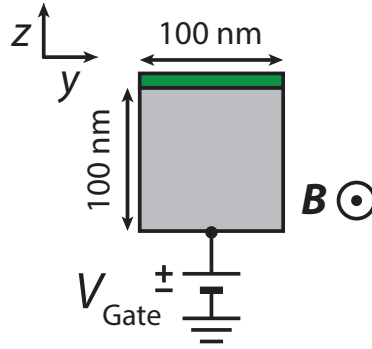


Figure 6.18: **Schematic cross-section of the geometry used to simulate the finite nanowire system.** A potential V_{Gate} is applied to the bottom facet, while the potential at the top facet is fixed by the work function difference between the two materials. The magnetic field is applied in the x -direction, along length of the nanowire.

of Zeeman energy E_Z for a fixed value of V_{Gate} and different values of α . An increase in the spin-orbit coupling strength leads to an increase in the level repulsion.

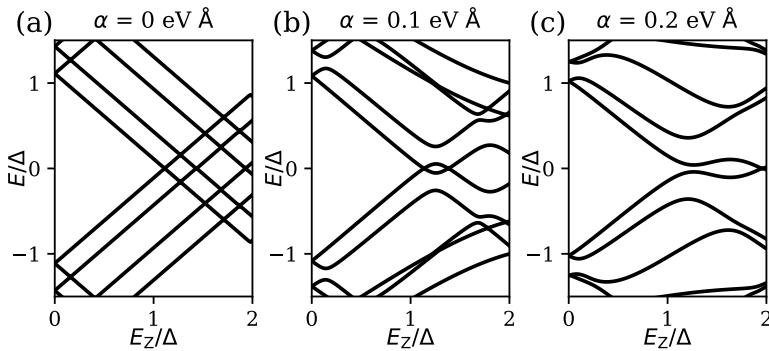


Figure 6.19: **Level repulsion of a function of spin-orbit strength.** Calculated low energy spectrum of the finite size nanowire as a function of Zeeman energy for different values of α . Values calculated for $V_{\text{Gate}} = -0.536\text{V}$, which is also used in Fig. 6.4(d). All energy scales are in units of the superconducting gap Δ .

However, even if α is fixed, the magnitude of the level repulsion can be changed by changing the confinement potential, as demonstrated in Fig. 6.20.

When the gate voltage is changed, it alters the confinement potential. This affects the energy of the levels coupled by the spin-orbit coupling, and as such directly influences the magnitude of δ , even though the spin-orbit coupling strength itself is not changed appreciatively. In Fig. 6.21 we plot the calculated energy gap due to level repulsion, 2δ , and the maximum splitting from zero energy of the lowest energy state after the first zero crossing, A , as a function of V_{Gate} . The two parameters follow opposite trends, consistent with the experimental observation in Fig. 6.4(f).

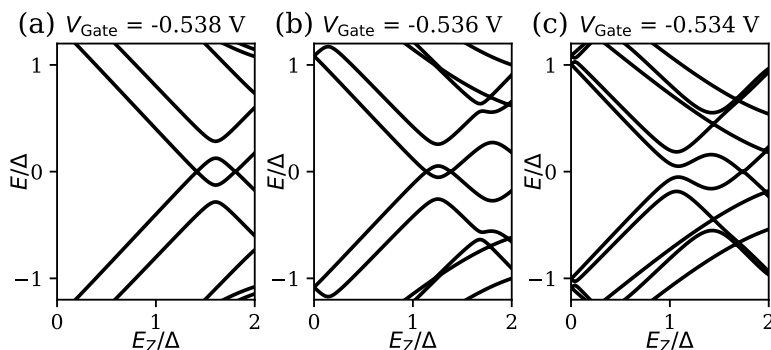


Figure 6.20: **Level repulsion as a function of gate voltage.** Calculated low energy spectrum of the finite size nanowire as a function of Zeeman energy for different values of V_{Gate} . Values calculated $\alpha = 0.1 \text{ eV \AA}$, energy scales in units of Δ .

However, the trend with gate voltage is opposite: δ increases with more positive gate voltage, whereas in the experiment it decreases. We note that the geometry used in this simulation is a simplified version of the one used in the experiment. The dependence of the confinement energy on gate voltage is strongly dependent on the geometry, which differs between the simulation and the experiment. It is therefore expected that the trend of δ with gate voltage is not universal, and requires the details of the systems to be very similar before comparisons can be made.

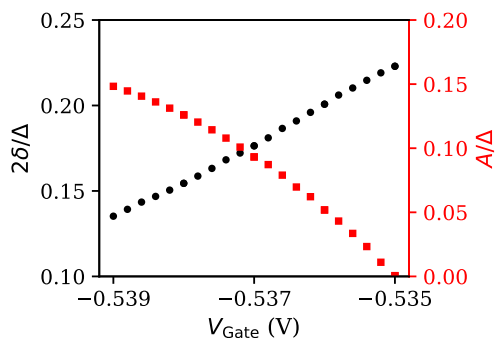


Figure 6.21: **Gate voltage dependent coupling.** Dependence of the energy gap 2δ and the splitting A , in units of Δ , on the gate voltage V_{Gate} .

6.9.9. ADDITIONAL ZBP DATA

Figure 6.22(a) shows the differential conductance measured in device A as a function of V_{Bias} and V_{Tunnel} , for $B = 0.35$ T and $V_{\text{BG}} = -0.37$ V. The low energy spectrum in this parameter regime does not depend on the transmission of the NS-junction. In Fig. 6.22(b), we show line traces for different values of V_{Tunnel} . Even though the transmission of the junction is changed by a factor of two, the peak position of the low energy states are not affected. Data from Fig. 6.5 was obtained for $V_{\text{Tunnel}} = -87$ mV.

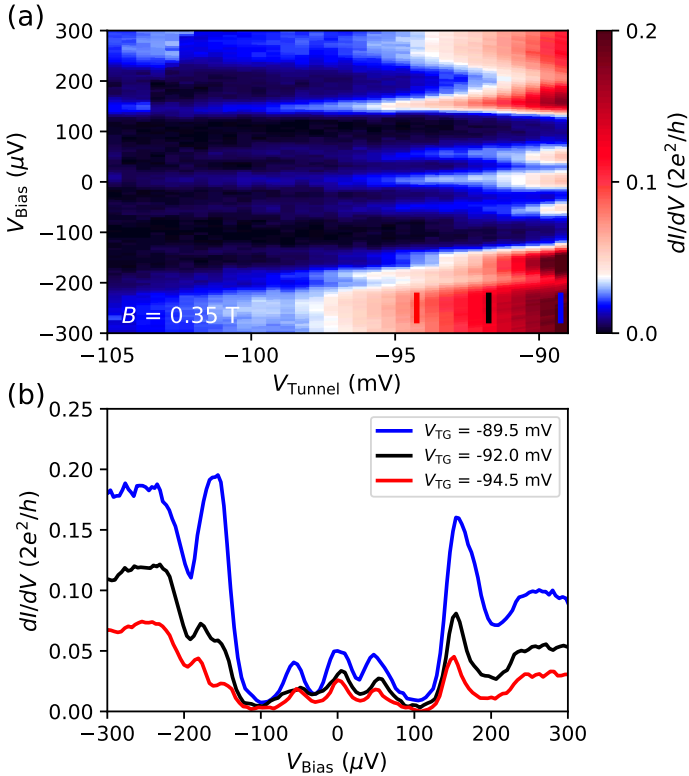


Figure 6.22: **Tunnel gate voltage dependence of low energy spectrum.** (a) dI/dV measured in device A as a function of V_{Bias} and V_{Tunnel} for $B = 0.35$ T and $V_{\text{BG}} = -0.37$ V. (b) Line traces at the values of V_{Tunnel} indicated by the colored lines in panel (a).

Figure 6.23 shows additional data on the evolution of the level repulsion between L_1 and L_2 in device A (supplementing the data presented in Figs. 6.5(a-c)) as the back gate voltage is increased. As discussed in section 6.7, we do not find an extended region in parameter space with a stable zero bias conductance peak.

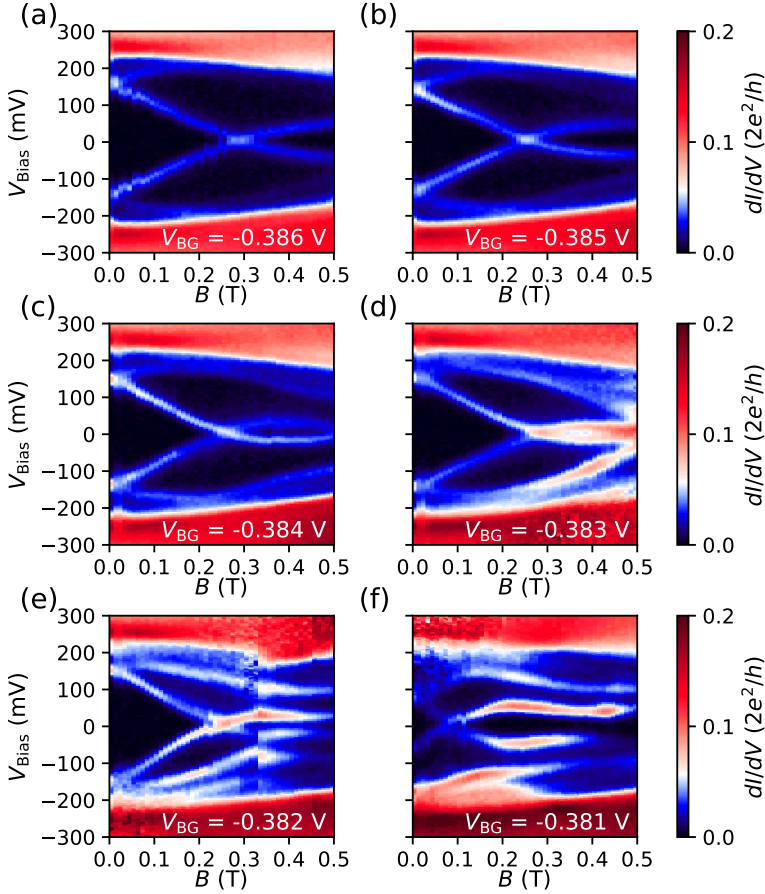


Figure 6.23: **Low energy spectrum as a function of field.** Differential conductance as a function of V_{Bias} and magnetic field. Although the lowest energy state stays near zero over an extended magnetic field range for some gate voltages, this behavior is not robust.

In Fig. 6.24 we show the low energy spectrum of device A as a function of V_{Bias} and V_{BG} for different magnetic fields (supplementing the data presented in Figs. 6.5(e,f)). For specific combinations of magnetic field and gate voltage, we can find a zero energy state. However, as we do not find an extended region in parameter space, it is unlikely that a topological phase transition is responsible for this observation.

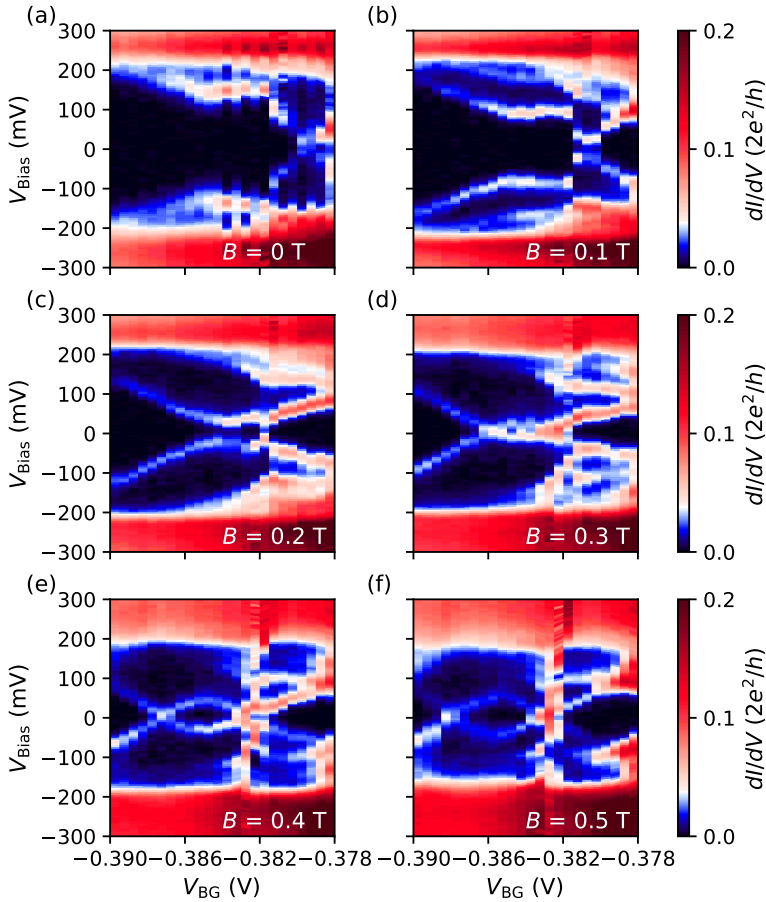


Figure 6.24: **Low energy spectrum as a function of gate voltage.** Differential conductance as a function of V_{Bias} and V_{BG} . We find some stable ZBPs for certain ranges in back gate voltage at specific fields, but this is only true for fine tuned parameters.

REFERENCES

- [1] C. Nayak, S. H. Simon, A. Stern, M. Freedman, and S. Das Sarma, *Non-Abelian anyons and topological quantum computation*, Rev. Mod. Phys. **80**, 1083 (2008).
- [2] S. Plugge, A. Rasmussen, R. Egger, and K. Flensberg, *Majorana box qubits*, New Journal of Physics **19**, 012001 (2017).
- [3] T. Karzig, C. Knapp, R. M. Lutchyn, P. Bonderson, M. B. Hastings, C. Nayak, J. Alicea, K. Flensberg, S. Plugge, Y. Oreg, C. M. Marcus, and M. H. Freedman, *Scalable designs for quasiparticle-poisoning-protected topological quantum computation with Majorana zero modes*, Phys. Rev. B **95**, 235305 (2017).

- [4] R. M. Lutchyn, J. D. Sau, and S. Das Sarma, *Majorana Fermions and a Topological Phase Transition in Semiconductor-Superconductor Heterostructures*, Phys. Rev. Lett. **105**, 077001 (2010).
- [5] Y. Oreg, G. Refael, and F. von Oppen, *Helical Liquids and Majorana Bound States in Quantum Wires*, Phys. Rev. Lett. **105**, 177002 (2010).
- [6] P. G. de Gennes, *Boundary Effects in Superconductors*, Rev. Mod. Phys. **36**, 225 (1964).
- [7] V. Mourik, K. Zuo, S. M. Frolov, S. R. Plissard, E. P. A. M. Bakkers, and L. P. Kouwenhoven, *Signatures of Majorana Fermions in Hybrid Superconductor-Semiconductor Nanowire Devices*, Science **336**, 1003 (2012).
- [8] A. Das, Y. Ronen, Y. Most, Y. Oreg, M. Heiblum, and H. Shtrikman, *Zero-bias peaks and splitting in an Al-InAs nanowire topological superconductor as a signature of Majorana fermions*, Nature Physics **8**, 887 (2012).
- [9] M. T. Deng, C. L. Yu, G. Y. Huang, M. Larsson, P. Caroff, and H. Q. Xu, *Anomalous Zero-Bias Conductance Peak in a Nb-InSb Nanowire-Nb Hybrid Device*, Nano Letters **12**, 6414 (2012).
- [10] H. O. H. Churchill, V. Fatemi, K. Grove-Rasmussen, M. T. Deng, P. Caroff, H. Q. Xu, and C. M. Marcus, *Superconductor-nanowire devices from tunneling to the multichannel regime: Zero-bias oscillations and magnetoconductance crossover*, Phys. Rev. B **87**, 241401 (2013).
- [11] O. Gül, H. Zhang, J. D. S. Bommer, M. W. A. de Moor, D. Car, S. R. Plissard, E. P. A. M. Bakkers, A. Geresdi, K. Watanabe, T. Taniguchi, and L. P. Kouwenhoven, *Ballistic Majorana nanowire devices*, Nature Nanotechnology **13**, 192 (2018).
- [12] M. T. Deng, S. Vaitiekėnas, E. B. Hansen, J. Danon, M. Leijnse, K. Flensberg, J. Nygård, P. Krogstrup, and C. M. Marcus, *Majorana bound state in a coupled quantum-dot hybrid-nanowire system*, Science **354**, 1557 (2016).
- [13] H. Zhang, C.-X. Liu, S. Gazibegovic, D. Xu, J. A. Logan, G. Wang, N. van Loo, J. D. S. Bommer, M. W. A. de Moor, D. Car, R. L. M. Op het Veld, P. J. van Veldhoven, S. Koelling, M. A. Verheijen, M. Pendharkar, D. J. Pennachio, B. Shojaei, J. S. Lee, C. J. Palmstrøm, E. P. A. M. Bakkers, S. Das Sarma, and L. P. Kouwenhoven, *Quantized Majorana conductance*, Nature **556**, 74 (2018).
- [14] R. M. Lutchyn, E. P. A. M. Bakkers, L. P. Kouwenhoven, P. Krogstrup, C. M. Marcus, and Y. Oreg, *Majorana zero modes in superconductor-semiconductor heterostructures*, Nature Reviews Materials **3**, 52 (2018).
- [15] O. Gül, H. Zhang, F. K. de Vries, J. van Veen, K. Zuo, V. Mourik, S. Conesa-Boj, M. P. Nowak, D. J. van Woerkom, M. Quintero-Pérez, M. C. Cassidy, A. Geresdi, S. Koelling, D. Car, S. R. Plissard, E. P. A. M. Bakkers, and L. P. Kouwenhoven, *Hard Superconducting Gap in InSb Nanowires*, Nano Letters **17**, 2690 (2017).

- [16] H. Zhang, O. Gül, S. Conesa-Boj, M. P. Nowak, M. Wimmer, K. Zuo, V. Mourik, F. K. de Vries, J. van Veen, M. W. A. de Moor, J. D. S. Bommer, D. J. van Woerkom, D. Car, S. R. Plissard, E. P. A. M. Bakkers, M. Quintero-Pérez, M. Cassidy, S. Koelling, S. Goswami, K. Watanabe, T. Taniguchi, and L. P. Kouwenhoven, *Ballistic superconductivity in semiconductor nanowires*, Nature Communications **8**, 16025 (2017).
- [17] S. T. Gill, J. Damasco, B. E. Janicek, M. S. Durkin, V. Humbert, S. Gazibegovic, D. Car, E. P. A. M. Bakkers, P. Y. Huang, and N. Mason, *Selective-Area Superconductor Epitaxy to Ballistic Semiconductor Nanowires*, Nano Letters **18**, 6121 (2018).
- [18] P. Krogstrup, N. L. B. Ziino, W. Chang, S. M. Albrecht, M. H. Madsen, E. Johnson, J. Nygård, C. M. Marcus, and T. S. Jespersen, *Epitaxy of semiconductor-superconductor nanowires*, Nature Materials **14**, 400 (2015).
- [19] W. Chang, S. M. Albrecht, T. S. Jespersen, F. Kuemmeth, P. Krogstrup, J. Nygård, and C. M. Marcus, *Hard gap in epitaxial semiconductor-superconductor nanowires*, Nature Nanotechnology **10**, 232 (2015).
- [20] S. Gazibegovic, D. Car, H. Zhang, S. C. Balk, J. A. Logan, M. W. A. de Moor, M. C. Cassidy, R. Schmits, D. Xu, G. Wang, P. Krogstrup, R. L. M. Op het Veld, K. Zuo, Y. Vos, J. Shen, D. Bouman, B. Shojaei, D. Pennachio, J. S. Lee, P. J. van Veldhoven, S. Koelling, M. A. Verheijen, L. P. Kouwenhoven, C. J. Palmstrøm, and E. P. A. M. Bakkers, *Epitaxy of advanced nanowire quantum devices*, Nature **548**, 434 (2017).
- [21] A. E. Antipov, A. Bargerbos, G. W. Winkler, B. Bauer, E. Rossi, and R. M. Lutchyn, *Effects of Gate-Induced Electric Fields on Semiconductor Majorana Nanowires*, Phys. Rev. X **8**, 031041 (2018).
- [22] A. F. Volkov, P. H. C. Magnée, B. J. van Wees, and T. M. Klapwijk, *Proximity and Josephson effects in superconductor-two-dimensional electron gas planar junctions*, Physica C: Superconductivity **242**, 261 (1995).
- [23] C. Reeg, D. Loss, and J. Klinovaja, *Metallization of a Rashba wire by a superconducting layer in the strong-proximity regime*, Phys. Rev. B **97**, 165425 (2018).
- [24] B. Nijholt and A. R. Akhmerov, *Orbital effect of magnetic field on the Majorana phase diagram*, Phys. Rev. B **93**, 235434 (2016).
- [25] C. W. Groth, M. Wimmer, A. R. Akhmerov, and X. Waintal, *Kwant: a software package for quantum transport*, New Journal of Physics **16**, 063065 (2014).
- [26] A. Vuik, D. Eeltink, A. R. Akhmerov, and M. Wimmer, *Effects of the electrostatic environment on the Majorana nanowire devices*, New Journal of Physics **18**, 033013 (2016).
- [27] A. E. G. Mikkelsen, P. Kotetes, P. Krogstrup, and K. Flensberg, *Hybridization at Superconductor-Semiconductor Interfaces*, Phys. Rev. X **8**, 031040 (2018).
- [28] J. Bardeen, *Tunnelling from a Many-Particle Point of View*, Phys. Rev. Lett. **6**, 57 (1961).

- [29] G. E. Blonder, M. Tinkham, and T. M. Klapwijk, *Transition from metallic to tunneling regimes in superconducting microconstrictions: Excess current, charge imbalance, and supercurrent conversion*, Phys. Rev. B **25**, 4515 (1982).
- [30] C. W. J. Beenakker, *Quantum transport in semiconductor-superconductor microjunctions*, Phys. Rev. B **46**, 12841 (1992).
- [31] R. C. Dynes, V. Narayanamurti, and J. P. Garno, *Direct Measurement of Quasiparticle-Lifetime Broadening in a Strong-Coupled Superconductor*, Phys. Rev. Lett. **41**, 1509 (1978).
- [32] G. W. Winkler, D. Varjas, R. Skolasinski, A. A. Soluyanov, M. Troyer, and M. Wimmer, *Orbital Contributions to the Electron g factor in Semiconductor Nanowires*, Phys. Rev. Lett. **119**, 037701 (2017).
- [33] T. D. Stanescu, R. M. Lutchyn, and S. Das Sarma, *Majorana fermions in semiconductor nanowires*, Phys. Rev. B **84**, 144522 (2011).
- [34] S. Vaitiekėnas, M.-T. Deng, J. Nygård, P. Krogstrup, and C. M. Marcus, *Effective g Factor of Subgap States in Hybrid Nanowires*, Phys. Rev. Lett. **121**, 037703 (2018).
- [35] J. Kammhuber, M. C. Cassidy, H. Zhang, O. Gül, F. Pei, M. W. A. de Moor, B. Nijholt, K. Watanabe, T. Taniguchi, D. Car, S. R. Plissard, E. P. A. M. Bakkers, and L. P. Kouwenhoven, *Conductance Quantization at Zero Magnetic Field in InSb Nanowires*, Nano Letters **16**, 3482 (2016).
- [36] J. Nitta, T. Akazaki, H. Takayanagi, and T. Enoki, *Gate Control of Spin-Orbit Interaction in an Inverted $\text{In}_{0.53}\text{Ga}_{0.47}\text{As}/\text{In}_{0.52}\text{Al}_{0.48}\text{As}$ Heterostructure*, Phys. Rev. Lett. **78**, 1335 (1997).
- [37] I. van Weperen, B. Tarasinski, D. Eeltink, V. S. Pribiag, S. R. Plissard, E. P. A. M. Bakkers, L. P. Kouwenhoven, and M. Wimmer, *Spin-orbit interaction in InSb nanowires*, Phys. Rev. B **91**, 201413 (2015).
- [38] Z. Scherübl, G. Fülöp, M. H. Madsen, J. Nygård, and S. Csonka, *Electrical tuning of Rashba spin-orbit interaction in multigated InAs nanowires*, Phys. Rev. B **94**, 035444 (2016).
- [39] T. D. Stanescu, R. M. Lutchyn, and S. Das Sarma, *Dimensional crossover in spin-orbit-coupled semiconductor nanowires with induced superconducting pairing*, Phys. Rev. B **87**, 094518 (2013).
- [40] E. J. H. Lee, X. Jiang, M. Houzet, R. Aguado, C. M. Lieber, and S. De Franceschi, *Spin-resolved Andreev levels and parity crossings in hybrid superconductor-semiconductor nanostructures*, Nature Nanotechnology **9**, 79 (2014).
- [41] B. van Heck, J. I. Väyrynen, and L. I. Glazman, *Zeeman and spin-orbit effects in the Andreev spectra of nanowire junctions*, Phys. Rev. B **96**, 075404 (2017).

- [42] E. C. T. O'Farrell, A. C. C. Drachmann, M. Hell, A. Fornieri, A. M. Whiticar, E. B. Hansen, S. Gronin, G. C. Gardener, C. Thomas, M. J. Manfra, K. Flensberg, C. M. Marcus, and F. Nichele, *Hybridization of sub-gap states in one-dimensional superconductor-semiconductor Coulomb islands*, (2018), arXiv:1804.09676 .
- [43] D. I. Pikulin, J. P. Dahlhaus, M. Wimmer, H. Schomerus, and C. W. J. Beenakker, *A zero-voltage conductance peak from weak antilocalization in a Majorana nanowire*, *New Journal of Physics* **14**, 125011 (2012).
- [44] S. Mi, D. I. Pikulin, M. Marciiani, and C. W. J. Beenakker, *X-shaped and Y-shaped Andreev resonance profiles in a superconducting quantum dot*, *Journal of Experimental and Theoretical Physics* **119**, 1018 (2014).
- [45] R. V. Mishmash, D. Aasen, A. P. Higginbotham, and J. Alicea, *Approaching a topological phase transition in Majorana nanowires*, *Phys. Rev. B* **93**, 245404 (2016).
- [46] S. M. Albrecht, A. P. Higginbotham, M. Madsen, F. Kuemmeth, T. S. Jespersen, J. Nygård, P. Krogstrup, and C. M. Marcus, *Exponential protection of zero modes in Majorana islands*, *Nature* **531**, 206 (2016).
- [47] S. Nadj-Perge, V. S. Pribiag, J. W. G. van den Berg, K. Zuo, S. R. Plissard, E. P. A. M. Bakkers, S. M. Frolov, and L. P. Kouwenhoven, *Spectroscopy of Spin-Orbit Quantum Bits in Indium Antimonide Nanowires*, *Phys. Rev. Lett.* **108**, 166801 (2012).
- [48] J. D. Sau, S. Tewari, and S. Das Sarma, *Experimental and materials considerations for the topological superconducting state in electron- and hole-doped semiconductors: Searching for non-Abelian Majorana modes in 1D nanowires and 2D heterostructures*, *Phys. Rev. B* **85**, 064512 (2012).
- [49] G. Kells, D. Meidan, and P. W. Brouwer, *Near-zero-energy end states in topologically trivial spin-orbit coupled superconducting nanowires with a smooth confinement*, *Phys. Rev. B* **86**, 100503 (2012).
- [50] E. Prada, P. San-Jose, and R. Aguado, *Transport spectroscopy of NS nanowire junctions with Majorana fermions*, *Phys. Rev. B* **86**, 180503 (2012).
- [51] C.-X. Liu, J. D. Sau, T. D. Stanescu, and S. Das Sarma, *Andreev bound states versus Majorana bound states in quantum dot-nanowire-superconductor hybrid structures: Trivial versus topological zero-bias conductance peaks*, *Phys. Rev. B* **96**, 075161 (2017).
- [52] R. Winkler, S. J. Papadakis, E. P. De Poortere, and M. Shayegan, *Spin-Orbit Coupling in Two-Dimensional Electron and Hole Systems*, Vol. 41 (Springer, 2003).
- [53] S. R. Plissard, I. van Weperen, D. Car, M. A. Verheijen, G. W. G. Immink, J. Kammerhuber, L. J. Cornelissen, D. B. Szombati, A. Geresdi, S. M. Frolov, L. P. Kouwenhoven, and E. P. A. M. Bakkers, *Formation and electronic properties of InSb nanocrosses*, *Nature Nanotechnology* **8**, 859 (2013).

- [54] R. Meservey and P. M. Tedrow, *Properties of Very Thin Aluminum Films*, Journal of Applied Physics **42**, 51 (1971).
- [55] N. Ashcroft and N. Mermin, *Solid State Physics* (Saunders College Publishing, 1976).
- [56] M. Tinkham, *Introduction to Superconductivity*, Dover Books on Physics Series (Dover Publications, 1996).

7

NANOCROSSES FOR MAJORANA CORRELATION EXPERIMENTS

In this chapter, we present experiments on InSb nanocrosses with epitaxial Al as a superconductor, with the goal of measuring correlated zero bias conductance peaks at both ends of the superconducting segment, demonstrating Majorana non-locality. Compared to the single wire geometry, the nanocross provides an easy way to ground to superconductor without damaging the active device area, as well as access to an additional tunnel probe in the bulk of the nanowire, which can be used to simultaneously probe the Majorana zero modes at the ends and the gap closing and reopening in the bulk.

7.1. INTRODUCTION

Since the prediction of Majorana zero modes in semiconductor-superconductor hybrid nanowires, a lot of experimental effort has gone into measuring zero bias conductance peaks in tunneling spectroscopy experiments, and studying their behavior as a function of various control parameters [1–4]. This has culminated in the detection of quantized zero bias conductance peaks in InSb-Al nanowires [5]. Although significant progress has been made, every experiment to date has used a single local probe, leaving open the possibility that the zero bias conductance peak is generated by local perturbations such as smooth potential barriers [6–9]. An important property of Majorana zero modes is their non-local nature, which can be probed by measuring a zero bias conductance peak at both sides of a grounded 1D topological superconductor [10]. In a finite system, overlap between the Majorana zero modes creates a state at finite energy, which oscillates as a function of control parameters such as the magnetic field [11]. If the splittings observed by the local probes are strongly correlated, this would give further confidence that this signal is due to a non-local state. Additionally, the appearance of end states at zero energy should be accompanied by a closing and reopening of the bulk gap, which is difficult to observe with probes at the ends of the wire as the bulk wave functions have very little weight there [12]. Thus, an additional probe capable of measuring the bulk gap is desirable. The nanocross geometry offers a unique capability to simultaneously probe all of these features of Majorana zero modes in a single device.

7.2. NANOCROSS DEVICE LAYOUT AND EXPERIMENTAL SETUP

The nanocrosses used in this chapter have been grown using the methods described in chapter 4. A scanning electron micrograph of device I is shown in figure 7.1(a). The device consists of an InSb nanocross with an epitaxial Al shell. We create normal-superconductor (NS) junctions on 3 of the 4 legs by selectively removing the Al shell with a wet chemical etch (BOE 7:1 for 10 s) and depositing Cr/Au leads. In figure 7.1(b) we show a schematic side view of such a junction, with a schematic top view of the entire device shown in figure 7.1(c). Each junction consists of a Cr/Au contact (yellow, N) to the InSb nanowire, which is partially covered by Al (green, S). The nanocross is covered by 20 nm of sputtered SiN_x dielectric (light blue) to isolate the leads from the gates (red and purple). The substrate is degenerately doped Si, which can be used as a back gate. In all experiments presented in this chapter, the back gate has been grounded.

We apply a voltage V_{Bias} to the lead connected directly to the Al shell (labeled D), and drain currents $I_{A,C}$ via contacts A and C. The local differential conductances are measured using standard lock-in techniques (see chapter 3), with the differential conductance through contact A denoted as dI_A/dV . The transparency of each junction is controlled by applying a voltage $V_{\text{TA,TC}}$ to a narrow tunnel gate (red). Finally, the density in the device region covered by the superconductor can be tuned by applying a voltage V_{SG} to a global top gate (purple). Contact B and the accompanying tunnel gate are kept at a floating potential during all experiments.

7.3. BALLISTIC NS JUNCTIONS IN NANOCROSS DEVICES

Figure 7.1(d) shows the differential conductance through contact A as a function of applied bias voltage V_{Bias} and the tunnel gate voltage V_{TA} . At high bias voltage, we see a plateau in conductance, indicative of 1D ballistic transport, with an enhancement of the conductance for small bias voltages (figure 7.1(e)). This enhancement is due to Andreev reflection, which occurs when the applied bias voltage is smaller than the superconducting gap. As shown figure 7.1(f), at low transparencies we resolve the coherence peaks of the gap at $\sim 75 \mu\text{V}$ (red line), while at high transparencies we see a conductance enhancement inside the gap (green line). Furthermore, we see additional features resembling coherence peaks at a bias voltage of $\sim 230 \mu\text{V}$, the expected induced superconducting gap in these nanowires.

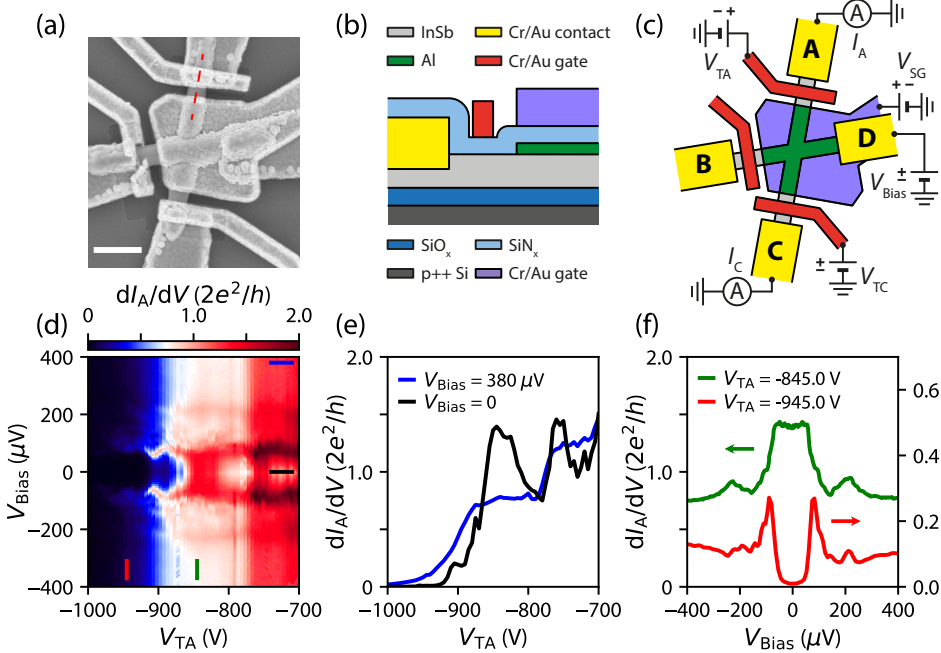


Figure 7.1: **InSb nanocross device for correlation experiments.** (a) Scanning electron micrograph of nanocross device I. Scale bar is 500 nm. (b) Schematic view along the red dashed line in (a). A NS junction is formed between the Cr/Au contact (N, yellow) and the part of the InSb nanowire covered by the Al shell (S, green). The transparency of the junction is controlled by the tunnel gate (red). (c) Schematic of the experimental set-up. The nanowire cross is contacted by four leads. A bias voltage is applied to lead D, and current is drained from leads A and C. Lead B is kept floating during all experiments. The direction of the applied magnetic field is collinear with contacts A and C unless otherwise noted. (d) Differential conductance of junction A dI_A/dV as a function of the bias voltage V_{Bias} and the tunnel gate voltage V_{TA} for $V_{\text{SG}} = 1.28 \text{ V}$. (e) Horizontal line-cuts from (d) (indicated by the black and blue bars). For $V_{\text{Bias}} > \Delta$, a quantized conductance plateau is observed (blue line). On the plateau, the conductance at zero bias is enhanced due to Andreev reflection (black line). (f) Vertical line-cuts from (d), indicated by the red and green bars, showing the conductance enhancement inside the gap for high transparency (green), as well as the conductance suppression and resolution of the superconducting density of states in the tunneling regime (red).

We can describe the transport through the junction with a two band BTK model [13]. The contribution of each band to the conductance depends on the barrier strength at the interface to the superconductor Z_n , the induced superconducting gap Δ_n , and the transparency of the normal contact \tilde{T}_n . The conductance through the junction as a function of energy is then

$$G(E) = \frac{2e^2}{h} \sum_{n=1,2} \tilde{T}_n [1 + A_n(E, Z_n, \Delta_n) - B_n(E, Z_n, \Delta_n)], \quad (7.1)$$

with A_n and B_n describing the probability of Andreev and normal reflection, respectively. For energies much larger than both superconducting gaps, the conductance through junction depends only on the normal state transmission T_n^N :

$$G_n^N = \frac{2e^2}{h} T_n^N = \frac{2e^2}{h} \frac{\tilde{T}_n}{1 + Z_n^2} = \frac{2e^2}{h} \tilde{T}_n \tilde{T}_{n,S}. \quad (7.2)$$

Additionally, the conductance at zero bias can be written as [14]

$$G_n^S = \frac{4e^2}{h} \tilde{T}_n \frac{\tilde{T}_{n,S}^2}{(2 - \tilde{T}_{n,S})^2}. \quad (7.3)$$

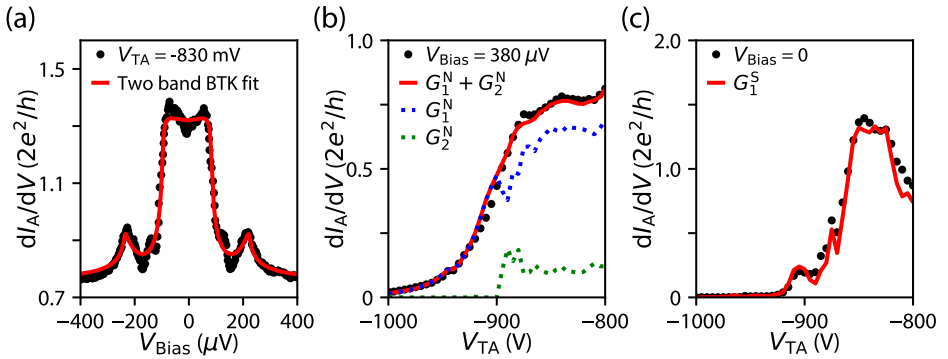


Figure 7.2: **Two band BTK fit.** (a) Differential conductance dI_A/dV for $V_{\text{TA}} = -830$ mV (black circles). Red line is a fit to equation (7.1) with $n = 2$. (b) dI_A/dV at $V_{\text{Bias}} = 380$ $\mu\text{V} > \Delta_1, \Delta_2$ (black circles). Lines show the contributions from the first (G_1^N , dashed blue line) and second (G_2^N , dashed green line) subbands, and their sum (solid red line). (c) Differential conductance at $V_{\text{Bias}} = 0$ plotted as a function of V_{TA} . Red line shows the expected conductance for the first subband, calculated using equation (7.3).

In Fig. 7.2(a), we plot the differential conductance through contact A as a function of bias voltage V_{Bias} (black circles), along with a fit to equation 7.1 (red line). The two sets of coherence peaks are related to two different modes with different transmissions and coupling to the superconductor. By fitting the conductance for different values of tunnel gate voltage V_{TA} , we see that for gate voltages below -900 mV only one mode contributes to the transport (Fig. 7.2(b)), with a gap of 75 μeV . For more positive gate voltages, a second mode starts to contribute to the transport, with a gap of 230 μeV . The transmission

remains small, however, and as such this mode does not significantly contribute to the Andreev enhancement, as can be seen in Fig. 7.2(c).

The fact that the strongest contribution to the Andreev enhancement comes from a mode with a gap that is much smaller than the expected superconducting gap indicates that we are in the long junction regime, where the Thouless energy in the junction is smaller than the superconducting gap Δ [15]. As has been described in chapter 3, wet chemical etching of the Al shell using buffered oxide etch is difficult to control, and it is not always obvious where the Al has actually been removed. We speculate that the distance between contact A and the superconductor is much larger than designed. This is also consistent with the fact that the central top gate has a strong influence on the local conductance through lead A. Interestingly, the transport still appears to be ballistic over this distance, demonstrating the high quality of the nanocrosses.

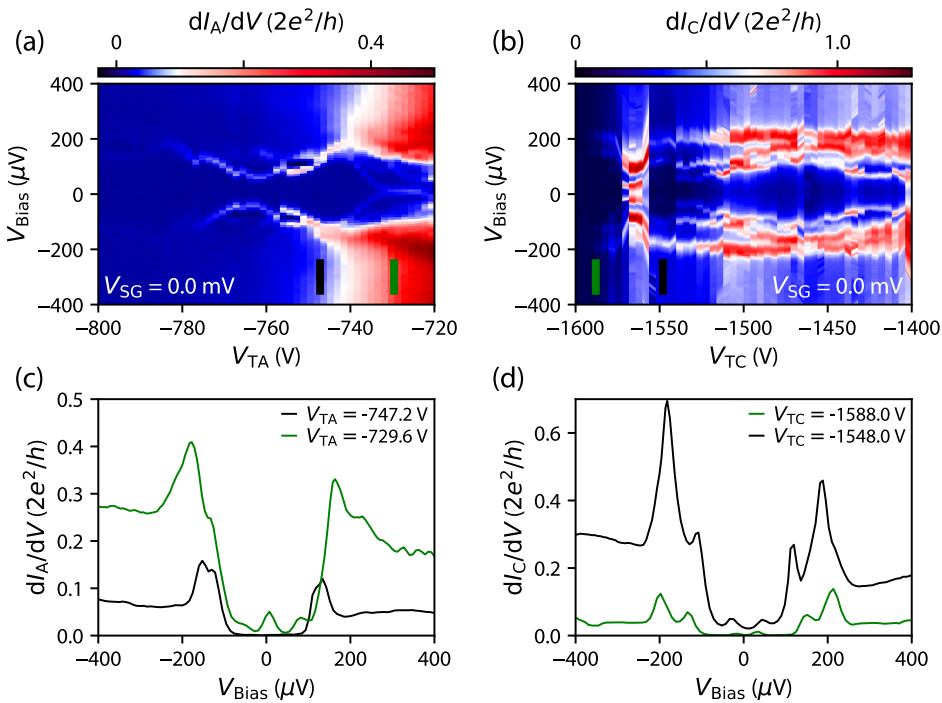


Figure 7.3: **Hard gap on both sides of the superconductor.** (a) Differential conductance of junction A dI_A/dV as a function of the bias voltage V_{Bias} and V_{TA} . Several subgap states are visible. (b) Differential conductance of junction C dI_C/dV as a function of the bias voltage V_{Bias} and V_{TC} . (c) Linecuts from (a) taken at the tunnel gate voltages indicated by the colored bars, showing a hard superconducting gap of $180 \mu\text{eV}$. (d) Linecuts from (b) taken at the tunnel gate voltages indicated by the colored bars. A hard gap is measured in both junctions simultaneously.

7.4. ZERO BIAS CONDUCTANCE PEAKS IN NANOCROSS DEVICES

In order to measure correlated zero bias conductance peaks, we require a hard gap to be present in both the A and C junctions. Figure 7.3(a) shows the differential conductance through contact A as a function of bias voltage and the voltage on tunnel gate A at $B = 0$ T. Looking at the linetraces at the gate voltages marked by the colored bars, we see a hard gap of $180 \mu\text{eV}$ (Fig. 7.3(c)). Additionally, subgap states are visible, including one that crosses zero energy. We simultaneously measure the local conductance through contact C, which is shown in Fig. 7.3(b). This junction also shows a hard gap (Fig. 7.3(d)), with a similar size to the gap measured in junction A. It is also apparent that while subgap states are visible in both junctions, these subgap states appear to be local to each junction.

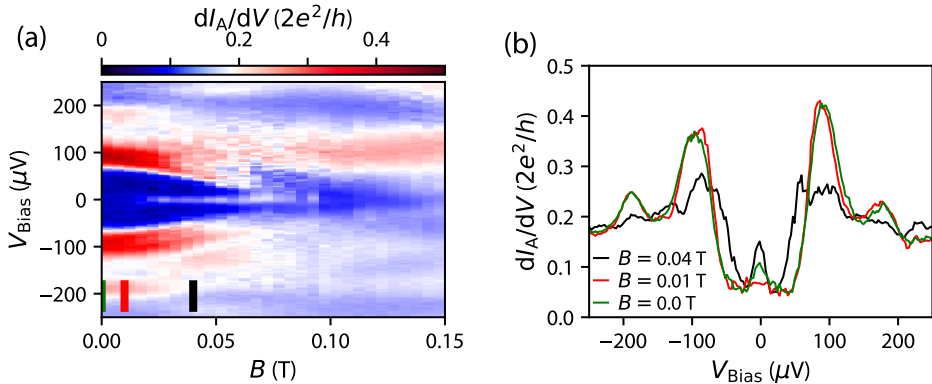


Figure 7.4: **Zero bias conductance peak in nanocross device.** (a) Differential conductance of junction A dI_A/dV as a function of the bias voltage V_{Bias} and magnetic field, showing a stable zero bias conductance peak in field. (b) Linecuts from (a) taken at the field values indicated by the colored bars. The zero bias peak appears to be present even at 0 T.

In Fig. 7.4(a) we show the differential conductance of junction A as a function of bias voltage and magnetic field, for $V_{\text{TA}} = -1193.2$ mV. For this measurement, all other junctions are completely pinched off. At $B = 0$ T, we see coherence peaks at $180 \mu\text{V}$, as well as a second set of coherence peaks around $100 \mu\text{V}$, indicating we are in the long junction regime discussed in the previous section. The gap closes around 150 mT, with a robust zero bias conductance peak visible over a range of 80 mT. Taking a closer look at the line-traces (Fig. 7.4(b)), however, we see that this zero bias peak is actually already present at zero magnetic field, with the visibility changing as the magnetic field is increased. Although it is unclear what the origin of this state is, its presence at zero magnetic field precludes it being a Majorana zero mode. It was not possible to find a regime where both the A and C junctions showed good behavior simultaneously at finite field in this device. Although sometimes clean transport signatures could be obtained (as shown in section 7.3 and Fig. 7.3), this behavior was not consistent and could be dramatically altered by charge switches. We therefore decided to pursue other devices at this point in the experiment.

Results from a different device on the same chip are shown in Fig. 7.5. We plot the differential conductance in junctions A (Fig. 7.5(a)) and C (Fig. 7.5(b)) as a function of bias voltage and magnetic field. Junction A shows a featureless hard gap with a critical field of 0.7 T. In contrast, in junction C there is a local subgap state which crosses zero energy at 0.2 T with a g -factor of 23, similar to the values found in InSb-Al nanowires. It's also apparent that junction C is affected by charge switches. In general, we were unable to find a regime where both junctions were suitable for in-depth exploration of their subgap spectrum. Because the parameter space is large, the decision to continue exploring a device or to fabricate a new one is difficult to make, as it is difficult to ascertain whether the device intrinsically has problems or if the tuning is just off.

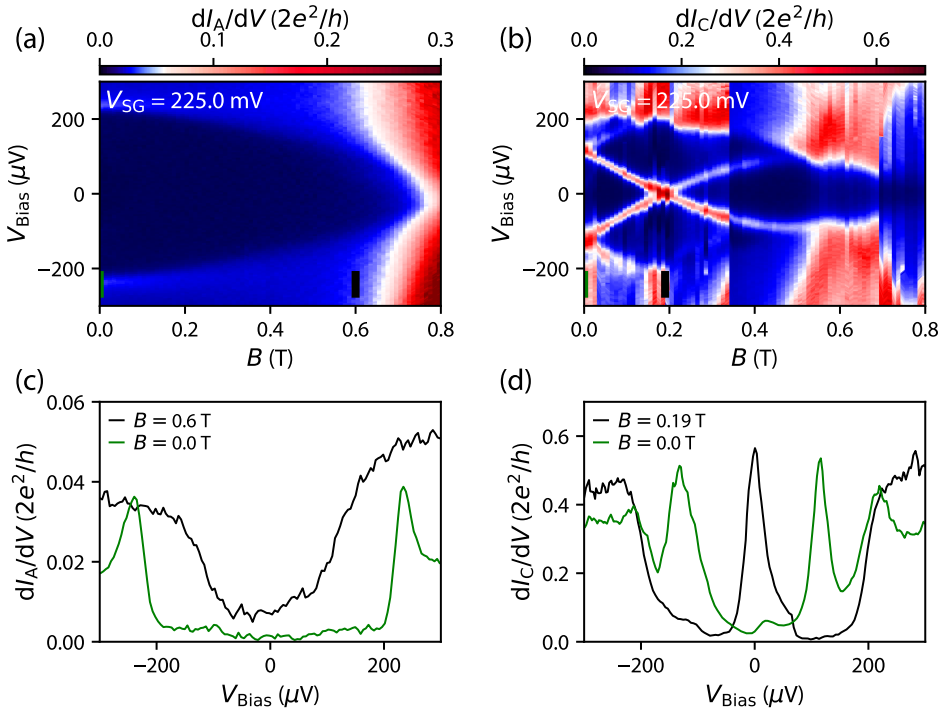


Figure 7.5: **Zero bias conductance peak in nanocross device II.** (a) Differential conductance of junction A dI_A/dV as a function of the bias voltage V_{Bias} and magnetic field, showing a hard gap up to 0.7 T. (b) Differential conductance of junction C dI_C/dV as a function of the bias voltage V_{Bias} and magnetic field, showing a subgap state crossing zero energy at 0.2 T. (c) Linecuts from (a) taken at the field values indicated by the colored bars. (d) Linecuts from (b) taken at the field values indicated by the colored bars.

7.5. DISCUSSION AND EXPERIMENTAL OUTLOOK

Although initial results seem promising, there are several important issues that limit the feasibility of performing a correlation experiment in InSb nanocrosses grown using the VLS mechanism. The yield of good individual junctions has proven to be too low to ef-

fectively make devices with three working NS-junctions. In some devices, such as device A, two junctions could sometimes be measured simultaneously with reasonably good results. However, often only a single junction was worth studying. We attribute this to the fact that the wet chemical etch to selectively remove the Al is far from optimized. Because the yield of a good etch on a single junction is low, the yield for a nanocross device with three good junctions is too small to achieve a fully functional device by chance alone.

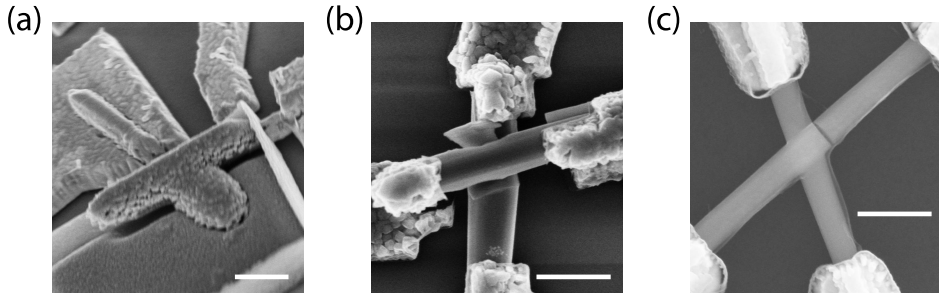


Figure 7.6: **Nanocrosses broken during fabrication.** (a) Nanocross lifted from the device substrate due to the stress in the NbTiN film deposited on it. (b) Fractured nanocross due to the stress in a 125 nm thick film of Al. (c) Fracture in a nanocross after contact deposition, compromising device operation. Scale bar in each panel is 400 nm.

7

Aside from the issues with selectively removing the Al to create the device functionality, as reported in chapter 3, the three dimensional nature of the nanocrosses significantly complicates the fabrication process. This is inherent to the method used to grow the crosses, as they will not grow into a cross if they are in a single two dimensional plane [16]. This means part of the device will be suspended over the device substrate, making it vulnerable to breaking or sudden stresses. This is illustrated in Fig. 7.6. It frequently occurs that one of the legs of the nanocross breaks off during fabrication (Fig. 7.6(c)), or that the junction between the two wires making up the cross fractures due to the stress applied during thin film deposition (Fig. 7.6(b)). Even when the cross does not break apart, these stresses can lift the cross from the substrate because the van der Waals forces are not sufficient to keep it flat (Fig. 7.6(a)).

An alternative approach is to use the selective area growth based platform discussed in chapter 5, which is planar by nature, simplifying the fabrication process. Additionally, because it is a priori known where each wire will be on the substrate, creating a shadow mask to selective deposit Al should be possible, circumventing the need for chemical etching. Because the network can be designed using lithography, multiple probes can be created along the length of the wire, possibly allowing the determination of the Majorana coherence length. This will be discussed in more detail in chapter 9.

CONTRIBUTIONS TO THE PROJECT

The nanocrosses used in this chapter were grown by S. Gazibegovic under the supervision of E. P. A. M. Bakkers at the Eindhoven University of Technology. The epitaxial Al shell was grown in the group of C. Palmstrøm at the University of California Santa Barbara. The nanocrosses were transferred to the device substrate by R. L. M. Op het Veld. The devices were fabricated and measured at Delft University of Technology. **M. W. A. de Moor**, D. Xu, and J. D. S. Bommer fabricated the devices. The measurements were performed **M. W. A. de Moor**, D. Xu, and J. D. S. Bommer, with supervision from H. Zhang. The analysis presented in this chapter was performed by **M. W. A. de Moor**. The project was supervised by H. Zhang and L. P. Kouwenhoven.

REFERENCES

- [1] V. Mourik, K. Zuo, S. M. Frolov, S. R. Plissard, E. P. A. M. Bakkers, and L. P. Kouwenhoven, *Signatures of Majorana Fermions in Hybrid Superconductor-Semiconductor Nanowire Devices*, *Science* **336**, 1003 (2012).
- [2] A. Das, Y. Ronen, Y. Most, Y. Oreg, M. Heiblum, and H. Shtrikman, *Zero-bias peaks and splitting in an Al-InAs nanowire topological superconductor as a signature of Majorana fermions*, *Nature Physics* **8**, 887 (2012).
- [3] M. T. Deng, S. Vaitiekėnas, E. B. Hansen, J. Danon, M. Leijnse, K. Flensberg, J. Nygård, P. Krogstrup, and C. M. Marcus, *Majorana bound state in a coupled quantum-dot hybrid-nanowire system*, *Science* **354**, 1557 (2016).
- [4] O. Gül, H. Zhang, J. D. S. Bommer, M. W. A. de Moor, D. Car, S. R. Plissard, E. P. A. M. Bakkers, A. Geresdi, K. Watanabe, T. Taniguchi, and L. P. Kouwenhoven, *Ballistic Majorana nanowire devices*, *Nature Nanotechnology* **13**, 192 (2018).
- [5] H. Zhang, C.-X. Liu, S. Gazibegovic, D. Xu, J. A. Logan, G. Wang, N. van Loo, J. D. S. Bommer, M. W. A. de Moor, D. Car, R. L. M. Op het Veld, P. J. van Veldhoven, S. Koelling, M. A. Verheijen, M. Pendharkar, D. J. Pennachio, B. Shojaei, J. S. Lee, C. J. Palmstrøm, E. P. A. M. Bakkers, S. Das Sarma, and L. P. Kouwenhoven, *Quantized Majorana conductance*, *Nature* **556**, 74 (2018).
- [6] E. Prada, P. San-Jose, and R. Aguado, *Transport spectroscopy of NS nanowire junctions with Majorana fermions*, *Phys. Rev. B* **86**, 180503 (2012).
- [7] G. Kells, D. Meidan, and P. W. Brouwer, *Near-zero-energy end states in topologically trivial spin-orbit coupled superconducting nanowires with a smooth confinement*, *Phys. Rev. B* **86**, 100503 (2012).
- [8] C.-X. Liu, J. D. Sau, T. D. Stanescu, and S. Das Sarma, *Andreev bound states versus Majorana bound states in quantum dot-nanowire-superconductor hybrid structures: Trivial versus topological zero-bias conductance peaks*, *Phys. Rev. B* **96**, 075161 (2017).
- [9] A. Vuik, B. Nijholt, A. R. Akhmerov, and M. Wimmer, *Reproducing topological properties with quasi-Majorana states*, (2018), arXiv:1806.02801 .

- [10] Y.-H. Lai, J. D. Sau, and S. Das Sarma, *Presence versus absence of end-to-end nonlocal conductance correlations in Majorana nanowires: Majorana bound states versus Andreev bound states*, (2019), arXiv:1901.02655 .
- [11] S. Das Sarma, J. D. Sau, and T. D. Stanescu, *Splitting of the zero-bias conductance peak as smoking gun evidence for the existence of the Majorana mode in a superconductor-semiconductor nanowire*, Phys. Rev. B **86**, 220506 (2012).
- [12] T. D. Stanescu, S. Tewari, J. D. Sau, and S. Das Sarma, *To Close or Not to Close: The Fate of the Superconducting Gap Across the Topological Quantum Phase Transition in Majorana-Carrying Semiconductor Nanowires*, Phys. Rev. Lett. **109**, 266402 (2012).
- [13] G. E. Blonder, M. Tinkham, and T. M. Klapwijk, *Transition from metallic to tunneling regimes in superconducting microconstrictions: Excess current, charge imbalance, and supercurrent conversion*, Phys. Rev. B **25**, 4515 (1982).
- [14] C. W. J. Beenakker, *Quantum transport in semiconductor-superconductor microjunctions*, Phys. Rev. B **46**, 12841 (1992).
- [15] B. L. Al'tshuler and B. Z. Spivak, *Mesoscopic fluctuations in a superconductor-normal metal-superconductor junction*, Zh. Eksp. Teor. Fiz. **92**, 609 (1987).
- [16] D. Car, J. Wang, M. A. Verheijen, E. P. A. M. Bakkers, and S. R. Plissard, *Rationally Designed Single-Crystalline Nanowire Networks*, Advanced Materials **26**, 4875 (2014).

8

BOUND STATES IN 1D MAJORANA NANOWIRES

Als ik wilde dat je het begreep, had ik het wel beter uitgelegd.

Johan Cruijff

Recently, there has been a flurry of activity focussed on understanding the theoretical consequences of spatially non-uniform parameters in Majorana nanowires. The purpose of this chapter is to give an overview of recent advances reported in the literature describing how a spatial dependence of parameters such as the chemical potential and the spin-orbit coupling near the end of a superconducting nanowire can introduce end states with features that are similar to those of Majorana zero modes. This is supplemented by numerical simulations of the low energy nanowire spectrum. All simulations in this chapter have been performed using code provided by A. Vuik.

8.1. INTRODUCTION

In section 2.4, we described the 1D Majorana nanowire model introduced by Lutchyn et al. [1] and Oreg et al. [2], which combines a semiconductor nanowire with spin-orbit coupling, superconductivity, and a magnetic field to create Majorana zero modes. These zero modes appear as bound states localized at the ends of the superconducting nanowire, which can be detected via tunneling spectroscopy [3] (see also section 2.3). In the case of a clean, uniform system, the only way to generate robust zero modes is to go through a topological phase transition. It has previously been noted that subgap states can arise due to disorder [4] or isolated impurities [5]. Even without introducing disorder, it turns out that if some parameter (e.g. the chemical potential, spin-orbit coupling, or the superconducting gap) varies slowly in space, these spatial inhomogeneities can generate bound states with energies exponentially close to zero for an extended range of parameter values [6–9]. These smooth spatial fluctuations can be caused by an external electrostatic potential, or by the local modification of the band structure due to strain [10], to name a few examples. In this chapter, we will focus on an electrostatic potential variation near one end of the superconductor nanowire. This represents the common experimental situation of an electrostatic barrier being used to probe the nanowire spectrum using tunneling spectroscopy.

8.2. EXPERIMENTAL CONTEXT AND THEORETICAL MODEL

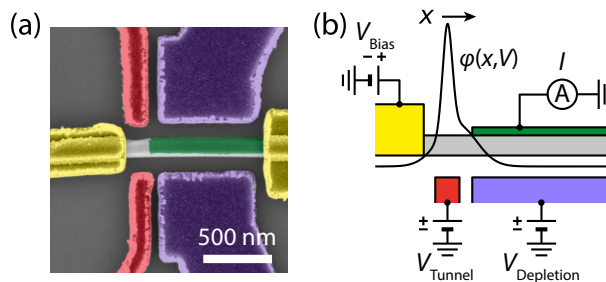


Figure 8.1: **Experimental context.** (a) False colored scanning electron micrograph of a typical N-NW-S device used in tunneling spectroscopy experiments. Electrostatic gates are shown in red (tunnel gates) and purple (depletion gate). (b) Schematic sideview of the device. Voltages are applied to the different gates, resulting in an electrostatic potential variation along the length of the nanowire, e.g. the one indicated by the black line.

The typical device used in experiments (see SEM image in Fig. 8.1(a)) consists of a semiconductor nanowire (shown in gray) partially covered by a superconducting material (shown in green), which is connected to normal metal (shown in yellow) via a NS-junction. This is schematically depicted in Fig. 8.1(b). A gate voltage V_{Tunnel} is used to change the potential in the junction region, such that a tunnel barrier is formed. This tunnel barrier then allows the spectroscopic study of the nanowire spectrum underneath the superconductor. Additional gates are used to tune device parameters, for example changing the density in the superconducting nanowire by changing $V_{\text{Depletion}}$. The combination of the various gate voltages creates an electrostatic potential along the junc-

tion.

We use the 1D Majorana nanowire model introduced in refs. [1, 2]. The nanowire is oriented in the x -direction, with a spatially varying potential along the wire. In the Nambu basis, the Hamiltonian for the superconducting part of the wire reads

$$H = \left(\frac{p_x^2}{2m^*} - \mu + V(x) \right) \tau_z - \frac{\alpha}{\hbar} p_x \sigma_y \tau_z + \Delta \tau_x + E_Z \sigma_x. \quad (8.1)$$

We have the familiar terms representing the kinetic energy $\frac{p_x^2}{2m^*}$, chemical potential μ , spin-orbit coupling α , superconducting pairing Δ , and the Zeeman energy E_Z , generated by a magnetic field along the x -direction. An important difference with the Hamiltonian introduced in section 2.4 is the inclusion of the potential $V(x)$, representing the barrier introduced at the NS-junction. In the following, we consider 3 different barriers, schematically depicted in Fig. 8.2. The NS-junction is located at x_0 . For all studied cases, the superconducting pairing Δ is constant in the S region (i.e. for $x \geq x_0$), and equal to 0 elsewhere.

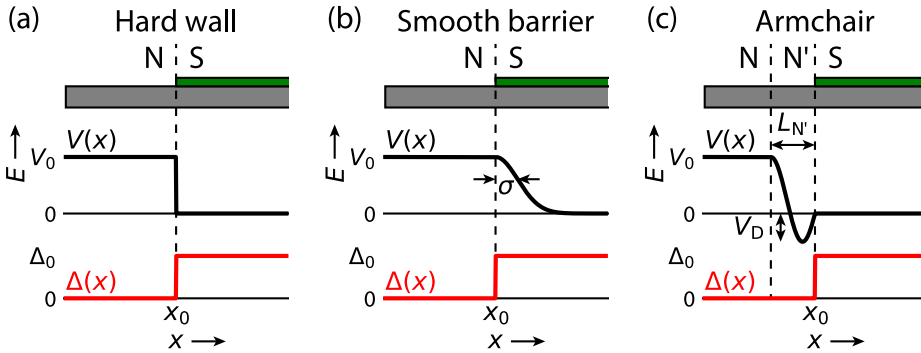


Figure 8.2: **Schematic overview of potential barriers at the NS-interface.** (a) Hard wall barrier at the interface between the normal (N, shown in gray, representing the semiconductor nanowire) and superconducting (S, shown in green, representing the superconductor) regions. The barrier potential $V(x)$ (black line) is given by equation 8.2. The superconducting pairing potential $\Delta(x)$ (red line) is constant in the S region, and 0 elsewhere. (b) Smooth barrier. Instead of a step at the NS-interface, $V(x)$ is characterized by a smooth decay into the superconducting region, parameterized by equation 8.3. (c) Armchair potential. In between the N and S regions a N' region of length $L_{N'}$ is formed, characterized by a smoothly varying $V(x)$ and a potential well of depth V_D (equation 8.4).

In the first case (Fig. 8.2(a)), the potential introduces a steep barrier at the NS-interface. This is represented by a step function,

$$V(x) = \begin{cases} V_0 & x < x_0 \\ 0 & x \geq x_0 \end{cases}, \quad (8.2)$$

where $V_0 \gg \mu$. We will call this the hard wall scenario. This is equivalent to the case of a finite wire (or at least, semi-infinite) without any additional potentials added. The spec-

trum of these wires has been studied extensively (see e.g. refs. [1, 2, 11–15]). This scenario is mostly added here as contrast to the other cases. Another possibility is depicted in Fig. 8.2(b). This is the smooth barrier scenario, where the potential smoothly decays into the superconducting region over a length parameterized by σ . We use a Gaussian decay to describe this type of potential:

$$V(x) = \begin{cases} V_0 & x < x_0 \\ V_0 e^{-\frac{(x-x_0)^2}{2\sigma^2}} & x \geq x_0 \end{cases}. \quad (8.3)$$

The potential gradient has important consequences for the nanowire spectrum (see refs. [6, 16]). Finally, we allow for the formation of a normal region between the potential barrier and the superconductor, labelled N' in Fig. 8.2(c). Additionally, a potential well can be created in this region, which localizes low energy excitations near the barrier. This can be seen as a type of quantum dot (albeit without charging energy), with a length $L_{N'}$, and a well depth V_D . This is the armchair scenario, which we parameterize with the potential

$$V(x) = \begin{cases} V_0 & x < (x_0 - L_{N'}) \\ \frac{V_0 - V_D}{2} + \frac{V_0 + V_D}{2} \cos(\pi \tilde{k}(x - x_0 + L_{N'})) & (x_0 - L_{N'}) \leq x < x_0 \\ 0 & x \geq x_0 \end{cases}, \quad (8.4)$$

with $\tilde{k} = \frac{1}{\pi L_{N'}} \left(2\pi - \arccos\left(\frac{V_D - V_0}{V_D + V_0}\right) \right)$. An interesting feature of this type of potential is the possibility of subgap states even at $E_Z = 0$ (see also refs. [7, 8, 17]).

The superconducting part of the wire has a length L_{SC} . In each case, the wire is terminated at the other end (located at $x_0 + L_{SC}$), effectively created an infinitely high barrier on that side. We discretize the Hamiltonian using the Kwant [18] package, and diagonalize it to obtain the nanowire spectrum. Additional details on the numerical procedures can be found in ref. [16]. In the following sections we will show how the potential barrier affects the nanowire spectrum, and how it alters the states in the wire, particularly near the NS-junction.

8

8.3. HARD WALL BARRIER

In Fig. 8.3(a) we schematically show the hard wall potential considered in our simulation, along with the simulation parameters. The spectrum of the nanowire system as a function of the Zeeman energy is plotted in Fig. 8.3(b) for $\mu = 0$. The lowest energy state (highlighted in purple) starts at the gap edge, with its energy linearly decreasing until the gap closes at $E_{Z,\text{crit}} = \sqrt{\Delta^2 + \mu^2} = |\Delta|$. After the reopening of the gap, a Majorana zero mode is present in the system, signaling the topological phase transition.

Just as fermionic creation and annihilation operators can be written as linear combinations of Majorana operators [19], we can decompose the lowest energy state $\psi_+(E)$ and its particle hole symmetric partner $\psi_-(-E)$ into two Majorana components, $\psi_{1,2}$. Rearranging the terms gives

$$\psi_1 = e^{i\phi} \psi_+ + e^{-i\phi} \psi_-, \quad (8.5)$$

$$\psi_2 = i e^{i\phi} \psi_+ - i e^{-i\phi} \psi_-. \quad (8.6)$$

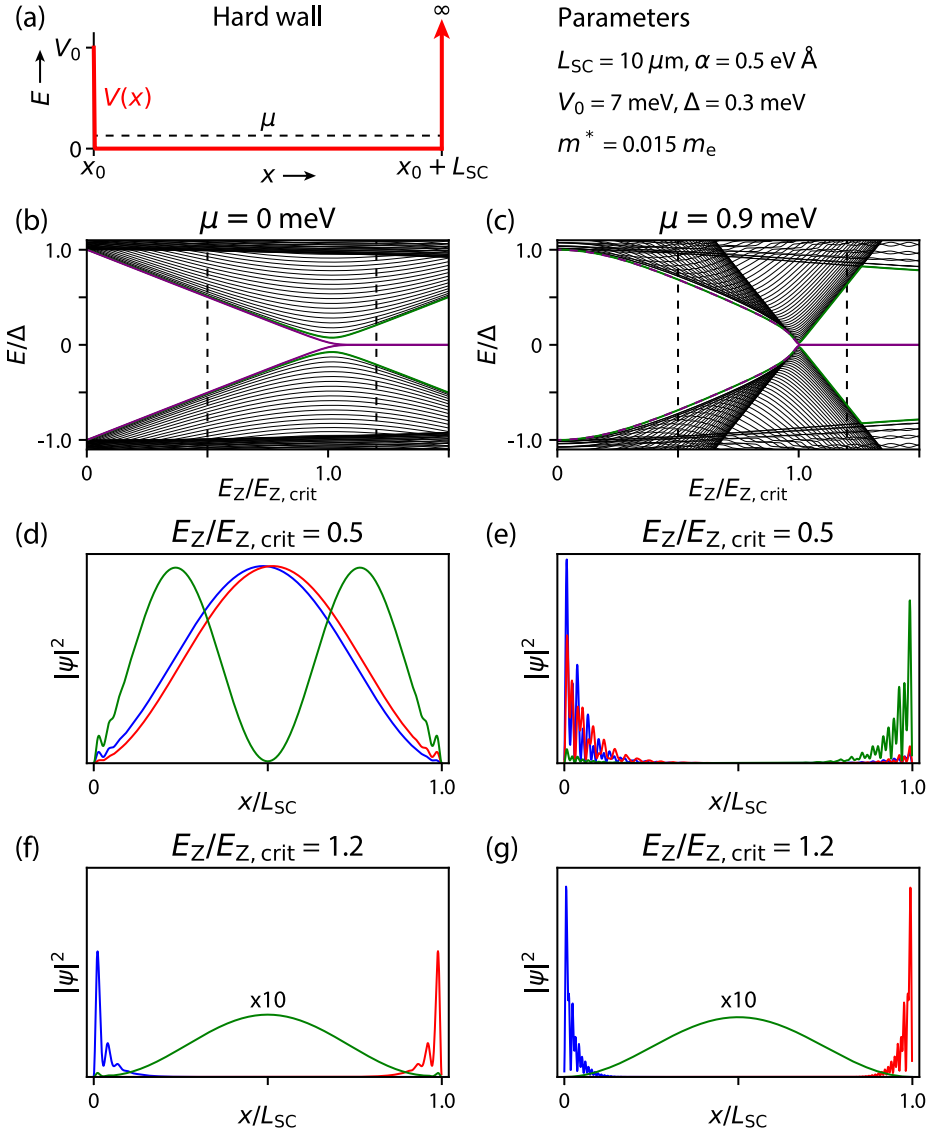


Figure 8.3: **Bound states with hard wall confinement.** (a) Schematic representation of the hard wall potential $V(x)$ (red line) used in the simulation. Other relevant simulation parameters are listed on the right. (b,c) Spectrum for $\mu = 0$ and $\mu = 0.9 \text{ meV}$, respectively. The lowest energy state is highlighted in purple, while the next lowest energy state is highlighted in green. (d) Wave functions of the two lowest energy states in (b) for $E_Z/E_{Z, \text{crit}} = 0.5$ (indicated by a dashed line in (b)), with the lowest energy state wave function decomposed into two Majorana components (red and blue), and the second lowest energy state wave function in green. (e) Wave functions of the two lowest energy states in (c) for $E_Z/E_{Z, \text{crit}} = 0.5$. The lowest energy state is a degenerate bound state localized near the end of the wire, with its partner localized at the opposite wire end. (f,g) Wave functions of the two lowest energy states in the topological regime ($E_Z/E_{Z, \text{crit}} = 1.2$, indicated by a dashed line in (b)) in panels (b) and (c), respectively. The lowest energy state consists of two Majorana components each localized to one end of the wire (red and blue). The next lowest energy state (green) has most of its weight at the center of wire. The wave function amplitude of the bulk state has been multiplied by 10 for clarity.

The phase ϕ is chosen such that $\langle \psi_1 | \sigma_x | \psi_2 \rangle$ is minimized, resulting in Majorana components with opposite spin character. When we look at the Majorana components of the lowest energy state (red and blue), we find that they are mainly localized in the bulk of the nanowire when the system is in the trivial phase (Fig. 8.3(d)), while in the topological phase, the two Majoranas are localized at opposite ends of the wire (Fig. 8.3(f)). In either case, the second lowest energy state (shown in green) is mainly located in the bulk.

For finite chemical potential, the dispersion of the lowest energy state is no longer linear in E_Z due to the spin-orbit coupling, as shown in Fig. 8.3(c). The transition to the topological phase still occurs at $E_{Z,\text{crit}} = \sqrt{\Delta^2 + \mu^2}$. The wave functions of the two lowest energy states in the topological regime (Fig. 8.3(f)) are similar to those for $\mu = 0$: the lowest energy state consists of two Majorana states localized at opposite wire ends, and the second lowest energy state is located in the bulk. However, the two lowest energy states in the trivial phase are now two degenerate bound states localized at opposite ends of the wire¹ (Fig. 8.3(e)). This type of bound state is generically present at finite chemical potential and Zeeman energy in finite (or semi-infinite) wires described by the model of refs. [1, 2], disappearing when the system enters the helical regime [15]. At $\mu = 0$, even an infinitesimally small Zeeman energy induces the helical state, explaining the absence of the bound state in that case. Because these states are localized near the end of the wire, they contribute strongly to the conductance, showing up as bright gap closing features in experiments (see e.g. Fig. 6.3). This is in contrast to the bulk gap closing, which is expected to be very faint due to the wave function vanishing near the end of the wire [20].

8.4. SMOOTH BARRIER CONFINEMENT

Instead of a hard wall barrier at x_0 , we now add a spatially dependent potential given by equation 8.3. The gradient of the potential is determined by the parameter σ , with larger σ giving a smoother potential profile. We schematically show the potential in Figure 8.3(a), along with a list of the parameters used in the simulation. The resulting spectrum for $\sigma = 50$ nm is plotted in Fig. 8.4(b). The asymmetry between the two wire ends lifts the degeneracy of the bound states localized at opposite sides (Fig. 8.4(d)). The state localized near the barrier (highlighted in purple in Fig. 8.4(b)) has a lower energy, which is still significant on the scale of the superconducting gap. In the topological regime (Fig. 8.4(f)), the lowest energy state is again composed of two Majorana states localized at opposite wire ends, similar to the hard wall scenario.

The question now is what happens if we make σ larger, decreasing the gradient of the potential. Figure 8.4(c) shows the nanowire spectrum for $\sigma = 250$ nm. Qualitatively the spectrum is similar to the one shown in (b): there are two states separated from the continuum, which are similar to the two bound states from the hard wall scenario. As shown

¹A small degree of asymmetry between the two ends is required to separate the bound states. If the system is mirror symmetric with respect to the x -axis, both bound state wave functions will be localized at both ends of the wire simultaneously. This symmetry is broken by applying a finite potential $V_0 > \mu$ at the left end of the wire, while the right end is simply terminated, which is equivalent to an infinitely sharp, infinitely high barrier.

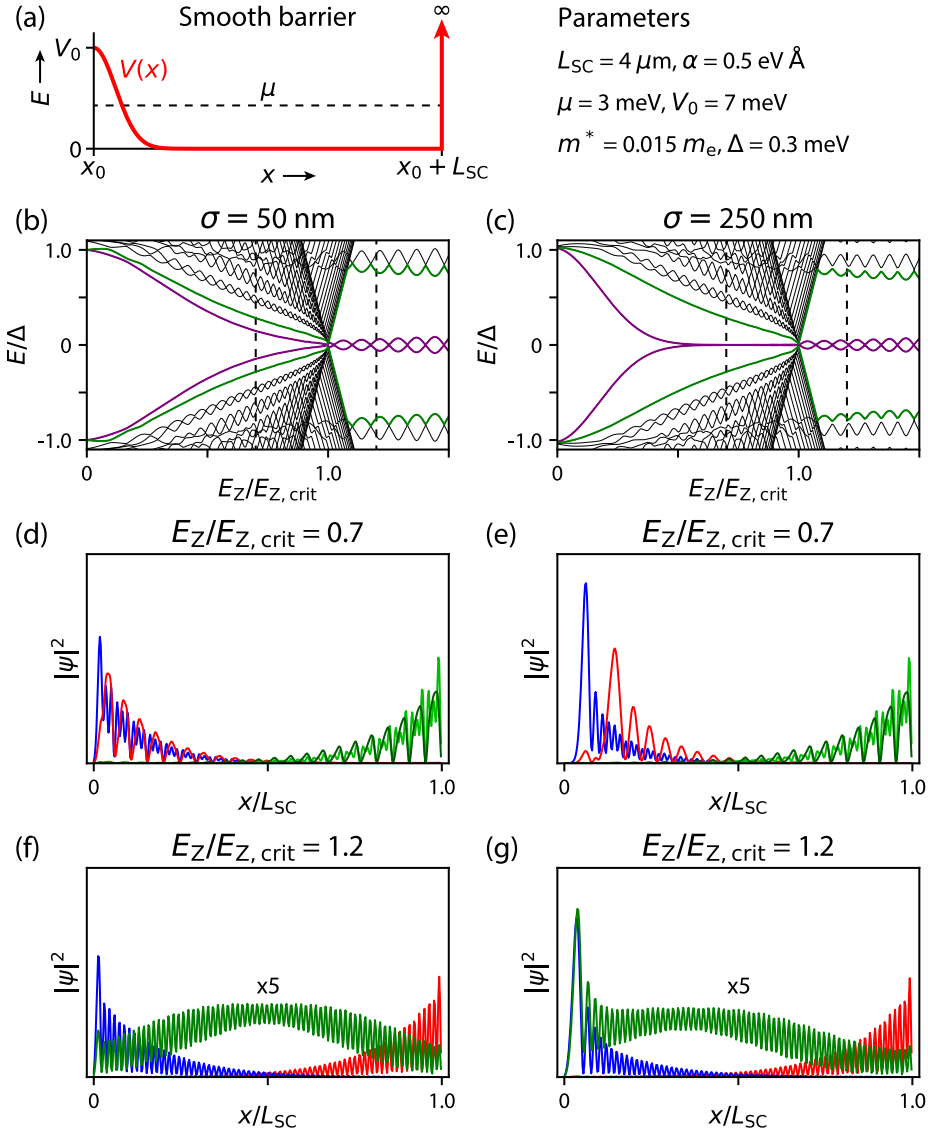


Figure 8.4: **Smooth barrier at the NS-junction.** (a) Schematic representation of the smooth barrier potential $V(x)$ (red line) used in the simulation. Other relevant simulation parameters are listed on the right. (b,c) Spectrum for $\sigma = 50 \text{ nm}$ and $\sigma = 250 \text{ nm}$, respectively. The lowest energy state is highlighted in purple, while the next lowest energy state is highlighted in green. (d) Wave functions of the two lowest energy states in (b) for $E_Z/E_{Z, \text{crit}} = 0.7$, decomposed into their Majorana components (red and blue for the lowest energy state, light green and dark green for the next lowest energy state). (e) Wave functions of the two lowest energy states in (c) for $E_Z/E_{Z, \text{crit}} = 0.7$. The lowest energy state is a bound state localized at the smooth barrier, while the second lowest energy state is localized at the opposite end. (f) Wave functions of the two lowest energy states in (b) in the topological regime. (g) Wave functions of the two lowest energy states in (c) in the topological regime. The wave function amplitude of the bulk states has been multiplied by 5 for clarity.

in Fig. 8.4(e), these two states are localized at opposite ends of the nanowire, and both consist of two Majorana components. An important difference is the fact that now there is a significant range in Zeeman energy where the lowest energy in the system is exponentially close to 0, without having the system go through a topological phase transition. We also observe that the main peaks of the two Majorana components in Fig. 8.4(e) are now separated in space [21]. Once the system enters the topological phase, we recover the familiar situation of two Majorana modes localized at opposite wire ends (Fig. 8.4(g)).

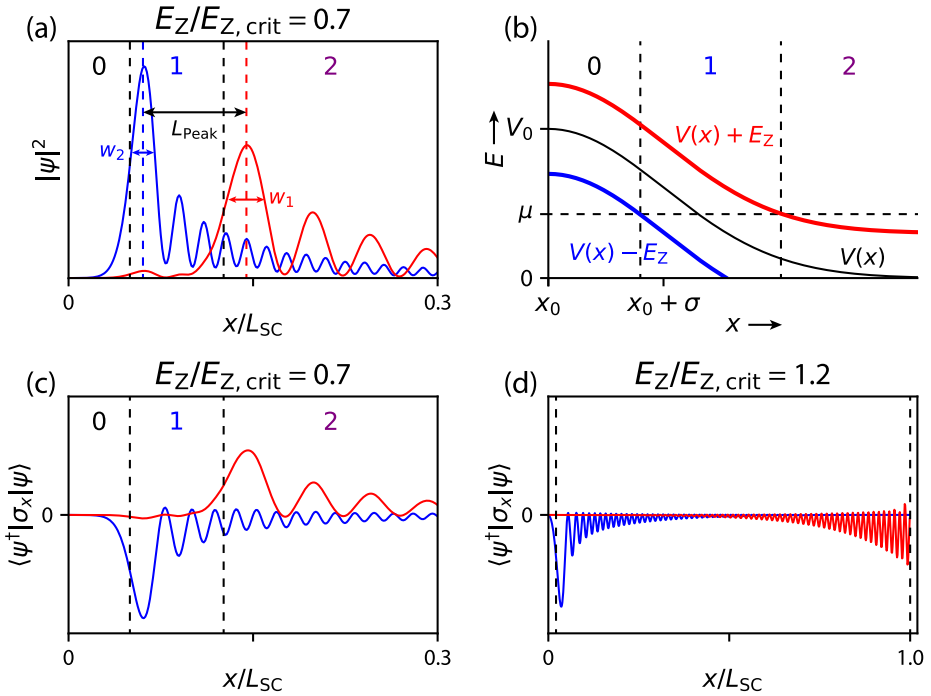


Figure 8.5: **Bound state spin structure.** (a) Close-up of the Majorana components (red and blue) of the near zero energy bound state in Fig. 8.4(e). The locations of the two main lobes are highlighted by the blue and red dashed lines. They have widths $w_{1,2}$, and are separated by a distance L_{Peak} . The black dashed lines indicate the boundaries between regions with different number of spin channels. (b) Schematic representation of the spin-split barrier due to finite Zeeman energy, creating regions with 0 (barrier), 1 (local topological superconductor), and 2 (trivial superconductor) occupied spin bands. (c) Spin densities of the two Majorana components in (a), showing the spatially separated Majorana components have opposite spin. (d) Spin densities of the two Majorana components from Fig. 8.4(g), showing they originate from the same spin channel.

In Fig. 8.5(a) we show a close-up of the Majorana components plotted in Fig. 8.4(e). The main peaks of the two components are separated over a distance L_{Peak} . As the Zeeman energy is increased, L_{Peak} increases as well, with the growth rate becoming larger when the slope of $V(x)$ is smaller. We can understand this spatial separation by examining the spin structure of the nanowire states. Calculating the spin densities for the two Majorana components of Fig. 8.5(a), plotted in Fig. 8.5(c), we see that the components

originate from different spin bands.

For $\Delta < E_Z < E_{Z,\text{crit}}$, we can view the superconducting nanowire as consisting of two independent 1D spinless channels with p-wave superconducting correlations [6]. In the homogeneous case, both channels have Majorana zero modes localized at the wire ends, where they are coupled and split off to finite energy [22], resulting in the bound states of section 8.3. Once $E_Z \geq E_{Z,\text{crit}}$, one of the channels is fully depleted, and we are left with a single channel with robust zero modes originating from a single spin channel, as illustrated in Fig. 8.5(d).

In the case of the smooth barrier, this depletion is no longer uniform. Provided $V(x)$ is monotonic and $V_0 > \mu$, there exists a classical turning point where the effective chemical potential $\mu_{\text{eff}} = \mu - V(x) = 0$ (see Fig. 8.5(b)). For $E_Z < \Delta$, this divides the wire into a region with two occupied spin bands ($\mu_{\text{eff}} > 0$, region 2), and a fully depleted region ($\mu_{\text{eff}} < 0$, region 0). Once E_Z exceeds Δ , locally the condition $E_Z \geq \sqrt{\Delta^2 + \mu_{\text{eff}}^2}$ can be satisfied. This introduces a third region with only one occupied spin band (region 1). The spatial separation of the two Majorana components is the result of the depletion of the spin up band in region 1.

Because this region is characterized by a single occupied spin channel with induced superconductivity, this could be labelled a “local topological phase”, with a Majorana zero mode localized at the boundary between regions 0 and 1. The other Majorana zero mode leaks out into region 2, extending to the right end of the wire located at $x_0 + LSC$. There it couples to the Majorana zero mode from the other spin channel, resulting in the state highlighted in green in Fig. 8.4(c). The two Majorana components localized at the boundaries of the local topological phase remain decoupled, however, resulting in a state with near zero energy, which we will refer to as a local Majorana zero mode. In general the energy of this local zero mode is determined by α , μ , and Δ [9], as well as the smoothness of the barrier as parameterized by σ .

We illustrate this point by plotting the lowest energy in the system as a function of E_Z for different values σ (Fig. 8.6). As σ is increased the range of E_Z over which the local zero mode can be observed increases. We also see that once $E_Z > E_{Z,\text{crit}}$ (indicated by the dashed black line), the energy is no longer affected by σ , apart from a change in the finite size oscillations originating from the fact that a larger σ effectively makes the wire a little bit shorter. In Fig. 8.6(b) we plot the energy of the local zero mode for different values of α and Δ . An increase in Δ increases the bound state energy before the phase transition (black dashed line), while it decreases the energy of the non-local Majorana zero modes after the phase transition has occurred. In the case of Majorana modes localized at opposite ends of the wire, increasing Δ decreases their overlap because the coherence length becomes shorter. Similarly, increasing α decreases the energy because the topological gap is larger. Before the topological phase transition, increasing Δ or α actually increases the energy of the local zero mode.

It has been argued that the spatial separation of the two Majorana components is re-

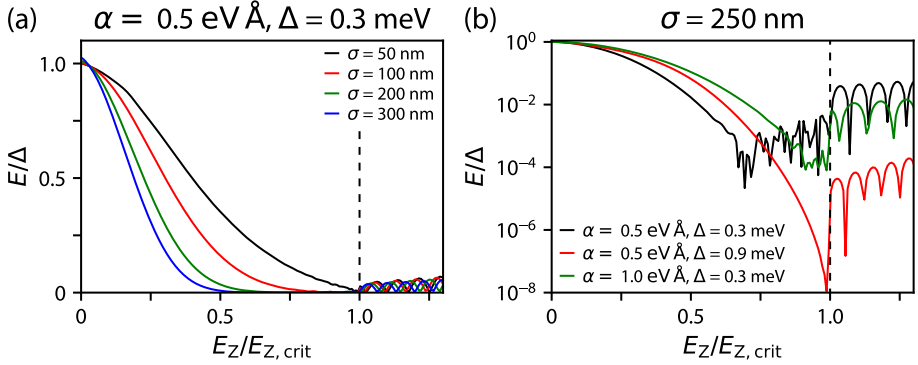


Figure 8.6: **Local Majorana zero mode energy.** (a) Local Majorana zero mode energy as a function of E_Z for different values of σ . Increasing σ decreases the energy of the local zero mode, and increases the range in E_Z over which it can be observed. (b) Energy of the local Majorana zero mode for different values of the spin-orbit strength and superconducting gap. All other parameters are the same as the ones in Fig. 8.4.

sponsible for the near zero energy of the bound state [21, 23, 24]. In this scenario, once the distance between the peaks L_{peak} becomes large enough compared to the peak widths $w_{1,2}$, set by π/k_F for weak ($E_Z \gg m^* \alpha^2/\hbar^2$) or π/k_{SO} for strong ($E_Z \ll m^* \alpha^2/\hbar^2$) spin-orbit interaction [22], the energy of the bound state collapses to 0. The smoothness of the potential serves only to create the spatial separation [24].

We investigate this claim by calculating the spectrum for a hard wall barrier, but including a section near the barrier with a lower chemical potential. This is schematically depicted in Fig. 8.7(a). Increasing the Zeeman energy will deplete one spin band in this section before the entire system goes through the topological phase transition, which will result in a spatial separation of the two Majorana components making of the lowest energy state in the system. Indeed, in Fig. 8.7(b) we see that the two Majorana components are spatially separated, and originate from different spin bands (Fig. 8.7(d)). However, from the calculated spectrum it is clear that the energy of the bound state is always a substantial fraction of the superconducting gap, despite the clear separation of the component wave functions.

This is because the decoupling of the two Majorana components in the smooth barrier scenario is not a consequence of the separation in real space, but rather of the separation in spin and momentum space. Near the barrier, the effect of spin-orbit interaction vanishes because k_F locally goes to zero, in contrast to the hard wall case, where the spin-orbit interaction remains finite in the entire system [6]. If in addition $E_Z > \Delta$, the Majorana components originating from the two spin bands become almost orthogonal near the barrier. Residual coupling is provided by the superconducting and spin-orbit terms in the Hamiltonian, which is why increasing Δ or α increases the energy of the local zero mode. The Majorana components composing this local zero mode originate from bands that not only have different spin, but also very different Fermi momenta. At a sharp barrier, these different momenta can be coupled effectively, because the Fourier

transform of a sharp barrier in real space has an algebraic dependence on momentum. In contrast, the Fourier transform of the Gaussian barrier used in this section is another Gaussian, which becomes narrower in momentum space as the smoothness parameter σ is increased. Thus, it is the smoothness of the barrier which is essential to decouple the two bands near the end and create a near zero energy state. This is further demonstrated by the analytical results of ref. [6]. For very high μ , the spatial separation is negligible, but a bound state with an exponentially suppressed energy can still be generated as long as the spin-orbit coupling smoothly vanishes. The spatial separation is merely a by-product of the smooth barrier, not the driving mechanism for the creation of a near zero energy state.

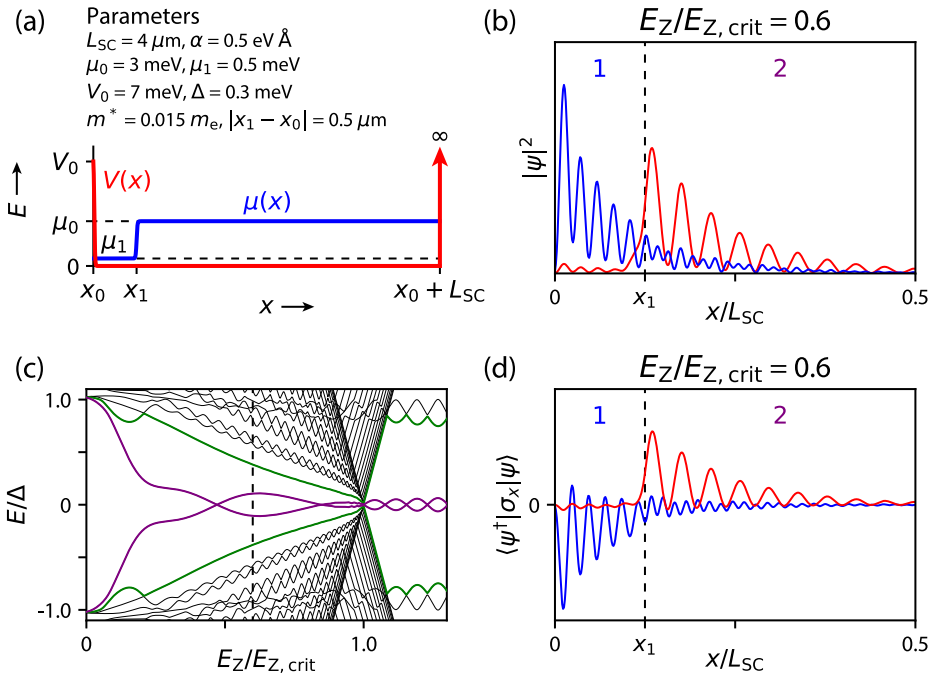


Figure 8.7: **Local bound state energy for sharp chemical potential step.** (a) Schematic representation of the set-up used in the simulation. A hard wall potential $V(x)$ (red line) is combined with a step in the chemical potential given by $\mu(x)$ (blue line). Relevant simulation parameters are listed on the top. (b) Majorana components of the lowest energy state for $E_Z/E_{Z, \text{crit}} = 0.6$, showing a clear spatial separation. (c) Spectrum calculated for the set-up in (a), with the lowest energy state highlighted in purple. Before the topological phase transition, the bound state energy is always significant on the scale of the gap. (d) Spin densities of the two Majorana components in (b), showing they indeed originate from different spin bands.

8.5. COUPLING TO LEAD THROUGH THE BARRIER

A feature of the topological Majorana zero mode is the fact that the conductance through the bound state is quantized at $2e^2/h$ at $T = 0$ [25, 26]. One might expect that as there is

no particular reason for the conductance through a local zero mode to be quantized, this distinction could be used to discriminate between the two types of zero energy bound states. However, it has been demonstrated that also for local zero modes due to smooth confinement, conductance plateaus quantized at $2e^2/h$ can be realized [16, 27].

The quantization is the result of a sign change in the reflection block of the scattering matrix [28], allowing only perfect Andreev reflection at zero bias when the superconducting nanowire is in the topological regime. It has been demonstrated, however, that the topology of the scattering matrix connecting the system to a reservoir can be non-trivial even if the system itself remains trivial [29, 30]. Coupling to system to a lead makes the Hamiltonian non-Hermitian, and can generate exceptional points where the real part of the eigenenergy (the energy level in the system) goes to zero while the imaginary part (the coupling to the reservoir) goes through a bifurcation [31]. This bifurcation results in strongly asymmetric couplings of the two Majorana components to the lead [32]. It has been proposed that this asymmetry can be utilized to probe the non-locality of the Majorana zero mode through a local measurement by coupling it to a quantum dot [33, 34].

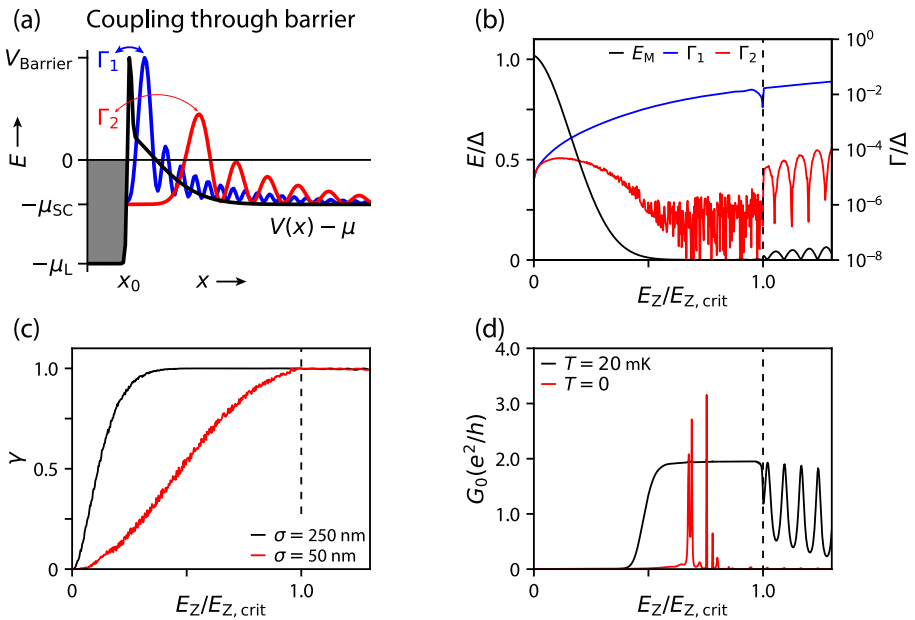


Figure 8.8: **Coupling to the lead through a smooth barrier.** (a) Schematic representation of the coupling of the two Majorana components of the lowest energy state through the effective barrier (black line) to a lead. The lead modes are represented by the shaded gray area. The two Majorana components (in blue and red) couple to the leads with coupling strengths $\Gamma_{1,2}$. (b) Couplings $\Gamma_{1,2}$ of the two Majorana components (in blue and red lines) as a function of Zeeman energy, plotted together with the energy of the lowest energy state E_M (black line). (c) Plot of the locality parameter γ as a function of E_Z for a steep ($\sigma = 50$ nm) and smooth ($\sigma = 250$ nm) barrier. (d) Calculated conductance at $V = 0$. At $T = 0$, the conductance is either 0 or shows a sharp spike to a value between 0 and $4e^2/h$. For $T = 20$ mK, the conductance shows a plateau near $2e^2/h$ before $E_Z = E_{Z,\text{crit}}$.

We couple the system to a lead, as schematically depicted in Fig. 8.8(a). The parameters of the superconducting nanowire system are the same as those used in Fig. 8.4(c). In order to create a good tunnel probe, we add a sharp, high barrier to mediate the coupling to the modes in the lead, with parameters $V_{\text{Barrier}} = 12$ meV and $\mu_L = 7$ meV. This ensures that both spin channels will be weakly coupled to the lead for the whole Zeeman energy range of interest.

The coupling of the local zero mode Majorana components to the modes in the lead is calculated using the Mahaux-Weidenmüller formula, following the approach of ref. [16]. The resulting couplings $\Gamma_{1,2}$ are plotted in Fig. 8.8(b). For $E_Z = 0$, the couplings are equal. As the Zeeman energy increases, the couplings become asymmetric, with Γ_1 more than four orders of magnitude larger than Γ_2 when the bound state energy E_M reaches zero. We also note that the asymmetry is larger for the local zero mode than in the topological regime. Introducing the coupling asymmetry parameter $\gamma = (\Gamma_1 - \Gamma_2)/(\Gamma_1 + \Gamma_2)$, we see that for the smooth potential γ reaches 1 well before the topological phase transition (Fig. 8.8(c), black line), while for a steep potential it remains smaller than 1 until the transition (Fig. 8.8(c), red line). While it has been argued that $\gamma = 1$ is a hallmark of the spatial non-locality of the Majorana zero modes [33, 34], we find that γ can also reach 1 when spatial separation is not a requirement. This suggests one can not use the coupling asymmetry as a proxy for spatial non-locality.

We also calculate the conductance at zero bias G_0 . At $T = 0$ K, it has been found that depending on the relative scales of Γ_1 , Γ_2 , and E_M , the conductance can show a sharp dip to 0, or a peak to $4e^2/h$, or something in between [7, 8, 16]. The width of this feature is set by Γ_2 , which we have shown is exponentially suppressed in the case of smooth barrier induced local zero modes. Therefore, it is likely impossible to detect in experiments. To illustrate this, we plot G_0 as a function of E_Z in Fig. 8.8(d). For $T = 0$ (red line), we find that G_0 is highly erratic. However, when we include broadening due to finite temperature with a temperature of 20 mK, we find a quantized plateau at a value very close to $2e^2/h$ (black line) for a large range of Zeeman energy. We therefore conclude that a local conductance measurement can not be used to distinguish between local zero modes and non-local Majorana zero modes. To truly distinguish the two, different experiments, such as those including non-local conductance signals, must be performed.

8.6. ARMCHAIR BARRIER

In the case of the armchair potential with a short normal region N' between the barrier and the superconducting nanowire, it is possible to generate subgap states even without a magnetic field, something which is commonly observed in experiments (see e.g. Fig. 6.5). Figure 8.9(a) schematically shows the potential landscape. The normal region has an additional potential well of depth V_D , which can localize bound states in the N' region under the right resonance conditions. In Fig. 8.9(b) we show the spectrum of the nanowire as a function of Zeeman energy for a short normal section ($L_{N'} = 200$ nm). The lowest energy bound state is localized in the N' region (see Fig. 8.9(d)), while the next lowest energy state is a bound state at the opposite end of the wire, similar to Fig. 8.4(d).

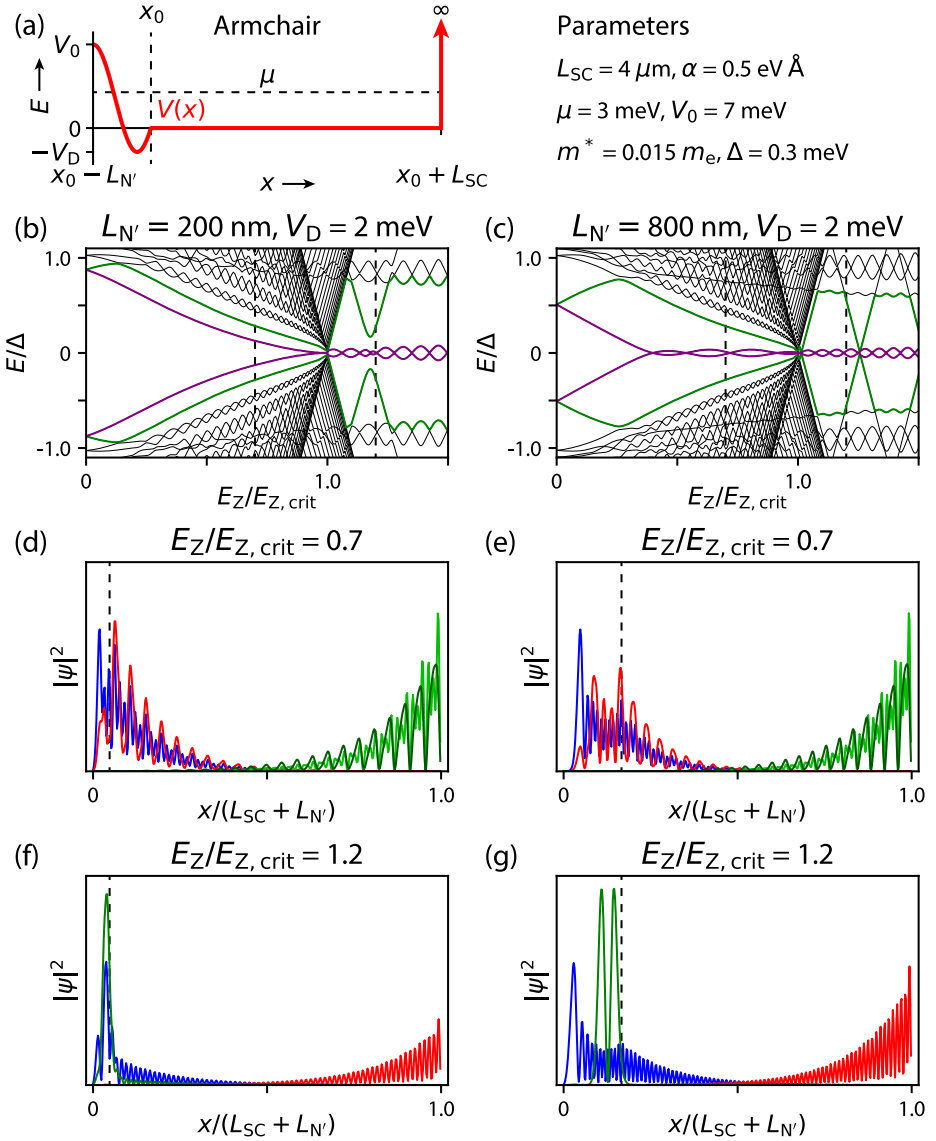


Figure 8.9: **Armchair potential with a normal section before the barrier.** (a) Schematic representation of the armchair potential $V(x)$ (red line) used in the simulation. Other relevant simulation parameters are listed on the right. (b) Nanowire spectrum as a function of E_Z for $L_{N'} = 200 \text{ nm}$ and $V_D = 2 \text{ meV}$. (c) Nanowire spectrum as a function of E_Z for $L_{N'} = 800 \text{ nm}$ and $V_D = 2 \text{ meV}$. As E_Z is increased, the energy of the subgap state comes closer to 0. (d) Wave functions of the two lowest energy states in (b) for $E_Z/E_{Z, \text{crit}} = 0.7$, decomposed into their Majorana components (red and blue for the lowest energy state, light green and dark green for the next lowest energy state). The dashed line indicates the extent of the N' region. (e) Wave functions of the two lowest energy states in (c) for $E_Z/E_{Z, \text{crit}} = 0.7$. The lowest energy state is localized in the normal region, with its Majorana components localized at opposite ends of N' . (f) Wave functions of the two lowest energy states in (a) in the topological regime. (g) Wave functions of the two lowest energy states in (c) in the topological regime.

Once the system goes through the phase transition, the familiar situation of the topological regime is recovered (Fig. 8.9(f)), albeit with additional resonances entirely localized in the N' region.

For longer N' regions, the energy of the subgap state at $E_Z = 0$ is further decreased (Fig. 8.9(c)). At sufficiently large Zeeman energy, the bound state energy nears 0. In Fig. 8.9(e) it is demonstrated that the two Majorana components of this bound state are localized at opposite ends of the N' region. Again, in the topological regime we recover the same situation as for the short N' region (Fig. 8.9(g)).

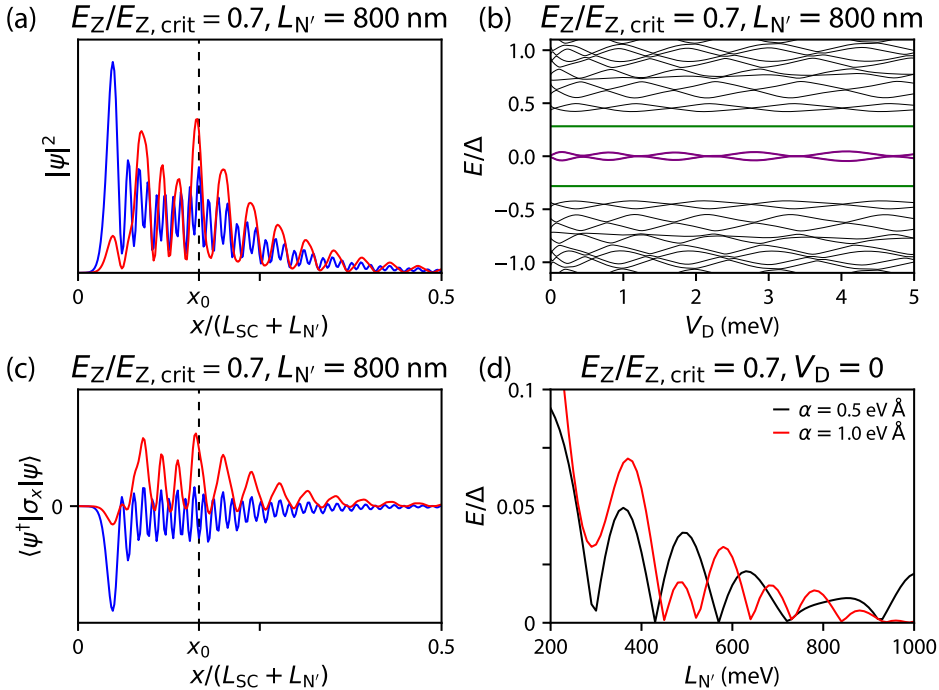


Figure 8.10: **Resonance condition in normal region.** (a) Close-up of the Majorana components (red and blue) of the near zero energy bound state in Fig. 8.9(e). (b) Spectrum of the nanowire as a function of well potential depth V_D . The energy of the lowest energy state (purple) oscillates with the well depth, while the energy of the bound state at the opposite end (green) is completely unaffected. (c) Spin densities of the two Majorana components in (a). In contrast to the smooth barrier case, there is no spatial separation between Majorana components from different spin channels. (d) Energy of the lowest energy state as a function of $L_{N'}$, showing oscillations with a period that depends on the spin-orbit strength.

One might expect that resonances in the N' region would sensitively depend on the region size N' or the well potential V_D , enabling one to distinguish them in experiments by changing the gate voltage V_{Tunnel} . However, this is not always the case, as we demonstrate in Fig. 8.10. The Majorana components of the lowest energy bound state are localized in the N' region, but in this case both spin bands are present (Fig. 8.10(c)). While the

energy of the bound state does oscillate with V_D , the amplitude of the oscillation is relatively small. As such, for the right parameters, the energy of the bound state can become almost insensitive to the well potential [8]. The oscillation amplitude and period can be changed by changing the length $L_{N'}$, or the spin-orbit strength α (Fig. 8.10(d)). This is further corroborated by an analytical model of a normal wire section proximity coupled to a superconductor, where it was found that the energy of the bound state goes to zero at finely tuned resonances depending only on $L_{N'}$ and α , with an amplitude that is exponentially suppressed in the Zeeman energy [17]². As the armchair scenario involves precise resonance conditions rather than exponential decoupling, it is distinct from the smooth barrier case. Additionally, it can be relatively easily identified in experimental data by the presence of subgap states at zero magnetic field.

8.7. CONCLUSION

In this chapter, we have investigated the effect of spatially non-uniform potentials on the spectrum of superconducting nanowires with Rashba spin-orbit coupling. While the only way to have a zero energy bound state in superconducting nanowires with uniform parameters is to drive the system through a topological phase transition, we have demonstrated that both in the case of smooth potential barriers or armchair potentials, near zero energy bound states can be found in the trivial phase, which are impossible to distinguish from topological Majorana zero modes using only local probes.

The model used in this chapter is a single band, strictly 1D model. It is not clear whether all of the conclusions drawn based on this model can be easily generalized to more realistic models, including multiband physics [35], orbital effects of magnetic field [36], self-consistent potentials based on Schrödinger-Poisson simulations [37–39], or the effect of a magnetic field on the bulk superconducting gap. In particular, interband transverse spin-orbit coupling is expected to be an effective way to couple two local Majorana states, as is the orbital effect of magnetic field. It has also been demonstrated that self-consistently calculated potentials have a non-trivial dependence on magnetic field, rather than the simple linear spin splitting found in this chapter [40].

The parameters values used in this chapter are derived from InSb nanowires with epitaxial Al as a superconductor. The typical nanowire length is 1 μm (see also chapter 6), while the simulations in this chapter have been performed using wires of 4 μm . Additionally, the typical junction length in experiments is 50–100 nm, while the smooth barriers in this chapter generally extend for several hundred nanometers. It is important to realize that these length scales depend on the effective mass, which has been taken to be the bulk InSb effective mass of $0.015m_e$. As has been demonstrated in chapter 6, the effective parameters in the semiconductor nanowire are strongly renormalized by the presence of the superconductor. If the effective mass is increased by a factor of 4, the parameters used in this chapter's simulations would be much closer to those of the experiment.

²This case is similar to the spin-orbit induced level repulsion described in section 6.6.

As the schemes for measurement-based topological quantum computation rely on locally coupling to a single Majorana zero mode [41, 42], the local zero modes studied in this chapter could be used in the same way [16]. There are two important differences when comparing the situation with topological Majorana zero modes to the one with only local zero modes. The first one is the fact that the energy of the bound state has a different dependence on the various control parameters, changing the susceptibility to environmental noise [43]. Because the states are local in space, there is also no way to increase noise resilience by increasing the system size. The second important difference is the fact that there are now guaranteed to be additional Majorana zero modes on the qubit island which can capture or release quasi-particles during operation. As long as the global parity of the island remains fixed and the dark zero modes do not couple to the zero modes used in operations, it seems like this should not be a problem. However, additional research is needed before this question can be definitively answered.

REFERENCES

- [1] R. M. Lutchyn, J. D. Sau, and S. Das Sarma, *Majorana Fermions and a Topological Phase Transition in Semiconductor-Superconductor Heterostructures*, Phys. Rev. Lett. **105**, 077001 (2010).
- [2] Y. Oreg, G. Refael, and F. von Oppen, *Helical Liquids and Majorana Bound States in Quantum Wires*, Phys. Rev. Lett. **105**, 177002 (2010).
- [3] T. D. Stanescu, R. M. Lutchyn, and S. Das Sarma, *Majorana fermions in semiconductor nanowires*, Phys. Rev. B **84**, 144522 (2011).
- [4] D. I. Pikulin, J. P. Dahlhaus, M. Wimmer, H. Schomerus, and C. W. J. Beenakker, *A zero-voltage conductance peak from weak antilocalization in a Majorana nanowire*, New Journal of Physics **14**, 125011 (2012).
- [5] D. E. Liu, E. Rossi, and R. M. Lutchyn, *Impurity-induced states in superconducting heterostructures*, Phys. Rev. B **97**, 161408 (2018).
- [6] G. Kells, D. Meidan, and P. W. Brouwer, *Near-zero-energy end states in topologically trivial spin-orbit coupled superconducting nanowires with a smooth confinement*, Phys. Rev. B **86**, 100503 (2012).
- [7] E. Prada, P. San-Jose, and R. Aguado, *Transport spectroscopy of NS nanowire junctions with Majorana fermions*, Phys. Rev. B **86**, 180503 (2012).
- [8] C.-X. Liu, J. D. Sau, T. D. Stanescu, and S. Das Sarma, *Andreev bound states versus Majorana bound states in quantum dot-nanowire-superconductor hybrid structures: Trivial versus topological zero-bias conductance peaks*, Phys. Rev. B **96**, 075161 (2017).
- [9] C. Fleckenstein, F. Domínguez, N. Traverso Ziani, and B. Trauzettel, *Decaying spectral oscillations in a Majorana wire with finite coherence length*, Phys. Rev. B **97**, 155425 (2018).

- [10] Y. Zhang, Z.-X. Xie, X. Yu, H.-B. Wang, Y.-X. Deng, and F. Ning, *First-principles study of size-, surface- and mechanical strain-dependent electronic properties of wurtzite and zinc-blende InSb nanowires*, Physics Letters A **380**, 2678 (2016).
- [11] S. Tewari, T. D. Stanescu, J. D. Sau, and S. Das Sarma, *Topologically non-trivial superconductivity in spin-orbit coupled systems: bulk phases and quantum phase transitions*, New Journal of Physics **13**, 065004 (2011).
- [12] J. D. Sau, S. Tewari, and S. Das Sarma, *Experimental and materials considerations for the topological superconducting state in electron- and hole-doped semiconductors: Searching for non-Abelian Majorana modes in 1D nanowires and 2D heterostructures*, Phys. Rev. B **85**, 064512 (2012).
- [13] T. D. Stanescu, R. M. Lutchyn, and S. Das Sarma, *Dimensional crossover in spin-orbit-coupled semiconductor nanowires with induced superconducting pairing*, Phys. Rev. B **87**, 094518 (2013).
- [14] R. V. Mishmash, D. Aasen, A. P. Higginbotham, and J. Alicea, *Approaching a topological phase transition in Majorana nanowires*, Phys. Rev. B **93**, 245404 (2016).
- [15] Y. Huang, H. Pan, C.-X. Liu, J. D. Sau, T. D. Stanescu, and S. Das Sarma, *Metamorphosis of Andreev bound states into Majorana bound states in pristine nanowires*, Phys. Rev. B **98**, 144511 (2018).
- [16] A. Vuik, B. Nijholt, A. R. Akhmerov, and M. Wimmer, *Reproducing topological properties with quasi-Majorana states*, (2018), arXiv:1806.02801 .
- [17] C. Reeg, O. Dmytruk, D. Chevallier, D. Loss, and J. Klinovaja, *Zero-energy Andreev bound states from quantum dots in proximitized Rashba nanowires*, Phys. Rev. B **98**, 245407 (2018).
- [18] C. W. Groth, M. Wimmer, A. R. Akhmerov, and X. Waintal, *Kwant: a software package for quantum transport*, New Journal of Physics **16**, 063065 (2014).
- [19] A. Y. Kitaev, *Unpaired majorana fermions in quantum wires*, Physics-Uspekhi **44**, 131 (2001).
- [20] T. D. Stanescu, S. Tewari, J. D. Sau, and S. Das Sarma, *To Close or Not to Close: The Fate of the Superconducting Gap Across the Topological Quantum Phase Transition in Majorana-Carrying Semiconductor Nanowires*, Phys. Rev. Lett. **109**, 266402 (2012).
- [21] C. Moore, T. D. Stanescu, and S. Tewari, *Two-terminal charge tunneling: Disentangling Majorana zero modes from partially separated Andreev bound states in semiconductor-superconductor heterostructures*, Phys. Rev. B **97**, 165302 (2018).
- [22] J. Klinovaja and D. Loss, *Composite Majorana fermion wave functions in nanowires*, Phys. Rev. B **86**, 085408 (2012).

- [23] F. Peñaranda, R. Aguado, P. San-Jose, and E. Prada, *Quantifying wave-function overlaps in inhomogeneous Majorana nanowires*, Phys. Rev. B **98**, 235406 (2018).
- [24] T. D. Stanescu and S. Tewari, *Illustrated guide to robust low-energy Andreev bound states in semiconductor-superconductor heterostructures: Importance of partial separation of component Majorana bound states*, (2018), arXiv:1811.02557 .
- [25] K. T. Law, P. A. Lee, and T. K. Ng, *Majorana Fermion Induced Resonant Andreev Reflection*, Phys. Rev. Lett. **103**, 237001 (2009).
- [26] K. Flensberg, *Tunneling characteristics of a chain of Majorana bound states*, Phys. Rev. B **82**, 180516 (2010).
- [27] C. Moore, C. Zeng, T. D. Stanescu, and S. Tewari, *Quantized zero-bias conductance plateau in semiconductor-superconductor heterostructures without topological Majorana zero modes*, Phys. Rev. B **98**, 155314 (2018).
- [28] M. Wimmer, A. R. Akhmerov, J. P. Dahlhaus, and C. W. J. Beenakker, *Quantum point contact as a probe of a topological superconductor*, New Journal of Physics **13**, 053016 (2011).
- [29] D. I. Pikulin and Y. V. Nazarov, *Topological properties of superconducting junctions*, JETP Letters **94**, 693 (2012).
- [30] D. I. Pikulin and Y. V. Nazarov, *Two types of topological transitions in finite Majorana wires*, Phys. Rev. B **87**, 235421 (2013).
- [31] P. San-Jose, J. Cayao, E. Prada, and R. Aguado, *Majorana bound states from exceptional points in non-topological superconductors*, Scientific Reports **6**, 21427 (2016).
- [32] J. Avila, F. Peñaranda, E. Prada, P. San-Jose, and R. Aguado, *Non-Hermitian topology: a unifying framework for the andreev for majoranas states controversy*, (2018), arXiv:1807.04677 .
- [33] E. Prada, R. Aguado, and P. San-Jose, *Measuring Majorana nonlocality and spin structure with a quantum dot*, Phys. Rev. B **96**, 085418 (2017).
- [34] D. J. Clarke, *Experimentally accessible topological quality factor for wires with zero energy modes*, Phys. Rev. B **96**, 201109 (2017).
- [35] S. Tewari, T. D. Stanescu, J. D. Sau, and S. Das Sarma, *Topological minigap in quasi-one-dimensional spin-orbit-coupled semiconductor Majorana wires*, Phys. Rev. B **86**, 024504 (2012).
- [36] B. Nijholt and A. R. Akhmerov, *Orbital effect of magnetic field on the Majorana phase diagram*, Phys. Rev. B **93**, 235434 (2016).
- [37] A. Vuik, D. Eeltink, A. R. Akhmerov, and M. Wimmer, *Effects of the electrostatic environment on the Majorana nanowire devices*, New Journal of Physics **18**, 033013 (2016).

- [38] A. E. Antipov, A. Bargerbos, G. W. Winkler, B. Bauer, E. Rossi, and R. M. Lutchyn, *Effects of Gate-Induced Electric Fields on Semiconductor Majorana Nanowires*, Phys. Rev. X **8**, 031041 (2018).
- [39] A. E. G. Mikkelsen, P. Kotetes, P. Krogstrup, and K. Flensberg, *Hybridization at Superconductor-Semiconductor Interfaces*, Phys. Rev. X **8**, 031040 (2018).
- [40] J. Kammhuber, M. C. Cassidy, F. Pei, M. P. Nowak, A. Vuik, O. Gül, D. Car, S. R. Plissard, E. P. A. M. Bakkers, M. Wimmer, and L. P. Kouwenhoven, *Conductance through a helical state in an Indium antimonide nanowire*, Nature Communications **8**, 478 (2017).
- [41] S. Plugge, A. Rasmussen, R. Egger, and K. Flensberg, *Majorana box qubits*, New Journal of Physics **19**, 012001 (2017).
- [42] T. Karzig, C. Knapp, R. M. Lutchyn, P. Bonderson, M. B. Hastings, C. Nayak, J. Alicea, K. Flensberg, S. Plugge, Y. Oreg, C. M. Marcus, and M. H. Freedman, *Scalable designs for quasiparticle-poisoning-protected topological quantum computation with Majorana zero modes*, Phys. Rev. B **95**, 235305 (2017).
- [43] C. Knapp, T. Karzig, R. M. Lutchyn, and C. Nayak, *Dephasing of Majorana-based qubits*, Phys. Rev. B **97**, 125404 (2018).

9

CONCLUSION AND OUTLOOK

The future will be better tomorrow.

Dan Quayle

In this chapter, we first briefly summarize the conclusions of each chapter in this thesis. Based on the results obtained during the completion of this work, we highlight possible improvements and new directions for experiments. Finally, we comment on the realization of proposed topological qubits based on semiconductor nanowire networks.

9.1. CONCLUSIONS

In chapter 4, we have reported on the transport properties of InSb semiconductor nanowire networks grown by the vapor-liquid-solid (VLS) method. We have demonstrated phase-coherent transport in these networks by measuring the Aharonov-Bohm effect in the magnetoconductance, and have extracted the phase coherence length by fitting the exponential decay of the Aharonov-Bohm oscillation amplitude with increasing temperature. Additionally, superconductivity has been induced by growing a thin layer of Al onto the InSb nanowire, resulting in a hard superconducting gap in magnetic fields up to 1 T.

While the networks studied in chapter 4 have promising properties for Majorana experiments, the connectivity required to create qubits is difficult to achieve using the VLS method. In Chapter 5 we have described measurements of the magnetoconductance in InSb semiconductor nanowire networks grown by selective area growth (SAG). Because the nanowire network is defined lithographically, different shapes and connectivities can be implemented in a straightforward fashion. We have described in detail the analysis of the Aharonov-Bohm effect in these networks, as well as how the temperature dependence can be exploited to study dephasing mechanisms.

In chapter 6, we have investigated the effects of the electrostatic environment on various parameters of the effective theory used to describe Majorana zero modes in semiconductor nanowires. We have demonstrated that the coupling between the InSb semiconductor nanowire and the Al superconductor can be altered by applying an electric field, which in turn changes the induced superconducting gap, the effective g -factor, and the spin-orbit coupling strength.

Chapter 7 describes initial experiments on InSb nanocrosses with a thin aluminum shell aimed at demonstrating Majorana correlations. We have demonstrated ballistic transport in NS-junctions obtained by locally removing the aluminum shell by wet chemical etching. Although a zero bias conductance peak has been found, its origin is most likely not a Majorana zero mode. Further investigations have been hampered by the low yield of the wet chemical etch, combined with difficulties in fabrication stemming from the three dimensional nature of the nanowire crosses.

We have conducted tight binding simulations to investigate the effect of spatial inhomogeneity in the 1D Majorana nanowire model in Chapter 8. We have found that smooth potential profiles, such as those generated by an electrostatic gate, can give rise to bound states with near zero energy. These bound states, termed local zero modes, cannot be easily distinguished from Majorana zero modes by local conductance experiments. Additionally, we have shown that the Majorana components constituting the local zero mode are separated in spin-momentum space rather than in real space.

9.2. MATERIALS AND FABRICATION IMPROVEMENTS

In this section, we discuss possible improvements to the devices used in the experiments described in this thesis. These improvements can broadly be categorized in two directions: improved fabrication and handling techniques to preserve a pristine superconductor-semiconductor interface in InSb nanowires with epitaxial Al, and improvements in growth methods to create nanowire networks with high quality.

Al tends to diffuse into InSb over time, as discussed in chapter 3, which leads to a degradation of the induced superconductivity. Since this process is thermally activated, it is crucial to keep the temperature as low as possible during device processing. This means that several processes that could be useful to improve device quality, e.g. atomic layer deposition (ALD) to create high quality gate dielectrics, cannot be used after the InSb-Al nanowires have been deposited onto the chip. A better understanding of the diffusion process would help us determine which processes and processing temperatures are acceptable for device fabrication using these nanowires. For example, by in situ monitoring of the Al-InSb interface in a TEM while the nanowire is being heated, we can study how quickly the Al atoms diffuse into the wire at a given temperature.

The lack of suitably selective chemical etchants to locally remove the Al shell from the nanowire also acts as a handicap during device fabrication. While a workaround using additional nanowires to act as a deposition mask has been demonstrated in chapter 4, this method is not scalable to more complex networks. The BOE recipe described in section 3.3 occasionally creates high quality junctions, but the yield and precision are too low to be used when multiple junctions are required (chapter 7). One approach to improving the etching quality is to use an etchant which is selective for AlO_x rather than for Al itself, such as 40% HF. By repeatedly removing the native oxide locally and then reoxidizing the Al film, the film thickness can gradually be reduced in steps of 2-3 nm at a time. As the Al film thickness is generally on the order of 10 nm, this procedure only requires 4-5 repetitions to remove the whole film. A remaining question is whether this etching method will result in the required precision and yield.

Alternatively, the SAG platform can be exploited in combination with an external shadow mask. Because the positions of the nanowires on the chip are predetermined, another chip with predefined holes can be used to shadow the nanowire chip during Al deposition. The alignment between the two chips would have to be extremely precise, however, especially for the more complex structures required by qubit proposals. An alternative is to use additional semiconductor structures close to target nanowire network to selectively block the Al flux when the Al is deposited under the right angle, similar to how the VLS wires block the flux to a small part of the wire behind them. It is unclear at this point if this can be achieved without interfering with the growth, however.

An important issue with the growth of InSb SAG is the lack of closely lattice matched substrates. Unlike nanowires grown via the VLS mechanism, where the nanowires are able to relax strain because they are free standing in space, the SAG nanowires are epitaxially connected to the substrate along their entire length. When growing on InP (111)B

substrates, this leads to a dislocation rich layer between the InSb nanowire and the underlying substrate [1]. It is possible that this layer is responsible for the diffusive nature of the transport reported in chapter 5.

It should be possible to overcome the lattice mismatch problem by including a buffer material, which slowly interpolates between the lattice constant of the substrate and the nanowire crystal to allow for elastic strain relaxation (i.e., without dislocations). This has been shown to be an effective way to improve the device performance of InAs SAG nanowires [2]. For InSb, a possible buffer material is $\text{In}_{1-x}\text{Al}_x\text{Sb}$ (x around 0.08), which has already been used as a buffer layer for dislocation free InSb quantum wells [3, 4]. This buffer can also be used to incorporate a highly doped layer which can act as a global back gate, which allows better control over the coupling between the nanowire and the superconductor on top of it.

9.3. MAJORANA EXPERIMENTS IN NANOWIRE NETWORKS

Most Majorana signatures reported to date have been based on local conductance measurements of the tunneling density of states. While these experiments give valuable information, we have seen in chapter 8 that it is unlikely that local tunneling measurements will resolve the debate as to whether zero bias peaks can be considered sufficient evidence of the presence of a topological phase. Extensions of this approach have been proposed as ways to discriminate between Majorana zero modes and other local zero energy excitations, for example by using spin resolved measurements [5]. It has also been suggested that the non-local character of the Majorana wave function can be probed by coupling the superconducting nanowire to a quantum dot at one of its ends [6–8]. Similar behavior is expected for local zero modes, however [9], making it questionable whether such an experiment can be used to distinguish between local and non-local states.

As the non-local nature of the Majorana state is crucial to its appeal as a building block for a topological quantum computer, it is imperative that this property is demonstrated in an experiment. One way to do so would be to measure the correlations between the two Majorana zero modes which should exist at opposite ends of the superconductor. In Fig. 9.1(a) we schematically draw a nanowire device designed for this purpose. We ignore the leads (yellow) labeled A, B, and C for now, and focus on a three terminal geometry consisting of leads L and R, and the grounded superconductor (green). The transparencies of the left and right junctions are controlled by the voltages V_{TL} and V_{TR} applied to the tunnel gates (red), respectively. For non-local Majorana zero modes, a conductance peak at zero bias should appear in the local conductances $\frac{dI_L}{dV_L}$ and $\frac{dI_R}{dV_R}$ at the same values of the magnetic field B and back gate voltage [10]. If the length of the superconductor is not too large compared to the decay length of the Majorana wave function, finite size induced splitting of the zero bias peaks is expected [11]. For correlated Majorana modes, the splitting as a function of control parameters such as the magnetic field should be the same in both local conductances. Additionally, in the regime of a relatively short super-

conductor the closing and reopening of the bulk gap should be visible in the non-local conductances $\frac{dI_R}{dV_L}$ and $\frac{dI_L}{dV_R}$ [12].

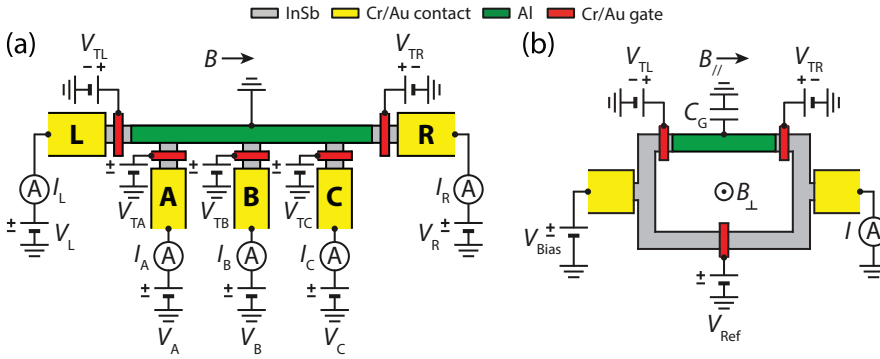


Figure 9.1: **Majorana experiments in nanowire networks.** (a) Nanowire based device to measure Majorana correlations. Two leads (L and R) are used to probe Majorana zero modes at the ends of a grounded superconductor (shown in green), which is brought into a topological phase by applying a magnetic field along the nanowire and an appropriate back gate voltage (back gate not shown). Local tunnel probes along the superconductor (A, B, and C) are used to measure the decay length of the Majoranas. (b) Nanowire network based interferometer consisting of a superconducting island (in green) capacitively coupled to ground, and a reference arm. Various tunnel gates (red) are used to control the device, as well as a global back gate (not shown). When the island is in the topological phase, the conductance as a function of the magnetic field through the loop B_{\perp} can be used to detect the parity of the Majorana bound state.

While this experiment can be performed using a single nanowire, using a nanowire network has several advantages. As described in chapter 7, the nanowire network can be used to ground the superconductor without the need for invasive fabrication procedure which can damage the active region of the device. Additionally, using a nanowire network allows one to connect additional tunnel probes along the length of the superconducting nanowire, which can be used to measure the local density of states (leads labeled A, B, and C in Fig. 9.1(a)). This way, the closing and reopening of the bulk gap can be resolved, as well as the coherence length of the Majorana zero modes. Such an experiment has already been reported [13]. However, the tunnel probes used in this implementation are likely too invasive, generating additional subgap states near the probe itself, obscuring the Majorana physics [14]. This is also a concern for the additional junctions introduced by branching the network. If the confinement in the radial direction of the nanowire changes significantly at the junction, this can lead to low energy subgap states [15]. As we have seen in chapter 6, however, using a suitable back gate voltage should ensure that the confinement in the radial direction is determined by the electrostatic potential along the entire length of the wire, with minimal variation in the junction area.

An alternative approach uses interferometry experiments similar to those performed in chapters 4 and 5, which leverage the nanowire network platform to do experiments which cannot be performed in single wire geometries. Figure 9.1(b) shows a schematic

of a nanowire network based interferometer consisting of two arms. A superconducting island (green) is embedded in one of the arms. It is capacitively coupled to ground with a capacitance C_G , which sets the charging energy E_C . The transmission through the island is controlled using tunnel gates (red). The other arm of the interferometer is used as a reference, with its transmission controlled by the gate voltage V_{Ref} . A magnetic field B_{\parallel} is applied along the direction of the island to create Majorana zero modes at its ends. The conductance $\frac{dI}{dV_{\text{Bias}}}$ is then measured as a function of the perpendicular magnetic field B_{\perp} .

As long as the charging energy is smaller than the superconducting gap, and the length of the superconductor is significantly longer than the coherence length (typically a few hundred nm for thin Al films), single electron tunneling through the island is greatly suppressed in the trivial phase, and there is no interference between the paths through the reference arm and the island [16]. When Majorana zero modes are present, however, an electron can tunnel through the island via a teleportation process [17, 18]. This leads to an Aharonov-Bohm effect, modulating the conductance with a period of h/e . Moreover, the phase of this oscillation depends on the parity of the island through the occupation of the Majorana zero mode, visible as a π phase shift in the conductance when the occupation of the Majorana zero mode changes from even to odd.

It should be noted that this effect is also present if a normal quantum dot is embedded in such an interferometer [19]. This is an example of a common problem in proposals which purport to have found an experiment which demonstrates the presence of Majorana zero modes: while it is the case that if the island has a hard superconducting gap and no trivial subgap states, the only way to achieve an h/e periodic conductance signal, which shifts by π when the parity of the island changes, is by the presence of Majorana zero modes, the reverse logic does not hold. That is, if we have an h/e periodic conductance signal in such an experiment which shifts by π when the parity of the island is changed, there are multiple plausible ways in which this signal could arise in our experiment, only one of which involves Majorana zero modes. Although one might be able to tell these scenarios apart by careful quantitative investigation [16], this is also not straightforward because one invariably needs to rely on numerical calculations, which have many parameters that are not known from the experiment. For this reason, while interferometric experiments appear better suited to leverage the capabilities of nanowire networks directly, the proposed experiments seem less likely to settle the debate on whether Majorana zero modes can be detected than the correlation based experiments.

A final remark on the most suitable material platform is in order. Using the VLS growth technique, it is non-trivial to grow the type of networks depicted in Fig. 9.1. The resulting networks are also suboptimal for other reasons, described in chapter 7. The SAG growth platform seems the ideal choice to grow such networks, because of its design flexibility. This is contingent on the improvement of the underlying material quality.

9.4. PERSPECTIVE ON QUBIT PROPOSALS

The ultimate goal for creating and characterizing nanowire networks is to use them as the basis for topological qubits. We have seen that the VLS growth technique, although it has achieved remarkable results in terms of nanowire quality, is likely insufficient to achieve the required connectivity in networks. Nanowire networks based on selective area growth are naturally scalable to the proposed qubit architectures [20–23]. In such proposals several general assumptions are made which should be discussed to assess their feasibility. First of all, it is generally assumed that the overlap between non-local Majorana zero modes can be made arbitrarily small by increasing the system size relative to the coherence length. Second, it is assumed that the parity of the superconducting island hosting the Majorana zero modes can be controlled by giving the superconducting island a finite charging energy. Finally, it is assumed that there are no low energy single particle states on the island apart from the Majorana states.

These assumptions can lead to conflicting practical requirements. To decrease the overlap between Majorana modes, it is convenient to increase the length of the superconducting island. This will naturally increase the capacitance of the island as well, decreases the charging energy. With standard gate designs, the charging energy for $2\ \mu\text{m}$ long island will already be below 20 mK [24]. This demonstrates that the qubit design will have to carefully consider electrostatics beyond its effects on the topological phase diagram discussed in chapter 6. For a superconducting island, the even-odd free energy difference determining the minimum energy of an unpaired quasiparticle on the island decreases with temperature and magnetic field [25, 26]. When it is reduced to zero, there is essentially no energy gap for single particle excitations anymore. At this point, unpaired quasiparticles are no longer restricted to states involving Majorana zero modes, spoiling any qubit operations we might want to perform. For larger islands, this will happen at lower temperatures and magnetic fields. As a finite magnetic field is required to reach the topological phase transition, and a finite temperature is unavoidable, making the island larger makes us more susceptible to this problem. Fortunately, the critical temperature scales logarithmically with island volume, but the combination with a finite magnetic field could still limit the island length to a few microns at best if Al is used as the superconductor. Most theoretical estimates show significant finite size overlap between the Majorana zero modes for islands this size. An alternative to increasing the size of the island is to increase the topological gap, decreasing the Majorana coherence length. This can be achieved for example by increasing the spin-orbit coupling strength, or by using a superconductor with a larger gap. Because this requires changing the material system, this option is not appealing as it would involve starting the optimization cycle from the beginning.

Assuming these design issues can be overcome, we now turn to the question of how qubit operation is affected in case local zero modes are present in the system. We will focus on the Majorana box qubit proposed in ref. [22], but the discussion is general to qubit proposals which rely on locally coupling to a single Majorana zero mode [9]. Figure 9.2 shows a schematic of a Majorana box qubit [22]. It consists of two superconducting nanowires (dark green) connected by a superconducting bridge (light green). Together,

they form a superconducting island with a finite charging energy. The superconducting bridge allows Cooper pairs to flow freely between the two wires, quenching the mutual charging energy while preventing quasiparticles from moving across. The island is coupled to quantum dots (purple) via tunnel barriers (white) at each wire end. The quantum dots are also connected to each other in pairs through a reference arm (gray).

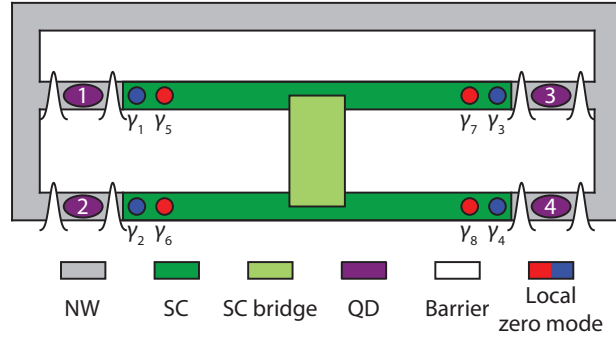


Figure 9.2: **Majorana box qubit with local zero modes.** Schematic representation of a Majorana box qubit. While in ref. [22] Majorana zero modes are present at the ends of the superconducting wires (green) which can be coupled to the quantum dots (purple), here we consider the case where the wires are still in the trivial regime, and feature local zero modes (blue and red circles) near the junctions with the dots.

In the original proposal, both nanowires are in the topologically non-trivial regime, hosting pairs of Majorana zero modes, labelled γ_1 through γ_4 (blue circles). The superconducting island is assumed to be long enough to avoid significant overlap of the Majorana wave functions. The parity of the island ground state can then be written as

$$P = - \prod_{i=1}^4 \gamma_i = \pm 1. \quad (9.1)$$

We assume the total parity of the island is even ($P = +1$), with the charging energy preventing any additional quasiparticles from tunneling into the island. In this case, the four Majorana zero modes form a two level system, which can be manipulated by the Pauli operators

$$\begin{aligned} \hat{x} &= i\gamma_1\gamma_3 = i\gamma_2\gamma_4 \\ \hat{y} &= -i\gamma_2\gamma_3 = -i\gamma_1\gamma_4 \\ \hat{z} &= i\gamma_1\gamma_2 = i\gamma_3\gamma_4. \end{aligned} \quad (9.2)$$

The parity of the Majorana pair consisting of γ_1 and γ_2 can be read out using the following procedure. The quantum dots 1 and 2 are initialized in a well-known charge state, sharing a single electron between them, e.g. one electron on dot 1, and zero on dot 2. When the energy levels of the dots are brought on resonance with each other, the electron will tunnel between the dots with a rate that depends on the tunnel coupling in the

reference arm and the coupling through the superconducting island¹. After some time, the dot energy levels are detuned from each other, and the charge on dot 1 is read out using a charge sensor. Because the coupling through the superconducting island depends on the parity of γ_1 and γ_2 , the charge readout projects the Majorana qubit into an eigenstate of the \hat{z} operator. Similarly, the qubit state can be projected along different axes by coupling different quantum dots via the reference arm and cotunneling process corresponding to the desired operator, e.g. quantum dots 1 and 3 to measure \hat{x} .

We now examine the situation where both wires are in the trivial regime, but have a local zero mode at each end of both superconducting wires. The additional Majorana modes constituting these zero modes are labeled γ_5 through γ_8 (red circles). As discussed in chapter 8, the red Majoranas couple to neither the blue Majoranas nor the quantum dots. In this sense, the operation of the box qubit is unchanged. However, an important distinction between the original proposal and the one shown here is the fact that the ground state degeneracy of the island is higher. We can write the different states of the island as $|n_1 n_2 n_3 n_4\rangle$, with $n_i = \frac{1}{2}(1 + i\gamma_{2i-1}\gamma_{2i}) = 0, 1$ the occupation number of a Majorana pair. We divide the states into a “bright” sector $|n_1 n_2\rangle$, consisting of Majoranas 1 through 4 which can interact with the outside, and a “dark” sector $|n_3 n_4\rangle$, consisting of Majoranas 5 through 8, which do not.

Because we can only interact with the Majoranas in the bright sector, we are under the impression that the total parity constraint restricts us to the computational states $|n_1 n_2\rangle = |00\rangle, |11\rangle$. However, the existence of the dark sector means that other states, such as $|01\rangle \otimes |01\rangle$, have the same total parity. What is problematic is the fact that if we now measure the parity of γ_1 and γ_2 , we no longer necessarily project γ_3 and γ_4 into the same parity, moving us out of our computational space. In principle the bright and dark sectors should be completely decoupled, and since the dark sector does not take part in any interactions with the quantum dots, we can assume that it stays in a fixed state such as $|n_3 n_4\rangle = |00\rangle$, restoring our ability to operate the qubit in the bright sector.

While at first glance it seems we can still operate the qubit as if we have non-local Majorana zero modes even if the zero modes are in fact local, there are some error processes to consider. A possible error process is a Cooper pair getting split into two quasiparticles, which each occupy a previously unoccupied pair of Majorana modes. If only the bright sector exists on the island, this corresponds to a bit-flip error, which can be detected. If one of the quasiparticles occupies a pair of Majorana modes in the dark sector, however, this process moves us outside our computational space, even though the total parity of the island has not changed. This can be a problem because we have no way to change the occupancy in the dark sector from the outside. This process is exponentially suppressed by the superconducting gap, and should therefore be rare if the gap is large enough.

We might try to avoid this situation altogether by creating a sufficiently large overlap be-

¹As the total parity of the island should remain fixed, this coupling should be achieved through a virtual cotunneling process.

tween γ_5 and γ_7 such that they split to finite energy, eliminating the dark sector from the ground state subspace. If this is possible we essentially recover the situation of a single topological phase with non-local Majorana zero modes. It seems unlikely we will be able to do so without also creating substantial overlap between γ_1 and γ_3 , which should be avoided as much as possible as it leads to dephasing [27]. It is also worth noting that while the Majoranas comprising a local zero mode are exponentially decoupled, their coupling is still finite, and depends only on local parameters. This means we cannot rely on increasing the system size to reduce the effect of this coupling. On top of that, there are now more such residual couplings as the total number of Majoranas has doubled. Compared to the case of non-local Majoranas, it is thus expected that a qubit based on local zero modes will be less robust to noise.

The basic building blocks for creating topological qubits based on semiconductor nanowire networks are falling into place, but it remains to be seen if they can fit together in a way that creates qubits with a significant advantage over currently more advanced platforms. In any case, even if the quest to build a topological qubit is ultimately unsuccessful, there is a lot of physics left to be discovered in hybrid superconductor-semiconductor systems. To quote the motivational speaker Jim Rohn: “Whatever good things we build end up building us.”

REFERENCES

- [1] R. L. M. Op het Veld et al., To be published.
- [2] F. Krizek, J. E. Sestoft, P. Aseev, S. Marti-Sanchez, S. Vaitiekėnas, L. Casparis, S. A. Khan, Y. Liu, T. Stankevič, A. M. Whitar, A. Fursina, F. Boekhout, R. Koops, E. Uccelli, L. P. Kouwenhoven, C. M. Marcus, J. Arbiol, and P. Krogstrup, *Field effect enhancement in buffered quantum nanowire networks*, Phys. Rev. Materials **2**, 093401 (2018).
- [3] W. Yi, A. A. Kiselev, J. Thorp, R. Noah, B.-M. Nguyen, S. Bui, R. D. Rajavel, T. Husain, M. F. Gyure, P. Kratz, Q. Qian, M. J. Manfra, V. S. Pribiag, L. P. Kouwenhoven, C. M. Marcus, and M. Sokolich, *Gate-tunable high mobility remote-doped InSb/In_{1-x}Al_xSb quantum well heterostructures*, Applied Physics Letters **106**, 142103 (2015).
- [4] F. Qu, J. van Veen, F. K. de Vries, A. J. A. Beukman, M. Wimmer, W. Yi, A. A. Kiselev, B.-M. Nguyen, M. Sokolich, M. J. Manfra, F. Nichele, C. M. Marcus, and L. P. Kouwenhoven, *Quantized Conductance and Large g-Factor Anisotropy in InSb Quantum Point Contacts*, Nano Letters **16**, 7509 (2016).
- [5] A. Haim, E. Berg, F. von Oppen, and Y. Oreg, *Signatures of Majorana Zero Modes in Spin-Resolved Current Correlations*, Phys. Rev. Lett. **114**, 166406 (2015).
- [6] D. J. Clarke, *Experimentally accessible topological quality factor for wires with zero energy modes*, Phys. Rev. B **96**, 201109 (2017).
- [7] E. Prada, R. Aguado, and P. San-Jose, *Measuring Majorana nonlocality and spin structure with a quantum dot*, Phys. Rev. B **96**, 085418 (2017).

- [8] M.-T. Deng, S. Vaitiekėnas, E. Prada, P. San-Jose, J. Nygård, P. Krogstrup, R. Aguado, and C. M. Marcus, *Nonlocality of Majorana modes in hybrid nanowires*, Phys. Rev. B **98**, 085125 (2018).
- [9] A. Vuik, B. Nijholt, A. R. Akhmerov, and M. Wimmer, *Reproducing topological properties with quasi-Majorana states*, (2018), arXiv:1806.02801 .
- [10] Y.-H. Lai, J. D. Sau, and S. Das Sarma, *Presence versus absence of end-to-end nonlocal conductance correlations in Majorana nanowires: Majorana bound states versus Andreev bound states*, (2019), arXiv:1901.02655 .
- [11] S. Das Sarma, J. D. Sau, and T. D. Stanescu, *Splitting of the zero-bias conductance peak as smoking gun evidence for the existence of the Majorana mode in a superconductor-semiconductor nanowire*, Phys. Rev. B **86**, 220506 (2012).
- [12] T. O. Rosdahl, A. Vuik, M. Kjaergaard, and A. R. Akhmerov, *Andreev rectifier: A non-local conductance signature of topological phase transitions*, Phys. Rev. B **97**, 045421 (2018).
- [13] A. Grivnin, E. Bor, M. Heiblum, Y. Oreg, and H. Shtrikman, *Concomitant opening of a topological bulk-gap with an emerging Majorana edge-state*, (2018), arXiv:1807.06632 .
- [14] Y. Huang, J. D. Sau, T. D. Stanescu, and S. Das Sarma, *Quasiparticle gaps in multi-probe Majorana nanowires*, (2018), arXiv:1809.08250 .
- [15] T. D. Stanescu and S. Das Sarma, *Building topological quantum circuits: Majorana nanowire junctions*, Phys. Rev. B **97**, 045410 (2018).
- [16] M. Hell, K. Flensberg, and M. Leijnse, *Distinguishing Majorana bound states from localized Andreev bound states by interferometry*, Phys. Rev. B **97**, 161401 (2018).
- [17] L. Fu, *Electron Teleportation via Majorana Bound States in a Mesoscopic Superconductor*, Phys. Rev. Lett. **104**, 056402 (2010).
- [18] S. Vijay and L. Fu, *Teleportation-based quantum information processing with Majorana zero modes*, Phys. Rev. B **94**, 235446 (2016).
- [19] R. Schuster, E. Buks, M. Heiblum, D. Mahalu, V. Umansky, and H. Shtrikman, *Phase measurement in a quantum dot via a double-slit interference experiment*, Nature **385**, 417 (1997).
- [20] T. Hyart, B. van Heck, I. C. Fulga, M. Burrello, A. R. Akhmerov, and C. W. J. Beenakker, *Flux-controlled quantum computation with Majorana fermions*, Phys. Rev. B **88**, 035121 (2013).
- [21] D. Aasen, M. Hell, R. V. Mishmash, A. Higginbotham, J. Danon, M. Leijnse, T. S. Jespersen, J. A. Folk, C. M. Marcus, K. Flensberg, and J. Alicea, *Milestones Toward Majorana-Based Quantum Computing*, Phys. Rev. X **6**, 031016 (2016).

- [22] S. Plugge, A. Rasmussen, R. Egger, and K. Flensberg, *Majorana box qubits*, *New Journal of Physics* **19**, 012001 (2017).
- [23] T. Karzig, C. Knapp, R. M. Lutchyn, P. Bonderson, M. B. Hastings, C. Nayak, J. Alicea, K. Flensberg, S. Plugge, Y. Oreg, C. M. Marcus, and M. H. Freedman, *Scalable designs for quasiparticle-poisoning-protected topological quantum computation with Majorana zero modes*, *Phys. Rev. B* **95**, 235305 (2017).
- [24] S. M. Albrecht, A. P. Higginbotham, M. Madsen, F. Kuemmeth, T. S. Jespersen, J. Nygård, P. Krogstrup, and C. M. Marcus, *Exponential protection of zero modes in Majorana islands*, *Nature* **531**, 206 (2016).
- [25] M. T. Tuominen, J. M. Hergenrother, T. S. Tighe, and M. Tinkham, *Experimental evidence for parity-based $2e$ periodicity in a superconducting single-electron tunneling transistor*, *Phys. Rev. Lett.* **69**, 1997 (1992).
- [26] P. Lafarge, P. Joyez, D. Esteve, C. Urbina, and M. H. Devoret, *Two-electron quantization of the charge on a superconductor*, *Nature* **365**, 422 (1993).
- [27] C. Knapp, T. Karzig, R. M. Lutchyn, and C. Nayak, *Dephasing of Majorana-based qubits*, *Phys. Rev. B* **97**, 125404 (2018).

ACKNOWLEDGEMENTS

When I first joined QuTech, the transition from Quantum Transport to QuTech had just started to take shape. The first years were marked by fast growth and the accompanying organizational problems. QuTech has since blossomed into a vibrant research community, and I have truly enjoyed my time here. None of this would have been possible without Leo. Leo, thank you for creating a research atmosphere based on genuine passion and scientific rigor. I admire your ability to inspire people and to ask exactly the right questions to get to the core of a physical problem. I also want to thank Attila for being my copromotor, and Ronald, Lieven, Leo DC and all the other QuTech PIs for creating a working environment I enjoyed almost every single day.

My research wouldn't have been possible without the nanowires grown in the groups of Erik Bakkers and Chris Palmstrøm. Special thanks to Sasa, Roy, and Sonia for providing us with excellent samples and answering all my naive questions about material science. I also want to thank Michael and Adriaan for letting me use their code and play theorist for a few months.

When I first joined Leo's research group, it immediately felt like a warm bath. David, Vincent, and Kun, thank you for welcoming me with open arms putting me through nanowire boot camp. After this introduction and some detours I ended up working in the ZBP team with Hao, which was the best decision of my PhD. Hao, without you the ZBP team would never have been as succesful as it has been over the past few years. Thank you for teaching me to be more excited about cool data, and that done is better than perfect. Önder, Jouri, Guan, Di, Kiefer, Qing, Vanessa, and Bart, thank you for sharing research challenges with me over the years, it has been a privilege. A special thanks to Yoram for tackling the Ultra Technical System with me to see if it would improve our devices (sadly, it did not).

Outside the ZBP team, Topo has sprawled into many different but related research activities. With these new activities also come new people, who add their unique personalities to the Topo ecosystem. With the risk of forgetting someone, I want to thank Jasper, Damaz, Willemijn, Francesco, Stijn, John, Jie, Daniël, Luca, Arno, Matt, Nikolai, Nicolò, Amrita, Dom, Vukan, Srijit, Christian, Ting, Lin, and all the others who helped make Topo the best roadmap in all of QuTech. Braiding 2020!

Sometimes the other roadmaps in QuTech are pretty cool too. Toivo, Jelmer, Udit, Suzanne, Stefan, Anais, Nodar, Adriaan, Niels, Chris, Jonas, Nathan, Thijs, Sal, Ramiro, Guoji, thank you for all the good times at the various uitjes and barbecues. The IDEA League summer school holds particularly good memories. Arne, Philip, Patrick, Felix, and all the

other guys from Aachen, I hope we will continue to have regular reunions.

The scientific progress at QuTech would surely come to a grinding halt without the excellent organisational efforts provided by the support staff. Marja, Yuki, Simone, Jenny, Chantal, and Joanna, thank you for helping me navigate all the forms and regulations the TU Delft has to offer. I doubt a PhD student could survive four years of working in the lab without the aid of the skilled QuTech technicians. Jason, Olaf, Mark, Jelle, Remco, and Siebe, many thanks for keeping our labs running and the cooling water flowing. I also want to thank Raymond, Raymond, Marijn, and the guys at DEMO for taking the time to answer any and all electronics questions, and teaching me how to solder. Finally, I want to express my appreciation for the Kavli Nanolab staff for keeping our cleanroom running, my research would have been impossible without you.

A few special people have been with me every step of the way on my PhD journey. Florian, you are the avatar of the QT spirit. I hope to encounter this energy in Portland in the near future. James, thank you for drinking with me when I was feeling down. And when I was happy. And all the other times as well. Norbert, I think we both agree that chess is a more interesting game after a few beers. Your environmentalism is both an inspiration and neverending annoyance. Peter, coming up with new variations on your last name has been one of my favorite ways to pass the time. I also want to thank your parents for giving you the silliest possible middle name. Fokko, it is a great honor to have the distinguished doctor as my paranymph. I'm sure you will have a sparkling future in Zürich. Alex, maybe one day I will actually find out what your house looks like. Also, there is one more thing that I need to address. And I hate to do this. Because you're a dear friend. But the amount of coffee you drink. Is blasphemous.

Wanneer het in Delft allemaal even te veel werd kon ik altijd even bijkomen in het zuiden van het land. Joris, Galin, Ferdi, Jim, en Marcel, bedankt voor alle steun in de loop der jaren. Ongeacht hoe lang we elkaar niet gezien hadden voelde het altijd als thuiskomen. Tot slot wil ik nog een dankwoord richten aan mijn familie. Pap, mam, Jasper, Kristel, zonder jullie was ik hier nooit gekomen. Woorden schieten tekort om uit te drukken hoeveel ik van jullie hou. Bedankt voor jullie liefde, geduld en goede raad tijdens de afgelopen jaren, ik hoop dat er nog vele zullen volgen.

CURRICULUM VITÆ

Michiel Wouter Adrianus DE MOOR

- 05-01-1987 Born in Tilburg, The Netherlands.
- 1999–2005 Gymnasium, Sondervick College, Veldhoven.
- 2005–2008 BSc Applied Physics, Eindhoven University of Technology.
- 2008–2014 MSc Applied Physics, Eindhoven University of Technology.
Supervisor: prof. dr. ir. E. P. A. M. Bakkers, Physics of Semiconductor Nanostructures group
Title: Photoluminescence Excitation Spectroscopy on Wurtzite Gallium Phosphide Nanowires
- 2014–2018 PhD Applied Physics, Delft University of Technology.
Promotor: prof. dr. ir. L. P. Kouwenhoven, Quantum Transport group/QuTech
Title: Quantum Transport in Nanowire Networks

LIST OF PUBLICATIONS

8. *Electric field tunable superconductor-semiconductor coupling in Majorana nanowires*
M. W. A. de Moor[†], J. D. S. Bommer[†], D. Xu[†], G. W. Winkler, A. E. Antipov, A. Bargerbos, G. Wang, N. van Loo, R. L. M. Op het Veld, S. Gazibegovic, D. Car, J. A. Logan, M. Pendharkar, J. S. Lee, E. P. A. M. Bakkers, C. J. Palmstrøm, R. M. Lutchyn, L. P. Kouwenhoven, H. Zhang
New Journal of Physics **20**, 103049 (2018)
7. *Quantized Majorana conductance*
H. Zhang[†], C.-X. Liu[†], S. Gazibegovic[†], D. Xu, J. A. Logan, G. Wang, N. van Loo, J. D. S. Bommer, **M. W. A. de Moor**, D. Car, R. L. M. Op het Veld, P. J. van Veldhoven, S. Koelling, M. A. Verheijen, M. Pendharkar, D. J. Pennachio, B. Shojaei, J. S. Lee, C. J. Palmstrøm, E. P. A. M. Bakkers, S. Das Sarma, L. P. Kouwenhoven
Nature **556**, 74–79 (2018)
6. *Ballistic Majorana nanowire devices*
Ö. Gül[†], H. Zhang[†], J. D. S. Bommer[†], **M. W. A. de Moor**, D. Car, S. R. Plissard, E. P. A. M. Bakkers, A. Geresdi, K. Watanabe, T. Taniguchi, L. P. Kouwenhoven
Nature Nanotechnology **13**, 192–197 (2018)
5. *Epitaxy of advanced nanowire quantum devices*
S. Gazibegovic[†], D. Car[†], H. Zhang[†], S. C. Balk, J. A. Logan, **M. W. A. de Moor**, M. C. Cassidy, R. Schmits, D. Xu, G. Wang, P. Krogstrup, R. L. M. Op het Veld, K. Zuo, Y. Vos, J. Shen, D. Bouman, B. Shojaei, D. Pennachio, J. S. Lee, P. J. van Veldhoven, S. Koelling, M. A. Verheijen, L. P. Kouwenhoven, C. J. Palmstrøm, E. P. A. M. Bakkers
Nature **548**, 434–438 (2017)
4. *Ballistic superconductivity in semiconductor nanowires*
H. Zhang[†], Ö. Gül[†], S. Conesa-Boj, M. P. Nowak, M. Wimmer, K. Zuo, V. Mourik, F. K. de Vries, J. van Veen, **M. W. A. de Moor**, J. D. S. Bommer, D. J. van Woerkom, D. Car, S. R. Plissard, E. P. A. M. Bakkers, M. Quintero-Pérez, M. C. Cassidy, S. Koelling, S. Goswami, K. Watanabe, T. Taniguchi, L. P. Kouwenhoven
Nature Communications **8**, 16025 (2017)
3. *InSb Nanowires with Built-In Ga_xIn_{1-x}Sb Tunnel Barriers for Majorana devices*
D. Car, S. Conesa-Boj, H. Zhang, R. L. M. Op het Veld, **M. W. A. de Moor**, E. Fadaly, Ö. Gül, S. Koelling, S. R. Plissard, V. Toresen, M. T. Wimmer, K. Watanabe, T. Taniguchi, L. P. Kouwenhoven, E. P. A. M. Bakkers
Nano Letters **17**, 721–727 (2017)
2. *Conductance Quantization at Zero Magnetic Field in InSb Nanowires*
J. Kammhuber, M. C. Cassidy, H. Zhang, Ö. Gül, F. Pei, **M. W. A. de Moor**, B. Nijholt, K. Watanabe, T. Taniguchi, D. Car, S. R. Plissard, E. P. A. M. Bakkers, L. P. Kouwenhoven
Nano Letters **16**, 3482–3486 (2016)

[†]Equal contribution.

1. *Optical study of the band structure of wurtzite GaP nanowires*
S. Assali, J. Greil, I. Zardo, A. Belabbes, **M. W. A. de Moor**, S. Koelling, P. M. Koenraad, F. Bechstedt, E. P. A. M. Bakkers, J. E. M. Haverkort *Journal of Applied Physics* **120**, 044304 (2016)